

November 2018

Optical Remote Sensing of Oil Spills in the Gulf of Mexico

Shaojie Sun

University of South Florida, sj.sun87@gmail.com

Follow this and additional works at: <https://digitalcommons.usf.edu/etd>



Part of the [Other Earth Sciences Commons](#)

Scholar Commons Citation

Sun, Shaojie, "Optical Remote Sensing of Oil Spills in the Gulf of Mexico" (2018). *USF Tampa Graduate Theses and Dissertations*.

<https://digitalcommons.usf.edu/etd/8144>

This Dissertation is brought to you for free and open access by the USF Graduate Theses and Dissertations at Digital Commons @ University of South Florida. It has been accepted for inclusion in USF Tampa Graduate Theses and Dissertations by an authorized administrator of Digital Commons @ University of South Florida. For more information, please contact digitalcommons@usf.edu.

Optical Remote Sensing of Oil Spills in the Gulf of Mexico

by

Shaojie Sun

A dissertation submitted in partial fulfillment
of the requirements for the degree of
Doctor of Philosophy
College of Marine Science
University of South Florida

Major Professor: Chuanmin Hu, Ph.D.
Kendra L. Daly, Ph.D.
Mark E. Luther, Ph.D.
Ian R. MacDonald, Ph.D.
David A. Palandro, Ph.D.

Date of Approval:
October 1, 2018

Keywords: oil detection, sun glint, thickness classification, oil emulsion, multiband, oil spill assessment

Copyright © 2018, Shaojie Sun

ACKNOWLEDGMENTS

I would like to thank my advisor Dr. Chuanmin Hu for his continuous support, encouragement and patient mentoring throughout my doctoral study. This dissertation would not have been possible without his guidance. I also want to thank my committee members, Dr. Kendra Daly, Dr. Mark Luther, Dr. Ian MacDonald, and Dr. David Palandro for their guidance of the dissertation work.

I want to thank my co-authors, and I am also grateful to friends and colleagues in the Optical Oceanography Lab (especially David English, Minwei Zhang, Brock Murch, Brian Barnes, Shuangling Chen, Mengqiu Wang, Lin Qi, Deyong Sun, and Yingcheng Lu) for their help and support. Thanks also go to Oscar Garcia-Pineda, Diana Garcia-Pineda, George Graettinger, Lisa DiPinto, Robyn Conmy, Daniel Hahn, Alan Guarino, and Douglas Mitchell for offering help and providing instructions in the field experiments.

This dissertation was made possible through a NASA Earth and Space Science Fellowship (NESSF, grant NNX16AN95H), NASA award NNX13AD08G from the Ocean Biology and Biogeochemistry program, grants from the BP/Gulf of Mexico Research Initiative (C-IMAGE II, and awards GOMA 23160700), and support from endowed fellowship from USF College of Marine Science (The Jack and Katharine Ann Lake Fellowship in Marine Science and Wells Fargo Fellowship). I also want to thank Water Mapping, LLC, Bureau of Safety and Environmental Enforcement, and ExxonMobil for supporting the field experiments of this dissertation.

TABLE OF CONTENTS

LIST OF TABLES.....	iii
LIST OF FIGURES.....	iv
ABSTRACT.....	vi
CHAPTER 1: INTRODUCTION.....	1
1. Oil spills in the Gulf of Mexico	1
2. Satellite remote sensing of oil spills.....	3
3. Research objectives	6
4. Dissertation outline.....	6
5. Literature cited.....	9
CHAPTER 2: SPECTRAL VARIABILITY OF OIL SLICKS UNDER DIFFERENT OBSERVING CONDITIONS.....	13
1. Note to Reader.....	13
CHAPTER 3: SUN GLINT REQUIREMENTS FOR THE REMOTE DETECTION OF SURFACE OIL FILMS.....	15
1. Note to Reader.....	15
CHAPTER 4: OIL SLICK MORPHOLOGY, HETEROGENEITY, AND THEIR IMPLICATIONS FOR OIL SPILL REMOTE SENSING.....	17
1. Note to Reader.....	17
CHAPTER 5: CLASSIFICATION OF OIL TYPE AND THICKNESS USING MULTIBAND OPTICAL REMOTE SENSING.....	19
Abstract.....	19
1. Introduction	20
2. Data and Methods	21
2.1 Field experiments.....	21
2.2 Optical imagery processing.....	23
3. Results.....	25
3.1 Oil emulsion	25
3.2 Non-emulsion.....	36
3.3 Classification scheme.....	43
4. Discussions.....	46
5. Conclusions	50
6. Literature cited.....	51

CHAPTER 6: OIL SPILL ASSESSMENT OF THE IXTOC-I ACCIDENT	53
1. Note to Reader	53
CHAPTER 7: ASSESSMENT OF THE MC-20 OIL SPILL	54
1. Note to Reader	54
CHAPTER 8: CASE STUDY: THE OIL TANKER COLLISION AND OIL SPILL EVENT IN THE EAST CHINA SEA	56
1. Note to Reader	56
CHAPTER 9: SUMMARY AND CONCLUSIONS	57
1. Research findings and potential impacts	57
2. Future research	59
2.1 Field measurements along with multiband or hyperspectral imaging cameras	59
2.2 Assessment of potential environmental impacts of natural hydrocarbon seeps in the Gulf of Mexico	60
3. Conclusions	61
4. Literature cited	62
APPENDIX A: THE CHALLENGES OF INTERPRETING OIL–WATER SPATIAL AND SPECTRAL CONTRASTS FOR THE ESTIMATION OF OIL THICKNESS: EXAMPLES FROM SATELLITE AND AIRBORNE MEASUREMENTS OF THE DEEPWATER HORIZON OIL SPILL	64
APPENDIX B: SUN GLINT REQUIREMENT FOR THE REMOTE DETECTION OF SURFACE OIL FILMS	81
APPENDIX C: OIL SLICK MORPHOLOGY DERIVED FROM AVIRIS MEASUREMENTS OF THE DEEPWATER HORIZON OIL SPILL: IMPLICATIONS FOR SPATIAL RESOLUTION REQUIREMENTS OF REMOTE SENSORS	90
APPENDIX D: SURFACE OIL FOOTPRINT AND TRAJECTORY OF THE IXTOC-I OIL SPILL DETERMINED FROM LANDSAT/MSS AND CZCS OBSERVATIONS	101
APPENDIX E: REMOTE SENSING ASSESSMENT OF OIL SPILLS NEAR A DAMAGED PLATFORM IN THE GULF OF MEXICO	112
APPENDIX F: TRACKING AN OIL TANKER COLLISION AND SPILLED OILS IN THE EAST CHINA SEA USING MULTISENSOR DAY AND NIGHT SATELLITE IMAGERY	124
APPENDIX G: PUBLICATION LIST AND COPYRIGHT CLEARANCES	134

LIST OF TABLES

Table 5. 1: Oil thickness from oil emulsions in the water tank..... 25

Table 5. 2: RTI-thickness relationships derived from histogram matching between Landsat RTI and
AVIRIS-derived oil emulsion thickness 31

LIST OF FIGURES

Figure 1. 1: a) Laboratory measured reflectance of oil on water with different thicknesses of Gippsland crude	5
Figure 5. 1: a) Oil experiment in a water tank by the USF College of Marine Science campus seawall in St. Petersburg, Florida	22
Figure 5. 2: Oil spill experiment at the Ohmsett facility in September 2017	23
Figure 5. 3: a) Reflectance spectra from the tank experiment	26
Figure 5. 4: True-color composite of oil slicks in two selected regions	27
Figure 5. 5: Hyperspectral (a) and multispectral (b) reflectance spectra from AVIRIS in the selected locations in Figs. 5.4c and 5.4d	27
Figure 5. 6: Scatter plot of relative thickness index (RTI, this study) versus USGS derived absolute oil thickness	28
Figure 5. 7: False-color composite (R: 1650; G: 835, B: 661 nm) of ETM+ imagery on 17 May 2010 showing brownish to reddish colors in (a) and mostly greenish colors in (b)	30
Figure 5. 8: Oil emulsion spectra in the two regions in Fig. 5.7	32
Figure 5. 9: Histograms of cumulative frequency from AVIRIS-derived oil thickness (after data binning to 30-m resolution) and from ETM+ derived oil thickness using the ETM+ RTI	32
Figure 5. 10: a) False-color composite (R: 1650; G: 835, B: 661 nm) of ETM+ imagery on 1 May 2010	33
Figure 5. 11: a) False-color composite (R: 1650; G: 835, B: 661 nm) of ETM+ imagery on 10 May 2010	34
Figure 5. 12: False-color composite (R: 1678; G: 839, B: 660 nm) of TM imagery on 25 May 2010 showing brownish to reddish colors in (a) and mostly greenish colors in (b).	35
Figure 5. 13: a) Reflectance spectra of Alaskan North Slope crude oil with various oil thicknesses (in μm) in a water tank.....	36
Figure 5. 14: Crude oil in the Ohmsett tank as viewed by WorldView-2 on 1 October 2017.....	38
Figure 5. 15: Digital photos taken on 2 October 2017 of the targets in Fig. 5.14a.....	39

Figure 5. 16: a) Top of atmosphere (TOA) reflectance of selected pixels in Fig. 5.14 and b) reflectance difference after subtracting the nearby water reflectance.	39
Figure 5. 17: a) OLI true color image (R: 655; G: 561, B: 483 nm) on 4 May 2014 showing oil slicks in the vicinity of the MC-20 site	41
Figure 5. 18: a) Reflectance spectra of selected pixels in Fig. 5.17a.....	41
Figure 5. 19: False-color RGB (R: 867 nm, G: 558 nm, B: 446 nm) composite MISR images taken at UTC 16:43 (at nadir, ± 4 minutes among all cameras) on 17 May 2010 in nine camera view angles.....	42
Figure 5. 20: Flow chart of the step-wise classification scheme to classify oil type and thickness from multiband remote sensing imagery.	46
Figure 5. 21: a) False-color composite (R: 1650; G: 835, B: 661 nm) of ETM+ imagery on 1 May 2010 during the DWH oil spill	47
Figure 5. 22: Typical reflectance of floating Sargassum, overlaid with positions of ETM+ green (green color), red (red color) and NIR (grey color) bands.....	48

ABSTRACT

Assessment of oil spills in the ocean using passive remote sensing (i.e., reflected sun light) faces two challenges: detect oil presence/absence and quantify oil volume. While the optical properties of oil allow it to be differentiated from the surrounding marine environment, sun glint can facilitate oil presence/absence detection because the oil-water spatial contrast is enhanced due to wave dampening. However, sun glint also modulates the magnitude and shape of the spectral reflectance of surface oil. In addition to this difficulty, the most critical challenge is how to quantify oil volume (or thickness) through remote sensing. To date, such quantifications have mainly been based on laboratory hyperspectral measurements over known oil volume for both oil emulsions and non-emulsions. Application of such laboratory-based methods to the real ocean environment faces two significant problems: 1) the observing conditions can be dramatically different (e.g., presence sun glint), and 2) lack of remote sensors with sufficient spectral bands and spatial resolution to apply the laboratory-based methods or to address the heterogeneity of oil slicks.

The objectives of this research are to understand oil slick reflectance spectra in the marine environment, delineate oil footprint, and develop practical methods to classify oil emulsions from non-emulsions and classify oil thickness, thus providing useful tools for oil spill assessment and for decision-making during an oil spill accident. Specifically, the objectives are to: 1) understand the various spatial and spectral oil-water contrasts in optical remote sensing imagery under different observing conditions; 2) develop algorithms and schemes to detect oil slicks, classify oil type (oil emulsion versus non-emulsion), and estimate oil thicknesses using multiband optical remote sensing imagery; and 3) apply the algorithms and schemes in the assessment of oil spill accidents. The Gulf of Mexico (GoM) is selected as the focus of this research because the continental slope of the GoM is recognized as a major hydrocarbon province

with widely distributed natural hydrocarbon seeps and where two of the largest marine oil spills occurred (the Ixtoc-I oil spill in 1979 and Deepwater Horizon oil spill in 2010).

The several approaches used to address these objectives include: 1) a literature search; 2) controlled tank measurements to understand oil-water spatial and spectral contrasts under various observing conditions; 3) a multi-sensor analysis to examine the spatial and spectral characteristics of oil slicks; 4) a step-wise classification scheme to classify oil type and oil thickness; and, 5) the application of the developed methods to several oil spill events through case studies.

Firstly, a thorough review of previous laboratory-developed reflectance—thickness relationships of both crude oil and oil emulsion is performed and compared to reflectance spectra collected by several satellite and airborne sensors (MERIS, MODIS, MISR, Landsat, AVIRIS) from the Deepwater Horizon oil spill (Chapter 2). Interpretation of the oil-water spatial and spectral contrasts under different observing conditions suggests that besides oil thickness, several other factors also affect oil–water spatial and spectral contrasts. These include sun glint strength, oil emulsification state, optical properties of surrounding water, and spatial and spectral resolutions of remote sensing imagery.

The impact of sun glint strength on oil slick detection is further investigated in Chapter 3, where concurrent (1-2 hours) image pairs collected by MODIS/Terra, MODIS/Aqua, and VIIRS over the same oil slicks from natural seeps are used to quantify the sun glint threshold, under which thin oil films cannot be observed. The threshold is determined to be 10^{-5} – 10^{-6} sr^{-1} for MODIS Terra and MODIS Aqua, and 10^{-6} – 10^{-7} sr^{-1} for VIIRS.

The impact of pixel resolution on spill detection is evaluated by studying oil slick morphology and size distributions for different oil thickness classes derived by the USGS using fine spatial resolution (~ 7.6 m) hyperspectral AVIRIS imagery collected over the Deepwater Horizon oil spill in the GoM (Chapter 4). Oil slicks are found to be elongated in shape for all thickness classes (≤ 50 μm but thicker than sheen, 50—200 μm , 200—1000 μm , and >1000 μm). They are found to be highly heterogeneous as well, where most

of the medium-resolution (30-m) pixels would be mixtures of different thickness classes of oil, or mixtures of oil and oil-free water. According to the AVIRIS derived results, to detect oil thicker than sheen with oil fractional pixel coverage >50% for at least half of the oil containing pixels, a 30-m or higher spatial resolution sensor would be needed. This suggests that most satellite remote sensing must consider mixed pixels when conducting analysis of spatial and spectral contrasts.

Based on the above understandings of oil-water spatial and spectral contrasts under different sun glint conditions, a stepwise classification scheme is proposed to extract oil features, classify oil types (oil emulsion versus non-emulsion), and classify oil thicknesses of each type under no glint condition and under various sun glint conditions in multiband optical imagery (Chapter 5). After oil feature extraction, reflectance in the Near Infrared and ShortWave Infrared (SWIR) bands is used to classify oil type, where elevated reflectance indicates oil emulsions. For oil emulsions, a histogram matching technique is used to compare the multiband measurements with hyperspectral AVIRIS measurements to classify oil thickness under various sun glint conditions. For the non-emulsion oil, a ratio between SWIR and blue bands is used to classify oil thickness. Furthermore, the spectral bands deemed necessary to apply the step-wise classification scheme and to discriminate false-positives are determined to be 480, 560, 670, 860, and 1600 nm.

The methods developed above are applied to several oil spill events as case studies (Chapter 6, 7 and 8). The Ixtoc-I oil spill footprint (over its > 9-month spill period) has been mapped with Landsat Multispectral Scanner and Coastal Zone Color Scanner (Chapter 6). The satellite-derived oil trajectory patterns agree well with physical modeling and field observations in the past. Another case study focuses on the ongoing oil spill in the MC-20 site in the northern GoM, where the spill is assessed systematically using medium- to high-resolution (10-30 m) optical remote sensing imagery between 2004 and 2016 (Chapter 7). These data allow for the determination of oil slick presence frequency and average spill size; further, the cumulative oil footprint are derived with daily discharge rate estimated. Finally, a multi-sensor

day-and-night approach, along with numerical modeling is used to track an oil tanker collision event in the East China Sea, where the unique value of VIIRS night time data is demonstrated (Chapter 8).

In summary, this dissertation provides a better understanding of oil-water spatial and spectral contrasts in multi-band optical remote sensing imagery, from which a step-wise classification scheme is developed to extract oil slick features, classify oil emulsion from non-emulsion, and estimate oil thicknesses in each type. The methods are then used in several case studies to assess oil spills. Although further research is still required to refine the methods and to provide direct field validation, the findings here expand our current knowledge in remote sensing of oil spills using multiband optical imagery. In particular, when compared with the remote sensing capacity during the DeepWater Horizon oil spill (where satellite remote sensing could only provide maps of oil presence/absence), the findings here suggest that much better data products can be derived from existing satellite platforms, to not only show oil presence/absence, but to also classify oil type and thickness, in future spills, for improved response and assessment.

CHAPTER 1:

INTRODUCTION

1. Oil spills in the Gulf of Mexico

Based on a report from the National Research Council (NRC, 2003), more than 1,300,000 metric tons of oil are released to the sea worldwide annually. For oil released into the ocean, more than 45% is from natural seeps, about 38% is from land-based sources, 12% comes from transportation activities such as oil tankers and pipelines, and 5% is from oil and gas exploration or production activities. Natural oil seeps have limited ecological impacts because the chronic rate of release allows surrounding ecosystems to adapt (Fisher, 1990; MacDonald et al. 1989; Sassen et al. 1999). Oil spill accidents, however, often release a large volume of hydrocarbons in a relatively short time period, thus potentially causing devastating impacts on the environment. Hydrocarbons can be toxic to multiple levels of the food web, from microscopic plankton (Almeda et al., 2014; Paul et al. 2013), to fishes and marine mammals (Schwacke et al., 2014; Venn-Watson et al., 2015). Massive oil spills may also contaminate shorelines (Michel et al., 2013) and deposit sediments to the seafloor (Chanton et al., 2015; Valentine et al., 2014), which may have long-term adverse impacts on the environment.

The Gulf of Mexico (GoM) contributes more than 98% of the outer continental shelf oil production in the United States (BSEE, 2018), and has been identified as one of the most highly polluted regions due to oil spills from oil tankers (Burgherr, 2007; Vieites et al., 2004). Moreover, the GoM has experienced two of the largest accidental oil spills in history, the DeepWater Horizon (DWH) oil spill in 2010, and the Ixtoc-I oil spill in 1979. The explosion and sinking of the DWH oil rig on 20 April 2010 in the northern GoM released an estimated 4.0 million barrels (3.19 million barrels after deducting recovered oil, U.S. vs BP et

al., 2015) of crude oil from a depth of ~1500 m (Crone and Tolstoy, 2010; McNutt et al., 2011), until the oil well was capped on 15 July 2010. The Ixtoc-I oil well, located in the Bay of Campeche, Mexico, blew out on 3 June 1979 and released oil at a depth of 50 m. It was not until 23 March 1980, 290 days after the blowout, that the well was finally capped (Jernelöv and Liden, 1981). The spill released 475,000 metric tons (3.3 million barrels, Patton et al., 1981) of crude oil from the well site (Jernelöv and Liden, 1981), making it the second largest accidental marine spill in history. In addition to these major oil spills, natural seeps are widely distributed across the GoM (De Beukelaer et al., 2003; MacDonald, 2015). Using Synthetic Aperture Radar (SAR) data, MacDonald et al. (2015) identified 914 distinct seep zones concentrated on the Texas-Louisiana Slope.

Crude oil released into the ocean undergoes a series of physical, chemical and biological processes, including oil spreading, wind and wave advection, evaporation, emulsification, dissolution, natural dispersion, sedimentation, photochemical oxidation, and biodegradation (NRC, 2003; Fingas, 2012). Oil on the sea surface will spread horizontally by gravity, viscosity, surface tension, winds, and currents (NRC, 2003; Fingas, 2012). Evaporation has the greatest effect on the amount of oil remaining on the surface after a spill. A light crude oil can lose more than 20% of its initial volume within a few hours of the spill (NRC, 2003). Another important weathering process is emulsification. Water-in-oil emulsification is the process of water getting entrained into oil in the form of small droplets. Mesostable emulsions and stable emulsions have reddish-brownish colors and stable emulsions often have water content greater than 60% (NRC, 2003). The formation of emulsions substantially increases the perceived spill volume and the viscosity as well, considerably slowing down the evaporation and biodegradation process and making cleanup operations more difficult (Fingas, 2012).

2. Satellite remote sensing of oil spills

With synoptic and frequent observations, remote sensing serves a vital role in assessing oil spills (Leifer et al., 2012; Fingas and Brown, 2014). The most frequently used remote sensing techniques include SAR, optical remote sensing, and thermal infrared imagery. Because oil can dampen both short-gravity and capillary waves on the ocean surface, a reduction in the backscattering SAR signal can be observed in oil containing image pixels under optimal wind conditions (Brekke and Solberg, 2005). SAR offers synoptic data under all sky conditions. However, Bio-films and bio-slicks (e.g., *Sargassum* mat and algal blooms), threshold wind areas, and wind sheltering can also cause negative contrast in SAR imagery. This makes it difficult to distinguish oil slicks from false-positives (Brekke and Solberg, 2005; Leifer et al., 2012). Moreover, SAR has been primarily used to detect oil extent instead of estimating oil thickness. Recent efforts suggest that SAR may be used to detect oil emulsions by volumetric fraction of oil (Garcia-Pineda et al., 2013; Jones and Holt, 2018; Macdonlad et al, 2015; Minchew, 2012), yet these preliminary demonstrations require further research to establish reliable algorithms.

Passive optical remote sensing is also widely used in oil spill detections (Leifer et al., 2012; Hu et al., 2009). Optical imagery from satellite sensors is useless under cloudy conditions, however, this weakness is compensated by wide-swaths (e.g., 2300 km for MODIS and 3300 km for VIIRS). Such wide-swath sensors can provide repeated coverage at any location in 1-2 days (more often in polar regions), at the price of reduced spatial resolutions (~300 m – 1 km) compared with SAR observations. Taking advantage of satellite constellations, recent medium-to high-resolution (finer than 30 m) sensor's revisit frequency has been greatly increased. For example, Sentinel-2 Multispectral Instrument (MSI, 10—60 m spatial resolution) has a revisit frequency of every five days when two satellites are combined, DigitalGlobe satellite constellation (including WorldView-1, GeoEye-1, WorldView-2, WorldView-3 and WorldView-4) offers intraday revisits around the globe at a spatial resolution <2 m, Pléiades 1A/1B constellation offers a daily revisit capability to any point on the globe at a spatial resolution of 2.8 m, and

the PlanetScope satellites provide a revisit frequency of once per day globally at a spatial resolution of 3–4 m. All these optical remote sensing satellite measurements, therefore, provide tremendous potentials in remote sensing of oil spills, yet our ability to realize such potential is still technically challenging.

Optical detection and quantification of floating oil on the ocean surface are based on the sun glint effect and optical properties of oil. First (and similar to SAR detections), the dampening of surface waves will enhance the spatial contrast of oil from water when under sun glint conditions (Hu et al., 2009; Jackson and Alpers, 2010). This sun glint effect in optical remote sensing, based on the same capillary-dampening principle of oil detection by SAR (Brekke and Solberg, 2005; Hu et al., 2011), has been used to detect oil slicks on the ocean surface (Macdonald, 1993; Adamo et al., 2009; Hu et al., 2009; Sun and Hu, 2016). The sun glint effect is actually caused by two factors: 1) dampening of the sea-surface capillary waves or gravity waves under optimal wind conditions, causing either higher or lower reflectance from oil than from water (Hu et al., 2009; Jackson and Alpers, 2010; Lu et al., 2016) and 2) the difference of refractive index between oil and water results in different Fresnel reflection, contributing additionally to the enhanced oil-water contrast (Lu et al., 2016). Oil also has different optical properties from water, with reflectance varying along increasing oil thickness: crude oils are characterized by high absorption in the blue band, which exponentially decays with increasing wavelengths. This results in lower reflectance in the blue and green wavelengths, as oil thickness increases (Wettle et al., 2009; Lu et al., 2013; Svejksky and Muskat, 2006; Fig. 1.1a). When oil is emulsified, the mixture of water molecules enables strong scattering in red, near infrared (NIR), and shortwave infrared (SWIR) wavelengths (Clark et al., 2010; Svejksky et al., 2012; Fig. 1.1b), thus exhibiting enhanced reflectance in the NIR-SWIR. Thick emulsified oil is also featured by C-H absorption at 1200 nm, 1700 nm and 2300 nm. The absorption depth at those featured wavelengths are associated with oil thicknesses by laboratory measurements – the thicker the oil emulsion, the deeper absorption depth in these wavelengths (Clark et al., 2010).

The spectral characteristics of oil can be used to infer relative oil thickness from optical remote sensing imagery (Lu et al., 2013; Wettle et al., 2009; Clark et al., 2010). Indeed, the laboratory-based look-up-tables (LUTs) of relating spectral reflectance to oil thickness have been used to map thicknesses of thick emulsions from the DWH oil spill in the GoM with hyperspectral data collected by airborne sensor Airborne Visible / Infrared Imaging Spectrometer (AVIRIS) (Clark et al., 2010).

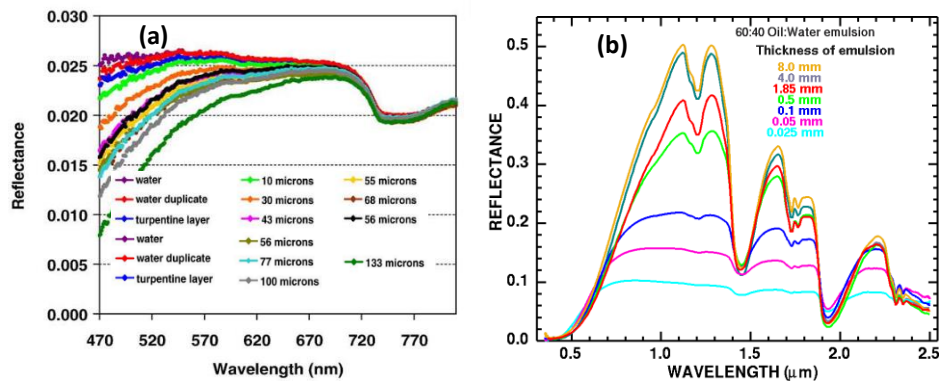


Figure 1. 1: a) Laboratory measured reflectance of oil on water with different thicknesses of Gippsland crude (Wettle et al., 2009). Note that reflectance in the blue spectra decreases with increasing oil thickness, but reflectance in the red spectra remains relatively stable. Figure reprinted from Wettle et al. (2009) with copyright permission from the publisher. b) Laboratory measured reflectance spectra of 60:40 oil-water emulsions with various oil thickness (Clark et al., 2010). The oil sample was collected in the Gulf of Mexico from the DWH oil spill. Figure reprinted from Clark et al. (2010). Note its dramatic contrast from panel a: with increasing oil thickness, there is little reflectance change in the blue-green wavelengths but there is dramatic reflectance change in the NIR-SWIR wavelengths.

The optical characteristics of oil and the laboratory-based LUT make it possible, at least in principle, to detect, classify (emulsion versus non-emulsion), and quantify oil thickness. However, these techniques face significant challenges when applied to satellite sensors such as Landsat or MODIS over the real ocean environment. These challenges include: 1) the presence of sun glint that makes these LUT-based approaches inapplicable; 2) that oil can be in the forms of emulsions and non-emulsions, yet these LUT-based approaches were designed for either oil emulsion or non-emulsion only; 3) the lack of spectral bands to apply the hyperspectral techniques; and 4) the spatial heterogeneity of oil (Sun et al., 2016)

makes the laboratory-based LUT invalid when applied to coarse-resolution data; other challenges include rough sea conditions that mix surface oil with water, and clouds that prevent any observation from satellites.

On the other hand, during accidental oil spills, the most available optical satellite sensors are Landsat (30-m), Sentinel-2/MSI (10-m), MODIS (250-m), VIIRS (375-m), and commercial high spatial resolution satellites (e.g., WorldView-3, 1.24 m). During a marine spill incident, optical satellites play a role in the ongoing situational awareness and possibly in tactical decision-making. Developing practical methods is an important step to fully utilize these systems.

3. Research objectives

The objectives of this research are to understand oil slick reflectance spectra in optical remote sensing imagery in the marine environment, to delineate oil footprint, and to develop practical methods to classify oil emulsions from non-emulsions and classify oil thickness. Meeting them will provide useful tools for oil spill assessment and for decision-making during an oil spill accident. The specific research objectives are:

- 1) Understand the various spatial and spectral oil-water contrasts in optical remote sensing imagery under different observing conditions.
- 2) Develop algorithms and schemes to detect oil slicks, classify oil type (oil emulsion versus non-emulsion), and estimate oil thicknesses using multiband optical remote sensing imagery.
- 3) Apply the algorithms and schemes in assessment of oil spill accidents.

4. Dissertation outline

To fulfill the research objectives described above, the dissertation is composed of four major components focusing on the understanding oil spectral variability in the real marine environment

(Chapter 2), quantifying environmental factors which affect oil spill detection and thickness estimation (Chapter 3 and Chapter 4), developing algorithms and stepwise schemes in classification of oil emulsions and non-emulsions as well as classification of oil thicknesses (Chapter 5), and assessing historical and ongoing oil spill accidents (Chapter 6, Chapter 7 and Chapter 8). Finally, the research findings are summarized, with recommendations provided on the use of optical remote sensing to detect and quantify oil spills.

Specifically, Chapter 2 presents various oil reflectance spectra and its contrast with water under different observing conditions. By examining the oil–water spectral contrasts from several multiband and hyperspectral measurements observed during the DWH oil spill, and by comparing the laboratory experimental results, the spatial/spectral contrasts of various oil slicks with water has been interpreted (Objective 1). In addition to oil thickness signal from oil optical properties, several other factors also affect oil–water spatial/spectral contrasts, including sun glint strength, oil emulsification state, optical properties of oil covered water, and spatial/spectral resolutions of remote sensing imagery. Despite the technical challenges, the results show that it is still possible to differentiate emulsified oil from non-emulsified oil under most circumstances, and it is possible to classify relative oil thickness for both emulsified and non-emulsified oil (Objective 2).

To further understand sun glint impact on oil spatial contrast with water (Objective 1), natural oil slicks in the western Gulf of Mexico are used to determine the sun glint requirement for the remote detection of surface oil films in Chapter 3. The threshold is determined using the same-day image pairs collected by MODIS Terra, MODIS Aqua, and VIIRS over the same oil slick locations where at least one of the sensors captures oil slicks. The determined sun glint thresholds here will provide critical information on which images are affected by sun glint impacts, thus reducing false negative detection and provides guidance for oil slicks detection, and classification (Objective 1 and Objective 2).

Using high spatial resolution (~7.6 m) hyperspectral AVIRIS derived oil slicks over the Deepwater Horizon oil spill in the Gulf of Mexico, slick lengths, widths and length/width ratios are statistically estimated in Chapter 4 to characterize oil slick morphology for different thickness classes. This provides a better understanding of the heterogeneity of oil slicks and the remote sensing spatial resolution that required to detect oil slicks and estimate oil thicknesses (Objective 1). According to results from the oil slicks detected by AVIRIS during the DWH oil spill, in order to detect oil thicker than sheen, with oil fractional pixel coverage >50% for at least half of the oil containing pixels, a 30-m or higher spatial resolution sensor would be needed.

Based on the above understandings of reflectance spectra of various slicks under different sun glint conditions, a stepwise scheme is then proposed to: extract oil slick features, classify emulsified oil from non-emulsified oil, and classify oil thicknesses via multiband optical remote sensing imagery in Chapter 5 (Objective 2). The elevated reflectance spectral features in the NIR (~860 nm) and SWIR (~1600 nm) bands were used to extract oil emulsions; increased and decreased reflectance caused by sun glint (in the visible to SWIR bands) was used to classify thick and thin oils. A band ratio model was used to classify the relative thicknesses of oil emulsions and thick oil. Required bands for the classifications and for discriminating oil from false positives were discussed in the chapter (Objective 1 and Objective 2).

In Chapter 6 to Chapter 7, the methods developed above are applied to the assessment of historical (Ixtoc-I oil spill) and ongoing (MC-20 oil spill) oil spill accidents (Objective 3). The Ixtoc-I oil spill footprint was derived using archived Landsat/MSS and CZCS imagery, in which the detected general patterns of oil trajectory agreed well with previously modelled results. The resulting cumulative oil footprint map was used to guide recent field measurements.

In Chapter 7, the ongoing MC-20 oil spill is assessed by Landsat and Sentinel-2/MSI imagery between 2004 and 2016, with statistical analysis of oil presence frequency in cloud-free images, oil slicks area, cumulative oil contaminated area, and an estimated oil discharge rate per day. Additional analysis

suggests that the detected oil slick distribution can be largely explained by surface currents, winds, and density fronts.

Chapter 8 shows a case example of satellite remote sensing being used in response to an oil spill accident, where a combination of multisensor day and night satellite imagery was used (Objective 3). An analysis of a recent SANCHI oil tanker collision event in January 2018 in the East China Sea showed that when traditional techniques using synthetic aperture radar or daytime optical imagery could not provide timely and adequate coverage, the VIIRS Nightfire product and Day/Night Band can be used to track the drifting tanker's pathway and locations. A numerical model to combine surface currents and wind can also simulate the tanker's locations. Satellite remote sensing during daytime shows smoke plumes and spilled oil on the ocean surface, some of which appears to be oil emulsion. This study demonstrates that a combination of all available remote sensing and modeling techniques can provide effective means to monitor marine accidents and oil spills to assist event response.

Chapter 9 summarizes major findings from this research, with recommendations provided for optical remote sensing of oil spills as well as for future research directions.

5. Literature cited

Adamo, M., De Carolis, G., De Pasquale, V., and Pasquariello, G. (2009). Detection and tracking of oil slicks on sun-glittered visible and near infrared satellite imagery. *International Journal of Remote Sensing*, 30(24), 6403-6427, doi:10.1080/01431160902865772

Almeda, R., Hyatt, C., and Buskey, E.J. (2014). Toxicity of dispersant Corexit 9500A and crude oil to marine microzooplankton. *Ecotoxicology and Environmental Safety*, 106, 76-85

Bureau of Safety and Environmental Enforcement (2018). Outer continental shelf oil and gas production. Retrieved on 4 Sept. 2018 from <https://www.data.bsee.gov/Production/OCSProduction/Default.aspx>

Brekke, C., and Solberg, A.H.S. (2005). Oil spill detection by satellite remote sensing. *Remote Sensing of Environment*, 95, 1-13

Burgherr, P. (2007). In-depth analysis of accidental oil spills from tankers in the context of global spill trends from all sources. *Journal of Hazardous Materials*, 140, 245-256

- Chanton, J., Zhao, T., Rosenheim, B.E., Joye, S., Bosman, S., Brunner, C., Yeager, K.M., Diercks, A.R., and Hollander, D. (2015). Using natural abundance radiocarbon to trace the flux of petrocarbon to the seafloor following the Deepwater Horizon oil spill. *Environmental Science & Technology*, 49, 847-854
- Clark, R.N., Swayze, G.A., Leifer, I., Livo, K.E., Kokaly, R., Hoefen, T., Lundeen, S., Eastwood, M., Green, R.O., and Pearson, N. (2010). A method for quantitative mapping of thick oil spills using imaging spectroscopy. US Geological Survey Open-File Report, 1167, 1-51
- Crone, T.J., Tolstoy, M. (2010). Magnitude of the 2010 Gulf of Mexico oil leak. *Science*, 330, 634
- De Beukelaer, S. M., MacDonald, I.R., Guinasso, N.L., and Murray, J.A. (2003). Distinct side-scan sonar, RADARSAT SAR, and acoustic profiler signatures of gas and oil seeps on the Gulf of Mexico slope. *Geo-Marine Letters*, 23(3-4), 177-186, doi:10.1007/s00367-003-0139-9
- Fingas, M. (2012). The basics of oil spill cleanup. CRC press
- Fingas, M., and Brown, C. (2014). Review of oil spill remote sensing. *Marine Pollution Bulletin*, 83, 9-23
- Fisher, C. R. (1990). Chemoautotrophic and methanotrophic symbioses in marine invertebrates. *Reviews in Aquatic Sciences*, 2, 399-436.
- Garcia-Pineda, O., MacDonald, I., Hu, C., Svejksky, J., Hess, M., Dukhovskoy, D., and Morey, S. (2013). Detection of floating oil anomalies from the DeepWater Horizon oil spill with synthetic aperture radar. *Oceanography*, 26
- Hu, C., Li, X., Pichel, W.G., and Muller-Karger, F.E. (2009). Detection of natural oil slicks in the NW Gulf of Mexico using MODIS imagery. *Geophysical Research Letters*, 36, L01604, doi:10.1029/2008GL036119
- Hu, C., Li, X., and Pichel, W.G. (2011). Detection of oil slicks using MODIS and SAR imagery. In: Morales, J., V. Stuart, T. Platt, and S. Sathyendranath (Eds.) (2011). Handbook of Satellite Remote Sensing Image Interpretation: Applications for Marine Living Resources Conservation and Management. EU PRESPO and IOCCG, Dartmouth, Canada. p21 - 34
- Jackson, C.R., and Alpers, W. (2010). The role of the critical angle in brightness reversals on sunglint images of the sea surface. *Journal of Geophysical Research*, 115, C09019, doi:10.1029/2009JC006037
- Jernelöv, A., Liden, O. (1981). Ixtoc I: a case study of the world's largest oil spill. *Ambio*. 10, 299–306.
- Jones, C.E., and Holt, B. (2018). Experimental L-Band airborne SAR for oil spill response at sea and in coastal waters. *Sensors*, 18, 641
- Leifer, I., Lehr, W.J., Simecek-Beatty, D., Bradley, E., Clark, R., Dennison, P., Hu, Y., Matheson, S., Jones, C.E., Holt, B., Reif, M., Roberts, D.A., Svejksky, J., Swayze, G., and Wozencraft, J. (2012). State of the art satellite and airborne marine oil spill remote sensing: Application to the BP Deepwater Horizon oil spill. *Remote Sensing of Environment*, 124, 185-209
- Lu, Y., Tian, Q., Wang, X., Zheng, G., and Li, X. (2013). Determining oil slick thickness using hyperspectral remote sensing in the Bohai Sea of China. *International Journal of Digital Earth*, 6, 76-93

- Lu, Y., Sun, S., Zhang, M., Murch, B., and Hu, C. (2016). Refinement of the critical angle calculation for the contrast reversal of oil slicks under sunglint. *Journal of Geophysical Research: Oceans*, 121, 148-161
- MacDonald, I.R., Boland, G.S., Baker, J.S., Brooks, J.M., Kennicutt, M.C., and Bidigare, R.R. (1989). Gulf of Mexico hydrocarbon seep communities. *Marine Biology*, 101, 235-247
- Macdonald, I. R., N. L. Guinasso, S. G. Ackleson, J. F. Amos, R. Duckworth, R. Sassen, and J. M. Brooks (1993). Natural oil slicks in the Gulf of Mexico visible from space. *Journal of Geophysical Research*, 98(C9), 16351, doi:10.1029/93jc01289.
- MacDonald, I.R., Garcia-Pineda, O., Beet, A., Daneshgar Asl, S., Feng, L., Graettinger, G., French-McCay, D., Holmes, J., Hu, C., Huffer, F., Leifer, I., Muller-Karger, F., Solow, A., Silva, M., and Swayze, G. (2015). Natural and unnatural oil slicks in the Gulf of Mexico. *Journal of Geophysical Research: Oceans*, 120, 8364-8380
- McNutt, M., Camilli, R., Guthrie, G., Hsieh, P., Labson, V., Lehr, B., Maclay, D., Ratzel, A., Sogge, M. (2011). Assessment of flow rate estimates for the Deepwater Horizon/Macondo well oil spill. Flow Rate Technical Group report to the National Incident Command, Interagency Solutions Group, March 10, 2011
- Michel, J., Owens, E.H., Zengel, S., Graham, A., Nixon, Z., Allard, T., Holton, W., Reimer, P.D., Lamarche, A., White, M., Rutherford, N., Childs, C., Mauseth, G., Challenger, G., and Taylor, E. (2013). Extent and degree of shoreline oiling: Deepwater Horizon oil spill, Gulf of Mexico, USA. *PLoS ONE*, 8, e65087
- Minchew, B. (2012). Determining the mixing of oil and sea water using polarimetric synthetic aperture radar. *Geophysical Research Letters*, 39, L16 607, doi:10.1029/2012GL052304
- NRC (2003). Oil in the sea III: Inputs, fates, and effects. National Academies Press, Washington, D.C.
- Patton, J.S., Rigler, M.W., Boehm, P.D., and Fiest, D.L. (1981). Ixtoc 1 oil spill: flaking of surface mousse in the Gulf of Mexico. *Nature*, 290, 235-238
- Paul, J.H., Hollander, D., Coble, P., Daly, K.L., Murasko, S., English, D., Basso, J., Delaney, J., McDaniel, L., and Kovach, C.W. (2013). Toxicity and mutagenicity of Gulf of Mexico waters during and after the DeepWater Horizon oil spill. *Environmental Science & Technology*, 47, 9651-9659
- Sassen, R., Joye, S., Sweet, S.T., DeFreitas, D.A., Milkov, A.V., and MacDonald, I.R. (1999). Thermogenic gas hydrates and hydrocarbon gases in complex chemosynthetic communities, Gulf of Mexico continental slope. *Organic Geochemistry*, 30, 485-497
- Schwacke, L.H., Smith, C.R., Townsend, F.I., Wells, R.S., Hart, L.B., Balmer, B.C., Collier, T.K., De Guise, S., Fry, M.M., Guillette, L.J., Jr., Lamb, S.V., Lane, S.M., McFee, W.E., Place, N.J., Tumlin, M.C., Ylitalo, G.M., Zolman, E.S., & Rowles, T.K. (2014). Health of common bottlenose dolphins (*Tursiops truncatus*) in Barataria Bay, Louisiana, following the DeepWater Horizon oil spill. *Environmental Science & Technology*, 48, 93-103
- Sun, S. and Hu, C. (2016). Sun glint requirement for the remote detection of surface oil films. *Geophysical Research Letters*, 43, 309-316, doi:10.1002/2015GL066884

- Sun, S., Hu, C., Feng, L., Swayze, G.A., Holmes, J., Graettinger, G., MacDonald, I., Garcia-Pineda, O., and Leifer, I. (2016). Oil slick morphology derived from AVIRIS measurements of the Deepwater Horizon oil spill: Implications for spatial resolution requirements of remote sensors. *Marine Pollution Bulletin*, 103, 276-285, doi:10.1016/j.marpolbul.2015.12.003
- Svejkovsky, J., and Muskat, J. (2006). Real-time detection of oil slick thickness patterns with a portable multispectral sensor. Report Submitted to the U.S. Department of the Interior Minerals Management Service, Herndon, VA, July 31, 2006, Contract No. 0105CT39144
- Svejkovsky, J., Lehr, W., Muskat, J., Graettinger, G., and Mullin, J. (2012). Operational Utilization of Aerial Multispectral Remote Sensing during Oil Spill Response. *Photogrammetric Engineering & Remote Sensing*, 78(10), 1089-1102
- United States of America v. BP Exploration & Production, Inc., et al. (2015). Findings of fact and conclusions of law: phase two trial. In re: oil spill by the oil rig "Deepwater Horizon" in the Gulf of Mexico, on April 20, 2010. U.S. District Court for the Eastern District of Louisiana, No. MDL 2179, Doc. 14021, (Retrieved from <http://www.laed.uscourts.gov/OilSpill/Orders/1152015FindingsPhaseTwo.pdf>)
- Valentine, D.L., Fisher, G.B., Bagby, S.C., Nelson, R.K., Reddy, C.M., Sylva, S.P., and Woo, M.A. (2014). Fallout plume of submerged oil from Deepwater Horizon. *Proceedings of the National Academy of Sciences*, 111, 15906-15911
- Venn-Watson, S., Colegrove, K.M., Litz, J., Kinsel, M., Terio, K., Saliki, J., Fire, S., Carmichael, R., Chevis, C., Hatchett, W., Pitchford, J., Tumlin, M., Field, C., Smith, S., Ewing, R., Fauquier, D., Lovewell, G., Whitehead, H., Rotstein, D., McFee, W., Fougères, E., and Rowles, T. (2015). Adrenal gland and lung lesions in Gulf of Mexico common bottlenose dolphins (*Tursiops truncatus*) found dead following the Deepwater Horizon oil spill. *PLoS ONE*, 10, e0126538
- Vieites, D.R., Nieto-Roman, S., Palanca, A., Ferrer, X., and Vences, M. (2004). European Atlantic: the hottest oil spill hotspot worldwide. *Naturwissenschaften*, 91, 535-538
- Wettle, M., Daniel, P.J., Logan, G.A., and Thankappan, M. (2009). Assessing the effect of hydrocarbon oil type and thickness on a remote sensing signal: A sensitivity study based on the optical properties of two different oil types and the HYMAP and Quickbird sensors. *Remote Sensing of Environment*, 113, 2000-2010

CHAPTER 2:

SPECTRAL VARIABILITY OF OIL SLICKS UNDER DIFFERENT OBSERVING CONDITIONS

1. Note to Reader

This chapter have been accepted for publication by the journal of *IEEE Transactions on Geoscience and Remote Sensing*, doi:10.1109/TGRS.2018.2876091, and have been reproduced with permission from IEEE. The paper is provided in Appendix A. This paper is focused on understanding the spectral variability of oil slicks under different observing conditions and interpreting environmental factors that contribute to the oil-water spatial/spectral contrasts besides oil type and thickness. A brief summary of this paper is provided below.

APPENDIX A – The challenges of interpreting oil–water spatial and spectral contrasts for the estimation of oil thickness: Examples from satellite and airborne measurements of the Deepwater Horizon oil spill (Sun and Hu, 2018)

Oil reflectance spectra—thickness relationships of both crude and emulsified oil measured by previous laboratory experiments have been reviewed, and the published results are then compared with reflectance spectra collected by several satellite and airborne sensors (MERIS, MODIS, MISR, Landsat, AVIRIS) from the Deepwater Horizon oil spill. Interpretation of the spatial/spectral contrasts of various oil slicks under different environmental conditions suggest that besides oil thickness, several other factors also affect oil–water spatial/spectral contrasts, which include sun glint strength, oil emulsification state, optical properties of oil covered water, and spatial/spectral resolutions of remote sensing imagery. Despite the technical challenges, the results show that it is still possible to separate emulsified oil from non-emulsified oil under most

circumstances, and it is possible to classify relative oil thickness for both emulsified and non-emulsified oil.

CHAPTER 3:

SUN GLINT REQUIREMENTS FOR THE REMOTE DETECTION OF SURFACE OIL FILMS

1. Note to Reader

This chapter have been previously published in *Geophysical Research Letters*, 43, 309-316, and have been reproduced with permission from John Wiley and Sons. The paper is provided in Appendix B. This paper quantifies sun glint requirement for the remote detection of surface oil films in order to better understand the impact of sun glint on oil-water contrast. A brief summary of this paper is provided below.

APPENDIX B – Sun glint requirement for the remote detection of surface oil films (Sun and Hu, 2016)

It has been known that the presence of sun glint can enhance oil-water spatial contrast and thus facilitating oil slick detection in optical imagery. However, the strength of sun glint required to detect thin oil films has never been quantified objectively. Natural oil slicks in the western Gulf of Mexico are used to determine the sun glint threshold required for optical remote sensing of oil films. Thin oil films from the natural seeps are used here to minimize reflectance signal from oil optical properties (absorption and scattering). The threshold is determined using the same-day image pairs collected by Moderate Resolution Imaging Spectroradiometer (MODIS) Terra, MODIS Aqua, and Visible Infrared Imaging Radiometer Suite (VIIRS) (N = 2297 images) over the same oil slick locations where at least one of the sensors captures the oil slicks. For each sensor, statistics of sun glint strengths, represented by the normalized glint reflectance (L_{GN} , sr^{-1}), when oil slicks can and cannot be observed are generated. The L_{GN} threshold for oil film detections is determined to be 10^{-5} – 10^{-6} sr^{-1} for MODIS Terra and MODIS Aqua, and 10^{-6} – 10^{-7} sr^{-1} for VIIRS. Below these thresholds, no oil films can be detected, while above these thresholds, oil films can always be

detected except near the critical-angle zone where oil slicks reverse their contrast against the background water. The sun glint thresholds determined here will provide critical information on which images (or which portions of an image) can be used to search for oil, thus reducing false negative detection. Optimal wind speed for sun glint detection of oil films has also been explored in the study.

CHAPTER 4:
OIL SLICK MORPHOLOGY, HETEROGENEITY, AND THEIR IMPLICATIONS FOR OIL SPILL REMOTE
SENSING

1. Note to Reader

This chapter have been previously published in *Marine Pollution Bulletin*, 103, 276-285, and have been reproduced with permission from Elsevier. The paper is provided in Appendix C. This paper characterizes oil slick morphology for different thickness classes in order to better understand the heterogeneity of oil slicks and its implication for remote sensing spatial resolution to detect oil slicks and estimate oil thicknesses. A brief summary of this paper is provided below.

APPENDIX C – Oil slick morphology derived from AVIRIS measurements of the Deepwater Horizon oil spill: Implications for spatial resolution requirements of remote sensors (Sun et al., 2016)

Oil is highly heterogeneous on the ocean surface. Oil slick size distributions, and especially slick size for different oil thickness classes, can be very useful in interpreting oil footprint and thickness for sensors with different resolutions, in helping to make management decisions. Taking advantage of oil thicknesses that derived by fine spatial resolution (~7.6 m) hyperspectral AVIRIS data collected over the Deepwater Horizon oil spill in the Gulf of Mexico, slick lengths, widths and length/width ratios are estimated to characterize oil slick morphology for different thickness classes. All AVIRIS-detected oil slicks (N = 52,100 continuous features) are binned into four thickness classes: ≤ 50 μm but thicker than sheen, 50–200 μm , 200–1000 μm , and >1000 μm . The median lengths, widths, and length/width ratios of these classes range between 22 and 38 m, 7–11 m, and 2.5–3.3, respectively. The AVIRIS data are further aggregated to 30-m (Landsat

resolution) and 300-m (MERIS resolution) spatial bins to determine the fractional oil coverage in each bin. It is found that most pixels in MODIS and MERIS resolution will have thick oil coverage of only a few percent of a given pixel footprint, thus mixed pixel must be considered for spectral and spatial analyses using these coarse spatial resolution sensors. If 50% fractional pixel coverage is required to detect oil with thickness greater than seen for most oil containing pixels, a 30-m resolution sensor would be needed, according to results from detected oil slicks in the DWH oil spill by AVIRIS. Landsat may be an optimal compromise between spatial resolution and swath width in order to capture actual thick-oil coverage within a pixel and full oil spill footprint.

CHAPTER 5:

CLASSIFICATION OF OIL TYPE AND THICKNESS USING MULTIBAND OPTICAL REMOTE SENSING

Abstract

Optical characteristics of oil floating on water have been determined from laboratory measurements. However, the laboratory-based relationships between oil type/thickness and spectral reflectance face significant challenges when applied to multiband satellite sensors in the real marine environment, because of sun glint perturbations and because of the lack of hyperspectral bands. In this study, a stepwise classification scheme is proposed to extract oil features, classify oil types (oil emulsion versus non-emulsion), and classify oil thicknesses of each type under no glint condition and under various sun glint conditions in multiband optical imagery. After oil feature extraction, reflectance in the Near Infrared (NIR) and ShortWave Infrared (SWIR) bands is used to classify oil type, where elevated reflectance indicates oil emulsions. For the oil emulsions, a histogram matching is used to compare with hyperspectral Airborne Visible / Infrared Imaging Spectrometer (AVIRIS) measurements to classify oil thickness under various sun glint conditions. For the non-emulsion oil, a ratio between SWIR and blue bands is used to classify oil thickness. The spectral bands deemed necessary to apply the step-wise classification scheme and to discriminate false-positives are 480, 560, 670, 860, and 1600 nm. Application of the step-wise classification scheme to multiband sensors for the DeepWater Horizon oil spill leads to reasonable spatial patterns for oil slicks of different types and thicknesses, suggesting that it cannot only be used for retrospective analysis, but also serve as a practical means for assessment of oil spill events to facilitate mitigation efforts.

Keywords: Oil spill, optical remote sensing, hyperspectral, multi-spectral, oil emulsion, Landsat, MSI, AVIRIS; WorldView-2

1. Introduction

Detection of oil presence and quantifying oil thickness (or volume) on the surface ocean requires understanding of spectral and spatial contrasts between oil and water. As shown in the previous chapter, these contrasts have been characterized in laboratory measurements by other researchers. Basically, crude oils are characterized by high absorption in the blue band, which exponentially decays with increasing wavelengths, resulting in lower reflectance in the blue with increasing amount of oil (Wettle et al., 2009; Lu et al., 2013; Svejksky and Muskat, 2006). When oil is emulsified, the mixture of water enables strong scattering in red and near infrared (NIR) and shortwave infrared (SWIR) wavelengths (Clark et al., 2010; Svejksky et al., 2012), thus showing enhanced reflectance in the NIR-SWIR. Ongoing research suggests that these spectral characteristics of oil could be used to infer relative oil thickness from optical remote sensing imagery (Lu et al., 2013; Wettle et al., 2009; Clark et al., 2010; Svejksky and Muskat, 2006; Svejksky et al., 2012). In particular, the laboratory-based look-up-tables (LUTs) of relating spectral reflectance to oil thickness have been used to map oil emulsion thicknesses from the DeepWater Horizon (DWH) oil spill in the Gulf of Mexico (GoM) with hyperspectral data collected by the airborne Airborne Visible / Infrared Imaging Spectrometer (AVIRIS) (Clark et al., 2010).

The known optical characteristics of oil on water and the laboratory-based LUTs make it possible, at least in principle, to detect, classify (oil emulsion versus non-emulsion), and quantify oil thickness or volume. However, these LUTs face significant challenges when applied to multiband satellite sensors (i.e., Landsat) over the real ocean environment. These challenges include the presence of sun glint that makes these laboratory-based LUTs inapplicable, co-existence of multiple oil types (emulsion versus non-emulsion), and lack of spectral bands to apply the hyperspectral techniques developed from laboratory

measurements. The goal of this study is to develop a practical method to detect surface oil and to classify oil types (emulsion versus non-emulsion) and classify oil thicknesses of each type using existing multiband sensors such as Landsat Thematic Mapper (TM), Enhanced Thematic Mapper Plus (ETM+), Operational Land Imager (OLI), Sentinel-2 MultiSpectral Instrument (MSI), and WorldView-2 under various observing conditions.

2. Data and Methods

2.1 Field experiments

An oil tank experiment was conducted on 27 March 2018 by the seawall of the USF campus at St. Petersburg, Florida. Known volumes of Alaskan North Slope (ANS) crude and emulsified oil were put on the water surface in two identical black plastic oval tanks, each with a size of 1.3-m in length, 0.9-m in width, and 0.5-m in depth. The experimental setup is shown in Fig. 5.1. Initially, oil on the surface spread, but not completely evenly in the tank even after a few minutes. Surface oil thickness was therefore estimated as the oil volume divided by area of the tank. This thickness represents the equivalent thickness if oil was evenly distributed in the tank. Reflectance spectra were collected between 10 am and 1 pm local time (Eastern Daylight Time) using a portable SR-1900 Spectroradiometer (manufactured by Spectral Evolution, Inc) with 8° field of view at a height of ~1.5 meters above the tank. The spectrometer measures spectral reflectance in the wavelength range of 280—1900 nm, with a spectral resolution of ≤ 4 nm in 280—1000 nm and ≤ 10 nm in 1000—1900 nm. The resulting reflectance spectra were averaged over three separate measurements, with each measurement an average of ten continuous scans. The ANS emulsions with a 60:40 oil-to-water ratio were created by mixing oil and water in a food blender and then blended, after which the emulsions were put in a pan for six hours. The process was repeated three times. Another field experiment was conducted at the National Oil Spill Response Research & Renewable Energy Test

Facility (Ohmsett) in September — October 2017. Ohmsett features an above-ground concrete test tank of 203 m long by 20 m wide by 3.4 m deep. The tank is filled with 2.6 million gallons of clear saltwater. Four 6.1 x 6.1 m PVC squares and nine 1.6 x 1.6 m PVC squares with different volumes of oil within the squares were setup in the middle of the tank (Fig. 5.2), with the purpose of being measured by WorldView-2 satellite sensor to evaluate the sensor's capacity in determining oil thickness from pure oil pixels within the squares. A known volume of HOOPS crude oil was transferred to the 6.1 m squares and 1.6 m squares on 29 September 2017, in order to create different thicknesses of pure oil within the squares, assuming the oil could be evenly distributed in the squares. Concurrent with the squares setup, there was also a bulk discharge of 400 gallons of HOOPS crude oil in the southern part of the tank (Fig. 5.2). The bulk discharged oil was well confined in a small region by booms to the south and water springs from below to the north.



Figure 5. 1: a) Oil experiment in a water tank by the USF College of Marine Science campus seawall in St. Petersburg, Florida. Shaojie Sun and Chuanmin Hu were measuring the oil spectral reflectance using the SR-1900 spectrometer (photo credit: George Graettinger). Two identical tanks were set side by side, each other with same volume of b) crude oil and c) oil emulsions.

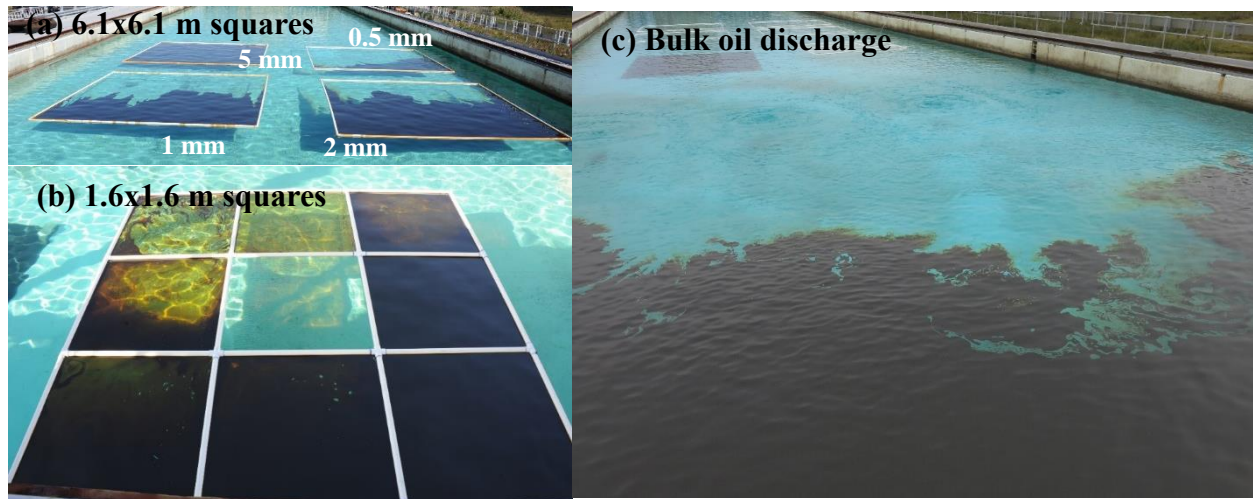


Figure 5. 2: Oil spill experiment at the Ohmsett facility in September 2017. a) Four 6.1 x 6.1 m squares, b) nine 1.6 x 1.6 m squares containing different volume of oil and clear water in the Ohmsett tank. The marked thicknesses in (a) were calculated as oil volume divided by the square area, assuming even distribution of the oil. c) Bulk discharge of 400 gallons of HOOPS crude oil south of the square setup region on 27 September 2017.

2.2 Optical imagery processing

Airborne Visible / Infrared Imaging Spectrometer (AVIRIS) measurements on 17 May 2010 over the DWH oil spill were used to test the multiband models to be developed in this study. AVIRIS collected hyperspectral data from 380 to 2500 nm in 224 spectral bands at a ground resolution of about ~ 7.6 m per image pixel on 17 May 2010. The data were first converted to apparent reflectance ($R(\lambda)$, dimensionless) by the USGS using the ACORN atmospheric correction module (AIG, 2001). $R(\lambda)$ was then used by the USGS to derive oil volume per pixel (<https://pubs.usgs.gov/of/2010/1167/downloads/figure16c-geotiff.tif>) of oil emulsions using the Tetracorder spectral shape matching algorithm described in Clark et al. (2003, 2010). Average oil thickness per pixel was then calculated as volume divided by the area of the pixel. Therefore, the oil thicknesses used in this study does not include water that is contained in the oil emulsions, but it simply indicates “oil” thickness after converting the emulsions into pure oil. The derived thickness map at 7.6-m resolution was reduced to 30-m resolution after spatial binning in order to accommodate the spatial resolutions of Landsat sensors (TM, ETM+, and OLI) (Sun et al., 2016).

Landsat TM and ETM+ data over the DWH oil spill and OLI data over the MC-20 oil spill were obtained from the USGS/EarthExplorer, and then processed to generate Rayleigh-corrected Reflectance ($R_{rc}(\lambda)$, dimensionless) using the ACOLITE software (20180611.0). Sun glint strength of the Landsat imagery was evaluated using the sun glint coefficient (L_{GN} , in units of sr^{-1}), estimated with the Cox and Munk (1954) model, wind speed, and solar and satellite geometry. Wind speed was retrieved from the Reanalysis-2 wind speed product of the National Centers for Environmental Prediction (NCEP). Solar and satellite geometry of Landsat measurement was calculated using the USGS “Landsat Angles Creation Tools” (<https://landsat.usgs.gov/solar-illumination-and-sensor-viewing-angle-coefficient-file>). Landsat cloud masks were created using the software Fmask (version 4.0, from <https://github.com/gersl/fmask>) through an object-based cloud and cloud shadow detection algorithm (Qiu et al., 2017; Zhu et al., 2015; Zhu et al., 2012).

In determining the best approaches to classify oil type (emulsion versus non-emulsion) and oil thickness, different band combinations and band ratios were tested, based on the principles of the spectral and spatial contrasts between oil and water. Furthermore, in order to convert the relative thickness into absolute thickness values, a method of histogram matching was developed to force the oil volume distributions derived from the multiband measurements to agree with AVIRIS-derived oil thickness maps. The underlying assumption is that under similar weathering conditions and in approximately similar locations relative to the DWH oil platform, the statistics of oil thickness observed from both measurements should be similar, regardless of the sun glint conditions. The various relationships between oil type/thickness and multiband reflectance under different conditions were used to construct the LUTs.

3. Results

3.1 Oil emulsion

Field experiments. The oil tank experiment showed increased reflectance in the NIR and SWIR wavelengths corresponding to thick emulsions (Fig. 5.3a). This agrees well with previous results by Clark et al. (2010). As shown in pictures in Fig. 5.3b, oil emulsions were not uniformly distributed in the tank due to their high viscosity, and actually formed scattered patches under calm conditions. The oil occupied surface area was estimated from digital photos taken above the tank, which was then used with the total oil volume to calculate the realistic oil thickness assuming all oil patches had the same oil thickness. For simplicity, oil thickness was also calculated as the total volume divided by the total tank area. In both approximations, oil thickness increased with oil volume, as shown in Table 5.1. The elevated reflectance in the NIR and SWIR wavelengths was a result of both increased emulsion thickness and increased emulsion coverage in the tank.

Table 5. 1: Oil thickness from oil emulsions in the water tank (Fig. 5.2). The first column is the thickness calculated from the oil volume and tank area, representing the equivalent thickness if oil were evenly distributed on the entire tank surface. The last column is the realistic thickness calculated from the oil volume and oil-occupied area. A subset of the tank area was selected for separating oil emulsion from water to avoid shadows from the tank. As the tank shadows changed with time, the total number of pixels here are different for different scenarios

Thickness from volume (μm)	Emulsion (# of pixels)	Water (# of pixels)	Total # of pixels	Emulsion/total ratio	Realistic thickness(μm)
750	110,000	200,000	310,000	0.36	2,000
500	100,000	190,000	290,000	0.35	1,400
100	36,000	230,000	260,000	0.14	730
50	35,000	240,000	280,000	0.13	390
10	26,000	190,000	220,000	0.12	86
5	19,000	190,000	210,000	0.09	56

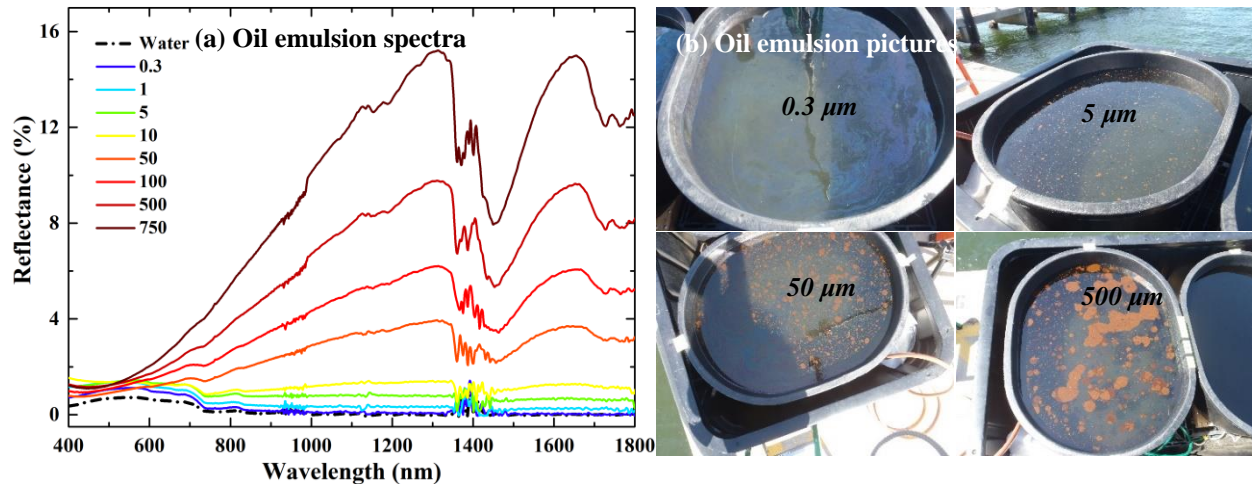


Figure 5. 3: a) Reflectance spectra from the tank experiment; (b) corresponding to different thickness of the oil emulsion. Note the elevated reflectance in the NIR to SWIR wavelengths in response to increased thicknesses (in μm). Here thickness is calculated as the total oil volume divided by the area of the tank. The pictures in (b) show different oil emulsion appearance and distribution in the tank. Note that the oil emulsion is very patchy and never homogeneous in the tank.

Hyperspectral AVIRIS imagery. A true color reflectance composite (R: 638; G: 550, B: 463 nm) shows reddish to brownish colors for oil emulsions in two selected regions (Figs. 5.4a and 5.4b) in AVIRIS run 10 over the DWH oil spill on 17 May 2010. A false color composite (R: 1612; G: 860, B: 638 nm), however, reveals mostly brownish colors in Fig. 5.4c and greenish to brownish colors in Fig. 5.4d. These different colors represent different oil emulsion states. The corresponding USGS oil fraction product (Clark et al., 2010) indicates that the green colored emulsions in Fig. 5.4d have a higher water content while the brown colored emulsions in Fig. 5.4c have more oil fractions in the emulsions (Figs. 5.4e and 5.4f). Spectra of selected points in Figs. 5.4e and 5.4f display different spectral shapes (Fig. 5.5), where the reflectance magnitude at 860 nm relative to reflectance at 1612 nm is an indicator of oil water fractions in the oil emulsions: higher reflectance at 860 nm indicate more water content in the emulsions, while higher reflectance at 1612 nm indicate more oil content in the emulsions (Fig. 5.5). The reflectance magnitude at 1612 nm is also related to the average oil thickness (i.e., total oil volume divided by the pixel size), as demonstrated in the USGS derived oil thickness map (Clark et al., 2010, in Figs. 5.4g and 5.4h).

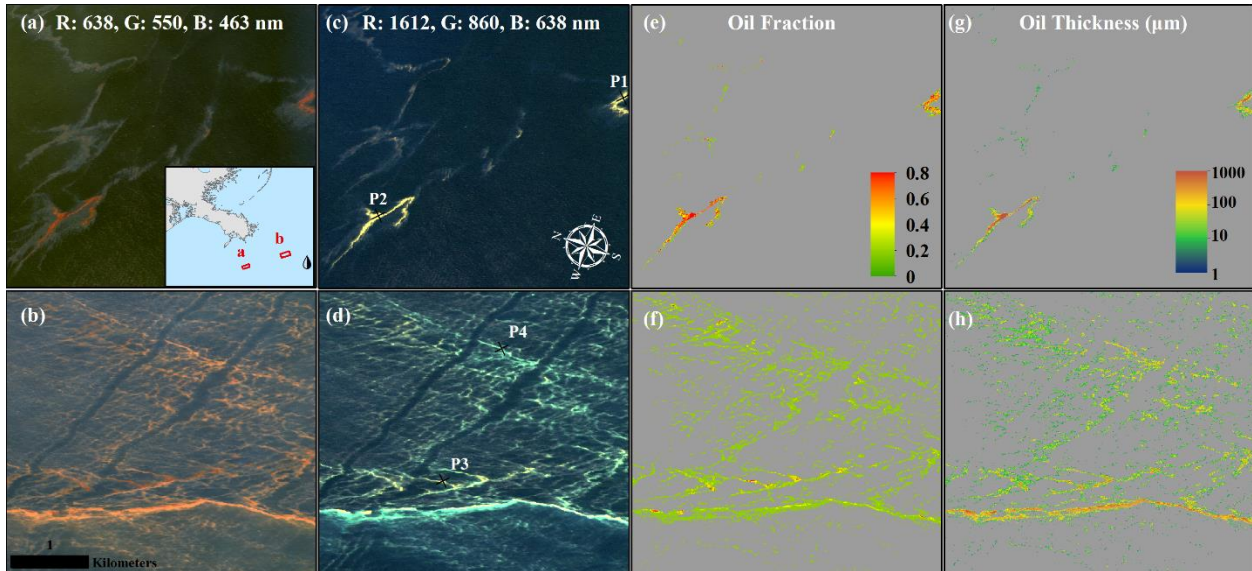


Figure 5. 4: True-color composite of oil slicks in two selected regions (a) and (b) in the AVIRIS imagery on 17 May 2010 during the DWH oil spill; False-color composites using different bands are shown in (c) and (d), respectively; Oil fraction maps in (e) and (f) and oil thickness maps in (g) and (h) are from USGS (Clark et al., 2010). Black droplet in the inset indicates the DWH oil platform location, while the locations of (a) and (b) are also annotated.

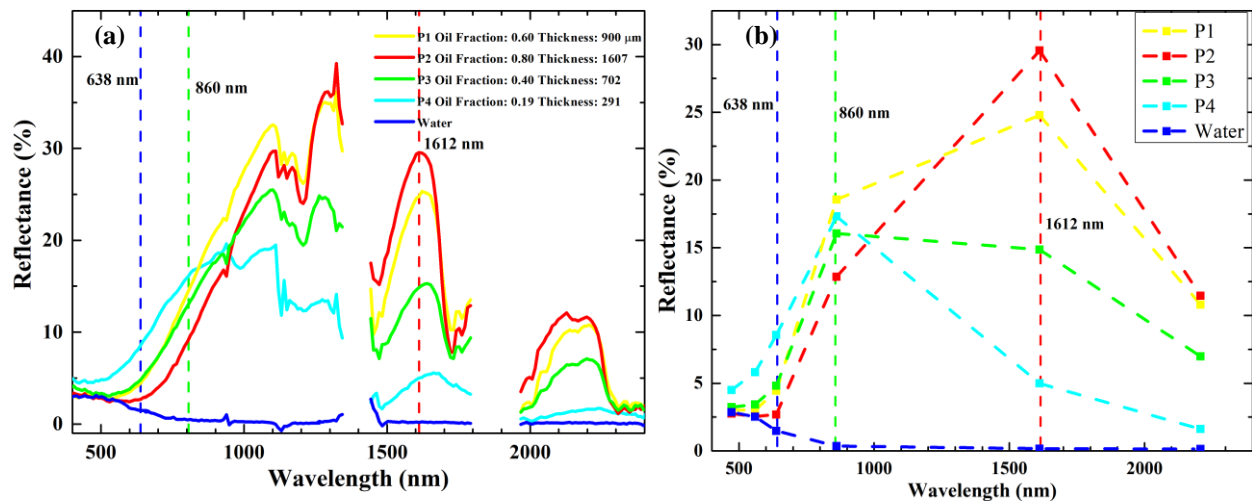


Figure 5. 5: Hyperspectral (a) and multispectral (b) reflectance spectra from AVIRIS in the selected locations in Figs. 5.4c and 5.4d, annotated with USGS derived oil fraction and oil thickness of the pixel.

Sun and Hu (2018) used a band ratio of SWIR (1612 nm) to blue (472 nm) to quantify relative oil thickness in the region of Fig. 5.4a, with higher ratios indicating thicker oil. Here the relationship of this

band ratio to USGS derived oil thicknesses (Clark et al., 2010) was re-assessed using statistical analysis from all the USGS mapped emulsion pixels of AVIRIS runs on 17 May 2010, which captured >30% of the core oil spill area (Sun et al., 2016). The statistical relationship in Fig. 5.6 shows that the relative emulsion thickness estimated from the SWIR to blue band ratio is tightly related to the absolute thickness estimated from the Clark et al. (2010) hyperspectral approach ($R^2 = 0.61$, $n = 497681$, $p < 0.05$, unbiased mean relative error = 139%), with the estimated thickness (T , μm) being modeled as:

$$\log_{10}(T) = 1.3303 * \log_{10}(RTI) + 1.8346 \quad (1)$$

where RTI is the Relative oil Thickness Index, calculated as the band ratio of SWIR (1612 nm) to blue (472nm) of AVIRIS images.

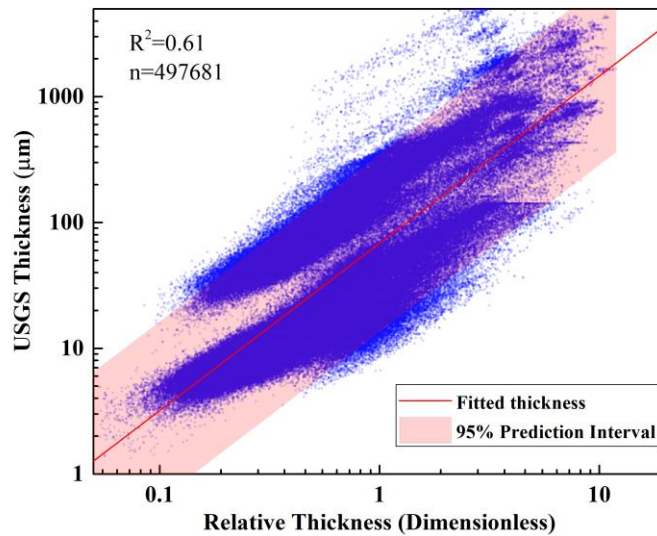


Figure 5. 6: Scatter plot of relative thickness index (RTI, this study) versus USGS derived absolute oil thickness (Clark et al., 2010).

Multiband Landsat imagery

Similar emulsion-induced colors in the false color composite (R: 1650; G: 835, B: 661 nm) have also been observed in the same day (17 May 2010) ETM+ image (Figs. 5.7 and 5.8) over the DWH oil spill. Figs. 5.7a and 5.4a, and Figs. 5.7b and 5.4b represent approximately the same regions (both regions are

within two km), although oil slicks were not at the same locations because the ETM+ image was collected four hours earlier than the AVIRIS image. Fig. 5.7a shows the brownish to reddish colors due to oil emulsions, while Fig. 5.7b shows the greenish colors due to oil emulsions, similar to the color patterns observed from the AVIRIS false color composite in those two regions. The AVIRIS image was captured under negligible sun glint conditions, while the ETM+ image was under weak sun glint in Fig. 5.7a ($L_{GN} = \sim 3E-3 \text{ sr}^{-1}$) and strong sun glint in Fig. 5.7b ($L_{GN} = \sim 1E-2 \text{ sr}^{-1}$), confirming the validity of identifying emulsion using the false color composite under both sun glint and non-glint conditions. While sun glint increases reflectance, the increase is spectrally flat, with minimal influence on the relative magnitudes between ~ 800 and ~ 1600 nm, as long as glint-induced reflectance is comparable to, or smaller than, the oil-water contrast in the absence of glint. The reflectance spectra (Fig. 5.8) of selected pixels in Fig. 5.7 clearly display the reflectance peaks in the 1650-nm or 835-nm band. Under weak sun glint conditions (Fig. 5.7a, $L_{GN} = \sim 3E-3 \text{ sr}^{-1}$), emulsions display lower than water reflectance in the blue green bands, but higher than water reflectance in the NIR and SWIR bands. This is because the emulsion signal overweighs sun glint caused negative contrast with water, while the negative contrast is due to oil's modulation of surface roughness. Under strong glint conditions (Fig. 5.7b, $L_{GN} = \sim 1E-2 \text{ sr}^{-1}$), emulsions show higher than water reflectance in all wavelengths, but still with a local peak in the 835-nm band. Because glint-induced reflectance is rather spectrally flat, RTI is still a reasonable indicator of oil emulsion thicknesses. However, because glint is red rich in reflectance (similar to a sunset due to higher scattering in shorter wavelengths), the relationship between RTI and absolute oil thicknesses may change with sun glint strength, suggesting that separate relationships may need to be derived for different sun glint conditions.

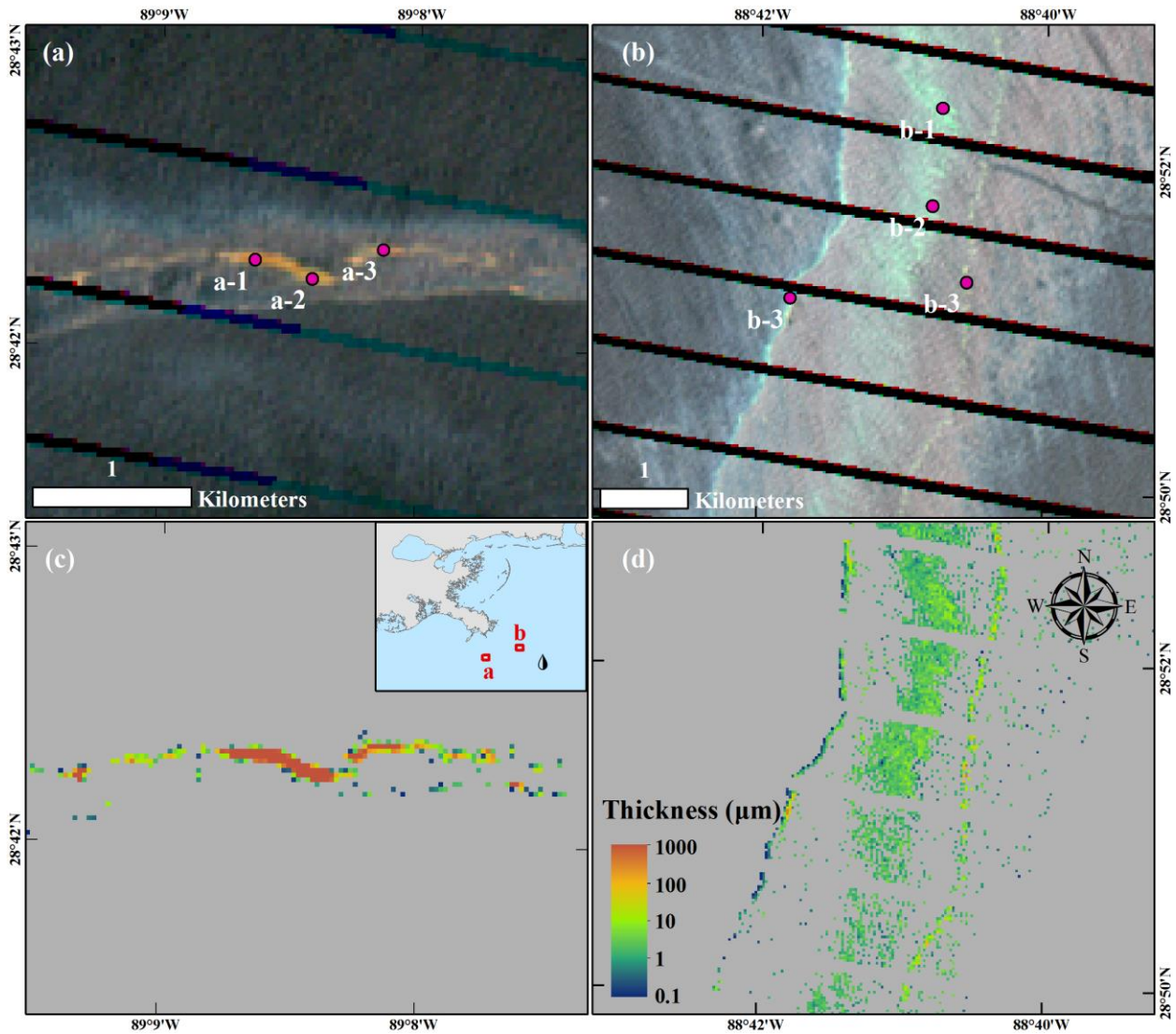


Figure 5. 7: False-color composite (R: 1650; G: 835, B: 661 nm) of ETM+ imagery on 17 May 2010 showing brownish to reddish colors in (a) and mostly greenish colors in (b); (a) and (b) show slick features close (within 2 km) to locations in Fig. 5.4a and Fig. 5.4b, respectively. (c) and (d) show the classified oil emulsion and emulsion thickness in the two regions.

The oil emulsions were classified using the elevated reflectance features in the NIR and SWIR bands (Figs. 5.7c and 5.7d, where the stepwise scheme was described in Section 3.3). As expected, sun glint may alter the relationship between RTI and absolute thickness, making it difficult to establish a universal relationship between reflectance ratio and oil thickness. Thus, a method of histogram matching was used to establish a relationship between RTI and oil thicknesses, where the former may be under

various glint conditions and the latter was derived by USGS from AVIRIS measurements. When the two images were both taken from similar locations relative to the DWH platform with similar areal coverage, I assume the oil thickness frequency distribution to be unchanged between the two images. This assumption is consistent with the popular rule of thumb used by the community, where 90% of the spilled oil is located in about 10% area of the oil footprint (NOAA, 2016). As long as the image covered a large portion of the total spilled area including both thin and thick oil, this assumption may be reasonable. Moreover, the AVIRIS measurements on 17 May 2010 sampled more than 30% of the core spill area, and these AVIRIS flight lines captured both the edge and the center of the spill, including both thick and thin oil regions (Sun et al., 2016). Therefore, the AVIRIS-derived thickness frequency distribution may represent a typical oil emulsion thickness frequency distribution during the DWH oil spill in during 17 May 2010 and other days. The derived RTI cumulative frequency histogram was then compared to and forced to match the AVIRIS thicknesses cumulative frequency histogram (Hu et al., 2018). Fig. 5.9 shows the RTI histogram as compared to the AVIRIS derived thickness histogram after histogram matching. The sun glint coefficient (L_{GN}) for the ETM+ image is $1.4E-2 \text{ sr}^{-1}$, and the estimate thickness (T , μm) from the ETM+ is:

$$\text{Log}_{10}(T) = 11.424 * \text{log}_{10}(\text{RTI}) + 0.3026 \quad (2)$$

where RTI is the band ratio of SWIR (1650 nm) to blue (479nm) in the ETM+ image. Such derived thickness maps are shown in Figs. 5.7c and 5.7d, which show similar thickness distributions as in Figs. 5.4c and 5.4d.

Table 5. 2: RTI-thickness relationships derived from histogram matching between Landsat RTI and AVIRIS-derived oil emulsion thickness (T , μm). These relationships vary with sun glint strength corresponding to each Landsat image. RTI is the band ratio of SWIR (1650 nm) to blue (479nm) in the ETM+ image, and ratio of SWIR (1678 nm) to blue (486 nm) in the TM image

Date	Sensor	$L_{GN} (\text{sr}^{-1})$	Emulsion Area (km^2)	Relationship
5/1/2010	ETM+	$\sim 1.5E-2$	7.9	$\text{Log}_{10}(T) = 8.0853 * \text{log}_{10}(\text{RTI}) + 0.68$
5/10/2010	ETM+	$\sim 6.0E-3$	11.3	$\text{Log}_{10}(T) = 4.6102 * \text{log}_{10}(\text{RTI}) + 0.5116$
5/25/2010	TM	$\sim 3.0E-3$	7.8	$\text{log}_{10}(T) = 2.3601 * \text{log}_{10}(\text{RTI}) + 1.1704$

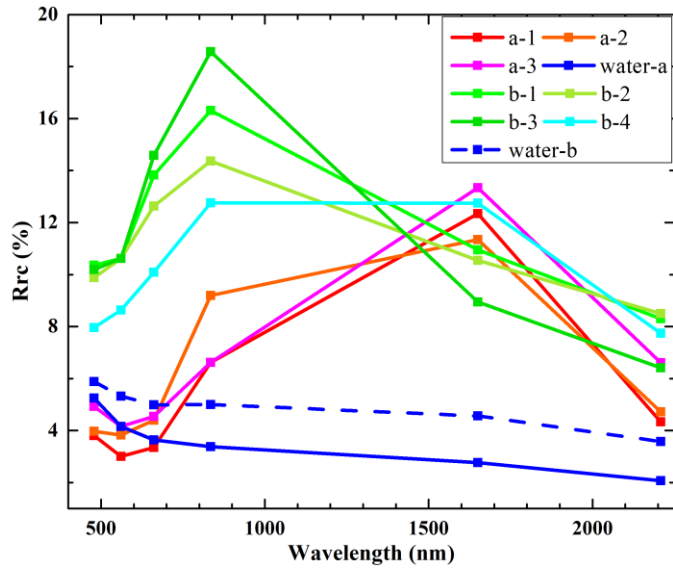


Figure 5. 8: Oil emulsion spectra in the two regions in Fig. 5.7

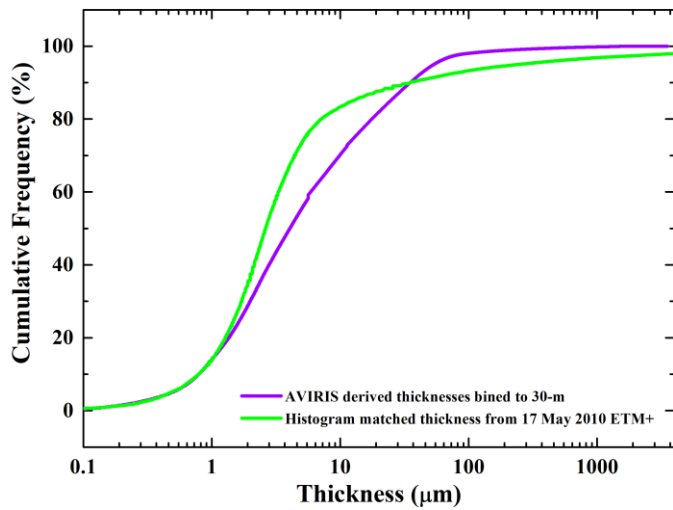


Figure 5. 9: Histograms of cumulative frequency from AVIRIS-derived oil thickness (after data binning to 30-m resolution) and from ETM+ derived oil thickness using the ETM+ RTI.

The same approach was used to classify and quantify oil emulsions from Landsat images in May 2010 (1 May 2010 ETM+, 10 May 2010 ETM+, and 25 May TM) under different sun glint conditions. In each case, the RTI histogram was forced to match the AVIRIS-derived thicknesses histogram, with image-specific coefficients derived between RTI and thickness. The false color composite imagery, spectra of

selected pixels of emulsions, and the histograms are displayed in Figs. 5.10, 5.11, and 5.12 for 1 May 2010 ETM+, 10 May 2010 ETM+, and 25 May TM, respectively. These images were collected under different sun glint conditions, where the RTI-thickness relationship varied among images, as listed in Table 5.2.

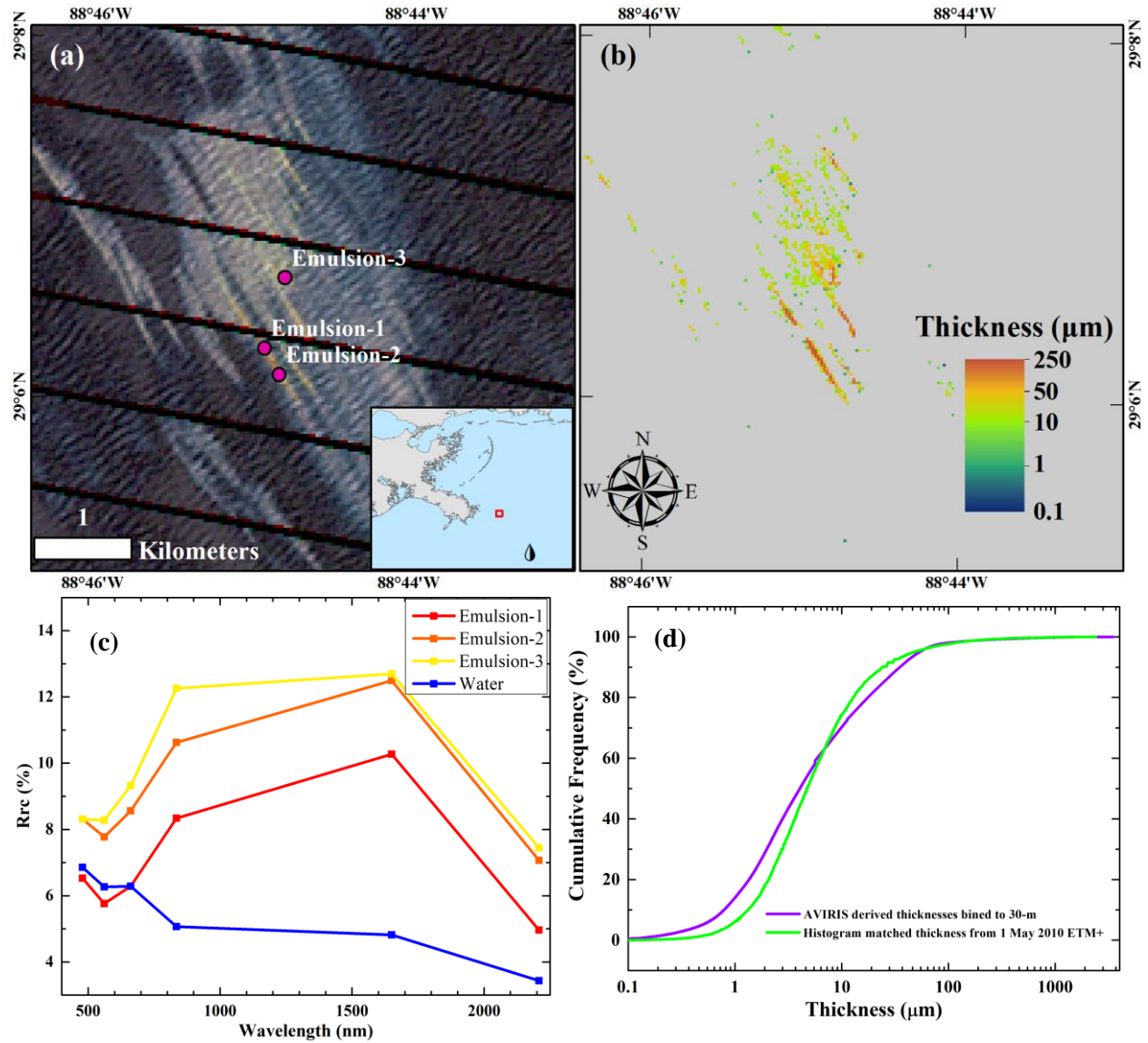


Figure 5. 10: a) False-color composite (R: 1650; G: 835, B: 661 nm) of ETM+ imagery on 1 May 2010. b) Classified oil emulsions and estimated emulsion thickness. c) Oil emulsion spectra from selected locations in (a). d) Histograms of cumulative frequency from AVIRIS-derived oil thickness (after data binning to 30-m resolution) and from ETM+ derived oil thickness using the ETM+ RTI.

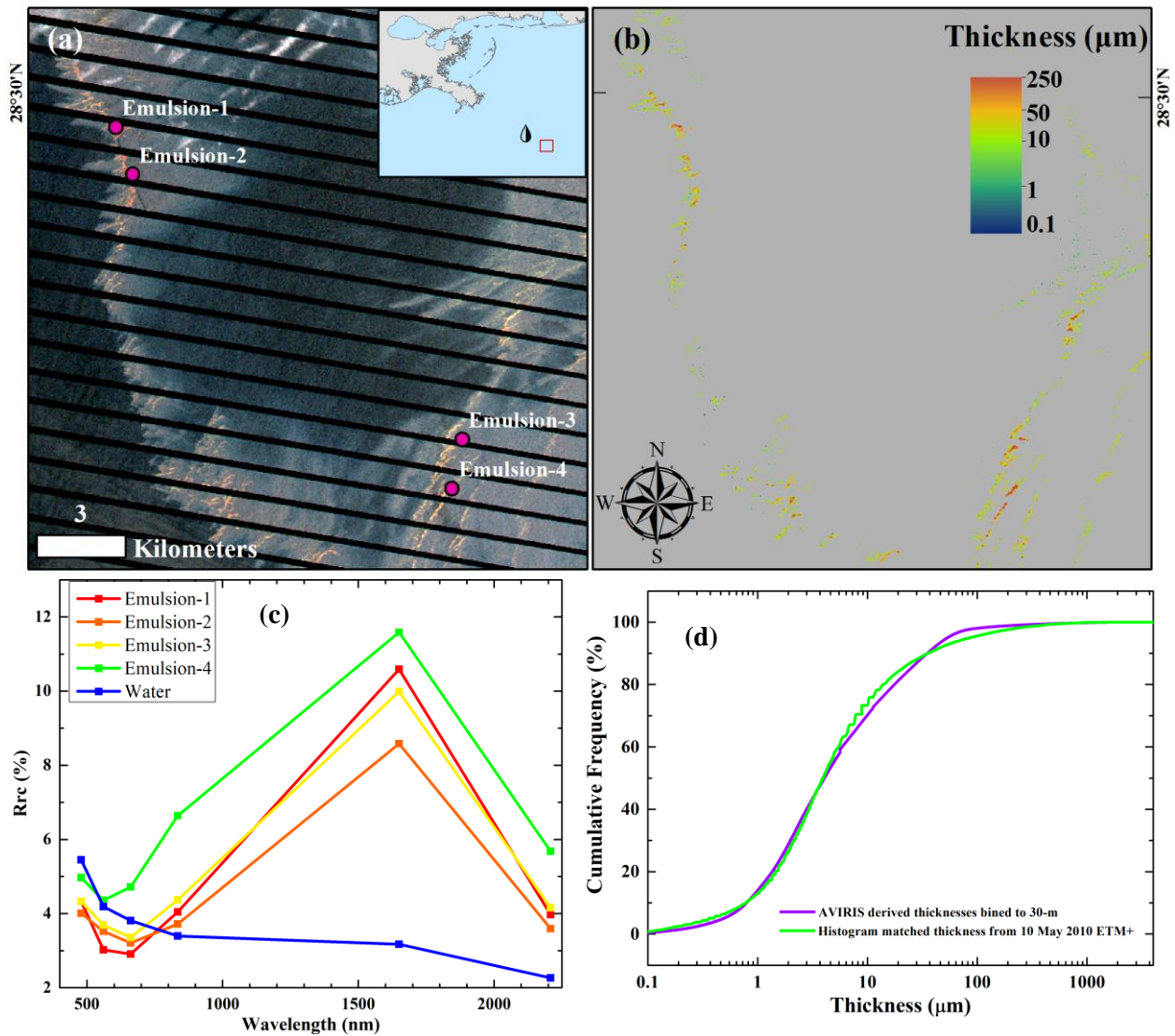


Figure 5. 11: a) False-color composite (R: 1650; G: 835, B: 661 nm) of ETM+ imagery on 10 May 2010. b) Classified oil emulsions and estimated emulsion thickness. c) Oil emulsion spectra from selected locations in (a). d) Histograms of cumulative frequency from AVIRIS-derived oil thickness (after data binning to 30-m resolution) and from ETM+ derived oil thickness using the ETM+ RTI.

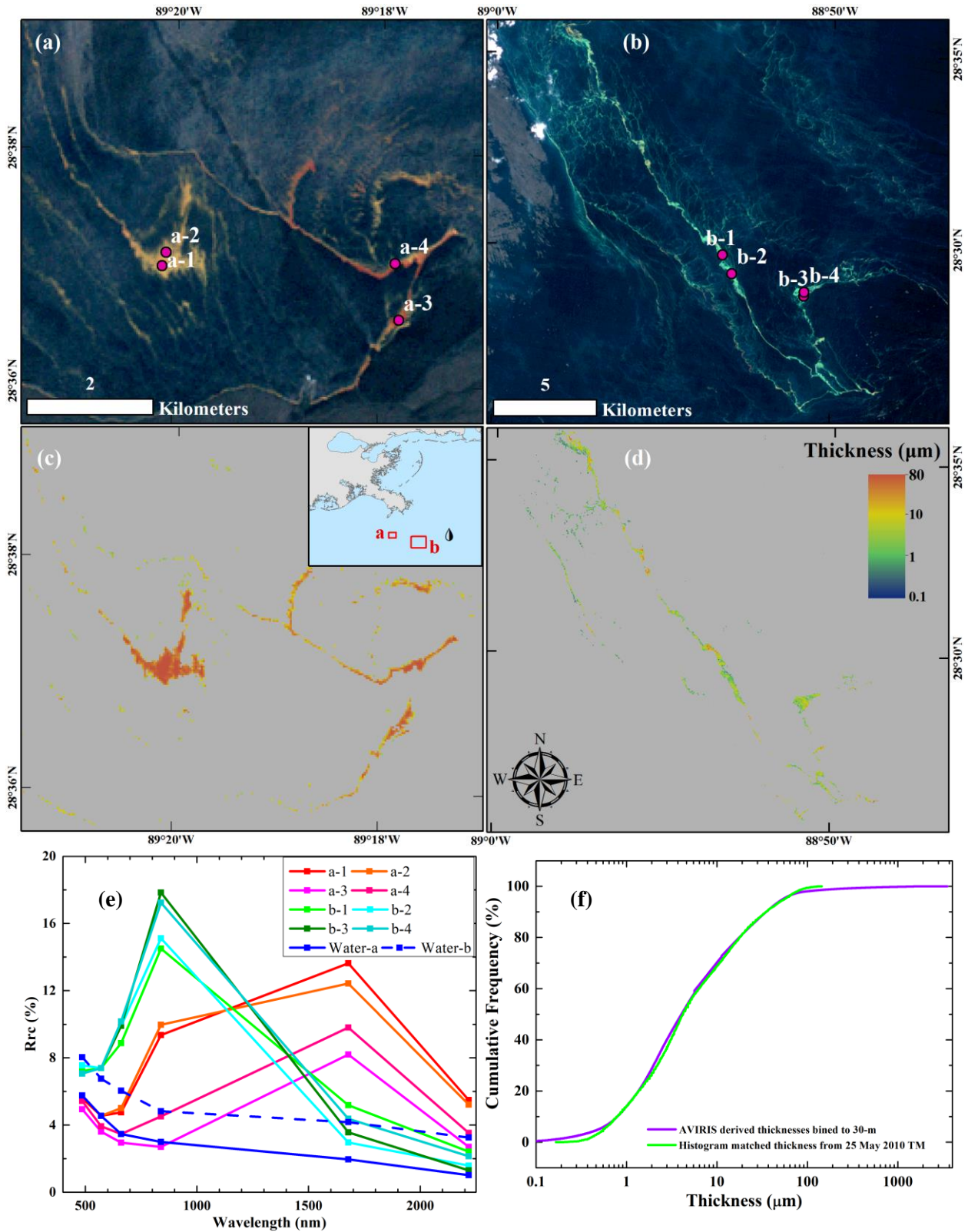


Figure 5. 12: False-color composite (R: 1678; G: 839, B: 660 nm) of TM imagery on 25 May 2010 showing brownish to reddish colors in (a) and mostly greenish colors in (b); (c) and (d) show the classified oil

emulsions and the estimated emulsion thickness in (a) and (b), respectively. e) Oil emulsion spectra in selected locations in (a) and (b). f) Histograms of cumulative frequency from AVIRIS-derived oil thickness (after data binning to 30-m resolution) and from TM derived oil thickness using the TM RTI.

3.2 Non-emulsion

Field experiments. The tank experiment shows that when oil is very thin ($\leq 1 \mu\text{m}$), crude oil reflectance is higher than water in the visible wavelengths (400-700 nm, in Fig. 5.13). This is apparently due to enhanced Fresnel reflectance because oil has a higher refraction index than water. However, when oil becomes thicker ($\geq 5 \mu\text{m}$), there is a clear trend of decreased reflectance in the visible wavelengths with increased oil thicknesses until oil thickness reaches 100 - 500 μm . Compared to reflectance in the visible wavelengths, reflectance in the NIR and SWIR wavelengths shows minimal changes. These results agree well with previous laboratory studies of crude oil (Wettle et al., 2009). Most importantly, reflectance in the NIR and SWIR bands is very low ($< 0.5\%$, Fig. 5.13) for all thickness, which contrasts the enhanced NIR and SWIR reflectance of oil emulsions (e.g., 4% - 15% in the 1650-nm band with emulsion thicknesses from 50 to 750 μm , Fig. 5.3).

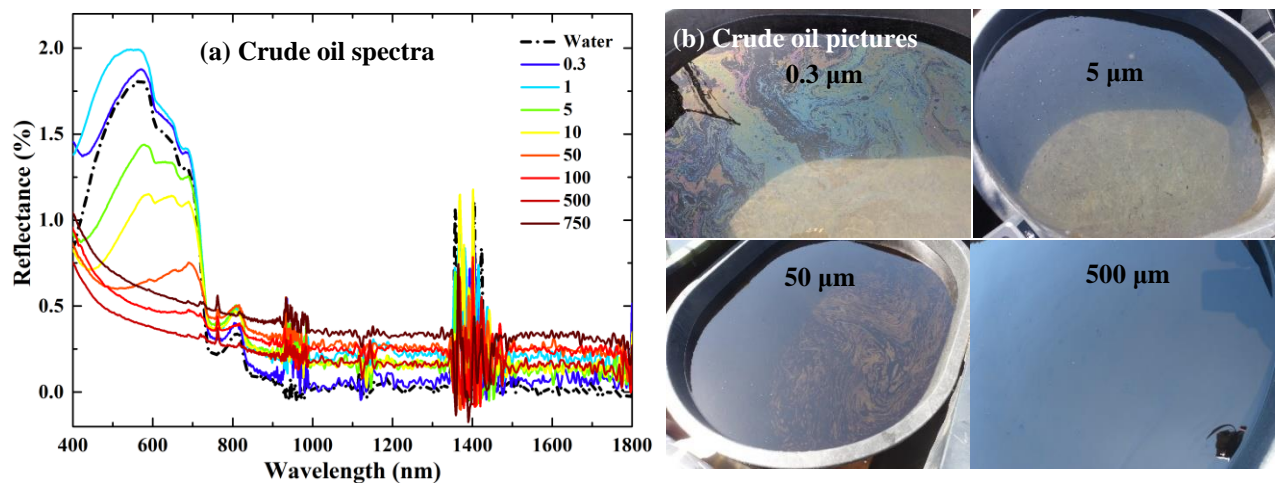


Figure 5. 13: a) Reflectance spectra of Alaskan North Slope crude oil with various oil thicknesses (in μm) in a water tank. Here thickness is calculated as the total volume divided by the area of the tank. b) Pictures showing crude oil appearances with different thicknesses.

The Ohmsett experiment in September – October 2017 was designed to measure crude oil of known thickness using a high-resolution WorldView image. The WorldView-2 image on 1 October 2017 (Fig. 5.14) shows two of the 6.1 m squares without oil and the other two (designed to have surface oil of 1 and 2 mm thick) with some oil on the southern side of the squares (Figs. 5.14 and 5.15). The square with 1-mm oil shows oil covering only $\sim 1/8$ of the square, while the square with 2-mm oil shows oil covering $\sim 1/3$ of the square. Some of the 1.6-m squares had more than half the square covered by oil, and the WorldView-2 multispectral image (Fig. 5.14b) also shows the impact of the bridge and bridge shadows on the 1.6-m squares. South of the 6.1 m squares, there was a black tarp on the bottom (Fig. 5.15c). Further south, Fig. 5.15d shows thick crude oil patch against the tank wall, which was also captured in the WorldView-2 image. Further south (Fig. 5.15e and 5.15f), the images show the thickest oil in the tank, a result of oil accumulation by booms from the south and by water springs from the north. This region contained most of the 400 gallons bulk discharged oil. Assuming the area contained half of the 400-gallon discharged oil at the time of the WorldView-2 image, the crude oil could have an average thickness of ~ 10 mm in this area.

Spectra of selected pixels in those areas show decreased reflectance with increased oil thickness in the blue and green bands, and minimal changes in the NIR bands (Fig. 5.16). This agrees well with our own tank experiment (Section 3.1) and previous studies (Wettle et al. 2009). However, the reflectance spectrum of the tarp is similar to that from thick oil (Fig. 5.16), suggesting that it is difficult to distinguish differences between the two. Oil in the two selected regions (red rectangles) in Fig. 5.14b was classified by comparing to the nearby clear water pixels: if both the blue (478 nm) and green (546 nm) bands were significantly lower than those of clean water (oil-water reflectance difference $>$ two standard deviations of 20 x 20 water pixels), the pixel was identified as a crude oil pixel. Then, a NIR (832 nm) to blue (478 nm) band ratio was used to estimate relative thickness of the identified crude oil, with higher ratio indicating

thicker oil. The classified oil pixels and estimated relative thickness are shown in Fig. 5.14c. The thickness patterns agree well with field-based visual inspections (Fig. 5.15).

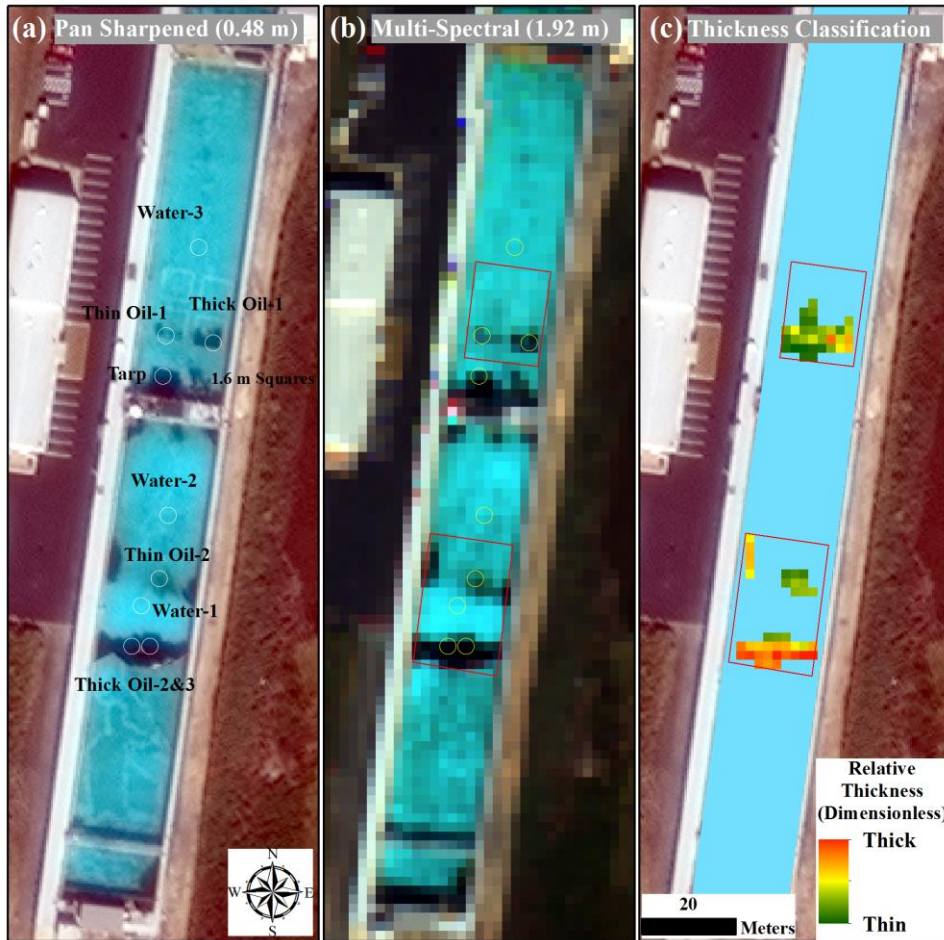


Figure 5. 14: Crude oil in the Ohmsett tank as viewed by WorldView-2 on 1 October 2017. a) Pan sharpened true color image (R: 659 nm; G: 546 nm; B: 478 nm), b) multispectral true color image with the two red rectangular box regions selected for oil classification, and c) results of classified crude-oil pixels and estimated relative thickness of the crude oil in the two selected regions.

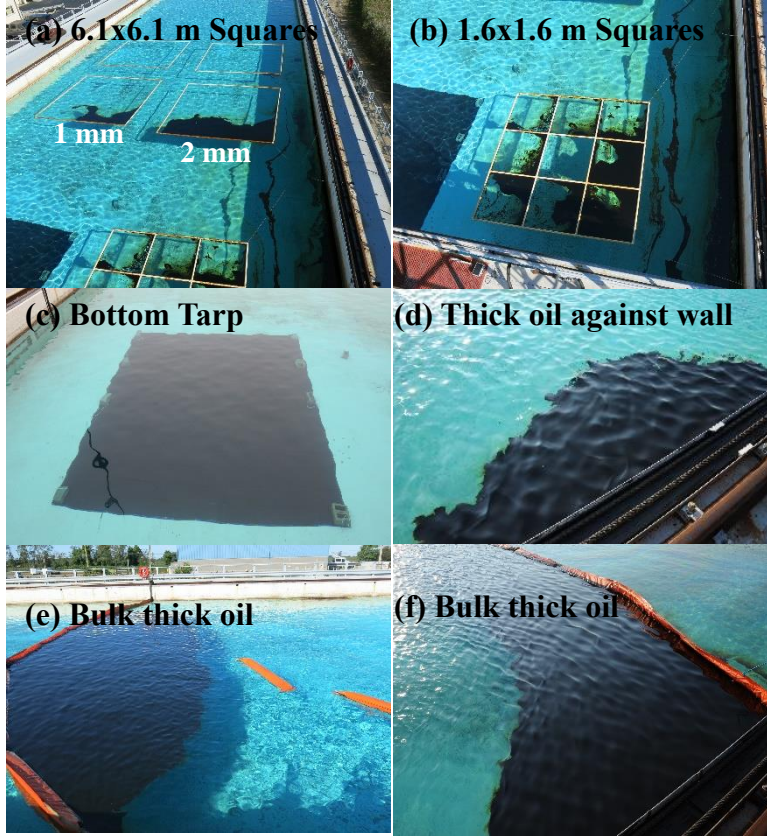


Figure 5. 15: Digital photos taken on 2 October 2017 of the targets in Fig. 5.14a.

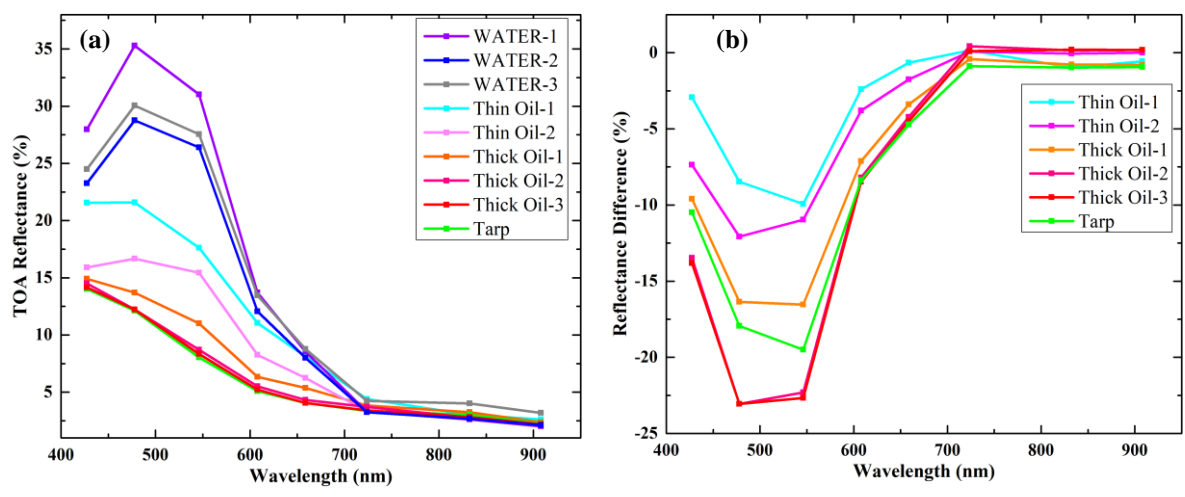


Figure 5. 16: a) Top of atmosphere (TOA) reflectance of selected pixels in Fig. 5.14 and b) reflectance difference after subtracting the nearby water reflectance.

Multiband imagery under sun glint conditions. Fig. 5.17 shows oil slicks that are usually observed from Landsat and Sentinel-2/MSI imagery in the MC-20 region. Reflectance spectra from selected oil-containing pixels and nearby oil-free pixels are shown in Fig. 5.18, where the former can be either higher or lower than the latter, and with spatial contrast enhanced by the sun glint effect ($L_{GN} = \sim 1E-2 sr^{-1}$, Hu et al., 2009; Sun et al., 2016). Sun glint strength is a function of satellite view angles, solar angles, and sea surface roughness (Cox and Munk, 1954; Jackson and Alpers, 2010). The effect of sun glint modulation on oil-water contrast can be visualized clearly by the examples in Fig. 19, where the Multi-angle Imaging SpectroRadiometer (MISR) images were collected over the same oil slicks of the DWH oil spill but at nine different camera zenith angles within 8 minutes (Sun and Hu, 2018). Under strong sun glint (CamZ = 0, $L_{GN} = 6.6E-2 sr^{-1}$ in Fig. 5.19), oil slicks all display positive contrasts from water, with thicker oil displaying higher positive contrast. The thin oil slicks change from positive contrast to negative contrast for zenith angle of forward 26.1° ($L_{GN} = 1E-2 sr^{-1}$ in Fig. 5.19) and afterward 26.1° ($L_{GN} = 8.2E-4 sr^{-1}$ in Fig. 5.19) cameras. Here, the thin slicks undergo a brightness reversal from positive contrast to negative contrast, an effect observed by previous studies (Hu et al., 2009; Jackson and Alpers, 2010). Thick oil, however, still shows positive contrast from water, but at a lower magnitude (Fig. 5.19). There is a smooth transition that with decreased sun glint strength (from $6.6E-2 sr^{-1}$ to $1E-2 sr^{-1}$ and $8.2E-4 sr^{-1}$), sun glint induced reflectance decreases in both thick and thin oil, with thin oil slick turning from positive to negative contrast first because of its relatively small positive contrast when sun glint strength is high. Therefore, under the same sun glint conditions when slicks of both positive and negative contrasts co-exist in the same location (i.e., same solar/viewing geometry and same environmental conditions), slicks of positive contrast appear to be thicker than slicks of negative contrast. Thus, slicks of positive contrast in Fig. 5.17 indicate thicker oil than the corresponding slicks of negative contrast.

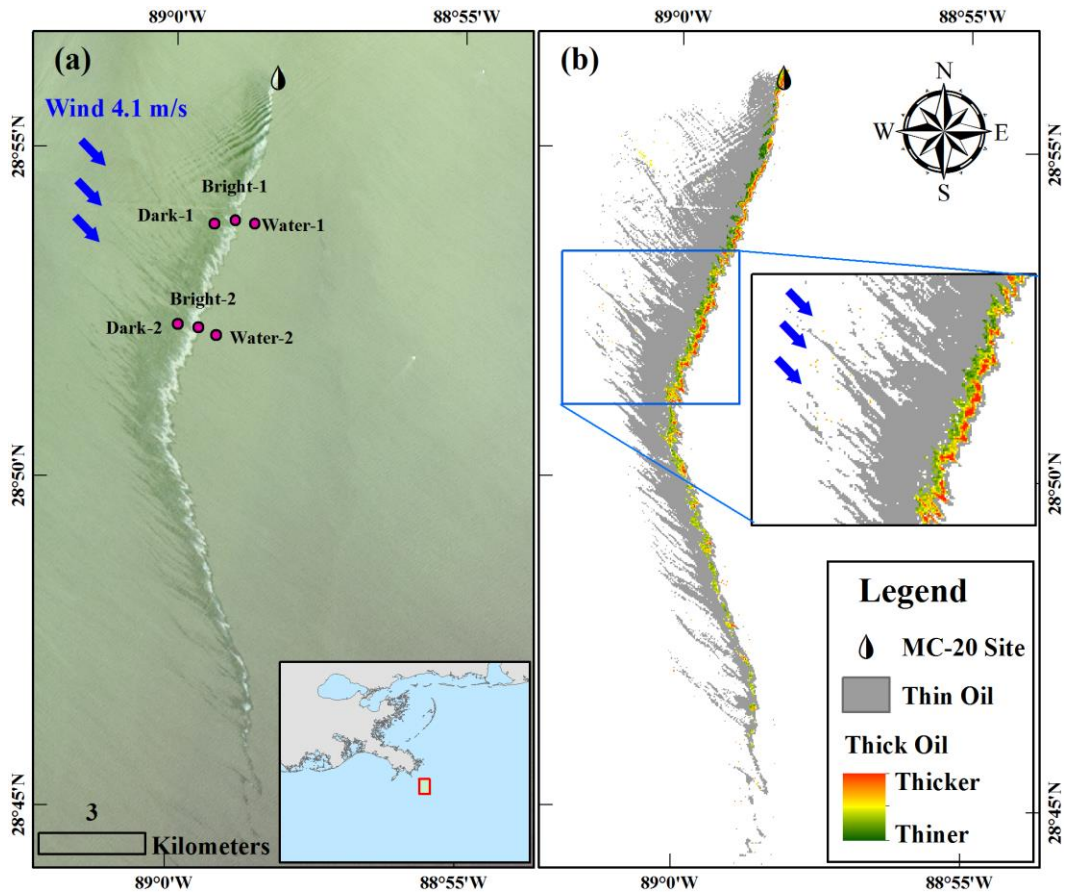


Figure 5. 17: a) OLI true color image (R: 655; G: 561, B: 483 nm) on 4 May 2014 showing oil slicks in the vicinity of the MC-20 site; b) classified thick and thin oil. The blue arrows indicate wind vectors.

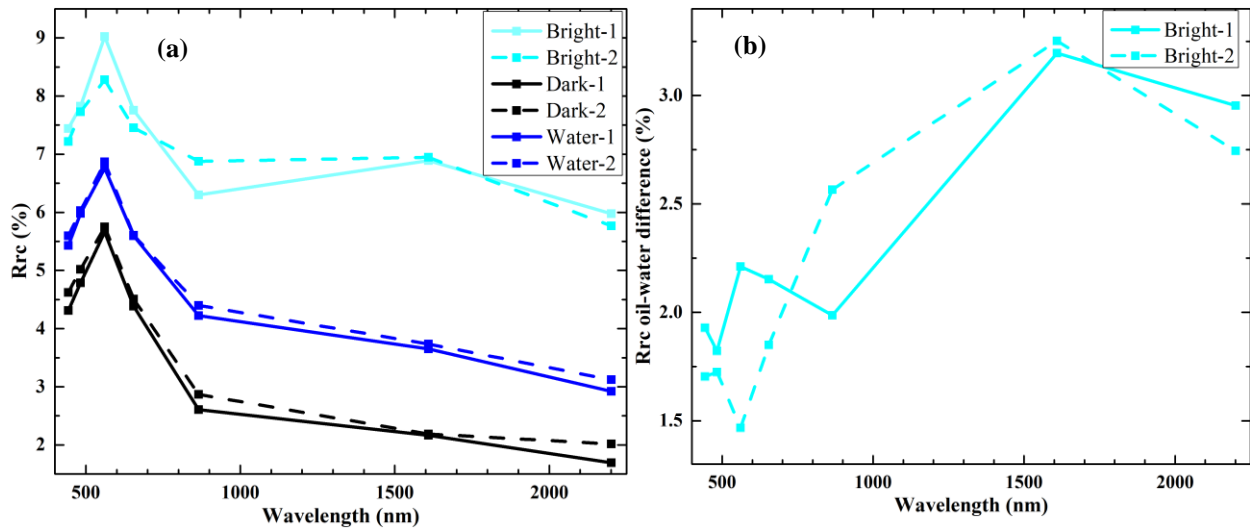


Figure 5. 18: a) Reflectance spectra of selected pixels in Fig. 5.17a, and b) reflectance difference after subtracting the nearby water reflectance.

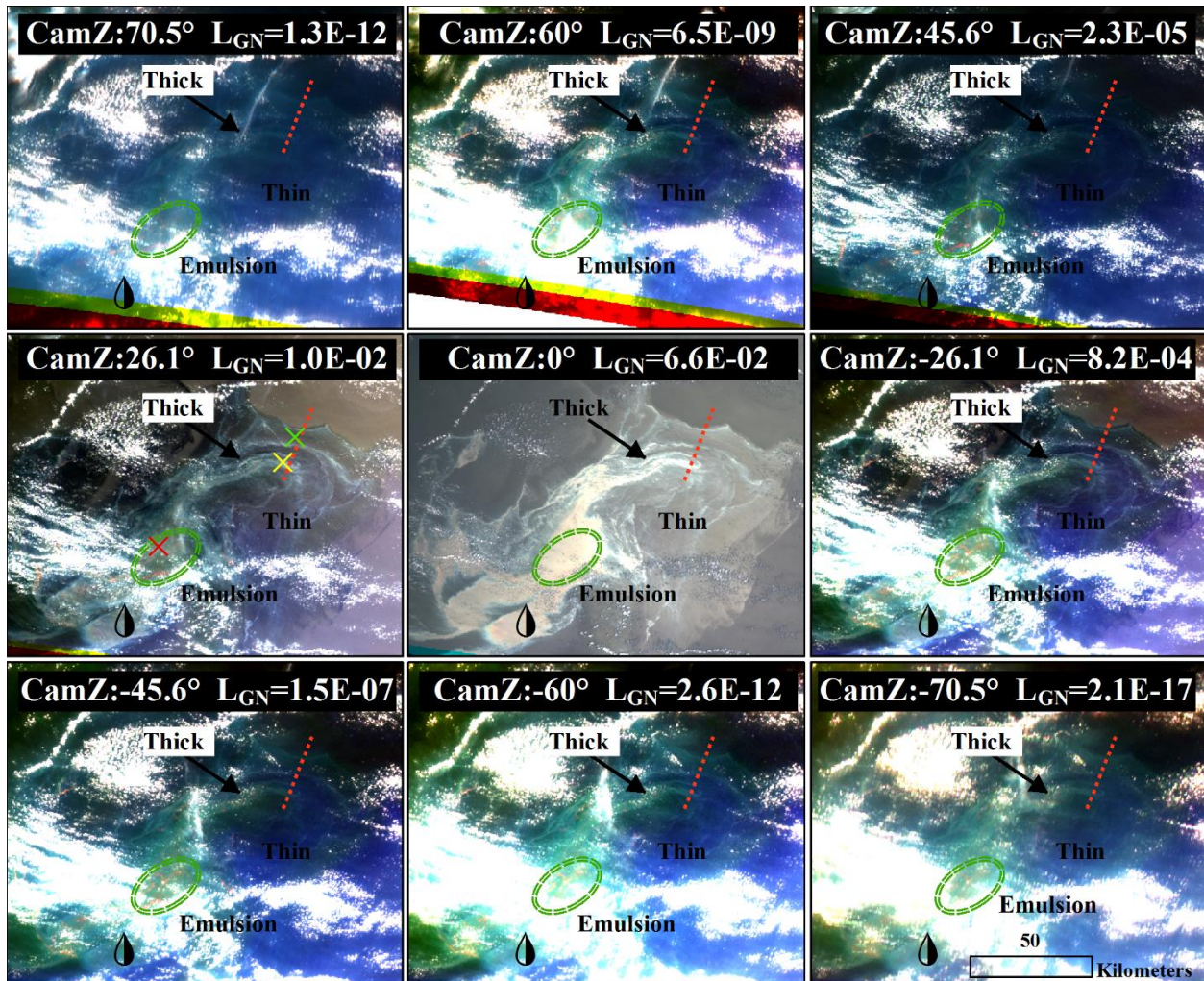


Figure 5. 19: False-color RGB (R: 867 nm, G: 558 nm, B: 446 nm) composite MISR images taken at UTC 16:43 (at nadir, ± 4 minutes among all cameras) on 17 May 2010 in nine camera view angles (Sun and Hu, 2018), with sun glint strengths annotated for the black arrow pointed regions. Positive angles indicate forward looking and negative angles indicate backward looking. The black droplet indicates the location of the DWH oil platform. The color strips on the bottom of top row are due to missing data in one or more bands.

Using the above concept, oil pixels can be first classified as thick and thin oil (i.e., sheen). If an oil pixel has either reflectance of blue and green bands, or NIR and SWIR bands significantly greater than the reference water reflectance, the pixel would be classified as thick oil. RTI will then be used to classify relative thicknesses from the thick oil pixels, with higher ratio indicate thicker oil. Details of the classification scheme are described in Section 3.3. The classification results are shown in Fig. 5.17b as an

example. The classification results appear to be reasonable as one can clearly visualize the thin oil orientation in windrows parallel to the wind direction and the smooth transitions from thin to thick oil (Fig. 5.17b), with the thickest oil patches in the downwind direction (IPIECA-IOGP, 2015; NOAA, 2016).

3.3 Classification scheme

With all the analysis above, this section summarizes the stepwise classification scheme used to classify oil type and thickness with multiband optical imagery from Landsat ETM+. While ETM+ imagery is used here as an example, similar schemes can be developed for other multiband sensors as long as they are equipped with appropriate spectral bands.

First, pre-processing is required to delineate oil slicks and determine sun glint strength, including:

- Download the Landsat Level-1 radiance data
- Process to Rrc (using the ACOLITE software)
- Generate true color and false color composite (R: 1650; G: 835, B: 661 nm) images from the Rrc reflectance
- Outline the regions of interest (ROIs) containing visually interpreted oil extent (not the oil slicks themselves) using ROI tools in ENVI or similar software (e.g., the red polygon in Fig. 5.21a)
- Outline the ROIs for reference water (e.g., the green polygon in Fig. 5.20b) and determine the kernel size according to the oil slick sizes (e.g., 100 x 100 pixels), within which water pixels will be used in calculating the statistics
- Calculate sun glint coefficient (L_{GN}) using the angle files and wind speed data
- Apply cloud mask to mask cloud and cloud shadows (i.e., using Fmask software to prepare cloud mask).

The classification is a pixel-wise classification that searches every non-cloud pixel in the potential oil polygons (red polygons in Fig. 5.20 for example), finds the nearest reference water pixel in the reference water areas (green polygons in Fig. 5.20 for example), opens a kernel window centered at the nearest water pixel (100 x 100 pixels kernel for example), and then calculates the mean and standard deviation of reflectance for each band from water pixels in the kernel window. Spectral bands used in this classification are blue (479 nm), green (561 nm), red (661 nm), NIR (835 nm), SWIR1 (1650 nm), and SWIR2 (2208 nm). Similar bands can be found from other multiband sensors including TM, OLI, Sentinel-2/MSI and WorldView-3.

The reflectance of each potential oil pixel is first compared to water reflectance from the nearest reference water window. If the difference is statistically significant (>2 standard deviations) in at least two of the bands (the reason of using two bands is to filter random sensor noise), the pixel will be classified as an oil-containing pixel. Otherwise, the potential oil pixel will be classified as a water pixel. The generated true color and false color composite images are used to roughly outline oil extent ROIs based on oil's spatial contrast with water (e.g., positive or negative contrast under sun glint, negative contrast of crude oil in true color imagery without sun glint, and reddish or greenish colors of oil emulsions in false color composite imagery). The following procedures will then be used to rule out false-positives and to refine the oil-water boundary within the ROIs.

Secondly, the oil pixels are classified into oil emulsions and non-emulsions. The reflectance peaks in the 835-nm and 1650-nm bands are used to classify oil emulsions: if the above-classified oil pixels follow rule 1 or 2 below, they will be classified as oil emulsions; if the above-classified oil pixels follow rule 1 or 2 but does not follow rule 3, they will be rejected as being oil pixels as they may be floating algae pixels.

- 1) If peak reflectance happens in the 1650-nm band, then verify if the following are true:
 $Rrc_{1650}(\text{oil}) > Rrc_{1650}(\text{water}); Rrc_{2208}(\text{oil}) > Rrc_{2208}(\text{water}); Rrc_{835}(\text{oil}) > Rrc_{835}$

(water); Rrc_1650 (oil) > Rrc_835 (oil); Rrc_1650 (oil) > Rrc_661 (oil); Rrc_1650 (oil) > Rrc_2208 (oil);

2) If peak reflectance happens in the 835-nm band, verify if the following are true: Rrc_835 (oil) > Rrc_835(water); Rrc_661 (oil) > Rrc_661 (water); Rrc_1650 (oil) > Rrc_1650 (water); Rrc_835 (oil) \geq Rrc_1650 (oil); Rrc_835 (oil) > Rrc_661 (oil);

3) If Rrc_661 (oil) is < Rrc_561 (oil), the pixel is rejected as being an oil pixel but likely a pixel containing floating algae.

Thirdly, after applying the above classification to separate oil emulsions from non-emulsions, two separate steps are used for oil emulsions and non-emulsions, respectively. For oil emulsions, the RTI (Rrc_1650/Rrc_472) is used to estimate the relative thicknesses of the classified oil-emulsion pixels using two models in equations (1), and relationships in Table 5.2 whose corresponding sun glint coefficients bracket the sun glint coefficient from the image of interest, with results linearly interpolated between the two model results. For non-emulsions, if sun glint impact is negligible ($L_{GN} < 1E-5 \sim 1E-6 sr^{-1}$, Sun and Hu, 2016), both Rrc_479 and Rrc_560 are significantly lower than water, and both Rrc_1650 and Rrc_835 are no different than water, the same RTI (Rrc_1650/Rrc_472) is then used to estimate the relative thicknesses of the classified non-emulsion pixels, with higher values indicating thicker oil.

Most of the oil slicks observed in the multiband images are under the influences of sun glint ($L_{GN} > 1E-5 \sim 1E-6 sr^{-1}$), showing positive or negative contrasts or both (e.g., Figure. 5.17). In this case, pixels will be classified as thick oil if both Rrc_835 and Rrc_1650 or both Rrc_479 and Rrc_561 are significantly higher than water. All other pixels will be classified as thin oil. The RTI (Rrc_1650/Rrc_472) is then used to indicate the relative thicknesses of the classified thick oil pixels, with higher values indicating thicker oil.

Finally, the results of the individual outputs are merged together and stored in shapefiles and geotiff images. The entire step-wise classification scheme is illustrated in Fig. 5.20.

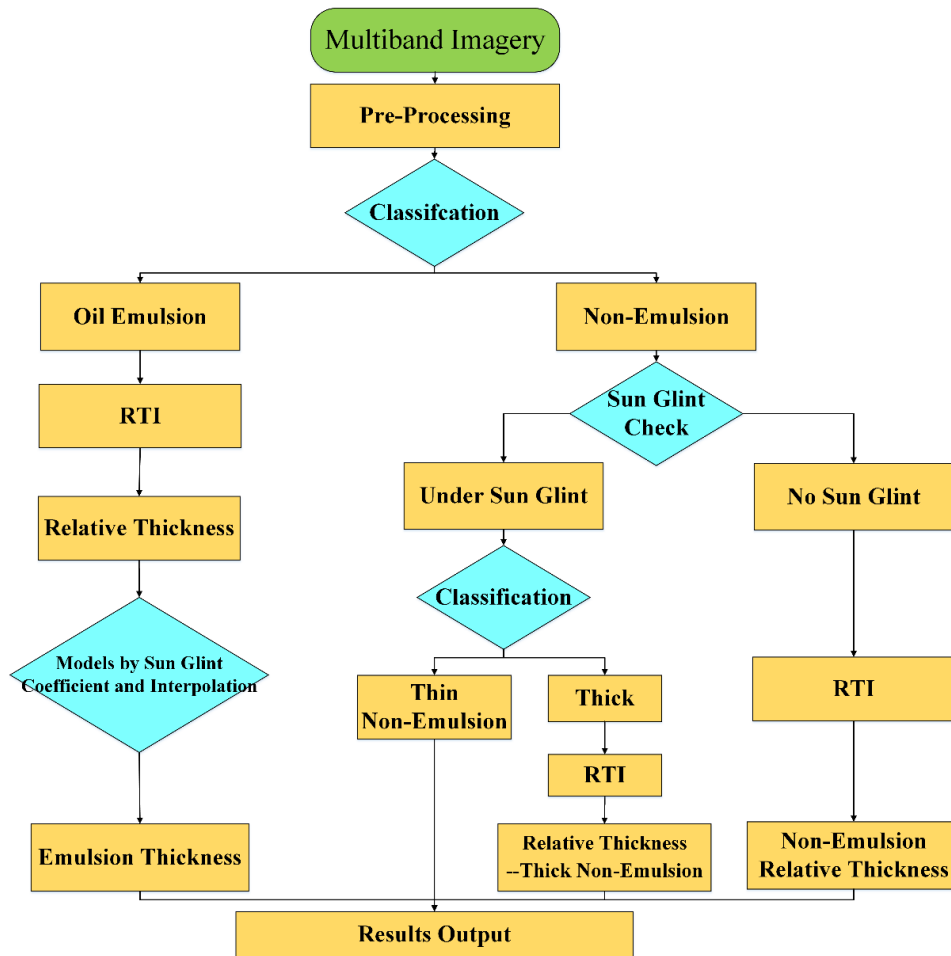


Figure 5. 20: Flow chart of the step-wise classification scheme to classify oil type and thickness from multiband remote sensing imagery. RTI: Relative Thickness Index defined as the ratio between SWIR (~1600 nm) and blue bands (~480 nm).

Fig. 5.21 shows an example of the classification results from the 1 May 2010 ETM+ image over the DWH location. It is clear that while most of the oil pixels contain thin oil, there are both oil emulsions and non-emulsions.

4. Discussions

An elevated reflectance in the NIR (~860 nm) band is often an indicator of oil emulsions. Furthermore, the ~1600-nm SWIR band is directly related to the oil volume contained in the emulsions.

Therefore, both the ~860-nm and the ~1600-nm bands provide critical information of oil emulsions for this specific method, and are both required for classifying oil types and thicknesses when considering the use of optical data.

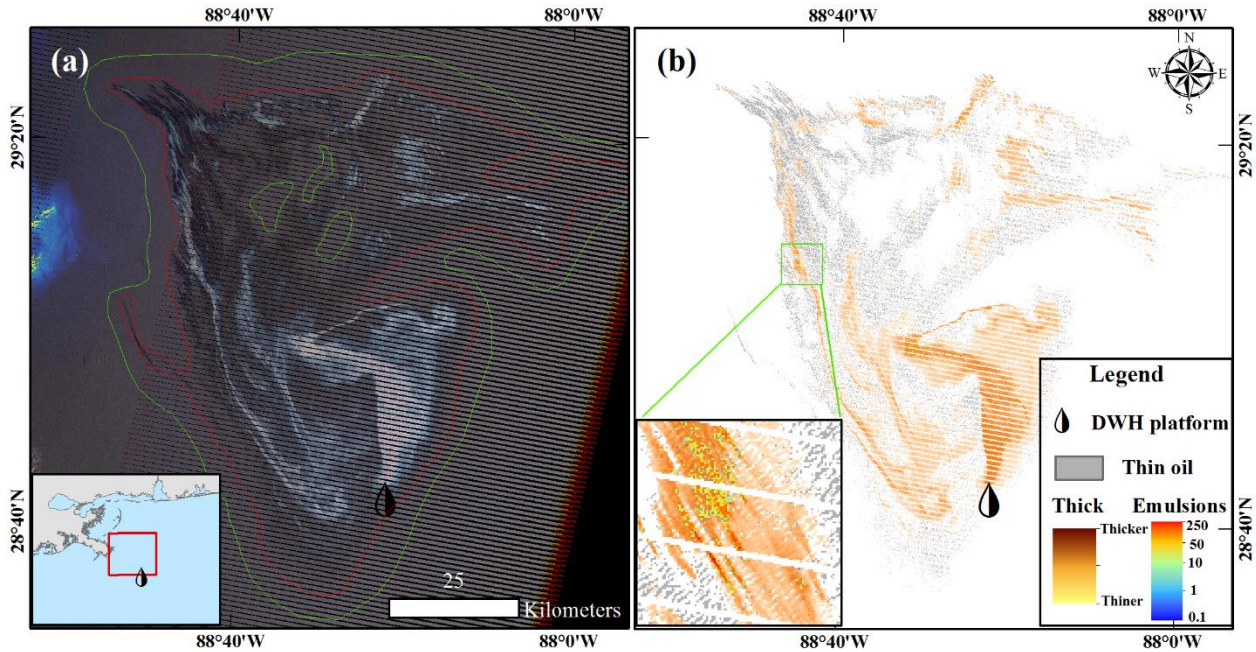


Figure 5. 21: a) False-color composite (R: 1650; G: 835, B: 661 nm) of ETM+ imagery on 1 May 2010 during the DWH oil spill. b) Results from the proposed classification scheme, with enlarged window showing details of the classified oil emulsion in the same region as in Fig. 5.10.

However, oil emulsion is not the only cause of elevated NIR and SWIR reflectance. For example, floating algae such as *Sargassum* also occur frequently in the GoM (Hu et al., 2015), which also cause elevated NIR and SWIR reflectance (Fig. 5.22). While oil emulsion reflectance is rather smooth (i.e., lack of features) from green to red and to the NIR band (Fig. 5.3), *Sargassum* reflectance spectra show strong chlorophyll absorption features around 675 nm (Fig. 5.22, Hu et al., 2015). This absorption feature is within the bandwidth of the TM and ETM+ red bands, and also covered partially by the OLI red band. By

examining and contrasting the spectral shape between the green, red, and NIR bands, *Sargassum* or other floating algae may be discriminated from oil emulsions, following the rules described in Section 3.3-3.

Blue bands are sensitive to oil presence/absence and changes in thicknesses because of the high absorption of oil in the blue (Clark et al., 2010; Wettle et al., 2009), thus essential in classification of thicknesses of both emulsions and non-emulsions. Therefore, in summary, the required bands for oil type (emulsions versus non-emulsions) and thickness classifications are blue (~480 nm), green (~560 nm), red (~670 nm), NIR (~860 nm), and SWIR (~1600 nm). Most of these bands can be found in typical multiband sensors such as Landsat (TM, ETM+, and OLI), MSI, and WorldView-3.

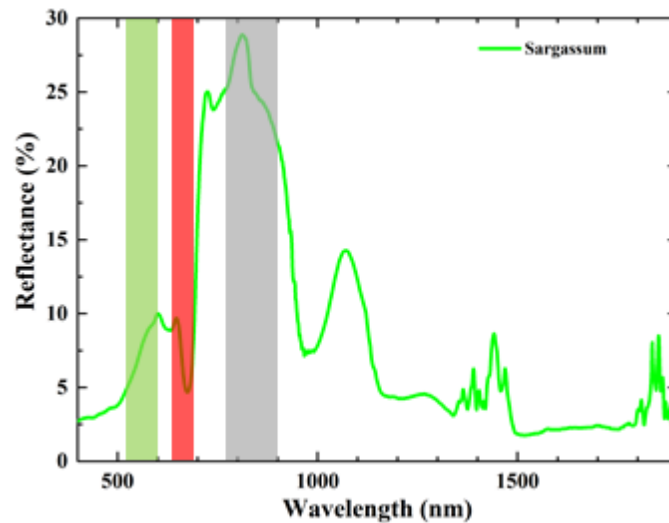


Figure 5. 22: Typical reflectance of floating *Sargassum*, overlaid with positions of ETM+ green (green color), red (red color) and NIR (grey color) bands.

Oil spill response activities require oil maps to be delivered in a timely manner (Leifer et al., 2015), usually within an hour by experienced observers on airplanes for tasking appropriate assets. The classification scheme here is a pixel-wise classification method, thus the turn over time is heavily dependent on the searching extent. Currently, with the existing computing speed it takes up to two hours processing time from raw data downloading to final shapefiles output for oil spill that comprises a couple

of kilometers in width and a few tens of kilometers in length in Landsat images. However, it may take more than 12 hours to process images of large oil spills (e.g., the DWH oil spill), with oil spill size of hundreds of kilometers by a few tens of kilometers. With the current turn over time, the classification scheme may still provide useful products for oil spill response during prolonged oil spills, large spills and oil spills in remote locations, especially when considering satellite remote sensing's advantages of large coverage, repeatable measurements and global coverage over the traditional airborne observations. The turn over time may be decreased through algorithm refinement in the near future, for example by using an object-based classification scheme (Blaschke, 2010) instead of the pixel-wise method presented in this study.

A statistical analysis of oil-water contrast over natural seep locations in the GoM shows that thin oil films have positive contrast from water in the MODIS 859-nm band for $L_{GN} > 0.025 \text{ sr}^{-1}$ (Sun and Hu, 2018). Under such strong sun glint conditions, sun glint induced reflectance increase may be comparable to, or even overwhelm, the original emulsion signals in the $\sim 480\text{-nm}$ and $\sim 1600\text{-nm}$ bands. As can be seen from Figs. 5.9, 5.10, 5.11, and 5.12, RTI has a better histogram matching with emulsion thickness when L_{GN} is $3\text{E-}3$ to $6\text{E-}3 \text{ sr}^{-1}$. Therefore, the classification scheme to quantify thicknesses of oil emulsions is applicable for $L_{GN} < 1\text{E-}2 \text{ sr}^{-1}$, while oil emulsion pixels can still be extracted (although not quantified) when L_{GN} is $> 1\text{E-}2 \text{ sr}^{-1}$.

The methodology to classify thick oil from thin oil under sun glint conditions ($L_{GN} < 0.025 \text{ sr}^{-1}$ and $L_{GN} > 1\text{E-}5 \sim 1\text{E-}6 \text{ sr}^{-1}$) is based on the concept that under the same solar/viewing geometry and environmental conditions, thick and thin oil modulate differently on reflected sun light. However for slicks over large distances (e.g., a few tens of kilometers to > 100 kilometers in a Landsat image), the satellite view angles and wind conditions are different in locations spatially separated. Therefore, the method proposed here to classify thick oil from thin oil and to classify relative thicknesses of thick oil is applicable only to oil slicks spatially close or at similar sun glint levels.

Finally, all classification results here are only verified through consistency checks (e.g., spectral shapes, comparison with AVIRIS, slick orientation relative to wind, etc.), rather than through direct field observations. The lack of direct field validation not only applies to this study, but is rather universal in remote sensing of oil spills. In addition to the fast-changing nature of oil spills (field surveys are difficult to plan), the fundamental problem is the lack of a reliable method to measure oil thickness in the field for both thick and thin oil, especially when oil is patchy (e.g., Figs. 5.1 and 5.3). This technical challenge needs to be addressed in order to advance the science of oil spill remote sensing.

5. Conclusions

In this study, a stepwise classification scheme is proposed to classify oil type (oil emulsion versus non-emulsion) and classify oil thickness of each type under no glint conditions and under various sun glint conditions in multiband optical imagery. The elevated spectral reflectance features in the NIR (~860 nm) and SWIR (~1600 nm) bands are used to identify oil emulsions. Increased and decreased reflectance in the visible to SWIR bands due to sun glint perturbation are used to classify thick from thin oil. The SWIR (~1600 nm) to blue (~480 nm) band ratio is used to classify the relative thicknesses of oil emulsions and thick oil. A look-up-table is developed to quantify oil emulsion thickness under different sun glint conditions using the relative thickness index (RTI). The classification results agree with field observations from the Ohmsett facility oil spill test, and the mapped oil emulsion thickness patterns agree with thickness map from USGS derived from hyperspectral airborne AVIRIS measurements.

Required bands for the classification scheme and for discriminating oil from false positives are discussed in the study, where the combination of blue (~480 nm), green (~560 nm), red (~670 nm), NIR (~860 nm) and SWIR (~1600 nm) appear to fulfill the requirements of the classification method proposed here. Most of these bands can be found in typical multiband optical sensors such as Landsat (TM, and ETM+, OLI), MSI, and WorldView-3. Although direct validation from field experiments is impossible due to

lack of field sampling methods to measure oil thickness, the classification scheme is based on the spectral characteristics of oil reflectance under different observing conditions, thus providing a practical method for oil spill assessment in both retrospective analysis and to facilitate mitigation.

6. Literature cited

- Analytical Imaging and Geophysics LLC (2001). ACORN user's guide, stand-alone version. Analytical Imaging and Geophysics LLC, pp. 64
- Blaschke, T. (2010). Object based image analysis for remote sensing. *ISPRS Journal of Photogrammetry and Remote Sensing*, 65, 2-16
- Clark, R.N., Swayze, G.A., Livo, K.E., Kokaly, R.F., Sutley, S.J., Dalton, J.B., McDougal, R.R., and Gent, C.A. (2003). Imaging spectroscopy: Earth and planetary remote sensing with the USGS Tetracorder and Expert Systems. *Journal of Geophysical Research*, 108 (E12), 5131, doi:10.1029/2002JE001847
- Clark, R.N., Swayze, G.A., Leifer, I., Livo, K.E., Kokaly, R., Hoefen, T., Lundeen, S., Eastwood, M., Green, R.O., and Pearson, N. (2010). A method for quantitative mapping of thick oil spills using imaging spectroscopy. US Geological Survey Open-File Report, 1167, 1-51
- Cox, C., and Munk, W. (1954). Measurement of the roughness of the sea surface from photographs of the sun's glitter. *Journal of the Optical Society of America*, 44, 838-850.
- Hu, C., Li, X., Pichel, W.G., and Muller-Karger, F.E. (2009). Detection of natural oil slicks in the NW Gulf of Mexico using MODIS imagery. *Geophysical Research Letters*, 36, L01604, doi:10.1029/2008GL036119
- Hu, C., Feng, L., Hardy, R.F., and Hochberg, E.J. (2015). Spectral and spatial requirements of remote measurements of pelagic Sargassum macroalgae. *Remote Sensing of Environment*, 167, 229-246
- Hu, C., Feng, L., Holmes, J., Swayze, G.A., Leifer, I., Melton, C., Garcia-Pineda, O., MacDonald, I., Hess, M., Muller-Karger, F., Graettinger, G., and Green, R. (2018). Remote sensing estimation of surface oil volume during the 2010 Deepwater Horizon oil blowout in the Gulf of Mexico: scaling up AVIRIS observations with MODIS measurements. *Journal of Applied Remote Sensing*, 12(2), 026008, <https://doi.org/10.1117/1.JRS.12.026008>
- IPIECA-IOGP (2015). Aerial observation of oil spills at sea London. February 2015: IPIECA-IOGP, pp. 17. Retrieved from <http://www.ipieca.org/resources/good-practice/aerial-observation-of-oil-spills-at-sea/>
- Jackson, C.R., and Alpers, W. (2010). The role of the critical angle in brightness reversals on sunglint images of the sea surface. *Journal of Geophysical Research*, 115, C09019, doi:10.1029/2009JC006037
- Leifer, I., Murray, J., Streett, D., Stough, T., Ramirez, E., and Gallegos, S. (2015). The federal oil spill team for emergency response remote sensing, FOSTERRS: Enabling remote sensing technology for

- marine disaster response. In: Lippitt, C., Stow, D., Coulter, L. (eds) Time-Sensitive remote sensing. Springer, New York, NY, 91-111
- Lu, Y., Tian, Q., Wang, X., Zheng, G., and Li, X. (2013). Determining oil slick thickness using hyperspectral remote sensing in the Bohai Sea of China. *International Journal of Digital Earth*, 6, 76-93
- NOAA (2016). Open water oil identification job aid for aerial observation. With standardized oil slick appearance and structure nomenclature and codes. NOAA Office of Response and Restoration, Emergency Response Division, Seattle, Washington, 1-51. Retrieved from https://response.restoration.noaa.gov/sites/default/files/OWJA_2016.pdf
- Qiu, S., He, B., Zhu, Z., Liao, Z., and Quan, X. (2017). Improving Fmask cloud and cloud shadow detection in mountainous area for Landsats 4–8 images. *Remote Sensing of Environment*, 199, 107-119
- Sun, S., Hu, C., Feng, L., Swayze, G.A., Holmes, J., Graettinger, G., MacDonald, I., Garcia-Pineda, O., and Leifer, I. (2016). Oil slick morphology derived from AVIRIS measurements of the Deepwater Horizon oil spill: Implications for spatial resolution requirements of remote sensors. *Marine Pollution Bulletin*, 103, 276-285, doi:10.1016/j.marpolbul.2015.12.003
- Sun, S. and Hu, C. (2016). Sun glint requirement for the remote detection of surface oil films. *Geophysical Research Letters*, 43, 309–316, doi:10.1002/2015GL066884
- Sun, S., and Hu, C. (2018). The challenges of interpreting oil–water spatial and spectral contrasts for the estimation of oil thickness: Examples from satellite and airborne measurements of the Deepwater Horizon oil spill. *IEEE Transactions on Geoscience and Remote Sensing*, doi:10.1109/TGRS.2018.2876091
- Svejkovsky, J., and Muskat, J. (2006). Real-time detection of oil slick thickness patterns with a portable multispectral sensor. Report Submitted to the U.S. Department of the Interior Minerals Management Service, Herndon, VA, July 31, 2006, Contract No. 0105CT39144
- Svejkovsky, J., Lehr, W., Muskat, J., Graettinger, G., and Mullin, J. (2012). Operational Utilization of Aerial Multispectral Remote Sensing during Oil Spill Response. *Photogrammetric Engineering & Remote Sensing*, 78(10), 1089-1102
- Wettle, M., Daniel, P.J., Logan, G.A., and Thankappan, M. (2009). Assessing the effect of hydrocarbon oil type and thickness on a remote sensing signal: A sensitivity study based on the optical properties of two different oil types and the HYMAP and Quickbird sensors. *Remote Sensing of Environment*, 113, 2000-2010
- Zhu, Z., Wang, S., and Woodcock, C.E. (2015). Improvement and expansion of the Fmask algorithm: cloud, cloud shadow, and snow detection for Landsats 4–7, 8, and Sentinel 2 images. *Remote Sensing of Environment*, 159, 269-277
- Zhu, Z., and Woodcock, C.E. (2012). Object-based cloud and cloud shadow detection in Landsat imagery. *Remote Sensing of Environment*, 118, 83-94

CHAPTER 6:

OIL SPILL ASSESSMENT OF THE IXTOC-I ACCIDENT

1. Note to Reader

This chapter have been previously published in *Marine Pollution Bulletin*, 101, 632-641, and have been reproduced with permission from Elsevier. The paper is provided in Appendix D. This paper applies methods and theories of optical remote sensing in the assessment of a historical oil spill – the 1979 Ixtoc-I oil spill. A brief summary of this paper is provided below.

APPENDIX D – Surface oil footprint and trajectory of the Ixtoc-I oil spill determined from Landsat/MSS and CZCS observations (Sun et al., 2015)

The Ixtoc-I oil spill occurred in 1979 in shallow waters (50 m) of the Bay of Campeche, Mexico. A large portion of the released oil from this second largest accidental marine oil spill in history reached the surface. This study assesses the oil spill footprint using remote sensing data collected by Landsat Multispectral Scanner and Coastal Zone Color Scanner. General patterns of oil trajectory are found to the northwest and north, nearly parallel to the coastline of the western Gulf of Mexico (GoM) with possible oil landing on Mexican and Texas beaches. Field observations at selected beaches and islands along the coast of the western and southern GoM during and after the spill confirm these satellite-based findings. And the result oil footprint map and cumulative frequency map were also used to help to determine field sampling locations and for ecological impact analysis.

CHAPTER 7:
ASSESSMENT OF THE MC-20 OIL SPILL

1. Note to Reader

This chapter have been previously published in *Marine Pollution Bulletin*, 136, 141-151, and have been reproduced with permission from Elsevier. The paper is provided in Appendix E. This paper uses medium- to high-resolution (10-30 m) optical remote sensing imagery to assess the ongoing MC-20 oil spill in the northern Gulf of Mexico. A brief summary of this paper is provided below.

APPENDIX E – Remote sensing assessment of oil spills near a damaged platform in the Gulf of Mexico

(Sun et al., 2018)

An oil platform in the Mississippi Canyon 20 (MC-20) site was damaged by Hurricane Ivan in September 2004. In this study, medium- to high-resolution (10-30 m) optical remote sensing imagery is used to systematically assess oil spills near this site for the period between 2004 and 2016. Image analysis detects no surface oil in 2004, but ~40% of the cloud-free images in 2005 show oil slicks, and this number increases to ~70% in 2006-2011, and >80% since 2012. For all cloud-free images from 2005 through 2016 (including those without oil slicks), delineated oil slicks show an average oil coverage of 14.9 km²/image, with an estimated oil discharge rate of ~50 to ~1700 barrels/day, and a cumulative oil-contaminated area of 1,900 km² around the MC-20 site. Having remote sensing observation of oil slicks in the same day (or a few consecutive days from different sensors) improves the understanding of oil slick movement over short temporal periods, especially in this region influenced by a large river plume. For the most part, oil slick distribution agrees well with circulation patterns that are largely controlled by the Mississippi River plume,

but can also be affected by direct wind forcing. The location of the river induced fronts with respect to the oil source also contributes to both onshore propagation and longer-term pathways of the hydrocarbons. Moreover, wind forces may dominate the oil spreading process when the Mississippi River plume does not encompass the MC-20 site.

CHAPTER 8:

CASE STUDY: THE OIL TANKER COLLISION AND OIL SPILL EVENT IN THE EAST CHINA SEA

1. Note to Reader

This chapter have been previously published in *Geophysical Research Letters*, 45, 3212-3220, and have been reproduced with permission from John Wiley and Sons. The paper is provided in Appendix F. This paper demonstrates a multisensor day and night approach of satellite remote sensing in response to an oil spill accident. A brief summary of this paper is provided below.

APPENDIX F – Tracking an oil tanker collision and spilled oils in the East China Sea using multisensor day and night satellite imagery (Sun et al., 2018)

The Iranian oil tanker SANCHI, carrying ~1 million U.S. barrels of condensate oil, collided with a grain freighter on 6 January 2018 in the East China Sea. The accident caused SANCHI on fire and tilted, drifting ablaze for a week, until it exploded and sunk on 14 January 2018. Traditional techniques using synthetic aperture radar or daytime optical imagery turn out not providing timely and adequate coverage for this specific case. In this study, however, Visible Infrared Imaging Radiometer Suite Nightfire product and Day/Night Band data demonstrate their values in tracking the oil tanker's drifting pathway and locations when all other means are not as effective for the same purpose. Such pathway and locations can also be reproduced with a numerical model, with root-mean-square error of <15 km. High-resolution optical imagery after 4 days of the tanker's sinking reveals oil spill area >350 km² near the tanker sinking site. This study demonstrates that a combination of all available remote sensing and modeling techniques can provide effective means to monitor marine accidents and oil spills to assist event response.

CHAPTER 9: SUMMARY AND CONCLUSIONS

1. Research findings and potential impacts

While optical remote sensing has the capacity to detect oil under sun glint and non-glint conditions, differentiating oil from false-positives, identifying oil emulsions, and quantifying oil thicknesses, fully realizing this capacity faces many challenges in the real marine environment using available multiband remote sensing imagery. These challenges include sun glint induced distortion in the reflectance spectra, mixed pixels from the heterogeneous oil patches, and insufficient spectral resolution to apply the laboratory-based hyperspectral algorithm to multiband optical imagery (Sun and Hu, 2018). These challenges have all been addressed in this dissertation, although continued research is still required to have complete solutions.

Specifically, of these challenges, the sun glint requirement for detecting thin oil films has been quantified. The threshold of sun glint strength (L_{GN}) is determined to be 10^{-5} – 10^{-6} sr^{-1} for Moderate Resolution Imaging Spectroradiometer (MODIS) on the Terra and Aqua satellites, and 10^{-6} – 10^{-7} sr^{-1} for Visible Infrared Imaging Radiometer Suite (VIIRS) on the Suomi-NPP satellite (Sun and Hu, 2016). Below these thresholds, oil films cannot be detected; above these thresholds oil films can always be detected except near the critical-angle zone where oil slicks reverse their contrast against the background water. The relationship between oil-water reflectance contrast and sun glint strength has also been statistically analyzed, with results showing that when L_{GN} is <0.001 sr^{-1} , the negative oil-water contrast (at 859 nm) of thin oil films is very small, and the contrast turns to be positive when L_{GN} is $> \sim 0.025$ sr^{-1} (Sun and Hu, 2018).

The sun glint thresholds determined here will provide critical information on which images (or which portions of an image) can be used to search for oil, thus reducing false negative detection.

The spatial heterogeneity of oil slicks, and slick size distributions of different thickness classes from the DeepWater Horizon (DWH) oil spill, have been characterized for the first time by using high spatial resolution (~ 7.6 m) hyperspectral AVIRIS data (Sun et al., 2016). Most oil slicks are found to be elongated, with a medium length/width ratio ranging from 2.5 to 4.6 depending on the thickness class: oil of >200 μm thick covers only 5% of the total oiled area but contains $>45\%$ of the total oil volume, confirming the rule of thumb that thick oil covers a small area but contains a considerably larger amount of oil. The characterized slick sizes of different thickness classes have significant implications on interpreting oil footprint and thickness for sensors with different resolutions. It is found that spectral and spatial analyses, or modeling using coarse-resolution sensors such as MODIS, need to consider mixed pixels for thick oil, as most pixels will have thick oil coverage in only a few percent of a given pixel. If non-commercial satellite is the only available means, Landsat/Sentinel-2 might be the best compromise between spatial resolutions and temporal resolutions in order to capture actual thick-oil coverage within a pixel and full oil-spill footprint. On the other hand, commercial satellite data (e.g., DigitalGlobe satellite constellation) can greatly expand oil spill detection capability in both spatial ($< 2\text{m}$ spatial resolution) and temporal resolutions (daily revisit with an imaging swath of <20 km).

Moreover, a stepwise classification scheme is proposed to extract oil features, classify oil types (oil emulsion versus non-emulsion), and classify oil thicknesses of each type under no glint conditions and under various sun glint conditions using multiband optical imagery. Most of the required spectral bands used in the application of the step-wise classification scheme, and to discriminate false-positives, can be found in typical multiband sensors such as Landsat (TM, ETM+, and OLI), MSI, and WorldView-3. This classification scheme may greatly expand the capacity to classify oil emulsions from non-emulsions, and

classify oil thicknesses of different types using current multiband optical sensors (under various sun glint conditions), thus providing a practical method for oil spill assessment and to facilitate mitigation.

Based on the above methods and current understanding of oil-water spatial and spectral contrasts in optical remote sensing imagery, several oil spill accidents have been assessed, including both historical and ongoing oil spills. The Ixtoc-I oil spill footprint has been delineated for its >9-month spill period, providing the first comprehensive map of oiled area from the spill (Sun et al., 2015). The cumulated oil footprint map has been used to guide field sampling, and has provided independent information to compare with physical modeling (Duran et al., 2018) and to assess the spill's potential impact on the benthic ecosystem. Moreover, the use of time-series remote sensing data provides oil presence frequency, slick size, cumulative area, and estimated oil discharge rate of oil spills near the Mississippi Canyon 20 (MC-20) site between 2004 and 2016 (Sun et al., 2018a), thus filling a knowledge gap of this long-term and ongoing spill. The study of oil slick changes over time in the MC-20 region also improves the understanding of how oil slicks respond to a large river plume. The study of the oil tanker collision event in the East China Sea shows the value of VIIRS night time data in response to an oil spill accident in addition to traditional synthetic aperture radar and optical detections (Sun et al., 2018b). A combination of multi-sensor, day and night data along with a numerical model may serve as a template in responding to similar collision and/or spill events in the future.

2. Future research

2.1 Field measurements along with multiband or hyperspectral imaging cameras

One notoriously difficult problem in oil spill remote sensing research is the lack of direct field validation. Although indirect validation of the derived maps in this research is provided through spectral analysis and cross-sensor consistency checks, development of practical ways to validate remote sensing

maps of oil type and thickness is still immediate and critically needed to further progress in this subject area.

Such a challenge cannot be addressed with just a technological innovation to sample oil accurately in the field, but must be addressed through coordinated efforts between field and remote sensing measurements. This is because that even if oil thickness can be determined accurately from *in situ* measurements, it is still extremely difficult to use these measurements to validate remote sensing interpretations because of the difficulty in matching *in situ* measurements with large image pixels (often 30 x 30 m, see Chapter 5). Therefore, multi-spectral or hyperspectral imaging cameras may be required to measure oil reflectance for each oil patch if the cameras are mounted on fixed platforms or used on low-altitude aircrafts (either manned or un-manned). In such measurements, because of the super-high resolution (sub-meter) each pixel may be a “pure” pixel containing uniform oil type and thickness, from which reflectance spectrum is obtained to apply the classification algorithm. Then, a recently developed Oil Thickness Sampler (WM-OTS, Garcia-Pineda et al., 2018) can be used to measure oil thickness from identified “pure” pixels, providing direct field validation. The two measurements together can also be used to develop new algorithms to classify oil type and estimate oil thickness, as the WM-OTS is demonstrated to measure oil thickness from 5 μm to 2 cm with a resolution of 10 μm in the laboratory setting. The above scheme can be tested by making simultaneous measurements over the MC-20 site under real marine oil spill condition.

2.2 Assessment of potential environmental impacts of natural hydrocarbon seeps in the Gulf of Mexico

Oil spill accidents are difficult to predict, and it is therefore often difficult to plan field trips to assess environmental impacts in a timely fashion. In the Gulf of Mexico (GoM), however, natural oil seeps are known to be a major source of oil input, thus serving as surrogates to evaluate the potential

environmental impacts of oil spills. Laboratory experiments suggest that high concentrations of crude oil may restrain phytoplankton growth while low concentrations of crude oil may even promote growth (Huang et al., 2011). *In situ* measurements in the natural seep zones also show elevated chlorophyll concentrations in surface waters (D'souza et al., 2016). Temperature and nutrient profiles suggest that this may be attributed to nutrient upwelling generated by the buoyant plume. Other possible reasons include an indirect 'top-down' effect by Protistan grazers, which may be tolerant to crude oil contamination (Rogerson and Berger, 1981). The grazers predate on bacteria that compete with phytoplankton for nutrients in the presence of crude oil. While a field-based study is plausible, it is unclear whether the findings can be generalized for all natural seeps in the northern GoM. Therefore, it will be important to assess how natural hydrocarbon seeps (e.g., the 914 distinct seep zones identified in MacDonald et al., 2015) may influence phytoplankton using satellite-estimated chlorophyll as a proxy.

3. Conclusions

In conclusion, the most noteworthy finding from this research is that once the oil-water spatial and spectral contrasts under different observing conditions are well understood, it is straightforward to implement a classification scheme to classify oil type (emulsion versus non-emulsion) and oil thickness using multi-band remote sensing data. During the DWH oil spill, nearly all satellite remote sensing efforts from both Federal agency (e.g., NOAA) and academia could only provide maps of oil presence/absence with little information on oil thicknesses and oil types (oil emulsion versus non-emulsion). Retrospective analysis of the DWH oil spill using Landsat imagery indicates that besides oil presence/absence, information of oil emulsion status, emulsion thicknesses, and information on relative thicknesses of non-emulsions can also be provided in future spills following the step-wise classification scheme proposed here. On the other hand, more work is required to accurately determine absolute oil thickness for both oil emulsions and non-emulsions, and more laboratory measurements are necessary to fully understand

the oil–water spectral contrasts for different oil types and different water types. Most importantly, reliable techniques to measure oil thickness in the field need to be developed, where the ongoing oil spill in the MC-20 site in the northern GoM may serve as a good experimental site to test both remote sensing and *in situ* techniques.

4. Literature cited

- D'souza, N. A., Subramaniam A., Juhl, A.R., Hafez, M., Chekalyuk, A., Phan, S., Yan, B., MacDonald, I.R., Weber, S.C., and Montoya, J.P. (2016). Elevated surface chlorophyll associated with natural oil seeps in the Gulf of Mexico. *Nature Geoscience*, 9(3), 215-218, doi:10.1038/ngeo2631
- Duran, R., Beron-Vera, F.J., and Olascoaga M.J. (2018). Extracting quasi-steady Lagrangian transport patterns from the ocean circulation: An application to the Gulf of Mexico. *Scientific Reports*, 8, 5218
- Garcia-Pineda, O., Staples, G., Jones, C.E., Hu, C., Holt, B., Kourafalou, V., Graettinger, G., DiPinto, L., Ramirez, E., Street, D., Cho, J., Swayze G., and Sun, S. (2018). Classification of oil spill thicknesses using satellite remote sensing for oil spill response. Submitted manuscript.
- Huang, Y., Jiang, Z., Zeng, J., Chen, Q., Zhao, Y., Liao, Y., Shou, L., and Xu, X. (2011). The chronic effects of oil pollution on marine phytoplankton in a subtropical bay, China. *Environmental Monitoring and Assessment*, 176(1-4), 517-530, doi:10.1007/s10661-010-1601-6.
- MacDonald, I.R., Garcia-Pineda, O., Beet, A., Daneshgar Asl, S., Feng, L., Graettinger, G., French-McCay, D., Holmes, J., Hu, C., Huffer, F., Leifer, I., Muller-Karger, F., Solow, A., Silva, M., and Swayze, G. (2015). Natural and unnatural oil slicks in the Gulf of Mexico. *Journal of Geophysical Research: Oceans*, 120, 8364-8380
- Rogerson, A., and Berger, J. (1981). Effect of crude oil and petroleum-degrading micro-organisms on the growth of freshwater and soil protozoa. *Microbiology*, 124, 53-59
- Sun, S., Hu, C., and Tunnell, J.W. (2015). Surface oil footprint and trajectory of the Ixtoc-I oil spill determined from Landsat/MSS and CZCS observations. *Marine Pollution Bulletin*, 101, 632-641, doi:10.1016/j.marpolbul.2015.10.036
- Sun, S., Hu, C., Feng, L., Swayze, G.A., Holmes, J., Graettinger, G., MacDonald, I., Garcia-Pineda, O., and Leifer, I. (2016). Oil slick morphology derived from AVIRIS measurements of the Deepwater Horizon oil spill: Implications for spatial resolution requirements of remote sensors. *Marine Pollution Bulletin*, 103, 276-285, doi:10.1016/j.marpolbul.2015.12.003
- Sun, S. and Hu C. (2016). Sun glint requirement for the remote detection of surface oil films. *Geophysical Research Letters*, 43, 309–316, doi:10.1002/2015GL066884.

- Sun, S., Hu, C., Garcia-Pineda, O., Kourafalou, V., Le Hénaff, M., and Androulidakis, Y. (2018a). Remote sensing assessment of oil spills near a damaged platform in the Gulf of Mexico. *Marine Pollution Bulletin*, 136, 141-151, doi:10.1016/j.marpolbul.2018.09.004
- Sun, S., Lu, Y., Liu, Y., Wang, M., and Hu, C. (2018b). Tracking an oil tanker collision and spilled oils in the East China Sea using multisensor day and night satellite imagery. *Geophysical Research Letters*, 45, 3212-3220, doi:10.1002/2018GL077433
- Sun, S., and Hu, C. (2018). The challenges of interpreting oil–water spatial and spectral contrasts for the estimation of oil thickness: Examples from satellite and airborne measurements of the Deepwater Horizon oil spill. *IEEE Transactions on Geoscience and Remote Sensing*, doi:10.1109/TGRS.2018.2876091

APPENDIX A:

THE CHALLENGES OF INTERPRETING OIL–WATER SPATIAL AND SPECTRAL CONTRASTS FOR THE ESTIMATION OF OIL THICKNESS: EXAMPLES FROM SATELLITE AND AIRBORNE MEASUREMENTS OF THE DEEPWATER HORIZON OIL SPILL

Sun, S., and Hu, C. (2018). The challenges of interpreting oil–water spatial and spectral contrasts for the estimation of oil thickness: Examples from satellite and airborne measurements of the Deepwater Horizon oil spill. *IEEE Transactions on Geoscience and Remote Sensing*, doi:10.1109/TGRS.2018.2876091

The Challenges of Interpreting Oil–Water Spatial and Spectral Contrasts for the Estimation of Oil Thickness: Examples From Satellite and Airborne Measurements of the Deepwater Horizon Oil Spill

Shaojie Sun¹ and Chuanmin Hu¹

Abstract—Optical remote sensing is one of the most commonly used techniques to detect oil in the surface ocean. This is because oil has optical properties that are different from water to modulate oil–water spatial and spectral contrasts. However, understanding these contrasts is challenging because of variable results from laboratory and field experiments as well as from different observing conditions and spatial/spectral resolutions of remote sensing imagery. Here, through reviewing published oil–water spectral contrasts and analyzing remotely sensed spectra collected by several satellite and airborne sensors (MERIS, MODIS, MISR, Landsat, and AVIRIS) from the Deepwater Horizon oil spill, we provide the interpretation of the spatial/spectral contrasts of various oil slicks and discuss the challenges in such interpretations. In addition to oil thickness, several other factors also affect oil–water spatial/spectral contrasts, including sun glint strength, oil emulsification state, optical properties of oil covered water, and spatial/spectral resolutions of remote sensing imagery. In the absence of high spatial- and spectral-resolution imagery, a multistep scheme may be used to classify oil type (emulsion and non-emulsion) and to estimate relative oil thickness for each type based on the known optical properties of oil, yet such a scheme requires further research to improve and validate.

Index Terms—AVIRIS, emulsification, hyperspectral, Landsat, MERIS, MISR, MODIS, multispectral, oil spill, oil thickness, optical remote sensing, resolution.

I. INTRODUCTION

THROUGH synoptic and frequent imaging capability, remote sensing plays a vital role in oil spill response and postspill assessment [1], [2]. Among the various remote sensing techniques [1], [3]–[8], synthetic aperture radar (SAR) is perhaps the most often used in oil spill assessment [3], [4].

Manuscript received February 18, 2018; revised July 27, 2018 and September 15, 2018; accepted October 8, 2018. This work was supported in part by the NASA Earth and Space Science Fellowship under Grant NNX16AN95H, and in part by the Gulf of Mexico Research Initiative/C-IMAGE II, No. SA 12-10. Data are publicly available through the Gulf of Mexico Research Initiative Information & Data Cooperative (GRI-IDC) at <https://data.gulfresearchinitiative.org> (doi: 10.7266/n7-1nhg-ez10). (Corresponding author: Chuanmin Hu.)

The authors are with the Optical Oceanography Laboratory, College of Marine Science, University of South Florida, St. Petersburg, FL 33701 USA (e-mail: suns@mail.usf.edu; huc@usf.edu).

Color versions of one or more of the figures in this paper are available online at <http://ieeexplore.ieee.org>.

Digital Object Identifier 10.1109/TGRS.2018.2876091

SAR offers medium- to high-resolution imagery under all weather conditions, in which the dampening surface capillary waves and short gravity waves by surface oil under optimal wind conditions results in a reduced Bragg scattering signal, making surface oil appear darker than surrounding water in SAR imagery [3]. However, bio-films and bio-slicks (e.g., Sargassum mat and algal blooms), threshold wind areas, and wind sheltering can also cause negative contrast in SAR imagery. This makes it difficult to distinguish oil slicks from lookalikes [1], [3]. More importantly, SAR is used primarily for oil detection (absence/presence) instead of oil thickness quantification, although several recent studies demonstrated that it might be possible to discriminate thick oil emulsion from non-emulsion in SAR imagery [5], [9].

Optical remote sensing offers supplemental techniques in oil detection and quantification, with various strengths and weaknesses as compared with SAR. Weaknesses mainly result from lack of coverage under cloudy conditions. Because, statistically, cloud cover occupies $\sim 72\%$ of the global ocean [10], approximately three quarters of optical remote sensing data are useless for oil spill studies. However, this weakness is compensated for by wide-swath sensors like Moderate Resolution Imaging Spectroradiometer (MODIS, 2300 km) and Visible Infrared Imaging Radiometer Suite (VIIRS, 3300 km), which can provide repeated coverage at any location in 1–2 days (more often in polar regions), at the price of reduced spatial resolutions (~ 300 m–1 km) compared with SAR observations. When higher resolution data from Landsat or SPOT-like sensors are used at reduced frequency, they may complement the coarse-resolution data and improve the detection and quantification capacity [11]. Indeed, low (or no) data cost, wide coverage, and high revisit frequency make optical remote sensing a reliable tool in oil spill studies [6], [12], [13]. Such a capacity may provide information that is difficult or even impossible with SAR remote sensing because it may be possible to differentiate oil type (emulsion or non-emulsion) and estimate oil thickness (or volume) through multiple-band optical remote sensing, but interpretation of multiband imagery is technically challenging for a number of reasons. One objective here is to demonstrate this capacity, while presenting technical challenges for future studies.

Oil can be differentiated from water in two ways, making absence/presence detection possible. First, similar to SAR applications, oil can modulate surface waves, causing changes in the surface Fresnel reflection of light that are detectable under proper sun glint conditions [12], [14]–[17], in which the minimal sun glint strength required to observe change has been determined to be 10^{-5} – 10^{-6} sr^{-1} for MODIS and 10^{-6} – 10^{-7} sr^{-1} for VIIRS [18]. The oil–water contrast in sun glint optical imagery, unlike in SAR imagery, can be either positive or negative [12], [15], [16], [18]–[20] based on sun glint strength (a function of solar/view geometry and sea surface roughness). On the other hand, while sun glint facilitates the absence/presence of oil detection, sun glint can modulate both the magnitude and shape of spectral reflectance, making oil type and/or thickness difficult to interpret (see the following).

Second, different absorption and scattering properties of oil from water also contribute to the oil–water contrast in optical remote sensing imagery. Crude oil has strong absorption in the short wavelengths, which decays exponentially toward longer wavelengths [21]. When oil is emulsified, mixing with water creates oil–water particles that have strong scattering in all wavelengths, manifested in the red–near infrared (NIR)–shortwave infrared (SWIR) wavelengths [22] because of water molecule’s negligible scattering in these wavelengths. In addition, the higher refractive index of crude oil (~ 1.5) over seawater (~ 1.34) leads to higher Fresnel reflection of oiled surface. These different optical properties, as well as the sun glint conditions mentioned above, collectively determine the oil–water spatial and spectral contrast.

Although the principles are well known, in practice it has been very difficult to develop inversion algorithms to infer the oil type and thickness from the oil’s reflectance spectra. Many experiments have been attempted for such inversions, mostly under controlled laboratory environments, yet the results often differ for many reasons [e.g., (Fig. 1)]. Wettle *et al.* [23] showed dramatic reflectance changes in blue–green wavelengths only and no change in the NIR for different oil thicknesses [Fig. 1(c)], while Clark *et al.* [22] showed the opposite [Fig. 1(b)]. The results from such laboratory-based measurements are always confounded in remote sensing imagery collected from the ocean environments due to variable solar/viewing conditions, wind, mixed pixels, and different water properties from those in the laboratory experiments.

Our primary objective here is to compare, contrast, and understand the various spectral responses of oil on water from both published literature and new multisensor remote sensing data collected from the DeepWater Horizon (DWH) oil spill, in which interpretation challenges are demonstrated and a preliminary solution to differentiate oil type and to quantify relative oil thickness is presented. Furthermore, potential methods that deal with the various perturbation factors in these interpretations are discussed.

II. DATA AND METHODS

A. Oil Spectra From Laboratory-Based and Well-Controlled Experiments

Numerous experiments have been conducted to determine the oil’s reflectance spectra using different oil types

and experimental settings. Here, we select some representative experiments to compare the results. Of these, reflectance spectra of pure oil [Fig. 1(a)] were obtained from Lammoglia and Filho [24], reflectance spectra of oil emulsion [Fig. 1(b)] were obtained from Clark *et al.* [22], and reflectance spectra of oil-on-water [Fig. 1(c), (d) and (e)] were obtained from Wettle *et al.* [23], and Byfield [21], respectively. These spectra were collected from the laboratory measurements using artificial light sources. For comparison, reflectance spectra collected from outdoor harbor water under solar illumination [Fig. 1(f)] were obtained from Svejtkovsky and Muskat [25].

B. Oil Spectra From Remote Sensing Imagery

The explosion and sinking of the DWH oil rig on April 20, 2010 led to three months of continuous oil spill in the northern Gulf of Mexico (GoM), releasing 3.19 million barrels of crude oil into the ocean [26], [27]. In this paper, remote sensing data from several satellite and airborne sensors were analyzed to examine the spatial and spectral contrast of oil and oil-free water. These include the following.

- 1) Coarse-resolution data from MODIS, Medium Resolution Imaging Spectrometer (MERIS), and local mode Multi-angle Imaging SpectroRadiometer (MISR), all obtained from the NASA Goddard Space Flight Center (GSFC). MODIS and MERIS data were processed with the software SeaDAS (version 7.0) to generate Rayleigh-corrected reflectance ($R_{rc}(\lambda)$, dimensionless) and resampled to 250 m resolution. The MISR sensor on board Terra views the earth simultaneously with nine cameras and four spectral bands (446, 558, 672, and 867 nm) in all directions at a spatial resolution of 275 m. Eight of the cameras point to zenith angles of 26.1°, 45.6°, 60.0°, and 70.5° forward (+) and afterward (–) off nadir, respectively, with an additional nadir view camera (0°) [28]. MISR L1B2 data were mapped to a rectangular projection using “the HDF-EOS To GeoTIFF Conversion Tool” (HEG, version 2.14), and then converted to radiance using scale factors [28]. Solar/viewing geometry data and top of atmosphere (TOA) reflectance were acquired through the MISR Interactive eXplorer (MINX, version 4.0) software.
- 2) Medium-resolution data (30 m) from Landsat Enhanced Thematic Mapper Plus (ETM+), obtained from the U.S. Geological Survey. The data were processed to generate $R_{rc}(\lambda)$ using the software ACOLITE (V20170718.0). Oil–water reflectance difference was calculated as the difference of R_{rc} of oil to the nearby oil-free water in MERIS, MODIS, and Landsat images, the difference of atmosphere corrected reflectance (also corrected for aerosol besides Rayleigh scattering) in Airborne Visible/InfraRed Imaging Spectrometer (AVIRIS) data.
- 3) High-resolution (7.6 m) data from AVIRIS, obtained from the NASA’s Jet Propulsion Lab. During the DWH oil spill, AVIRIS was deployed on an aircraft to collect hyperspectral data (224 consecutive bands from 350 to 2500 nm). The data used in this paper were collected on May 17, 2010 (run 10), with a spatial resolution of

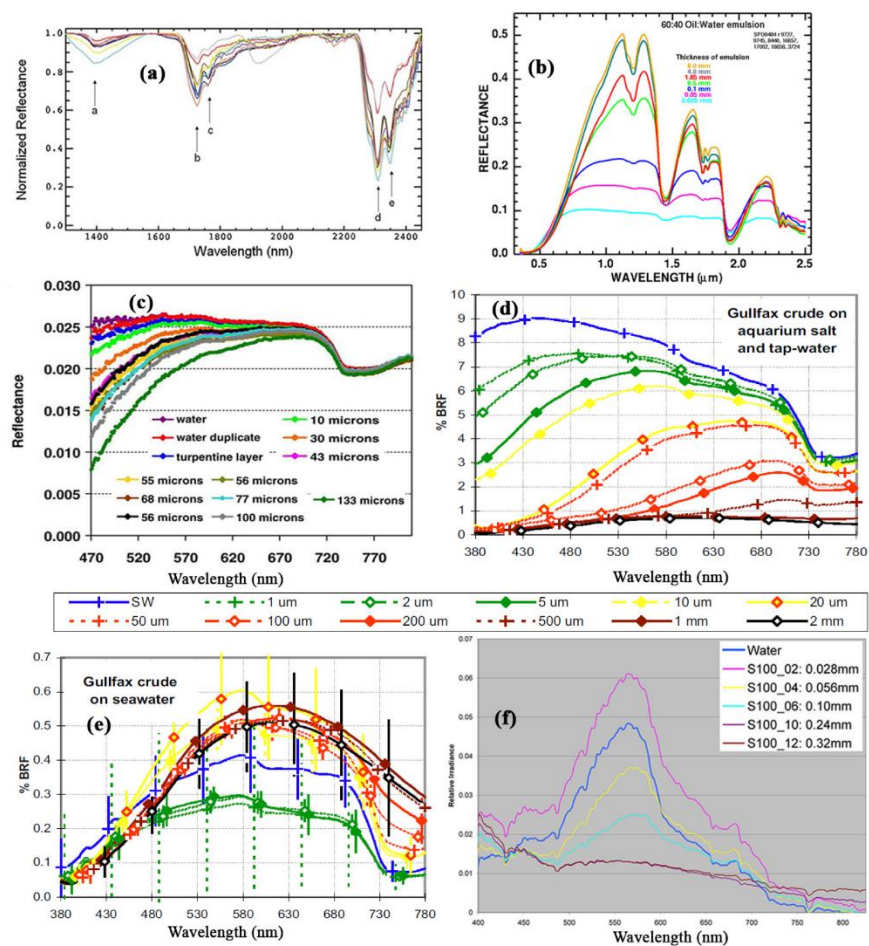


Fig. 1. Contrasting reflectance spectra of oil on water measured under different conditions by several groups. (a) Pure oil: continuum removed reflectance spectra of 17 pure oil samples obtained from the main Brazilian sedimentary basins show features of {a} O–H absorption at 1400 nm, C–H absorption features at {b} 1720–1730 nm. {c} 1750–1760 nm, {d} 2310 nm, {e} 2350 nm [24]. Figure reprinted from Lammoglia and Filho [24] with copyright permission from the publisher. (b) Oil on water spectra: varying thicknesses of 60:40 oil–water mixing ratio emulsions over quartz plates on an empty painted black glass jar. The emulsions were collected from the GoM during the DWH oil spill. Figure reprinted from Clark *et al.* [22]. (c) Oil on water spectra: Gippsland crude oil of different thicknesses on top of pure water, measured in a beaker. Figure reprinted from Wettle *et al.* [23] with copyright permission from the publisher. (d) Oil on water spectra: Gullfax crude oil of different thicknesses on artificial seawater. (e) Oil on water spectra: the same Gullfax crude oil of different thicknesses on dockside seawater. Figure reprinted from Byfield (1998, University of Southampton Ph.D. dissertation) [21] with permission from the author. (f) Oil on water spectra: Arabian Medium Crude oil of different thicknesses over the background of seawater in Oceanside Harbor, CA, USA. Figure reprinted from Svejkovsky and Muskat [25].

~7.6 m. Surface reflectance data were generated through atmospheric correction [29], and then fine-tuned through spectral matching with overflight calibration sites [30]. The AVIRIS flight time and direction were desired to avoid reflected sun glint [22].

Red–green–blue composite images were generated from all five sensors: MERIS (R: 665, G: 560, and B: 443 nm), MODIS (R: 645, G: 555, and B: 469 nm), AVIRIS (R: 638, G: 550, and B: 462 nm), Landsat ETM+ (R: 661, G: 561, and B: 479 nm), and MISR (R: 867, G: 558, and B: 446 nm). Sun

glint reflectance (L_{GN} in units of sr^{-1}) was estimated using the model from [31], where the solar/viewing geometry was known from the imagery and wind data were obtained from the National Center of Environmental Prediction.

C. Simple Conceptual Model to Classify Oil Type and Estimate Oil Thickness

Based on the published works and results of oil–water spatial and spectral contrasts from the observations below, a simple stepwise model is developed to classify oil type and

quantify relative oil thickness. Because the model development depends on analysis and interpretation of the oil–water contrasts, the method is detailed after presenting the major results of spectral analysis.

III. RESULTS

A. Laboratory Experimental Results From the Literature

1) *Signature of Pure Oil*: Many features on the ocean surface can have broadband reflectance responses that make spectral discrimination difficult or impossible. In contrast, pure oil has narrowband reflectance signatures [Fig. 1(a)] in the NIR–SWIR spectral range due to combinations of organic molecules and compounds [24]: (a) at 1390/1410 nm due to O–H first overtone and C–H combinations first overtone; (b) at 1720–1730 nm from the combination of the CH₃ and CH₂ stretching and the combination of symmetric and asymmetric CH₂ stretching; (c) at 1750–1760 nm, overtone of the CH₂ vibration; (d) at 2310 nm, due to the combination of the CH₃ asymmetric axial deformation with the CH₃ symmetric angular deformation; (e) at 2350 nm, yielded by the combination of the CH₃ symmetric axial deformation and the CH₃ symmetric angular deformation; and (f) at 1190/1210 nm some oil presents subtle spectral features as second overtones of C–H. In their experiments, Lammoglia and Filho [24] did not find narrowband diagnostic features in the visible wavelengths.

2) *Oil on Water*: The narrowband oil signature [Fig. 1(b)] in the SWIR wavelength was observed from the DWH water-in-oil emulsion samples [22]. With 60:40 oil–water mixing ratios, reflectance in the NIR–SWIR wavelengths also increases with increasing oil thickness, and so do the line depths in the SWIR wavelength corresponding to the C–H compounds. These features (enhanced reflectance in the NIR–SWIR and C–H line depth) serve as indicators of oil emulsion, and their magnitudes can be used to infer oil thickness [22] for fixed oil–water mixing ratios. Note that compared to the NIR–SWIR wavelengths, there are negligible changes in the visible wavelengths, especially in the blue–green.

In contrast to the Clark *et al.* [22] measurements, the laboratory experiments of Wettle *et al.* [23] led to different results. The Gippsland crude showed no reflectance change in the NIR–SWIR wavelengths but monotonically decreased blue–green reflectance with increasing oil thickness [Fig. 1(c)]. This is understandable because when crude oil is not emulsified, the high absorption and relatively low scattering in the short wavelengths lead to the reflectance shapes shown in Fig. 1(c). In the same experiment, the Australian northwestern shelf light condensate showed no apparent reflectance change with increasing oil thickness, because this type of oil is nearly transparent (e.g., ~100% light transmission from 400 to 1000 nm at a thickness of 200 μm , [23]).

Wettle *et al.* [23] experimental results are consistent with some of the experiments in Byfield [21], where Gullfax crude shows decreased reflectance with increasing oil thickness when oil is on artificial seawater [Fig. 1(d)]. What is different is that such decreased reflectance also occurs in the NIR. When oil is put on real seawater, the same crude oil first shows decreased

reflectance with increasing oil thickness, but then increased reflectance with increasing oil thickness [Fig. 1(e)]. Although the reason is unclear, the former reflectance decrease might be because the introduced higher reflectance from oil does not compensate the suppressing effect of surface oil fresnel reflection on signal from the water column, as oil's reflection spectra are not changing much when oil thickness is above a certain threshold [Fig. 1(d) and (e)].

Overall, these laboratory experiments suggest that, at least in principle, when crude oil is non-emulsified, reflectance changes mainly occur in the blue–green wavelengths where reflectance decreases with increasing oil thickness; when oil is emulsified, reflectance changes mainly occur in the NIR–SWIR wavelengths where reflectance increases with increasing oil thickness. These observations may form the basis to interpret remote sensing imagery.

When similar experiments are conducted outdoors in a more realistic environment under ambient sunlight, different water types and illumination conditions may cause results to differ. Svejksky and Muskat [25] measured Arabian Medium Crude oil in Oceanside Harbor, CA, USA, and found that reflectance initially increased then decreased with increasing oil thickness [Fig. 1(f)]. Reflectance of oil films in the visible wavelengths is generally lower than that of background water, with green wavelengths showing the largest changes with increasing oil thickness. This is possibly because unlike clear waters in laboratory experiments, turbid waters in a natural environment often have reflectance maximum in the green wavelengths because of strong absorption of phytoplankton and/or colored dissolved organic matter in the blue wavelengths and strong absorption of water molecules in the red and NIR wavelengths. An increase in oil thickness will thus “dampen” the green reflectance more than in other wavelengths. Note that thin films in this experiment show higher reflectance than water [Fig. 1(f)]. We believe this is caused by increased Fresnel reflectance at the surface, which is not compensated for by oil absorption because the oil is very thin.

B. Results From Remote Sensing Imagery

The laboratory experiments above measured the reflectance of oil on water under monotonic conditions for each experiment: same oil type, same emulsification state, same illumination and viewing conditions, same water type, and same experimental setting. In remote sensing imagery, these conditions may change from image to image and from pixel to pixel. Furthermore, due to the natural patchiness of oil (i.e., heterogeneity), most oil-containing pixels are mixed pixels with oil patches or slicks of different type and thickness within a pixel [32]. These factors can confuse interpretations of the oil–water spatial and spectral contrasts observed from remote sensing imagery. Below we present examples from coarse-, medium-, and high-resolution imagery to show the challenges of interpreting the spatial and spectral oil–water contrasts.

1) *Coarse-Resolution MERIS and MODIS Imagery*: Fig. 2 shows the oil–water spatial and spectral contrasts from MERIS and MODIS imagery under different solar/viewing

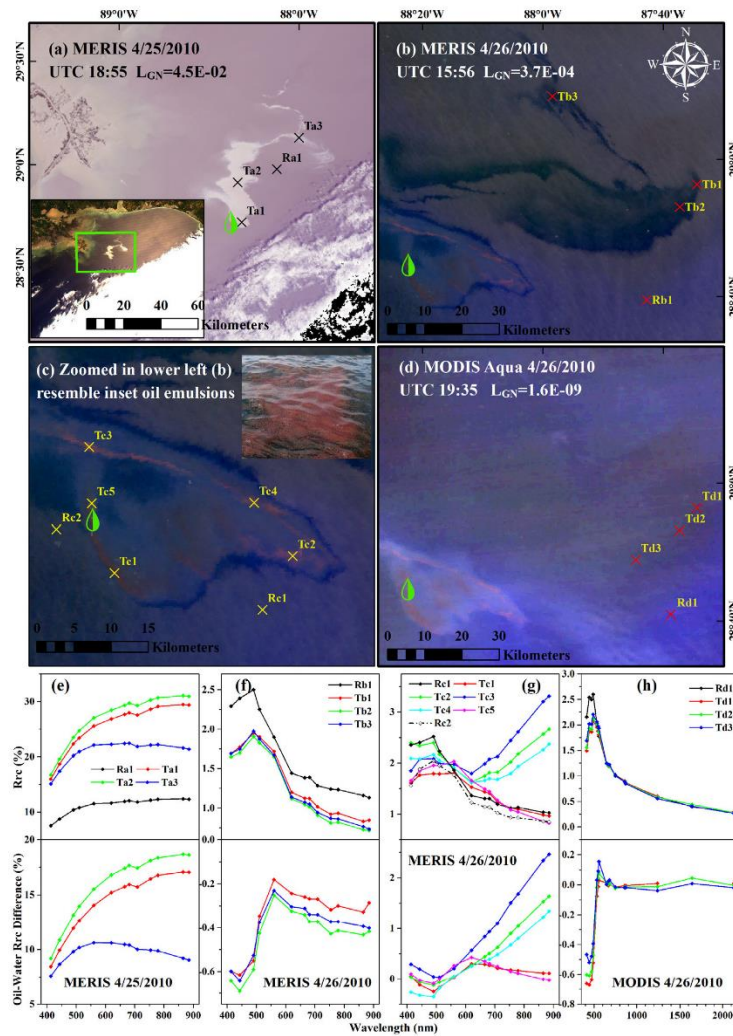


Fig. 2. MERIS and MODIS imagery showing oil slick spatial and spectral contrasts under different sun glint conditions. (a) Under strong sun glint, oil is brighter than water. The sun glint coefficient (L_{GN} , in units of sr^{-1}) calculated over water (Ra1) is annotated. The green symbol shows the location of the Macondo well location. (b) Under weak sun glint, oil is darker than water. (c) Subscene of (b) is enlarged to show oil emulsions (inset photograph credited to Sonia Gallegos and Gregg Swayze [22]). (d) Same spatial extent as in (b), image captured by MODIS Aqua 3.5 h later with negligible sun glint. Except for the bottom left portion, most oil features observed in (b) are not observable. In all images, T denotes targets (i.e., oil slicks), and R denotes reference (i.e., water). (e)–(h) Rayleigh corrected reflectance (R_{rc}) spectra of oil and water as well as their difference for the four cases in (a)–(d).

geometry. Fig. 2(a) was captured by MERIS on April 25, 2010, which shows strong positive oil–water contrast under strong sun glint conditions ($L_{GN} = 4.5E-02 sr^{-1}$). Spectrally, the oil spectra from three randomly selected locations are all higher than the nearby water in all Visible-NIR wavelengths [Fig. 2(e)]. Because sun glint reflectance is red rich after attenuation of the solar beam, the spectral shape of increased reflectance toward the red-NIR does not indicate the spectral

shape under no or negligible sun glint. Indeed, under low sun glint in the MERIS image collected on April 26, 2010 [Fig. 2(b), $L_{GN} = 3.7E-04 sr^{-1}$], none of the oil spectral shapes from the Tb and Tc locations resemble those from Fig. 2(a). From the Tb location, oil spectra show negative contrast from water [Fig. 2(f)] for all wavelengths, with the highest negative contrast shown in the blue wavelengths. While the latter is caused by strong absorption of oil in the

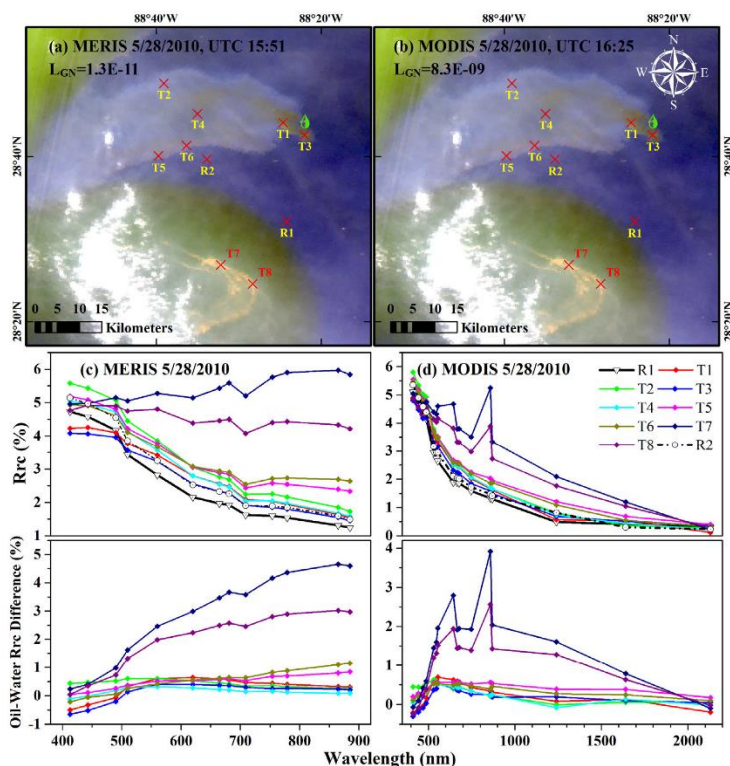


Fig. 3. (a) MERIS and (b) MODIS Terra images on May 28, 2010 showing oil-water contrasts. The spectral contrasts for selected (c) oil and (d) water pixels are shown. The local reflectance peaks around 645 and 859 nm in (d) are due to their different spatial resolution (250 m) from other bands (1 km and 500 m) and due to oil patchiness.

blue wavelengths [Fig. 1(c) and (d)], the former is due to dampening of the surface wave.

Under low or negligible sun glint conditions some spectral shapes show characteristics of typical oil emulsion [Fig. 2(c) and (g)]. The lower left portion of Fig. 2(b) is enlarged in Fig. 2(c), in which the ring-shaped slick to the east of the Macondo well location shows brownish colors that appear like oil emulsion [22]. Spectral analysis of Fig. 2(g) confirms this speculation, in which locations of Tc2, Tc3, and Tc4 all show increased reflectance toward the NIR wavelengths. The spectral analysis also ruled out the possibility of *Trichodesmium* and *Sargassum* mats because of the lack of typical algae absorption features [33], [34]. Note that although Tc1 and Tc5 also show brownish colors in the RGB image [Fig. 2(c)], they do not show elevated reflectance in the NIR, thus representing non-emulsion. Clearly, visual inspection of the RGB images is not a reliable means to infer oil type; spectral analysis is required for this purpose.

The MERIS-based observations are confirmed from MODIS observations 3.5 h later, when MODIS data were collected under negligible sun glint. The MODIS/Aqua image

in Fig. 2(d) shows similar patterns around the ring-shaped slick but less contrast in the non-emulsion T_b locations compared with the MERIS image in Fig. 2(b). Spectral analysis in Fig. 2(h) shows negative oil-water contrast in the blue with similar magnitudes to the MERIS spectra [Fig. 2(f)], resembling strong blue-light absorption of non-emulsion [Fig. 1(b)]. Unlike Fig. 2(f) where oil-water contrast is negative even in the red-NIR wavelengths because of the presence of low sun glint, there is negligible oil-water contrast in the red-NIR wavelengths in Fig. 2(h) because sun glint is negligible. The green wavelength (555 nm) shows positive oil-water contrast, and we believe this is possibly an effect caused by mixed pixels in patchy waters.

Fig. 3 presents two other examples from MERIS and MODIS (30 min apart), respectively, in which, under negligible sun glint conditions, oil slicks of both emulsion, and non-emulsion can be identified through spectral analysis. In several randomly selected locations near the oil well (T1–T6), oil spectra show typical decreased reflectance in the blue wavelengths [Fig. 3(c) and (d)] in both MERIS and MODIS images due to strong absorption in the blue, consistent with those from

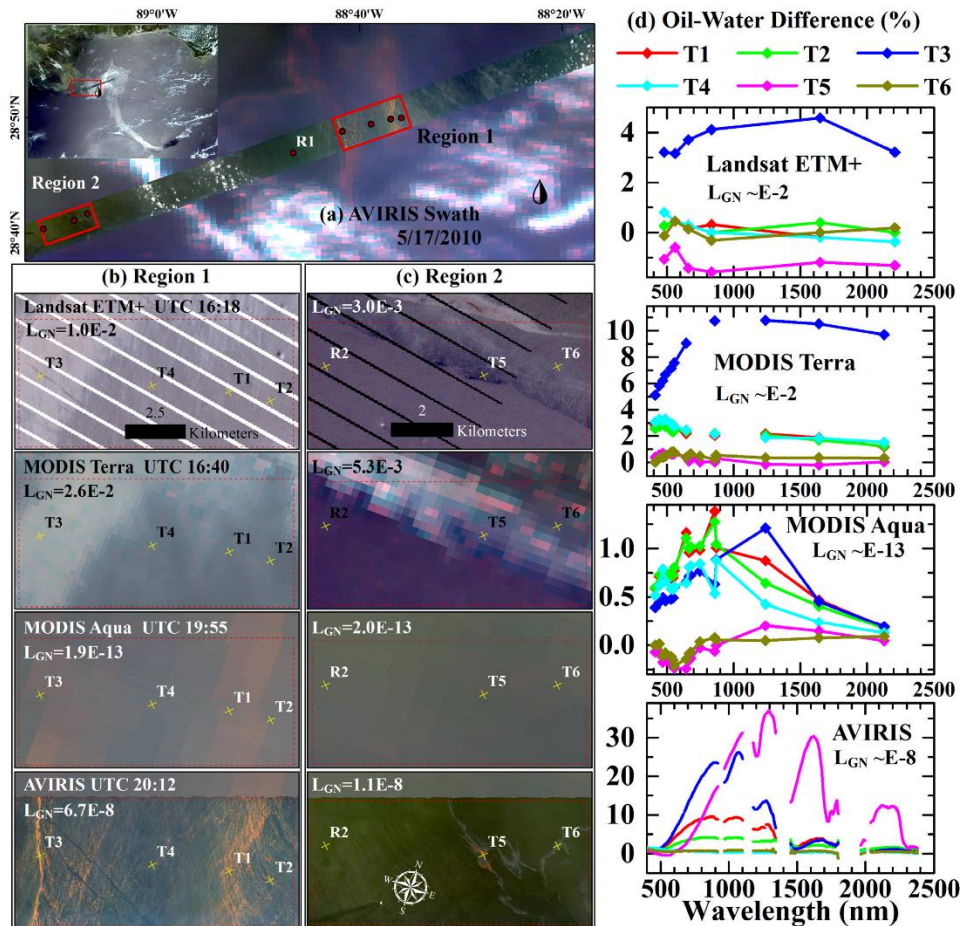


Fig. 4. (a) AVIRIS image captured on May 17, 2010 (run 10 at UTC 20:12) overlaid on the same-day MODIS Aqua image (negligible sun glint). Inset: same-day MODIS Terra image (strong sun glint). Two regions (red rectangles) along with AVIRIS swath are selected to show (b) and (c) oil-water spatial contrasts and (d) spectral contrasts in using the same-day Landsat ETM+ (UTC 16:18), MODIS Terra (UTC 16:40), MODIS Aqua (UTC 19:55), and AVIRIS. Note the dramatic difference between T5 and T3 on AVIRIS spectra, and dramatic difference between AVIRIS and other sensors on T3 and T5 spectra. The local reflectance peaks around 645 and 859 nm in the MODIS Aqua spectra in (d) are due to their different spatial resolution (250 m) from other bands (1 km and 500 m) and due to oil patchiness.

laboratory measurements [23]. Some of the pixels do not show negative contrasts in the blue or red-NIR wavelengths, likely due to mixed pixels. For oil slicks that appear brownish in the RGB images (T7 and T8), both MERIS and MODIS show increased reflectance toward longer wavelengths, resembling those reported in Clark *et al.* [22] for oil emulsion [Fig. 1(b)]. In the MODIS spectra there are several spikes at 645 and 859 nm; because of different resolutions—these bands have nadir resolution of 250 m, while most other bands have nadir resolution of 1 km or 500 m, therefore they do not measure the same area, causing discontinuity in the spectra.

2) *Higher-Resolution Landsat and AVIRIS Imagery:* Oil slicks are known to be patchy, leading to mixed pixels in coarse-resolution imagery from MODIS and MERIS as well as from Landsat [32]. On the other hand, the high-resolution (7.6 m) AVIRIS data, especially with the hyperspectral capacity to the SWIR wavelengths, can be used to gauge the coarse- and medium-resolution multiband sensors on their ability to differentiate oil type and estimate oil thickness. The examples shown in Fig. 4 demonstrate the comparison among these sensors observed within 3.5 h in the same day over the same oil slicks.

Specifically, AVIRIS collected data along the southwest–northeast transect (run 10) on May 17, 2010 [Fig. 4(a)], in which Landsat ETM+, MODIS/Terra, and MODIS/Aqua data were also collected under different sun glint conditions. In this set of images, both Landsat and MODIS/Terra images are under strong sun glint ($L_{GN} > \sim 0.005 \text{ sr}^{-1}$ in region 1), and MODIS/Aqua and AVIRIS are under negligible sun glint.

Two regions were selected to diagnose and interpret the oil–water spatial and spectral contrasts, with Region 1 closer to the oil well showing more oil slicks. Oil–water reflectance difference for selected locations from all four sensors is presented in Fig. 4(d) in two groups as follows:

- 1) Landsat ETM+ and MODIS/Terra images (20 min apart) with strong sun glint. Similar to the previous MERIS and MODIS images with strong sun glint, the oil–water spectral contrast is rather flat, with positive contrast in most locations but slightly negative contrast in one location (T5, in Landsat ETM+) because of lower sun glint. Overall, because of the modulation of sun glint to the spectral shapes, it is difficult to interpret these spectra in relation to oil type and oil thickness, especially when considering the mixed pixels from these medium- and coarse-resolution images.
- 2) MODIS/Aqua and AVIRIS images (20 min part) with negligible sun glint. For region 1, both images show brownish colors. MODIS/Aqua has much larger pixels than AVIRIS, causing the features to be smeared. In this region, all T1–T4 locations show elevated reflectance in the NIR–SWIR wavelengths, indicating possible oil emulsion. The corresponding AVIRIS spectra confirm this observation except at T4. However, the contrasting spectra at T4 between MODIS/Aqua and AVIRIS do not indicate inconsistency; it is simply a result of pixel resolution. Likewise, for T5 in region 2, the dramatic difference between MODIS/Aqua and AVIRIS spectra is also due to their different resolutions: while AVIRIS is focused on an oil emulsion pixel, most surrounding pixels contain oil-free water or very thin oil films, leading to smeared MODIS/Aqua pixel for T5.

From these comparisons, one may conclude that: 1) with the presence of strong sun glint, interpretation of oil–water spectral contrast is more difficult than with negligible sun glint; 2) under the latter circumstances, oil–water spectral contrast can be dramatically different between coarse-resolution and high-resolution sensors because of oil patchiness and mixed pixels; and 3) although the presence of sun glint facilitates visualizing oil–water spatial contrast, differentiating the oil type and estimating oil thickness are more feasible without strong sun glint. Indeed, the AVIRIS example in Fig. 4 clearly shows its potentials for differentiating oil type and estimating oil thickness, where most of those C–H absorption signatures [22], [24] in the NIR–SWIR wavelengths (~ 1200 , 1700, and 2300 nm) are clearly visible [Fig. 4(d)].

These comparisons show that sun glint strength is an important factor affecting oil–water spatial contrast. Further analysis of oil slicks from natural oil seeps in the GoM provided more quantitative estimates of the perturbation of sun glint to oil–

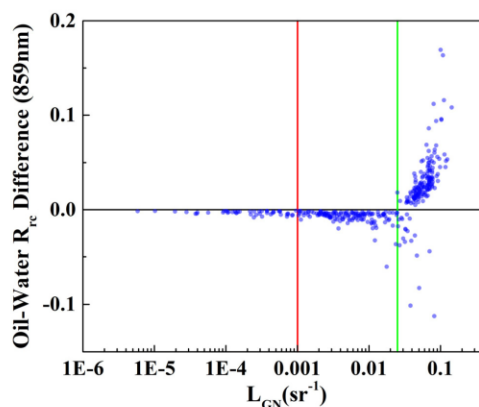


Fig. 5. Oil–water contrast (i.e., R_{rc} difference between oil pixels and nearby oil-free pixels) versus sun glint strength (L_{GN}), calculated from >300 natural slicks in the Gulf of Mexico using MODIS data. When L_{GN} is $< 0.001 \text{ sr}^{-1}$ (red line), oil–water contrast of natural oil slicks (mostly thin films from natural seeps) is very small, thus will not impact the interpretation of oil–water contrast from oil emulsions, because the latter is dominated by the contrasting optical properties of oil and water. Thin oil turns to show positive contrast with water (at 859 nm) when L_{GN} is $> \sim 0.025 \text{ sr}^{-1}$ (green line).

water contrast for thin oil films, as shown in Fig. 5. More than 300 natural slicks were used in this analysis using the method described in Sun and Hu [18]. When L_{GN} is $< 1E-03 \text{ sr}^{-1}$ (red line in Fig. 5), oil–water reflectance contrast from the natural slicks (mostly thin oil films) is very small in the NIR band. For oil emulsion, such small modulations would be overwhelmed by the elevated NIR (and SWIR) reflectance from the oil pixels, thus would not impact the image interpretation. For stronger sun glint strength (e.g., $> 0.01 \text{ sr}^{-1}$), interpretation of different oil types would become difficult.

3) *Multiangl e Imagery*: On May 17, 2010, in addition to Landsat, MODIS, and AVIRIS [Fig. 4], MISR images over the same DWH oil spill region were also obtained [Fig. 6]. The nadir-viewing image has the highest sun glint ($L_{GN} = 6.6E-02 \text{ sr}^{-1}$), where oil–water spatial contrast is always positive regardless of the oil type, oil thickness, or spectral bands [Fig. 6]. At a view angle of $\pm 26.1^\circ$, sun glint decreased to $1.0E-02 \text{ sr}^{-1}$ and $8.4E-04 \text{ sr}^{-1}$, respectively, when thin oil showed negative oil–water contrast but thicker oil still showed positive contrast. This negative to positive contrast reversal can be visualized clearly along the artificial transect (dashed red line) in Fig. 5. Furthermore, some reddish slicks appear, for example, in the green outlined region. Because the 867 nm band was used as the red channel in the RGB composite, the reddish color results from enhanced NIR reflectance, indicating oil emulsion. When the viewing angle increased further, sun glint decreased, but the general spatial contrast patterns for the three types of oil (i.e., thin, thicker, and emulsion) remain the same even though the magnitudes of contrasts change with the viewing angles. However, at large angles ($\geq 60^\circ$) when sun glint is negligible, oil–water contrast for thin oil starts to disappear, a result that is consistent

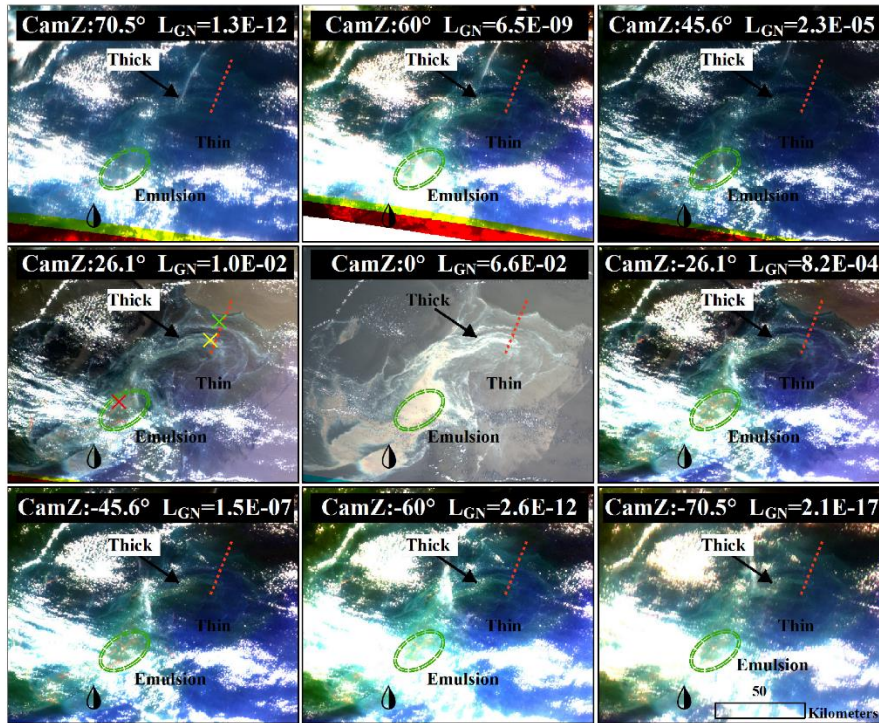


Fig. 6. False color RGB (R: 867 nm, G: 558 nm, and B: 446 nm) composite MISR images taken at UTC 16:43 (at nadir, ± 4 min among all cameras), May 17, 2010 in nine camera view angles, with sun glint strengths (from black arrow pointed thick oil regions) annotated. Positive angles indicate forward looking and negative angles indicate backward looking. Oil slicks can be clearly visualized at three angles: nadir, 26.1° and -26.1° . For images collected at other angles, it is difficult to visualize the oil–water contrast, although oil emulsion (reddish color) in the green outlined region can be discerned. Black arrows indicate thick slicks. Annotated crosses on camera angle 26.1° image displayed spectral diagnose [Fig. 7] locations of oil emulsion (red cross), non-emulsion thick oil (yellow cross) and thin oil (green cross). The dashed red line is an arbitrary transect to show reflectance changes across oil and water, shown in Fig. 8.

with [18] which concluded that under negligible sun glint ($L_{GN} < 1E-06 \text{ sr}^{-1}$) thin oil films cannot be observed in coarse-resolution imagery.

These observations are further demonstrated in Fig. 7, in which oil–water contrasts from three representative oil types: thin, thick, and emulsion. Under relatively low sun glint ($L_{GN} < 1E-04 \text{ sr}^{-1}$) oil emulsion is dramatically different from the other two types, where there is significant enhancement in the NIR reflectance. The other two types under low sun glint have more enhancement in the blue wavelengths than in the NIR wavelengths. When sun glint is extremely strong (nadir view), the magnitude of oil–water contrast between oil emulsion and non-emulsion thick oil reverses, with the latter being higher. What is interesting is that under low sun glint, the oil–water contrast has a spectral shape dramatically different from those of the laboratory experiments of Wettle *et al.* [23]; although the former shows a decrease in contrast with increasing wavelengths, the latter shows the opposite. This is possibly because of the different water types between the northern GoM and the laboratory experiments, but it does suggest difficulty when applying rules established from laboratory experiments to the real environment.

Fig. 8 shows the spatial contrast of two MISR bands, at 446 and 867 nm, respectively, along the artificial transect across oil-free water, thin oil, thick oil, and oil emulsion. Similar to previous results, strong sun glint on three of the close to nadir view cameras makes it difficult to interpret oil types, while stronger oil–water contrast is found at 867 nm than at 446 nm under low sun glint, suggesting that the use of NIR bands is preferred over blue bands for observing oil emulsions.

C. Simple Stepwise Model to Classify Oil Types

Although the laboratory and remote sensing observations above are not always consistent, several rules may be summarized as follows.

- 1) Under strong sun glint ($L_{GN} > 1E-03 \text{ sr}^{-1}$), all laboratory-established rules may fail. Not only is the oil-contrast significantly enhanced for all oil types [Fig. 5], but also the spectral shapes between visible and NIR (and some SWIR) wavelengths also change. Therefore, interpreting oil–water contrast and differentiating oil types becomes very difficult. On the other

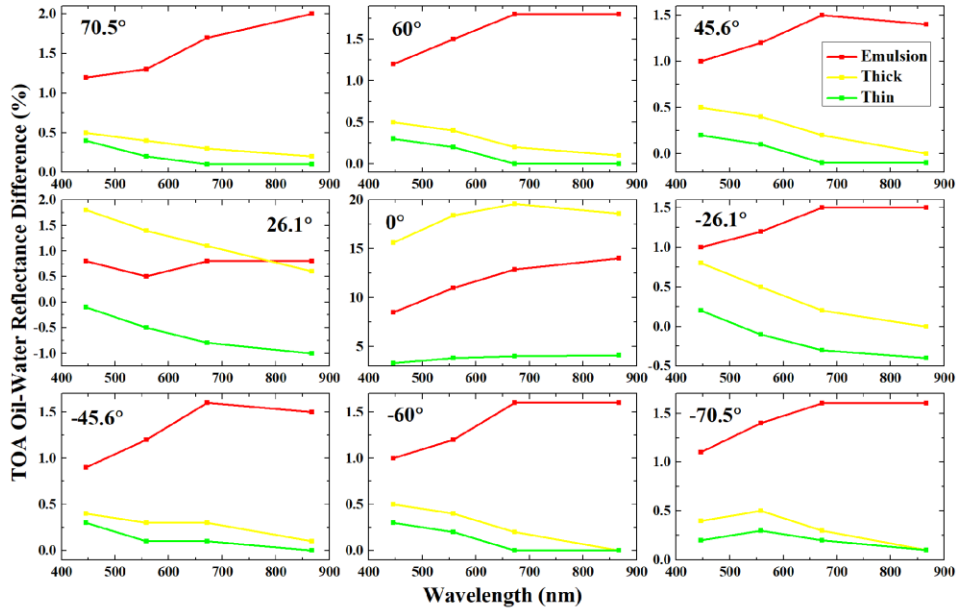


Fig. 7. TOA oil-water reflectance difference of corresponding camera view angles for oil emulsion, non-emulsion thick oil, thin oil with water in annotated locations in Fig. 6.

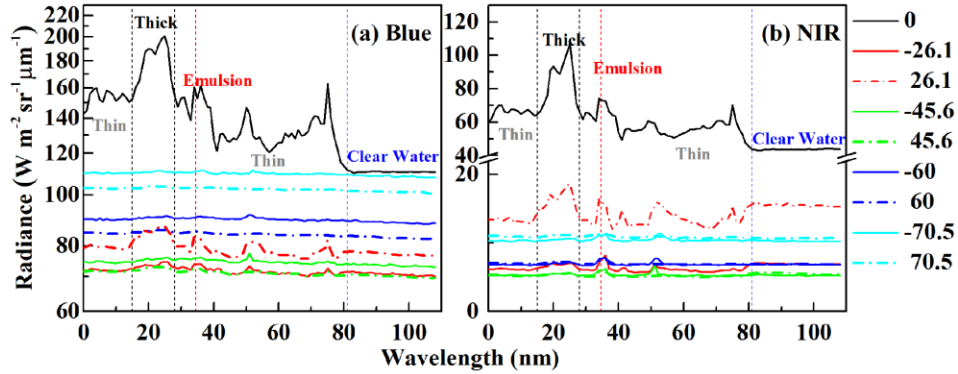


Fig. 8. Radiance changes along the artificial transect line in Fig. 6 for all nine cameras of (a) blue band (446 nm) and (b) NIR band (867 nm).

hand, the presence of strong sun glint makes oil detection (presence/absence) much easier, because oil-water contrast for thin oil films may disappear under negligible sun glint ($L_{GN} < 1E-06 \text{ sr}^{-1}$) [18].

2) Under weak sun glint ($L_{GN} < 1E-03 \text{ sr}^{-1}$ but $> 1E-06 \text{ sr}^{-1}$) [Fig. 5], it is possible to differentiate the three oil types: thin, thick, and emulsion. The last type has enhanced NIR reflectance that can be differentiated easily from the other two, thick oil has higher reflectance in the red than thin oil.

3) Under negligible sun glint ($L_{GN} < 1E-06 \text{ sr}^{-1}$), oil-water contrast for thin oil starts to disappear [18], but the rules to differentiate thick non-emulsion from emulsion still holds true.

While the second rule is known from the Clark *et al.* [22] experiment, the other two rules can be observed only through remote sensing imagery analysis and not generalized from previous lab-based experiments.

Based on these observations, a three-step simple classification scheme was developed to classify oil type and relative

oil thickness for each type using multiband data from AVIRIS measurements. Specifically, five bands of AVIRIS were used in the scheme: blue (472 nm), green (560 nm), NIR (860 nm), and SWIR (1612 and 2208 nm). These three steps are as follows.

- 1) Determine and delineate oil pixels using spatial contrast on each pixel. A crude oil–water boundary was first determined through visual inspection. Then, a 201×201 kernel was applied to each oil pixel to find all nonoil pixels within the kernel, from which mean and standard deviation of reflectance were calculated. If the oil pixel showed a difference (from water) of $< 2\sigma$ in all five bands, it was reclassified as a nonoil pixel.
- 2) Classify oil types from the delineated oil pixels into two types: emulsion and non-emulsion. If an oil pixel has a contrast (referenced against the nearest nonoil pixels) $> 2\sigma$ of the nearest nonoil pixels in all the three NIR and SWIR (860, 1612, and 2208 nm) bands, it is classified as oil emulsion, otherwise it is classified as non-emulsion.
- 3) Estimate relative oil thickness for both oil types. Oil emulsion was quantified using the band ratio of SWIR (1612 nm) to blue (472 nm): higher ratios indicate thicker oil [22]. Non-emulsion was quantified also using the band ratio of SWIR (1612 nm) to blue (472 nm): higher ratios indicate thicker oil, according to the spectral analysis above.

The three-step classification scheme (hereafter referred to as multiband approach) was applied to multiband data extracted from the hyperspectral AVIRIS data collected on May 17, 2010, with results shown in Fig. 9. Clearly, the classification results in Fig. 9(b) agree well with the visual inspection of the RGB image in Fig. 9(a). To further evaluate the performance of the multiband approach, results from the USGS hyperspectral approach by Clark *et al.* [22] (hereafter referred to as the USGS approach or hyperspectral approach) are presented in Figs. 9(c) and (d) and 10. The USGS approach has been used to quantitatively map oil volumes for a large area [35], which were used in the oil budget calculations for the DHW oil spill [26], [36].

Fig. 9(c) shows that the USGS approach resulted in similar spatial distribution patterns of oil emulsion as those from the multiband approach [Fig. 9(b)], yet the former has smaller footprint. This is because the USGS approach [22] was designed to map only thick emulsions as opposed to thin emulsions and non-emulsions, therefore representing a conservative estimation. In contrast, the multiband approach not only identified the same pixels of thick oil emulsions, but also detected thin oil emulsion and non-emulsion pixels, as shown in Fig. 9(b) and (d). A total of 14 205 AVIRIS pixels (Table I) were classified as oil emulsion by the multiband approach, 2616 of which agreed with the USGS-derived oil emulsion pixels [Fig. 9(c)]. These 2616 pixels actually represent $>99.8\%$ of all oil emulsion pixels identified by the USGS approach [Table I]. The reflectance spectra of these 2616 pixels display typical features in the NIR and SWIR bands for oil emulsion [Fig. 9(d)]. Yet the oil emulsion pixels only identified by the multiband approach also show similar features in the

TABLE I
COMPARISON BETWEEN NUMBERS OF AVIRIS PIXELS CLASSIFIED AS THREE TYPES (EMULSION, NON-EMULSION, AND WATER) FROM THE MULTIBAND APPROACH PROPOSED IN THIS PAPER AND NUMBER OF OIL EMULSION PIXELS DETERMINED FROM THE USGS HYPERSPECTRAL APPROACH [22] FOR THE AVIRIS IMAGE SHOWN IN FIG. 9

AVIRIS Pixel Type	# of Pixels (this study)	# of USGS oil emulsion pixels classified as the three types in this study
Emulsion	14205	2616
Non-Emulsion	16021	2
Water	329618	3
Total	359844	2621

NIR and SWIR although at lower magnitudes [“additional emulsion: this paper” in Fig. 9(d)], suggesting the validity of the multiband approach in identifying both thick oil emulsions and thin oil emulsions. Those spectral features are clearly different from the non-emulsion oil pixels [Fig. 9(d)], whose spectra are close to water reflectance in the NIR and SWIR bands but different from water reflectance in the blue–green bands. These results agree well with the spectral characteristics determined from laboratory measurements in the absence of sun glint, thus confirming the validity of the multiband approach in classifying oil types. Furthermore, the relative thickness estimated from the oil emulsion pixels using the multiband approach is tightly related to the absolute thickness estimated from the USGS approach from the common oil emulsion pixels ($R^2 = 0.857$, $n = 2616$, $p < 0.05$, unbiased mean relative error (UMRE, defined in the following equation) = 50%, as shown in Fig. 10), suggesting the validity of the multiband approach in quantifying relative oil thickness:

$$\text{UMRE} = \frac{1}{n} \sum_{i=1}^n \left| \frac{x_i - y_i}{0.5x_i + 0.5y_i} \right| \quad (1)$$

where x_i and y_i represent oil thickness estimated from the multiband approach (this paper, after regression) and the USGS hyperspectral approach [22], respectively. Note that the data pairs do not appear to be in parallel with the regression line because of: 1) the uneven data density in both ends of the regression line and 2) different emulsion state (i.e., different oil-to-water ratio in the emulsion), which may lead to different relationship between the hyperspectral results and multiband results. However, despite the relatively large data spread, the overall patterns between the hyperspectral and multiband results agree well with quantified uncertainties ($\sim 50\%$ in this case).

Although AVIRIS provides hyperspectral data, the multiband approach used only five bands that are often available in the commonly used multiband satellite sensors such as MODIS, Landsat-8 Operational Land Imager, and Sentinel-2 MultiSpectral Instrument. Therefore, the approach should be applicable to those multiband sensors even though these sensors have coarser resolution than AVIRIS. An example is shown in Fig. 11, where the MODIS-derived relative thickness and AVIRIS-derived oil thickness show similar spatial distri-

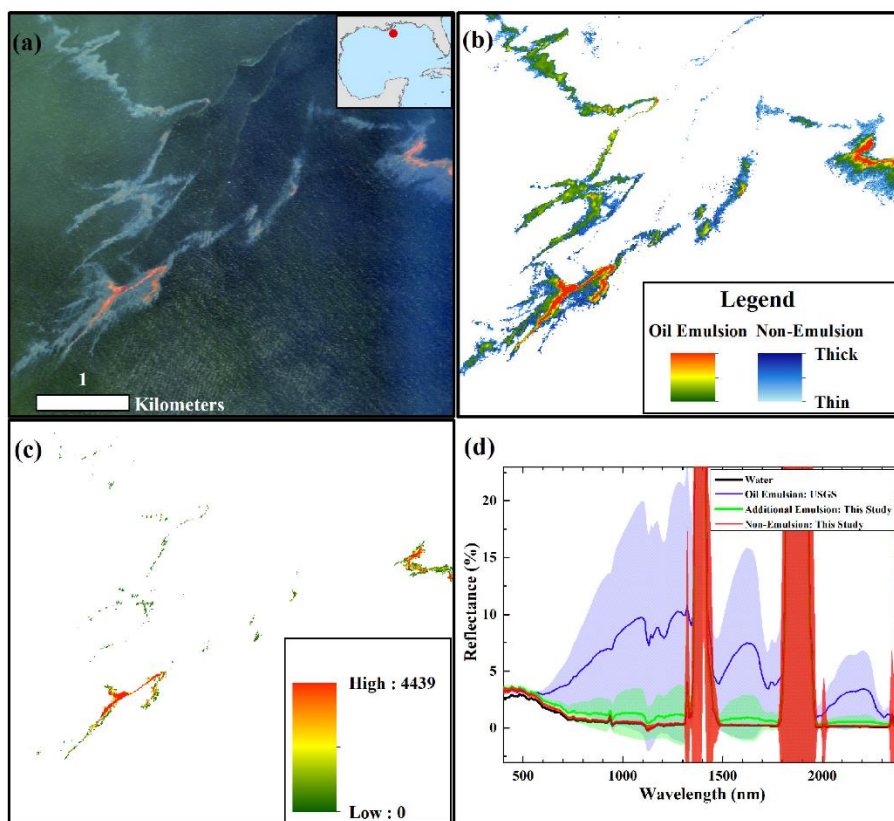


Fig. 9. Demonstration of a three-step classification scheme to determine oil type and thickness using selected AVIRIS bands from region 2 in Fig. 4. The first is to determine oiled pixels from the oil–water spatial contrast. The second is a classification of such determined oiled pixels in two categories: oil emulsion and non-emulsion. The third is to classify relative oil thickness in both categories. (a) AVIRIS image taken on May 17, 2010. The RGB (R: 638 nm, G: 550 nm, and B: 463 nm) image shows the color difference between oil emulsion and non-emulsion, with inset figures showing the location of AVIRIS image in the GoM. (b) Multiband classification results of oil emulsion and non-emulsion and their relative thickness. (c) Oil emulsion determined from the hyperspectral data using the USGS approach [22]. Here the oil emulsion thickness was calculated as oil volume divided by the pixel size ($7.6 \times 7.6 \text{ m}^2$). The entire map is openly available at <https://pubs.usgs.gov/of/2010/1167/downloads/figure16c-geotiff.tif>. (d) Mean and standard deviation spectra of several classified pixels, using both the USGS approach and the approach developed in this paper. “Oil Emulsion: USGS” indicates the oil pixels identified by the USGS hyperspectral algorithm by Clark *et al.* [22]. “Additional emulsion: this paper” and “non-emulsion: this paper” indicate the oil pixels identified by the multiband algorithm developed in this paper which were not identified by the USGS algorithm.

bution patterns. Indeed, the capacity of multiband MODIS in estimating oil volume (and therefore thickness) has been demonstrated in Hu *et al.* [37] but due to the presence of strong sun glint a different approach was used to scale AVIRIS estimates using MODIS data. In the example of Fig. 11, because of negligible sun glint, the multiband approach can be applied to MODIS R_{rc} data to estimate the relative oil thickness.

IV. DISCUSSION

A. Oil Quantification Under Idealized Conditions

Based on the contrasting results from Wettle *et al.* [23] for crude oil (i.e., non-emulsion) and Clark *et al.* [22] for oil

emulsion, if oil–water contrasts in the real environment were the same as in those lab-based experiments, it would be rather simple to differentiate oil type and quantify absolute (instead of relative) oil thickness. Specifically, the first two steps to delineate oil and differentiate oil types would be identical as in Section III-C, but the last step would be different. In the last step, once pixels of oil emulsion are determined, the lookup table approach proposed by Clark *et al.* [22] can be used to determine the absolute oil thickness. Also in the last step, for pixels of non-emulsion oil, a simple two-layer radiative transfer model could be used to determine the absolute oil thickness, as shown in the following.

Assuming a two-layer system where the top layer is oil and the bottom layer is water, following the literature for

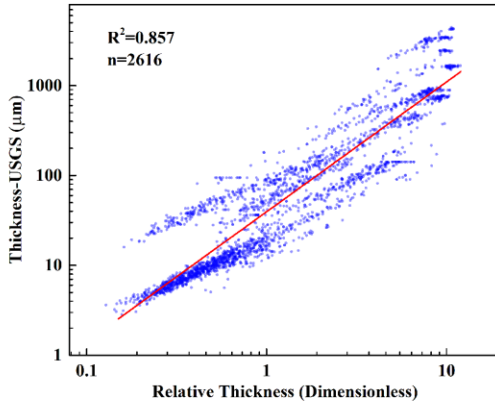


Fig. 10. Relationship between the USGS-estimated oil thickness (μm , y-axis) and multiband-derived relative thickness (dimensionless, x-axis) from common oil emulsion pixels in Fig. 9.

modeling two-layer systems [38], the pixel's reflectance R can be expressed as

$$R \approx R_o(1 - e^{-2KT}) + R_w e^{-2KT} \quad (2)$$

in which R_o is the oil reflectance when the oil layer is very thick (in practice, further increases in thickness would not lead to reflectance change), R_w is reflectance of the underneath water (assuming to be same as nearby oil-free water), K is the oil diffuse attenuation coefficient (assuming the same for downwelling and upwelling, thus the factor of 2), and T is the thickness of the oil layer. In (2), the reduction of reflectance in the first term, $R_o e^{-2KT}$, is compensated for by the water's contribution below the surface layer, $R_w e^{-2KT}$.

Then, we can derive the oil thickness as

$$T = \frac{1}{2K} \ln \left(\frac{R_w - R_o}{R - R_o} \right) \quad (3)$$

From (3), when both K and R_o are known from the laboratory measurements, in remote sensing imagery because R_w from oil-free pixels can be derived after atmospheric correction, for each R (from the oil pixel) T can be derived. From the Wettle *et al.* [23] experiment [Fig. 1(c)], a numerical regression between R and T can be used to estimate K and R_o , which can be applied to remote sensing imagery if oil optical properties in the ocean are the same as those in the experiments.

Of course, oil in the real environment may be different. For example, instead of $R_o < R_w$ [i.e., oil is darker than water, as in Fig. 1(c)], R_o may be higher than R_w . However, in this case both (2) and (3) still hold true, therefore T can still be derived for each R if K and R_o are known. When they are unknown, a number of oil pixels can be used to determine K and R_o through numerical nonlinear regression using the functional form of (2). The classification of relative thickness of non-emulsions in Fig. 9(b) followed this principle.

B. Challenges in Oil Quantification Under Realistic Conditions

The above conceptual scheme is for idealized situations. Realistically, in addition to the complexity of measurements in the real ocean environment, difficulty also comes from the different results from laboratory measurements alone. For example, the response of oil-on-water reflectance to increased oil thickness has been shown to be different between Fig. 1(c) (monotonic changes in the blue–green wavelengths) and Fig. 1(d) and (e) (more dramatic changes in the red wavelengths when oil is relatively thick). This may be a result of different crude oil types and different water properties beneath the oil layer, but these contrasting results do cause additional difficulty when interpreting remote sensing images, especially when the optical properties of both oil and water may be different from those of the laboratory experiments. One such example [Fig. 1(f)] is shown in Svejkovsky and Muskat [25].

Regardless of the different experimental results for non-emulsions, the biggest challenge comes from the changing observing conditions and complexity of the real environment.

- 1) *Sun Glint "Contaminations"*: While the presence of sun glint ($L_{GN} > 1\text{E-}06 \text{ sr}^{-1}$, [18]) greatly facilitates oil detection, it also distorts the spectral shape of oil–water contrast, making oil thickness interpretation more difficult [Figs. 2, 4–6, and 8]. When sun glint is extremely strong ($L_{GN} > 1\text{E-}02 \text{ sr}^{-1}$), because sun glint is red rich in reflectance (similar to the sunset), distortion makes it difficult to separate non-emulsion from emulsion pixels [Fig. 7]. Clearly, for oil classification, strong sun glint should be avoided. Under weak sun glint (L_{GN} between $1\text{E-}03 \text{ sr}^{-1}$ and $1\text{E-}06 \text{ sr}^{-1}$), oil classification (thin, thick, and oil emulsion) is possible with the established rules. Although it is unclear whether quantifying absolute oil thickness is still possible due to the modulated reflectance shape, it may still be possible to quantify relative oil thickness because the modulation is unlikely to change the principle of band ratios.
- 2) *Mixed Pixels*: Oil slicks are typically very patchy due to complex physical and chemical processes at different scales [22], [39]), resulting in mixed pixels. Using statistics of AVIRIS observations, Sun and Hu [32] concluded that even for Landsat 30-m resolution pixels, very few pixels are covered largely by thick oil. For coarser-resolution imagery from MODIS, MERIS, and MISR, only a small portion of any oil pixel is covered by thick oil (this is why the spectra from MODIS 250 and 500 m land bands and 1 km ocean bands do not appear smooth). In turn, the reflectance spectrum of the oil pixel can be a mixture of thin oil, thick oil, and oil emulsion. Because of this, oil–water spectral contrast can be different from any laboratory measurements, making interpretation difficult. Indeed, none of the coarse-resolution oil–water contrast spectra shown above matches perfectly with those from laboratory measurements, even under negligible sun glint. Mixed pixels may be the primary cause of this discrepancy.

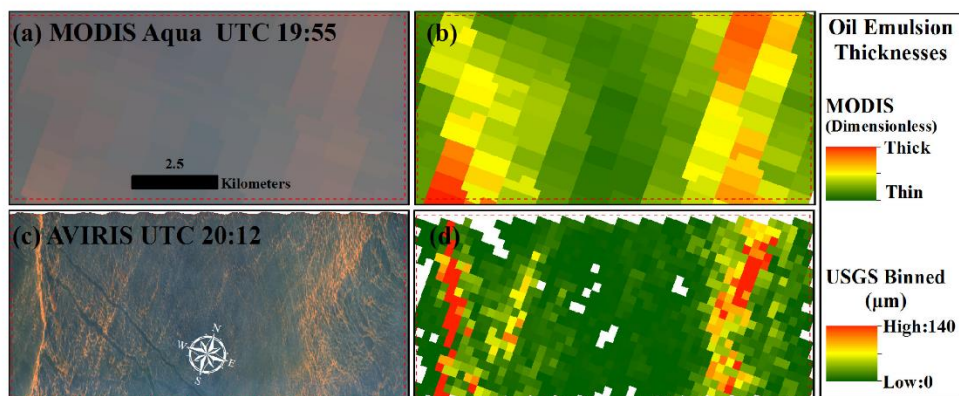


Fig. 11. Comparison between (Top) multiband MODIS and (Bottom) Hyperspectral AVIRIS for their derived oil thickness from the classified oil emulsion on May 17, 2010. The region corresponds to region 1 in Fig. 4, and the (a) and (c) RGB images in the left column are the same as those in Fig. 4. (b) Relative oil thickness image derived from MODIS multiband R_{rc} data (469, 555, 645, and 859 nm) using the methods proposed in this paper. Instead of using NIR and SWIR bands to classify oil emulsion, 645 and 859 nm bands were used for the MODIS classification here because of their higher spatial resolution (250 versus 500 m), which provide more detailed information. Accordingly, the band ratio of 859–469 nm was used in quantifying the oil emulsion thickness. (d) Absolute oil thickness image derived from AVIRIS hyperspectral data by the USGS [22] after binning to 250 m resolution. The MODIS bands have nadir resolutions of 250–500 m, but for this scan-edge image the resolution is about 1–2 km.

- 3) *Different Water Types*: In the laboratory settings, water reflectance is often higher than oil reflectance in the blue–green bands, resulting in negative oil–water contrast, and the contrast becomes stronger with increasing oil thickness. In the real environment, because of high absorption in the blue–green bands by colored dissolved organic matter, water reflectance can be lower than oil reflectance. This is believed to be the reason why positive oil–water contrast is observed from coarse-resolution imagery under negligible sun glint.
- 4) *Insufficient Spectral Resolution*: Although the C–II absorptions [22], [24] in wavelengths around 1200, 1730, and 2300 nm [Fig. 1(a) and (b)] can be well captured by hyperspectral sensors such as AVIRIS, they cannot be captured by typical multiband sensors such as MODIS and Landsat. Therefore, although multiband data can differentiate oil emulsions from others, the estimation of oil thickness is only relative.

Finally, the most significant challenge is how to validate the remote sensing interpretations. Even if oil thickness can be determined accurately from *in situ* measurements (not shown in the current literature), it is still extremely difficult to use these measurements to validate remote sensing interpretations because of the difficulty in matching *in situ* measurements with image pixels that have large pixel size and oil patchiness. Nevertheless, developing reliable *in situ* methods to measure oil thickness in the field appears to be the most critical need for oil spill remote sensing research.

C. Recommendation for Future Efforts

In the absence of high-spatial high-spectral satellite or airborne measurements, it appears that the best achievements

from coarse-resolution multiband measurements are classification of oil types and relative thickness, if strong sun glint is avoided during the measurements. Indeed, because of elevated reflectance of oil emulsions in the NIR and SWIR bands, false-color RGB images incorporating these bands may also be used to qualitatively separate oil emulsions from non emulsions (e.g., Sun *et al.* [40]). Although the ability to classify oil types and estimate relative oil thickness is very useful, especially when determining the location of “actionable” oil (i.e., can be burned or skimmed) in near real time, yet more work is required to determine absolute oil thickness. From the examples and discussions above, it is proposed that the following are in immediate need to advance oil spill quantification:

First, more lab-based measurements are required to fully understand oil–water spectral contrast under different emulsification conditions and different water environments. To simulate the real environment, the water tank needs to be large enough to minimize the impact of internal reflection. Realistic ocean water, with various water turbidity and CDOM content, needs to be used in the tank to simulate the real environment. Given that there are only a handful of published laboratory experiments in the literature, more is needed to better understand oil–water contrasts. Second, innovative *in situ* techniques to measure oil thickness in the field need to be developed. Even if oil slicks are patchy, repeated oil thickness measurements in a large area may provide statistically meaningful data to validate remote-sensing-based interpretations. Finally, unlike studies of ocean’s biogeochemical properties where field measurements can be well planned to determine the optimal sampling time and location, most oil spill studies are results of oil spill response without strategic planning. This is simply the nature of the problem. However, there are many natural seeps in different ocean basins (e.g., GoM, [41]), as well

as continuous spills from damaged oil platform locations (e.g., the Taylor platform, [42], [43]). These may serve as natural laboratories to design field measurements together with airborne remote sensing to develop, improve, and validate algorithms.

In any case, all results and discussions in this paper refer to optical remote sensing from the visible to the SWIR wavelengths. There are other techniques (beyond the scope of this paper) to estimate relative oil thickness, for example through thermal remote sensing [44], [45] and SAR remote sensing [5], [9]. It is desirable to compare the multiband approach described here with those published in the literature for a cross validation in future studies.

V. CONCLUSION

Optical remote sensing is one of the key techniques used routinely to study oil spills, but interpretation of oil–water spatial and spectral contrasts is challenging because of different results from laboratory experiments, variable observation and ocean conditions, and lack of sufficient spatial and spectral resolutions from most satellite sensors. However, through inspection of the oil–water spectral contrasts from several multiband and hyperspectral measurements of the DWH oil spill and by comparing the laboratory experimental results, it is shown that regardless of the technical challenges, it is still possible to separate oil emulsions from non-emulsions under most circumstances, and it is possible to classify relative oil thickness for both oil emulsions and non-emulsions. Meanwhile, the conditions under which such classifications are possible are discussed, and the immediate future efforts required to improve such interpretations are also proposed. Although still preliminary in nature, we hope that this paper may help the research community to improve interpretation of remote sensing imagery of oil spills, and help design future laboratory and field experiments to improve and validate algorithms.

ACKNOWLEDGMENT

The authors would like to thank USGS for providing Landsat data, which are openly accessible from <https://earthexplorer.usgs.gov/> and NASA for providing MODIS and MERIS, AVIRIS, and MISR data, which are openly accessible from <https://oceancolor.gsfc.nasa.gov/>, https://aviris.jpl.nasa.gov/alt_locator/, and <https://eosweb.larc.nasa.gov/order-data>, respectively. They would like to thank Dr. P. Hallock Muller, Dr. A. Laureano-Rosario, and K. Colna from USF to improve the presentation of the manuscript. They would also like to thank the two anonymous reviewers for their efforts to improve this paper.

REFERENCES

- [1] I. Leifer *et al.*, "State of the art satellite and airborne marine oil spill remote sensing: Application to the BP *Deepwater Horizon* oil spill," *Remote Sens. Environ.*, vol. 124, pp. 185–209, Sep. 2012.
- [2] J. V. Holmes, G. Graettinger, and I. R. MacDonald, "Remote sensing of oil slicks for the *Deepwater Horizon* damage assessment," in *Oil Spill Science and Technology*, 2nd ed. Boston, MA, USA: Gulf, pp. 889–923, 2017.
- [3] C. Brekke and A. H. S. Solberg, "Oil spill detection by satellite remote sensing," *Remote Sens. Environ.*, vol. 95, no. 1, pp. 1–13, Mar. 2005.
- [4] M. Fingas and C. Brown, "Review of oil spill remote sensing," *Marine Pollution Bull.*, vol. 83, no. 1, pp. 9–23, 2014.
- [5] O. Garcia-Pineda *et al.*, "Detection of floating oil anomalies from the *Deepwater Horizon* oil spill with synthetic aperture radar," *Oceanography*, vol. 26, no. 2, pp. 124–137, 2013.
- [6] C. Hu *et al.*, "MODIS detects oil spills in lake Maracaibo, Venezuela," *EOS, Trans., Amer. Geophys. Union*, vol. 84, no. 33, pp. 313–319, 2003.
- [7] A. K. Liu, S. Y. Wu, W. Y. Tseng, and W. G. Pichel, "Wavelet analysis of SAR images for coastal monitoring," *Can. J. Remote Sens.*, vol. 26, no. 6, pp. 494–500, 2000.
- [8] Y. C. Lu *et al.*, "Progress in marine oil spill optical remote sensing: Detected targets, spectral response characteristics, and theories," *Marine Geodesy*, vol. 36, no. 3, pp. 334–346, 2013.
- [9] B. Minchew, "Determining the mixing of oil and sea water using polarimetric synthetic aperture radar," *Geophys. Res. Lett.*, vol. 39, no. 16, p. L16607, 2012.
- [10] M. D. King, S. Platnick, W. P. Menzel, S. A. Ackerman, and P. A. Hubanks, "Spatial and temporal distribution of clouds observed by MODIS onboard the Terra and Aqua satellites," *IEEE Trans. Geosci. Remote Sens.*, vol. 51, no. 7, pp. 3826–3852, Jul. 2013.
- [11] Y. Lu, Q. Tian, X. Wang, G. Zheng, and X. Li, "Determining oil slick thickness using hyperspectral remote sensing in the Bohai Sea of China," *Int. J. Digit. Earth*, vol. 6, no. 1, pp. 76–93, Jan. 2013.
- [12] C. Hu, X. Li, W. G. Pichel, and F. E. Müller-Karger, "Detection of natural oil slicks in the NW Gulf of Mexico using MODIS imagery," *Geophys. Res. Lett.*, vol. 36, p. L01604, 2009.
- [13] B. Bulgarelli and S. Djavidnia, "On MODIS retrieval of oil spill spectral properties in the marine environment," *IEEE Geosci. Remote Sens. Lett.*, vol. 9, no. 3, pp. 398–402, May 2012.
- [14] M. Adamo, G. De Carolis, V. De Pasquale, and G. Pasquariello, "Detection and tracking of oil slicks on sun-glittered visible and near infrared satellite imagery," *Int. J. Remote Sens.*, vol. 30, no. 24, pp. 6403–6427, 2009.
- [15] Y. Lu, S. Sun, M. Zhang, B. Murch, and C. Hu, "Refinement of the critical angle calculation for the contrast reversal of oil slicks under sunglint," *J. Geophys. Res.*, vol. 121, no. 1, pp. 148–161, Jan. 2016.
- [16] C. R. Jackson and W. Alpers, "The role of the critical angle in brightness reversals on sunglint images of the sea surface," *J. Geophys. Res.*, vol. 115, p. C09019, 2010.
- [17] I. R. MacDonald *et al.*, "Natural oil slicks in the Gulf of Mexico visible from space," *J. Geophys. Res.*, vol. 98, no. C9, pp. 16351–16364, 1993.
- [18] S. Sun and C. Hu, "Sun glint requirement for the remote detection of surface oil films," *Geophys. Res. Lett.*, vol. 43, no. 1, pp. 309–316, Jan. 2016.
- [19] Z. Otremba and J. Piskozub, "Modelling of the optical contrast of an oil film on a sea surface," *Opt. Express*, vol. 9, no. 8, pp. 411–416, Oct. 2001.
- [20] G. Chust and Y. Sagarmiraga, "The multi-angle view of MISR detects oil slicks under sun glitter conditions," *Remote Sens. Environ.*, vol. 107, nos. 1–2, pp. 232–239, 2007.
- [21] V. Byfield, "Optical remote sensing of oil in the marine environment," Ph.D. dissertation, School Earth Ocean Sci., Univ. Southampton, Southampton, U.K., 1998.
- [22] R. N. Clark *et al.*, "A method for quantitative mapping of thick oil spills using imaging spectroscopy," US Geological Surv., Reston, VA, USA, Open-File Rep. 2010-1167, 2010, pp. 1–51.
- [23] M. Wettle, P. J. Daniel, G. A. Logan, and M. Thankappan, "Assessing the effect of hydrocarbon oil type and thickness on a remote sensing signal: A sensitivity study based on the optical properties of two different oil types and the HYMAP and Quickbird sensors," *Remote Sens. Environ.*, vol. 113, no. 9, pp. 2000–2010, 2009.
- [24] T. Lammoglia and C. R. de Souza Filho, "Spectroscopic characterization of oils yielded from Brazilian offshore basins: Potential applications of remote sensing," *Remote Sens. Environ.*, vol. 115, no. 10, pp. 2525–2535, 2011.
- [25] J. Svejkovsky and J. Muskat, "Real-time detection of oil slick thickness patterns with a portable multispectral sensor," U.S. Dept. Interior Minerals Manage. Service, Herndon, VA, USA, Tech. Rep., Jul. 2006.
- [26] M. K. McNutt *et al.*, "Review of flow rate estimates of the *Deepwater Horizon* oil spill," *Proc. Nat. Acad. Sci. USA*, vol. 109, no. 50, pp. 20260–20267, Dec. 2012.
- [27] U.S. District Court, "Findings of fact and conclusions of law: Phase two trial. In re: Oil spill by the oil rig 'Deepwater Horizon' in the Gulf of Mexico, on April 20, 2010," U.S. District Court for the Eastern District of Louisiana, New Orleans, LA, USA, Tech. Rep. MDL 2179, Doc. 14021, 2015.

- [28] M. Bull *et al.*, "MISR data product specifications," Jet Propuls. Lab., Caltech., Pasadena, CA, USA, Tech. Rep., 2011.
- [29] *ACORN User's Guide, Stand Alone Version*, Anal. Imag. Geophys. LLC, Boulder, CO, USA, Jan. 2001, p. 64.
- [30] R. N. Clark *et al.*, "Surface reflectance calibration of terrestrial imaging spectroscopy data: A tutorial using AVIRIS," in *Proc. 10th Airborne Earth Sci. Workshop*, 2012, pp. 43–63.
- [31] C. Cox and W. Munk, "Measurement of the roughness of the sea surface from photographs of the sun's glitter," *J. Opt. Soc. Amer.*, vol. 44, no. 11, pp. 838–850, 1954.
- [32] S. Sun *et al.*, "Oil slick morphology derived from AVIRIS measurements of the Deepwater Horizon oil spill: Implications for spatial resolution requirements of remote sensors," *Mar. Pollut. Bull.*, vol. 103, nos. 1–2, pp. 276–285, Feb. 2016.
- [33] C. Hu, J. Cannizzaro, K. L. Carder, F. E. Müller-Karger, and R. Hardy, "Remote detection of *Trichodesmium* blooms in optically complex coastal waters: Examples with MODIS full-spectral data," *Remote Sens. Environ.*, vol. 114, no. 9, pp. 2048–2058, 2010.
- [34] C. Hu, L. Feng, R. F. Hardy, and E. J. Hochberg, "Spectral and spatial requirements of remote measurements of pelagic *Sargassum* macroalgae," *Remote Sens. Environ.*, vol. 167, pp. 229–246, Sep. 2015.
- [35] I. Leifer, J. Murray, D. Streett, T. Stough, E. Ramirez, and S. Gallegos, "The Federal Oil Spill Team for Emergency Response Remote Sensing, FOSTERS: Enabling remote sensing technology for marine disaster response," in *Time-Sensitive Remote Sensing*, New York, NY, USA: Springer, 2015, pp. 91–111.
- [36] W. Lehr, S. Bristol, and A. Possolo, "Oil budget calculator: Deepwater horizon, technical documentation, A report to the National Incident Command," Federal Interagency Solutions Group, Oil Budget Calculator Sci. Eng. Team, Nov. 2010, pp. 1–49.
- [37] C. Hu *et al.*, "Remote sensing estimation of surface oil volume during the 2010 Deepwater Horizon oil blowout in the Gulf of Mexico: Scaling up AVIRIS observations with MODIS measurements," *J. Appl. Remote Sens.*, vol. 12, no. 2, p. 026008, 2018.
- [38] Z. Lee, K. L. Carder, C. D. Mobley, R. G. Steward, and J. S. Patch, "Hyperspectral remote sensing for shallow waters: 2. Deriving bottom depths and water properties by optimization," *Appl. Opt.*, vol. 38, no. 18, pp. 3831–3843, Jun. 1999.
- [39] I. Leifer, B. Luyendyk, and K. Broderick, "Tracking an oil slick from multiple natural sources, coal oil point, California," *Mar. Petroleum Geol.*, vol. 23, no. 5, pp. 621–630, 2006.
- [40] S. Sun, Y. Lu, Y. Liu, M. Wang, and C. Hu, "Tracking an oil tanker collision and spilled oils in the East China Sea using multi-sensor day and night satellite imagery," *Geophys. Res. Lett.*, vol. 45, pp. 3212–3220, 2018.
- [41] I. R. MacDonald *et al.*, "Natural and unnatural oil slicks in the Gulf of Mexico," *J. Geophys. Res., Oceans*, vol. 120, no. 12, pp. 8364–8380, Dec. 2015.
- [42] S. D. Asl, J. Amos, P. Woods, O. Garcia-Pineda, and I. R. MacDonald, "Chronic, anthropogenic hydrocarbon discharges in the Gulf of Mexico," *Deep Sea Res. II, Top. Stud. Oceanogr.*, vol. 129, pp. 187–195, Jul. 2016.
- [43] S. Sun, C. Hu, O. Garcia-Pineda, V. Kourafalou, M. Le Hénaff, and Y. Androulidakis, "Remote sensing assessment of oil spills near a damaged platform in the Gulf of Mexico," *Mar. Pollut. Bull.*, vol. 136, pp. 141–151, 2018.
- [44] Y. Lu, W. Zhan, and C. Hu, "Detecting and quantifying oil slick thickness by thermal remote sensing: A ground-based experiment," *Remote Sens. Environ.*, vol. 181, pp. 207–217, Aug. 2016.
- [45] J. Svejkovsky, M. Hess, J. Muskat, T. J. Nedwed, J. McCall, and O. Garcia, "Characterization of surface oil thickness distribution patterns observed during the Deepwater Horizon (MC-252) oil spill with aerial and satellite remote sensing," *Mar. Pollut. Bull.*, vol. 110, no. 1, pp. 162–176, Sep. 2016.



Shaojie Sun received the B.S. degree in geographical information system from the Shandong University of Science and Technology, Qingdao, China, in 2010, the M.S. degree in cartography and geography information system from the Nanjing University, Nanjing, China, in 2013, and the Ph.D. degree in marine science from the University of South Florida, St. Petersburg, FL, USA, in 2018.

He is currently with the Optical Oceanography Laboratory, College of Marine Science, University of South Florida. His research interests include remote sensing to detect and quantify oil spills in the ocean.



Chuannin Hu received the B.S. degree in physics from the University of Science and Technology of China, Hefei, China, in 1989, and the Ph.D. degree in physics (ocean optics) from the University of Miami, Coral Gables, FL, USA, in 1997.

He is a Principal or a Co-Principal Investigator of several projects funded by the U.S. National Aeronautics and Space Administration, the National Oceanic and Atmospheric Administration, the Environmental Protection Agency, and the U.S. Geological Survey to study river plumes, red tides, water quality and benthic habitat health, and connectivity of various ecosystems. He is currently a Professor with the College of Marine Science, University of South Florida, St. Petersburg, FL, USA, where he is also Director of the Optical Oceanography Laboratory.

APPENDIX B:

SUN GLINT REQUIREMENT FOR THE REMOTE DETECTION OF SURFACE OIL FILMS

Sun, S. and Hu, C. (2016). Sun glint requirement for the remote detection of surface oil films. *Geophysical Research Letters*, 43, 309–316, doi:10.1002/2015GL066884



RESEARCH LETTER

10.1002/2015GL066884

Key Points:

- Sun glint requirement for oil detection is quantified for MODIS Terra, MODIS Aqua, and VIIRS
- VIIRS appears to be more sensitive for oil detection under the same glint strength
- All three sensors show more optimal detection conditions than previously thought

Correspondence to:

C. Hu,
huc@usf.edu

Citation:

Sun, S., and C. Hu (2016), Sun glint requirement for the remote detection of surface oil films, *Geophys. Res. Lett.*, *43*, 309–316, doi:10.1002/2015GL066884.

Received 5 NOV 2015

Accepted 14 DEC 2015

Accepted article online 17 DEC 2015

Published online 14 JAN 2016

Sun glint requirement for the remote detection of surface oil films

Shaojie Sun¹ and Chuanmin Hu¹¹College of Marine Science, University of South Florida, St. Petersburg, Florida, USA

Abstract Natural oil slicks in the western Gulf of Mexico are used to determine the sun glint threshold required for optical remote sensing of oil films. The threshold is determined using the same-day image pairs collected by Moderate Resolution Imaging Spectroradiometer (MODIS) Terra (MODIST), MODIS Aqua (MODISA), and Visible Infrared Imaging Radiometer Suite (VIIRS) ($N=2297$ images) over the same oil slick locations where at least one of the sensors captures the oil slicks. For each sensor, statistics of sun glint strengths, represented by the normalized glint reflectance (L_{GN} , sr^{-1}), when oil slicks can and cannot be observed are generated. The L_{GN} threshold for oil film detections is determined to be 10^{-5} – 10^{-6} sr^{-1} for MODIST and MODISA, and 10^{-6} – 10^{-7} sr^{-1} for VIIRS. Below these thresholds, no oil films can be detected, while above these thresholds, oil films can always be detected except near the critical-angle zone where oil slicks reverse their contrast against the background water.

1. Introduction

In addition to synthetic aperture radar (SAR) and other active sensors, passive optical remote sensing using reflected sunlight has also been used to detect and monitor oil spills in the marine environments [Brekke and Solberg, 2005; Fingas and Brown, 1997, 2014; Leifer et al., 2012; Garcia-Pineda et al., 2013]. The principle of oil detection on the ocean surface using SAR is through oil's dampening of surface capillary and short gravity waves under certain wind conditions, resulting in reduced Bragg scattering signal and negative oil-water contrast in SAR imagery. In contrast, optical remote sensing of oil spill is based on the difference between oil and water's optical properties (absorption and scattering) in addition to the same wave damping effect as observed in SAR imagery. The latter effect makes it possible to observe thin oil films in optical remote sensing imagery under sun glint conditions [Adamo et al., 2009; Chust and Sagarminaga, 2007; De Carolis et al., 2014; Hu et al., 2009; Jackson and Alpers, 2010; Macdonald et al., 1993]. In particular, Hu et al. [2009] reported that oil slicks from natural seeps of the Gulf of Mexico (GoM) can be observed only when sun glint is present in the Moderate Resolution Imaging Spectroradiometer (MODIS) imagery. However, the strength of sun glint required to detect thin oil films has never been quantified objectively. It is therefore difficult or even impossible to answer the following question: if a cloud-free image does not show oil slicks, is it because there is no oil or because oil is not detectable under that observing condition? Being able to answer this question is of critical importance to avoid false negative detection. Thus, the objective of this study is to determine the sun glint threshold required for detecting thin oil films in optical remote sensing imagery. This is achieved through comparing same-day (usually within 1–2 h) imagery of multiple sensors over the same natural seeps.

2. Data and Methods

Instead of using a theoretical approach [e.g., Otremba and Piskozub, 2001, 2003; Otremba et al., 2013], the sun glint threshold in this study is determined through statistical analysis of multisensor imagery collected on the same day. Such an analysis has two critical requirements: (1) oil slicks must be sufficiently thin so that their modulation to the remote sensing signal is primarily through the wave damping effect and (2) there are simultaneous measurements of the same oil slicks by two sensors, with oil slicks captured by at least one of them (to assure there is indeed oil on the surface). For this reason, the natural oil slicks in the GoM are used together with two MODIS sensors (on Terra and Aqua, respectively) and the recently launched Visible Infrared Imaging Radiometer Suite (VIIRS).

2.1. GoM Natural Oil Slicks

Oil has its own optical properties, characterized by strong absorption in the short wavelengths and an exponential decay toward longer wavelengths [Byfield, 1998; Howari, 2004; Ma et al., 2009]. Emulsified oil is also characterized

by strong scattering in the red-NIR (near-infrared)-SWIR (shortwave infrared) wavelengths, making oil appear dark reddish [Clark *et al.*, 2010]. Thick or emulsified oil, for example, during the Deepwater Horizon oil spill, can thus be captured by MODIS imagery without sun glint [Hu *et al.*, 2011]. To determine the sun glint threshold, the oil-water contrast modulation through oil's optical properties must be minimized, making it necessary to use thin oil films to test the detectability under various sun glint strengths. The western GoM has long been known to have thin oil slicks from natural seeps [Garcia-Pineda *et al.*, 2010; Hu *et al.*, 2009; Macdonald *et al.*, 1993]. These natural oil slicks are very thin, usually 1 μm or less, due to the high evaporation rate during their initial spreading after reaching the ocean surface from the ocean floor [MacDonald *et al.*, 2002]. The modulation of the surface reflectance by these thin sheens is mostly through specular reflection [Adamo *et al.*, 2009], thus making them suitable for the purpose of determining sun glint threshold.

2.2. Remote Sensing Data and Processing

MODIS Terra (MODIST) and MODIS Aqua (MODISA) Level 0 data between 2012 and 2014 were obtained from NASA Goddard Space Flight Center and processed to calibrated radiance (Level 1B) using the SeaWiFS Data Analysis System (SeaDAS, version 7.0). Then, ozone and Rayleigh correction were applied to generate Rayleigh corrected reflectance (R_{rc}) for all spectral bands, which were then mapped to a rectangular projection at approximately 250 m per pixel to match the nominal resolution of the 645 and 859 nm bands. The 500 m resolution bands of 469 and 555 nm were resampled to 250 m using a sharpening scheme. R_{rc} data at 645, 555, and 469 nm were used to compose the red-green-blue (RGB) images for visual inspection. During this processing, the solar/viewing geometry (solar zenith, sensor zenith, and relative azimuth angles) for each pixel was also recorded.

VIIRS Level 1 calibrated radiance data for the imagery bands (640, 865, and 1610 nm, 375 m resolution) between 2012 and 2014 were obtained from the NOAA Comprehensive Large Array-data Stewardship System and then mapped to a rectangular projection. To coregister with the MODIS images for cross comparison, the VIIRS data were resampled to 250 m resolution, and RGB images were generated using the 1610 (R), 640 (G) and 865 nm (B) bands. Similar to MODIS processing, the solar/viewing geometry for each pixel was recorded during the map projection. Although due to technical difficulties R_{rc} data were not generated, this study relies on the spatial contrast between adjacent oil and oil-free pixels, and the use of total radiance instead of R_{rc} will therefore not impact any image interpretation or result.

2.3. Estimating Sun Glint Strength

Following the published literature for ocean color data processing [Wang and Bailey, 2001a; Zhang and Wang, 2010], sun glint strength was defined as the normalized sun glint reflectance (L_{GN} , in units of sr^{-1}). Based on the evaluation of several models using MODIS data, Zhang and Wang [2010] showed that the Cox and Munk [1954] model performed the best and therefore was selected to estimate L_{GN} . The model inputs included wind speed (to estimate the surface roughness) and solar/viewing geometry.

Wind speed data (4 times a day) between 2012 and 2014 were obtained from the National Centers for Environmental Prediction (NCEP). The NCEP wind product was gridded at 1° but was interpolated to 1 km resolution during processing [Wang and Bailey, 2001a]. For each MODIS or VIIRS pixel, with known wind speed and solar/viewing geometry, L_{GN} was then derived using the above model.

2.4. Determine L_{GN} Threshold for Oil Film Detection

All images were visually inspected first, from which a total of 742 MODIST images, 735 MODISA images, and 820 VIIRS images were found to contain minimal cloud cover. These images were used to determine the L_{GN} threshold for each sensor through the following steps.

1. Determine natural oil slicks from each image. Each RGB image was visually inspected using the color stretch functions in software Environment for Visualizing Images (ENVI, version 4.8) to detect spatially anomalous and elongated features as oil slicks tend to be elongated [Sun *et al.*, 2015]. An objective analysis was used to test whether the slick was statistically different from its surrounding water, which calculated the difference between the pixel of interest and a 40×100 pixel window centered at the pixel. If the difference was greater than 2 standard deviations from the mean value of the window, the pixel was then classified as a statistically significant anomaly. The anomalies were compared with those determined from other coregistered images using the same method. Recurrent anomalies at the same locations were

regarded as oil slicks from natural seeps. In short, a spatially anomalous (after color stretch) feature was regarded as a natural oil slick if (1) it is elongated, (2) it is recurrent in the same location, and (3) its spatial contrast from surrounding waters is above 2 times standard deviation.

2. Determine L_{GN} threshold for each sensor. To determine L_{GN} threshold for MODIST, each of the MODISA and VIIRS images containing oil slicks was searched for its same-day MODIST image. Once the MODIST image was found, L_{GN} from MODIST for the oil slick location (identified by either MODISA or VIIRS) was recorded. Note that here the emphasis is the *location* instead of oil slick, as the MODIST image may or may not reveal such slicks even though oil is known to exist at that time and location (from MODISA or VIIRS). Together with the already established records for MODIST oil slicks and their associated L_{GN} , a library was created where each case of oil slick presence/absence in MODIST imagery was associated with an L_{GN} value. Such a library was used to generate statistics (histogram) to determine below which L_{GN} value (i.e., threshold) oil slicks could not be detected in MODIST imagery and to determine above which L_{GN} value oil slicks could always be detected in MODIST imagery. The same method was applied to MODISA and VIIRS, with thresholds determined for each sensor.

3. Results

Figure 1 shows several examples of the same-day image pairs where one sensor revealed oil presence (first and second columns) while the paired sensor showed either oil presence or absence (third column). The corresponding L_{GN} value is annotated on each image. Figure 1a shows a case where both VIIRS and MODISA revealed oil presence, where statistically significant anomalies were found over the slick pixels. Figure 1b presents another case where the paired MODIST and VIIRS images both show oil slicks but with opposite contrasts. The other three cases (Figures 1c–1e) are examples where one sensor shows oil presence but the paired sensor does not.

A total of 2297 images between 2012 and 2014 (742 MODIST, 735 MODISA, and 820 VIIRS) were examined. Of these, 136 images were found to show oil slicks, but these slicks were not detected by the same-day images from other sensors; 167 same-day image pairs (from different sensors) were found to show oil slicks at the same locations. The remaining images were not appropriate for the study purpose because they either contained significant amount of cloud cover, did not form same-day image pairs, or did not show oil slicks in either of the paired images.

The statistical results are displayed in histograms in Figure 2 to facilitate visualization and determination of the L_{GN} threshold for oil film detection by each sensor. It is clear that the data for each sensor are separated into two groups: oil exists and detected (red) and oil exists but not detected (blue). Therefore, the L_{GN} value separating the blue and red groups was determined to be the threshold for the detection limit. Similar to any other binary classifications (e.g., cloud detection), there is always a gray zone to separate the two classes. In this case the L_{GN} threshold for the detection limit was taken as a range and determined to be 10^{-5} – 10^{-6} sr^{-1} for MODIST and MODISA and 10^{-6} – 10^{-7} sr^{-1} for VIIRS. Below the lower bound of this range, at least for 98% of the cases oil films cannot be detected. Above the higher bound of this range, at least for 98% of the cases oil films can always be detected. Within this range, oil films can sometimes be detected.

4. Discussion

The entire procedure was based on the assumption that between the same-day image pair oil slicks on the surface, if any, did not change much. This is because all three polar orbiting satellites have an equatorial crossing time of either late morning or early afternoon, making the time difference within at most 3 h. Indeed, time difference for most image pairs was < 2 h. In such a short time oil slicks are unlikely to change dramatically [Adamo *et al.*, 2009]. This has been demonstrated in both Figures 1a (time difference: 18 min) and 1b (time difference: 2 h and 23 min). Even for the latter case, the positions and shapes of identified oil slicks remained nearly unchanged in both images, confirming such an assumption.

It is interesting to see that VIIRS has improved capacity in detecting oil films than MODIST and MODISA, with its L_{GN} threshold nearly 1 order of magnitude lower (10^{-6} – 10^{-7} versus 10^{-5} – 10^{-6}). Although there are some uncertainties in the exact values, one can safely argue that VIIRS is more sensitive than MODIS in detecting oil

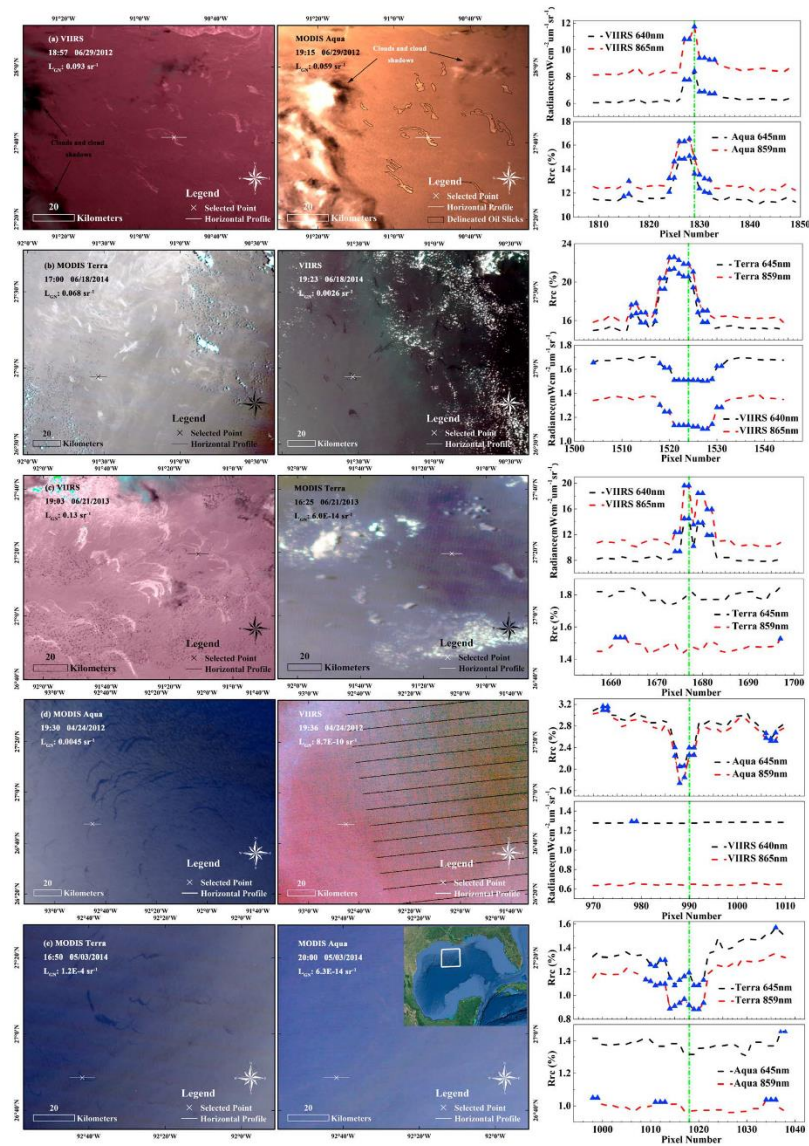


Figure 1. Examples of image pairs collected on the same day by two different sensors showing their different capacity in detecting oil slicks. (a) Oil slicks detected by both VIIRS and MODISA, (b) oil slicks detected by both MODIST and VIIRS, (c) oil slicks detected by VIIRS but not by MODIST, (d) oil slicks detected by MODISA but not by VIIRS, and (e) oil slicks detected by MODIST but not by MODISA. The corresponding plots show reflectance (for MODISA and MODIST) or radiance (for VIIRS) in the red and NIR bands along artificial transects across oil slicks (white/black lines in the images). For each selected point in the image (white/black crosses), sun glint strengths are represented by the normalized glint reflectance (L_{GNr} sr^{-1}). The blue triangles in the plots indicate outliers (>2 times standard deviation from the mean) along the transect, which represent statistically significant difference and therefore are used quantitatively to verify presence or absence of oil slicks. Sample illustration of the slick delineation and annotation of clouds and cloud shadow features is presented in Figure 1a MODISA image, while the detection rule is described in section 2.4. The inset figure (in Figure 1e) shows the approximate locations of the study region in the Gulf of Mexico.

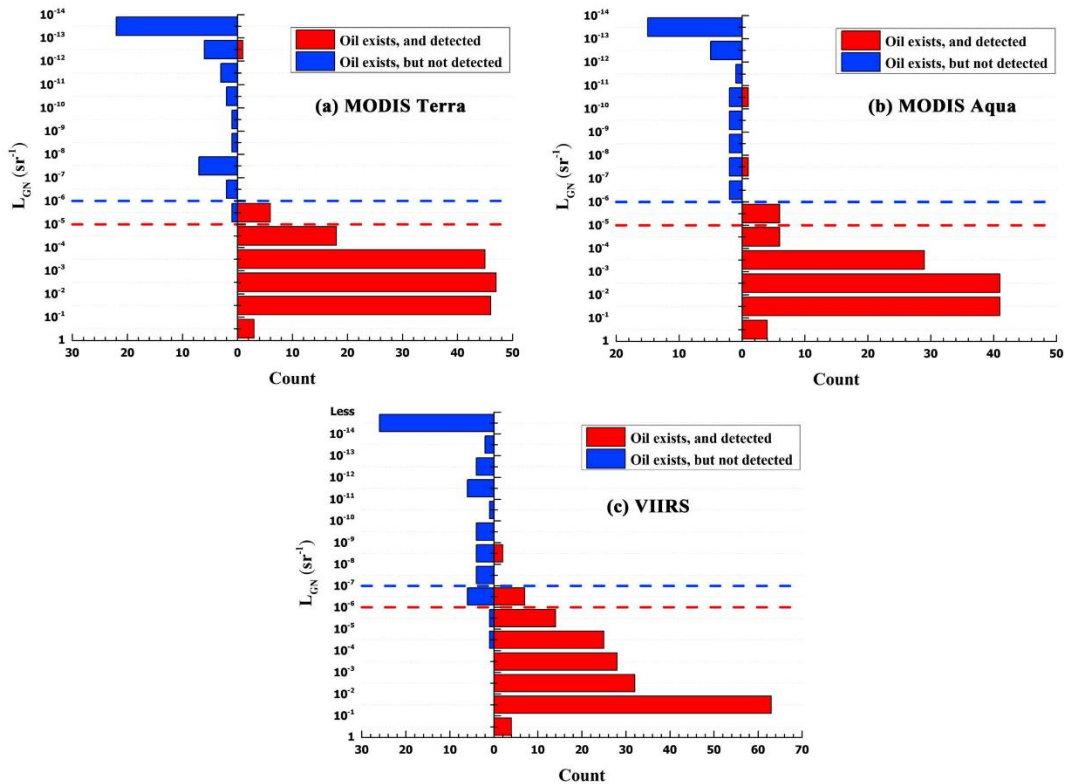


Figure 2. Statistics of sun glint strengths (L_{GN}) where oil slicks exist can or cannot be detected from satellite images. (a) MODIST, (b) MODISA, and (c) VIIRS. Count on the horizontal axis indicates number of images. The L_{GN} threshold for oil slick detection is about 10^{-5} – 10^{-6} sr^{-1} for Terra, 10^{-5} – 10^{-6} sr^{-1} for Aqua, and 10^{-6} – 10^{-7} sr^{-1} for VIIRS. For example, for MODIST, oil slicks cannot be detected if L_{GN} is $< 10^{-6}$ sr^{-1} but can be detected if L_{GN} is $> 10^{-5}$ sr^{-1} . Between 10^{-5} and 10^{-6} sr^{-1} oil slicks may or may not be detected.

films under sun glint. This may be explained by the improved signal-to-noise ratio of VIIRS over MODIS in their corresponding imaging bands [Xiong et al., 2014].

We want to emphasize that the findings here only apply to oil films where the oil's influence to the image signal (either R_{fc} or total radiance) is through primarily its modulation of surface waves. When oil is thicker, oil's optical properties play more important roles in changing the image signal, and oil may be detected even under negligible sun glint. This has been evidenced during the Deepwater Horizon oil spill through MODIS observations [Hu et al., 2011]. The same reason could also be used to explain the rare cases in Figure 2 when oil was observed in the blue zone. It is possible that some of the oil slicks could form thick layers under low wind and weak currents. However, these cases are rare ($< 2\%$), thus would not impact the findings and conclusions here. For the same reason, such detected L_{GN} thresholds can apply to biogenic surfactants (from phytoplankton), below which the surfactants could not be detected even if they exist.

The L_{GN} thresholds have at least three significant implications for monitoring oil spills and studying oil seeps. First, oil absence in cloud-free satellite imagery does not necessarily suggest that there is no oil, but it can be due to unfavorable sun glint conditions. Only when L_{GN} is greater than the higher bound of the threshold range can one conclude that there is indeed no oil. This information will then help

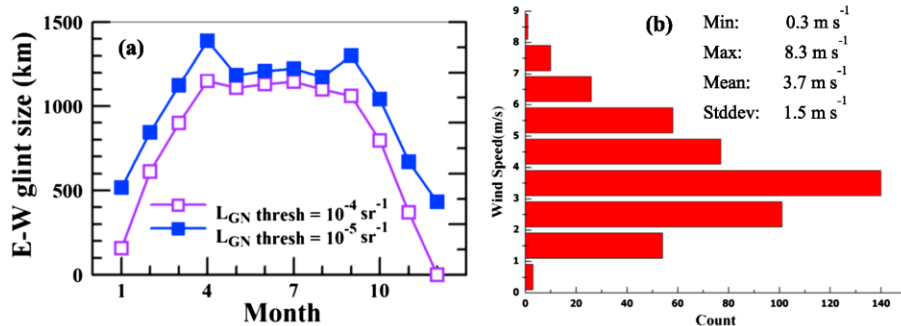


Figure 3. (a) Seasonal glint coverage (glint defined as $L_{GN} > L_{GN}$ threshold) in the MODIS Aqua swath at 25°N assuming wind speed = 5 m s^{-1} . Results for MODIS Terra and VIIRS are similar. Note that the results for L_{GN} threshold = 10^{-4} sr^{-1} are the same as in Figure 4 of Hu *et al.* [2009]. (b) Wind speed distribution for all sun glint images where oil slicks were identified ($N=470$ images). Note that the data for the two extremes ($>8 \text{ m s}^{-1}$ and $<1 \text{ m s}^{-1}$) were from the nearby buoys (after adjustment to 10 m above surface), while other data were from NCEP.

make decisions during an oil spill on whether and where to put sampling or mitigation efforts. Second, for the same reason, images associated with unfavorable sun glint conditions ($L_{GN} < \text{threshold}$) should not be used to determine whether oil seeps release oil continuously. Instead, those images should be regarded as “no data” when performing statistical analysis of oil seeps. In this regard, the L_{GN} thresholds will help address the critical question of whether oil seeps in the GoM continuously release oil, as such a question has been difficult to address with SAR observations due to their infrequent coverage or with MODIS observations due to lack of knowledge whether oil absence in the image means no oil on the ocean surface. Third, due to the limited number of images used in the original study, Hu *et al.* [2009] assumed that $L_{GN} > 10^{-4} \text{ sr}^{-1}$ when calculating sun glint “size” in terms of kilometers in the east-west direction for the GoM at 25°N . Such an assumption agreed with independent observations by Adamo *et al.* [2009]. The findings here suggest that the L_{GN} threshold is at least 1 order of magnitude lower (10^{-5} sr^{-1}), leading to increased sun glint size usable for slick detection. Figure 3a shows that when 10^{-5} was used as the threshold, the estimated sun glint size was significantly higher than the original estimation using the 10^{-4} threshold [Hu *et al.*, 2009]. Even during the winter, a significant portion of MODIS and VIIRS images meets the criteria of $L_{GN} > 10^{-5} \text{ sr}^{-1}$, thus suitable for detecting oil films.

L_{GN} is a function of wind, and it is therefore desirable to know which wind conditions are optimal for slick detection. While the optimal wind speed required to detect thin oil slicks in SAR imagery has been reported to vary slightly (e.g., 3 to $7\text{--}10 \text{ m s}^{-1}$ in Brekke and Solberg [2005]; 3.5 to 7 m s^{-1} in Garcia-Pineda *et al.* [2009]), a general consensus is that the wind limits are around $1.5\text{--}10 \text{ m s}^{-1}$ [Fingas and Brown, 2014], beyond which thin oil cannot be observed in SAR imagery. In this study, for all images where slicks were identified, wind ranged between 0.3 and 8.3 m s^{-1} (Figure 3b), with $1.0\text{--}8.0 \text{ m s}^{-1}$ for $> 99\%$ of the oil slick images. On the accuracy of wind conditions, the extremes (<1.0 and $> 8.0 \text{ m s}^{-1}$) of original NCEP wind data were substituted by data obtained from the nearest National Data Buoy Center buoys (after adjustment to 10 m above sea surface) in this analysis. Clearly, these results are comparable to those reported in the literature, further confirming that optical detection of thin oil films in sun glint imagery is primarily due to the wave damping effect. There are three cases showing wind speed of $< 1.0 \text{ m s}^{-1}$ (Figure 3b), possibly because these optical channels are more sensitive than SAR to wave damping-induced spatial contrast.

While the judgment on the sun glint conditions is through the use of L_{GN} , in practice a researcher or a flight pilot may not have an easy way to calculate L_{GN} even when the solar/viewing geometry and wind are all known. As a simple guide, Figure 4 provides L_{GN} as a function of solar zenith and sensor zenith angles at four relative azimuth angles ($0^\circ, 90^\circ, 270^\circ$, and 180°) and two wind speeds (3 m s^{-1} and 6 m s^{-1}). The L_{GN} thresholds are also annotated. From these graphs, one may make a quick and relatively accurate judgment on whether the measurement geometry under certain wind conditions favors the detection of thin oil films. Note that NCEP wind product is known to contain about 20% uncertainties without any obvious bias when evaluated against buoy

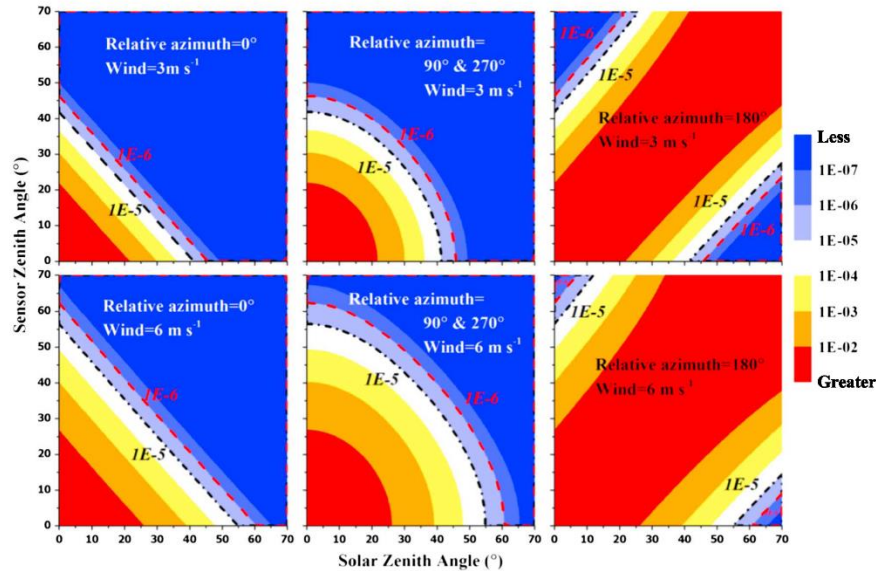


Figure 4. L_{GN} (sr^{-1}) as a function of solar zenith angle, sensor zenith angle, their relative azimuth, and wind speed. For illustration purpose only several values of relative azimuth and wind speed are chosen. The L_{GN} thresholds to observe thin oil films are highlighted with dashed lines. The relative azimuth is defined as 180° when the Sun and the sensor are at mirroring positions.

data [Wang and Bailey, 2001b]. A sensitivity analysis indicated that when wind speed was 20% underestimated, L_{GN} would also be underestimated (1 order of magnitude lower for L_{GN} around $10^{-5} sr^{-1}$). When wind speed was 20% overestimated, L_{GN} around $10^{-5} sr^{-1}$ would be overestimated by 4 times.

Note that the results obtained here are for the lower detection limit with low sun glint strengths. For extremely strong sun glint ($L_{GN} \sim 0.05 sr^{-1}$ [Hu et al., 2009]), oil slicks may reverse their contrast from negative to positive around a critical angle [Jackson and Alpers, 2010]. In the narrow transition zone oil slicks lose their contrast from water. However, the transition zone is typically small (several kilometers for a sensor at 700 km altitude), thus would not impact the statistics here.

Finally, the detection capacity will also depend on a sensor's sensitivity (i.e., signal-to-noise ratio), and application of the findings here to other sensors may therefore require some caution before a similar study is conducted for the specific sensor of interest.

5. Conclusion

For the first time, sun glint requirement for detecting oil films in optical remote sensing imagery from the three widely used ocean color sensors is quantified through multisensor comparisons, with the following two main findings:

1. L_{GN} threshold for oil film detections is 10^{-5} – $10^{-6} sr^{-1}$ for MODIST and MODISA, and 10^{-6} – $10^{-7} sr^{-1}$ for VIIRS. Below the lower bounds of these thresholds, no oil films can be detected, while above the upper bounds oil films can always be detected;
2. The optimal wind range for the three sensors is 1.0 – $8 m s^{-1}$, while the lower and upper bounds are found to be 0.3 and $8.3 m s^{-1}$ from this analysis.

The sun glint thresholds determined here will provide critical information on which images (or which portions of an image) can be used to search for oil, thus reducing false negative detection and improving statistics for oil slick occurrence. From these results, the image portion suitable for detecting oil films has been found to be

higher than previously thought, further reinforcing the conclusion that optical remote sensing imagery provides a significant data source to complement SAR and other observations to study oil spills.

Acknowledgments

This study was possible because of the financial support from the NASA Ocean Biology and Biogeochemistry (OBB) program (grant NNX13AD08G), the BP/Gulf of Mexico Research Initiative through C-IMAGE (SA 15-16), the Bureau of Ocean Energy Management (BOEM, contract M12PC00003), and NOAA NESDIS (subaward S14-0006 from the University of Miami). We thank NASA for providing MODIS Terra and Aqua data, which are openly accessible from <http://oceancolor.gsfc.nasa.gov>, and NOAA for providing VIIRS data, which are openly accessible from http://www.nsof.class.noaa.gov/saa/products/search?datatype_family=VIIRS.

References

- Adamo, M., G. De Carolis, V. De Pasquale, and G. Pasquariello (2009), Detection and tracking of oil slicks on sun-glittered visible and near infrared satellite imagery, *Int. J. Remote Sens.*, *30*, 6403–6427.
- Brekke, C., and A. H. S. Solberg (2005), Oil spill detection by satellite remote sensing, *Remote Sens. Environ.*, *95*, 1–13.
- Byfield, V. (1998), Optical remote sensing of oil in the marine environment, PhD thesis, School of Ocean and Earth Science, pp. 302, Univ. of Southampton, Southampton, U. K.
- Chust, G., and Y. Sagarmínaga (2007), The multi-angle view of MISR detects oil slicks under sun glitter conditions, *Remote Sens. Environ.*, *107*, 232–239.
- Clark, R. N., G. A. Swayze, I. Leifer, K. E. Livo, R. Kokaly, T. Hoefen, S. Lundeen, M. Eastwood, R. O. Green, and N. Pearson (2010), A method for quantitative mapping of thick oil spills using imaging spectroscopy, *U.S. Geol. Surv. Open File Rep.*, *1167*, 1–51.
- Cox, C., and W. Munk (1954), Measurement of the roughness of the sea surface from photographs of the sun's glitter, *J. Opt. Soc. Am.*, *44*, 838–850.
- De Carolis, G., M. Adamo, and G. Pasquariello (2014), On the estimation of thickness of marine oil slicks from sun-glittered, near-infrared MERIS and MODIS imagery: The Lebanon oil spill case study, *IEEE Trans. Geosci. Remote Sens.*, *52*, 559–573.
- Fingas, M., and C. E. Brown (2014), Review of oil spill remote sensing, *Mar. Pollut. Bull.*, *83*, 9–23.
- Fingas, M. F., and C. E. Brown (1997), Review of oil spill remote sensing, *Spill Sci. Technol. Bull.*, *4*, 199–208.
- García-Pineda, O., B. Zimmer, M. Howard, W. Pichel, X. Li, and I. R. MacDonald (2009), Using SAR images to delineate ocean oil slicks with a texture-classifying neural network algorithm (TCNNA), *Can. J. Remote Sens.*, *35*, 411–421.
- García-Pineda, O., I. MacDonald, B. Zimmer, B. Shedd, and H. Roberts (2010), Remote-sensing evaluation of geophysical anomaly sites in the outer continental slope, northern Gulf of Mexico, *Deep Sea Res., Part II*, *57*, 1859–1869.
- García-Pineda, O., I. MacDonald, C. Hu, J. Svejkský, M. Hess, D. Dukhovskoy, and S. Morey (2013), Detection of floating oil anomalies from the Deepwater Horizon oil spill with synthetic aperture radar, *Oceanography*, *26*(2), 124–137.
- Howari, F. M. (2004), Investigation of hydrocarbon pollution in the vicinity of United Arab Emirates coasts using visible and near infrared remote sensing data, *J. Coastal Res.*, *20*(4), 1089–1095.
- Hu, C., X. Li, W. G. Pichel, and F. E. Muller-Karger (2009), Detection of natural oil slicks in the NW Gulf of Mexico using MODIS imagery, *Geophys. Res. Lett.*, *36*, L01604, doi:10.1029/2008GL036119.
- Hu, C., R. H. Weisberg, Y. Liu, L. Zheng, K. Daly, D. English, J. Zhao, and G. Vargo (2011), Did the northeastern Gulf of Mexico become greener after the Deepwater Horizon oil spill?, *Geophys. Res. Lett.*, *38*, L09601, doi:10.1029/2011GL047184.
- Jackson, C. R., and W. Alpers (2010), The role of the critical angle in brightness reversals on sunglint images of the sea surface, *J. Geophys. Res.*, *115*, C09019, doi:10.1029/2009JC006037.
- Leifer, I., et al. (2012), State of the art satellite and airborne marine oil spill remote sensing: Application to the BP Deepwater Horizon oil spill, *Remote Sens. Environ.*, *124*, 185–209.
- Ma, L., Y. Li, and Y. Liu (2009), Oil spill monitoring based on its spectral characteristics, *Environ. Forensics*, *10*, 317–323.
- Macdonald, I. R., N. L. Guinasso, S. G. Ackleson, J. F. Amos, R. Duckworth, R. Sassen, and J. M. Brooks (1993), Natural oil slicks in the Gulf of Mexico visible from space, *J. Geophys. Res.*, *98*(C9), 16,351–16,364, doi:10.1029/93JC01289.
- MacDonald, I. R., I. Leifer, R. Sassen, P. Stine, R. Mitchell, and N. Guinasso (2002), Transfer of hydrocarbons from natural seeps to the water column and atmosphere, *Geofluids*, *2*, 95–107.
- Otremba, Z., and J. Piskozub (2001), Modeling of the optical contrast of an oil film on a sea surface, *Opt. Express*, *9*, 411–416.
- Otremba, Z., and J. Piskozub (2003), Modeling the remotely sensed optical contrast caused by oil suspended in the sea water column, *Opt. Express*, *11*, 2–6.
- Otremba, Z., O. Zielinski, and C. Hu (2013), Optical contrast of oil dispersed in seawater under windy conditions, *J. Eur. Opt. Soc. - Rapid Publ.*, *8*, 13051, doi:10.2971/jeos.2013.13051.
- Sun, S., C. Hu, L. Feng, G. Swayze, J. Holmes, G. Graettinger, I. MacDonald, O. Garcia, and I. Leifer (2015), Oil slick morphology derived from AVIRIS measurements of the Deepwater Horizon oil spill: Implications for spatial resolution requirements of remote sensors, *Mar. Pollut. Bull.*, doi:10.1016/j.marpolbul.2015.12.003.
- Wang, M., and S. W. Bailey (2001a), Correction of sun glint contamination on the SeaWiFS ocean and atmosphere products, *Appl. Opt.*, *40*, 4790–4798.
- Wang, M., and S. W. Bailey (2001b), Correction of the sun glint contamination on the SeaWiFS aerosol optical thickness retrievals, in *SeaWiFS Postlaunch Technical Report Series, NASA Tech. Memo. 2000-206892*, vol. 9, edited by S. B. Hooker and E. R. Firestone, pp. 64–68, NASA Goddard Space Flight Center, Greenbelt, Md.
- Xiong, X., et al. (2014), VIIRS on-orbit calibration methodology and performance, *J. Geophys. Res. Atmos.*, *119*, 5065–5078, doi:10.1002/2013JD020423.
- Zhang, H., and M. Wang (2010), Evaluation of sun glint models using MODIS measurements, *J. Quant. Spectros. Radiat. Transfer*, *111*, 492–506.

APPENDIX C:

OIL SLICK MORPHOLOGY DERIVED FROM AVIRIS MEASUREMENTS OF THE DEEPWATER HORIZON OIL

SPILL: IMPLICATIONS FOR SPATIAL RESOLUTION REQUIREMENTS OF REMOTE SENSORS

Sun, S., Hu, C., Feng, L., Swayze, G.A., Holmes, J., Graettinger, G., MacDonald, I., Garcia-Pineda, O., and Leifer, I. (2016). Oil slick morphology derived from AVIRIS measurements of the Deepwater Horizon oil spill: Implications for spatial resolution requirements of remote sensors. *Marine Pollution Bulletin*, 103, 276-285, doi:10.1016/j.marpolbul.2015.12.003



Contents lists available at ScienceDirect

Marine Pollution Bulletin

journal homepage: www.elsevier.com/locate/marpolbul

Oil slick morphology derived from AVIRIS measurements of the Deepwater Horizon oil spill: Implications for spatial resolution requirements of remote sensors



Shaojie Sun^{a,*}, Chuanmin Hu^{a,*}, Lian Feng^a, Gregg A. Swayze^b, Jamie Holmes^c, George Graettinger^d, Ian MacDonald^e, Oscar Garcia^e, Ira Leifer^f

^a College of Marine Science, University of South Florida, 140 Seventh Avenue South, St. Petersburg, FL 33701, United States

^b U.S. Geological Survey, Crustal Geophysics and Geochemistry Science Center, MS XXX, Denver, CO 80225, United States

^c Abt Associates Inc., 1881 Ninth St, Suite 201, Boulder, CO 80302, United States

^d NOAA Ocean Service, 7600 Sand Point Way NE, Seattle, WA 98115, United States

^e Earth Ocean and Atmospheric Science Department, Florida State University, 117 N. Woodward Ave., Tallahassee, FL 32306, United States

^f Bubbleology Research International (BRI), 5910 Matthews St, Goleta, CA 93117, United States

ARTICLE INFO

Article history:

Received 23 July 2015

Received in revised form 14 November 2015

Accepted 5 December 2015

Available online 22 December 2015

Keywords:

Oil spill

Remote sensing

AVIRIS

Landsat

MERIS

Morphology

ABSTRACT

Using fine spatial resolution (~7.6 m) hyperspectral AVIRIS data collected over the Deepwater Horizon oil spill in the Gulf of Mexico, we statistically estimated slick lengths, widths and length/width ratios to characterize oil slick morphology for different thickness classes. For all AVIRIS-detected oil slicks ($N = 52,100$ continuous features) binned into four thickness classes ($\leq 50 \mu\text{m}$ but thicker than sheen, 50–200 μm , 200–1000 μm , and $> 1000 \mu\text{m}$), the median lengths, widths, and length/width ratios of these classes ranged between 22 and 38 m, 7–11 m, and 2.5–3.3, respectively. The AVIRIS data were further aggregated to 30-m (Landsat resolution) and 300-m (MERIS resolution) spatial bins to determine the fractional oil coverage in each bin. Overall, if 50% fractional pixel coverage were to be required to detect oil with thickness greater than sheen for most oil containing pixels, a 30-m resolution sensor would be needed.

© 2015 Elsevier Ltd. All rights reserved.

1. Introduction

Oil spills in the ocean can pose a significant threat to the ecosystem (NRC, 2003). One recent example is the Deepwater Horizon (DWH) oil spill in the northern Gulf of Mexico (Fig. 1), a result of the explosion and sinking of the DWH oil rig on 20 April 2010. The spill continued until the oil well was capped on 15 July 2010, with an estimated 3.19 million barrels of crude oil released into the ocean (Crone and Tolstoy, 2010; McNutt et al., 2011; U.S. v. BP et al., 2015) and a significant portion accumulated on the sea surface (De Gouw et al., 2011).

Accurate detection of surface oil distribution and estimation of oil volume are valuable for oil spill response and for understanding the spill's potential environmental impacts. Remote sensing has been used effectively for some of these assessments (Fingas and Brown, 1997; Brekke and Solberg, 2005; Leifer et al., 2012). Of all remote sensing techniques, Synthetic Aperture Radar (SAR) is the most frequently used (e.g., Garcia-Pineda et al., 2013), which offers synoptic data under all sky conditions. Because oil can dampen short-gravity and capillary waves on the ocean surface, a reduction in the backscattering

SAR signal can be observed in oil containing image pixels under optimal wind conditions. Although recent research has shown the potential of using SAR to discriminate thick emulsified oil from other oil (Garcia-Pineda et al., 2013; MacDonald et al., 2015), SAR has been primarily used to delineate surface oil footprint instead of estimating oil thickness. The same concept of wave dampening can also be extended to passive optical remote sensing when sun glint is present (e.g., MacDonald et al., 1993; Adamo et al., 2009; Hu et al., 2003, 2009; De Carolis et al., 2014). When oil slicks are sufficiently thick, they can also be observed in optical remote sensing imagery in the absence of sun glint (Bulgarelli and Djavidnia, 2012).

While determining the oil spill footprint can be achieved through different remote sensing techniques (e.g., SAR, optical, thermal, and others), estimating the surface oil volume (or thickness) is much more difficult (Svejkovsky et al., 2015; Fingas and Brown, 2015). Some recent advances showed that spectral and spatial contrast analyses could be used to infer relative oil thickness from optical remote sensing imagery, which could then be used for management actions during a spill (Svejkovsky et al., 2012). Some case studies showed the possibility to infer oil thickness from optical remote sensing imagery based on laboratory-derived look up tables (e.g., Lu et al., 2013). Furthermore, recent research demonstrated the use of hyperspectral C–H absorption

* Corresponding author.

E-mail address: huc@usf.edu (C. Hu).

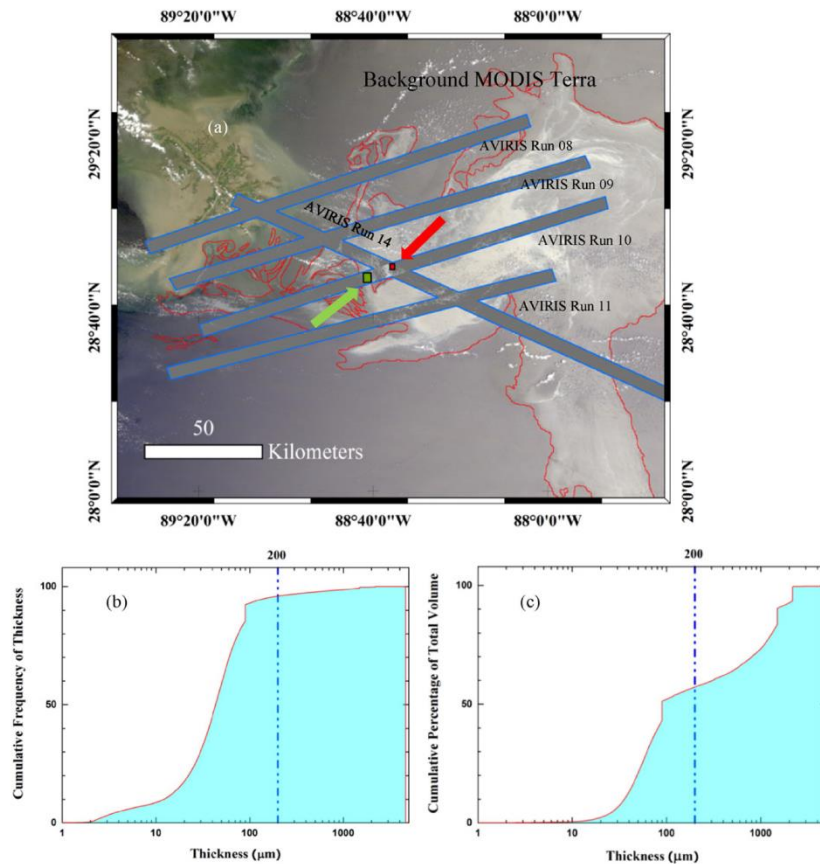


Fig. 1. (a) AVIRIS flight lines overlaid on MODIS Red–Green–Blue (RGB) image showing the DWH oil spill on 17 May 2010. The MODIS image was collected around 16:40 UTC and the 5 AVIRIS flight lines began on 19:07 UTC and were finished within 3 h. The gray scale of the AVIRIS lines represents oil volume derived from the approach of Clark et al. (2010). The red and green arrows annotate locations where examples of AVIRIS data are extracted and shown in Figs. 2 and 3. Cumulative frequency distribution of AVIRIS-derived surface oil thickness (b) and oil volume (c).

signatures in the near-infrared (NIR) and shortwave-infrared (SWIR) to quantify the oil:water ratio of emulsions and ultimately the oil volume (Clark et al., 2010). Given the availability of optical remote sensing data from a variety of satellite and airborne platforms, it is anticipated that the research community may make significant progress in estimating surface oil volume using optical remote sensing in the coming years.

Multiple factors can affect oil thickness/volume quantification from optical remote sensing imagery, such as the oil's weathering state (Svejkovsky et al., 2012), solar/view geometry, oil type (De Carolis et al., 2014) and sea state (Otremba et al., 2013). Another important factor in estimating surface oil volume is a sensor's spatial resolution. This critical parameter not only determines the detection limit of a remote sensor but also influences the ability to estimate oil thickness or volume from spectral and spatial contrast, as a large oil-containing pixel will contain oil of different thicknesses and emulsions of different water content (Leifer et al., 2012). Brown and Fingas (2001) noted that a spatial resolution of finer than 10 m was required because the width of a typical oil slick (defined as a continuous feature from the background water) was less than 10 m. Brekke and Solberg (2005) suggested that a spatial resolution of 50–150 m was sufficient for SAR to detect oil. However, these are based on the oil slick footprint instead of thickness, and there still

lacks statistical analysis documenting slick size under typical conditions. In particular, there is no published report showing slick size distributions for different oil thickness classes, although such information can be very useful in interpreting oil footprint and thickness for sensors with different resolutions, in helping to make management decisions (e.g., physical removal or other mitigations for thick oil as it is more toxic and harmful to the marine environment).

The optical sensors that have been frequently used to detect oil slicks include the Moderate Resolution Imaging Spectroradiometer (MODIS) (Hu et al., 2009; Hu et al., 2011), MEdium Resolution Imaging Spectrometer (MERIS) (De Carolis et al., 2014), and Landsat Thematic Mapper (TM) (Zhao et al., 2014), with spatial resolutions of 250 m, 300 m and 30 m, respectively. To understand spatial resolution limitations of these sensors for detecting slicks and quantifying oil thickness, it is useful to document oil slick size of various thicknesses. Furthermore, knowledge of the oil slick morphology can also help differentiate oil slicks from other look-alikes (e.g., *Trichodesmium* mats) in unknown regions. Unfortunately, similar to SAR detections, despite numerous remote sensing studies of oil spills, to our best knowledge statistics of oil slick size for different thickness classes have never been reported through optical remote sensing or other means.

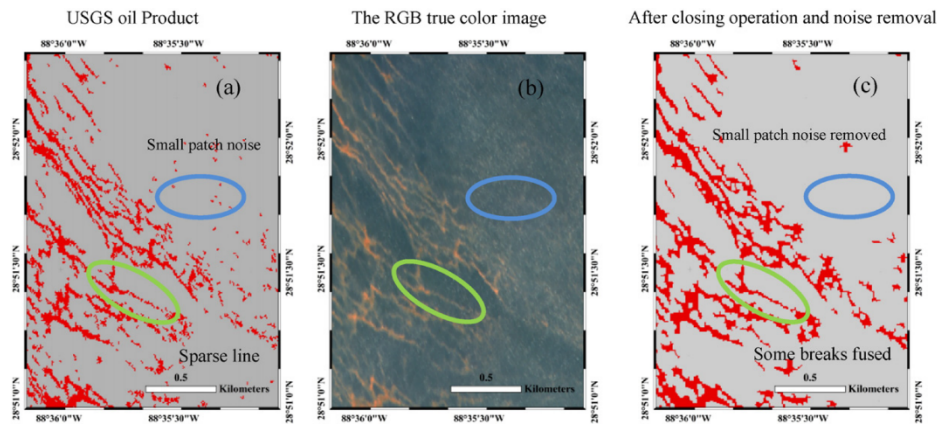


Fig. 2. Examples showing a) USGS-derived oil thickness product (red represents all oil thickness classes) from a sub-region of AVIRIS measurements on 17 May 2010, b) the corresponding RGB true color image (R: 638.2 nm; G: 550.3 nm; B: 462.8 nm), and c) the same oil thickness product after noise removal (blue circle) and feature connection (green circle). The location of the image is annotated in Fig. 1 with the red arrow.

The DWH oil spill presents an opportunity to address these questions as it occurred in a typical ocean environment (both nearshore and offshore) and, more importantly, there are fine spatial resolution (~7.6 m) hyperspectral data that were collected by the Airborne Visible/Infrared Imaging Spectrometer (AVIRIS) at approximately the same time as MODIS and Landsat data. Clark et al. (2010) had calculated surface oil volume per pixel using the AVIRIS data, enabling partitioning of oil slicks into different thickness classes and subsequent study of slick morphology and size distributions.

Thus, the objective of this study is to use the high-resolution AVIRIS data to document the morphology of oil slicks of various thicknesses, and to analyze the capacity of the current optical sensors at representative spatial resolutions of 30 m and 300 m to detect and quantify oil slicks.

2. Data and methods

Distributions of oil slicks of various thicknesses were derived from oil volume estimates by the U.S. Geological Survey (USGS; Clark et al., 2010) based on AVIRIS measurements on 17 May 2010 over the DWH oil spill (Fig. 1a). AVIRIS collected hyperspectral data from 380 to 2500 nm in 224 spectral bands at a ground resolution of about ~7.6 m per image pixel. The data were first converted to apparent reflectance ($R(\lambda)$, dimensionless) using the ACORN atmospheric correction module (AIG, 2001). The residual errors from the atmospheric correction, possibly due to the long path length of sun light (flight was in late afternoon), were minimized using continuous field-measured spectra from calibration sites located on beaches and airport tarmacs (Clark et al., 2010). $R(\lambda)$ was then used to derive oil volume of thick water-in-oil emulsions using the Tetracorder spectral shape matching algorithm described by Clark et al. (2003, 2010). Based on laboratory reflectance measurements of emulsions of variable water content, constructed by adding to or evaporating water from a natural DWH emulsion, relative differences in shortwave infrared (SWIR) C–H and water absorptions were used to determine the oil:water ratio, fractional coverage of oil in each AVIRIS pixel, and oil volume in each pixel (Clark et al., 2010). Five AVIRIS flight lines were used in this study; they all covered the spill area as outlined in a MODIS image collected on the same day (Fig. 1a).

Visual inspection of the AVIRIS-derived oil slicks revealed isolated pixelization noise even in areas away from the spill (Fig. 2). This is probably because of small cloud patches or other noise in the hyperspectral data that can affect spectral identification of features

(Swayze et al., 2003). The noise was removed with a smoothing algorithm that used a size operator where the size threshold was determined empirically: if an identified oil patch contained less than 3×4 pixels, it was regarded as noise. Furthermore, the pixel-wise processing of AVIRIS data sometimes resulted in discontinuous slicks due to random noise mimicking the spectral signature of emulsion, that otherwise appear continuous to the Human eye. These discontinuous slicks were connected through a 3×3 running kernel with the same weight (1.0) for all 9 cells, where a closing operation (to connect the broken slicks) was defined by first dilating the image features followed by subsequent erosion of the same image using the same 3×3 kernel. The closing operation was performed using the software ENVI (Environment for Visualizing Images, version 4.8). An example is shown in Fig. 2 (green circles).

The AVIRIS-derived oil volume maps from the USGS (Clark et al., 2010) were converted to different thickness classes to study the slick morphology for each class. For each pixel, the derived oil volume was divided by the area of an image pixel ($7.6 \text{ m} \times 7.6 \text{ m}$) after image georectification, resulting in oil thickness (in μm).

As explained by Clark et al. (2010), light penetration in the SWIR wavelengths is limited to a few millimeters within oil–water emulsions, representing the maximum thickness that could be probed. Because of time constraints, Tetracorder (Clark et al., 2003) was not used to map the extent and thickness of oil sheens, which are usually only a few micrometers thick. The AVIRIS-derived oil thickness was partitioned to several classes in order to characterize the morphology and size distribution of oil slicks within each class. In doing so, a modification of the original Bonn Agreement (2012) (Table 1) in defining oil thickness classes was used. This is because that the Bonn Agreement was

Table 1
Oil appearance and thickness definitions in the Bonn Agreement (2012) and thickness classification in this study.

Bonn Agreement classes			This study	
Code	Description/appearance	Layer thickness (μm)	Class	Layer thickness (μm)
1	Sheen	0.04–0.3		
2	Rainbow	0.3–5.0		
3	Metallic	5.0–50	1	≤ 50
4	Discontinuous true color	50–200	2	50–200
5	Continuous true color	>200	3	200–1000
			4	>1000

mainly focused on oil's visual appearance (Leifer et al., 2012; Lehr, 2009) from a small area (often 10s of centimeters) but the AVIRIS pixel is much larger and therefore oil thickness within a pixel may not be homogenous. The Bonn Agreement has 3 classes below 50 μm . However, thickness $< 25 \mu\text{m}$ was not detected by Tetracorder in the USGS estimates (Clark et al., 2010). From the cumulative frequency distribution of thickness and volume shown in Fig. 1b and c, respectively, AVIRIS oil pixels with thickness $> 200 \mu\text{m}$ occupy about 5% of the total slick area but their contribution to total oil volume exceeds 45%. Thus, the first two classes of oil thickness were defined as $\leq 50 \mu\text{m}$ (but excluding sheen) and 50–200 μm , similar to those in the Bonn Agreement. However, the last class in the Bonn Agreement ($> 200 \mu\text{m}$) was further divided in to two classes in our study: 200–1000 μm and $> 1000 \mu\text{m}$ (Table 1). This is because that thick oil may be more harmful to the marine environment, and thick oil can also be efficiently removed or

recovered by skimming, in situ burning, and aircraft dispersant treatment. Effective in situ burning requires at least about 1000 μm oil thickness to allow for combustion (Goodman, 2009; Fingas, 2011; Svejksky et al., 2015; Fingas and Brown, 2015). As a result, the AVIRIS-derived oil thicknesses are partitioned into the following 4 classes: ≤ 50 , 50–200, 200–1000 and $> 1000 \mu\text{m}$ (Table 1). Fig. 3 shows an example of the classified thickness and the corresponding AVIRIS Red–Green–Blue (RGB) image. The spectra of AVIRIS pixels of various oil thicknesses (Fig. 3) illustrate their differing spectral shapes and magnitudes.

In this paper, the term slick morphology refers to the slick length, width, and length/width ratio. Because oil slicks may have irregular shapes, it was difficult to determine the true length and width of a slick, and thus the length and width parameters were only used as proxies to determine the morphology. Several methods were tried,

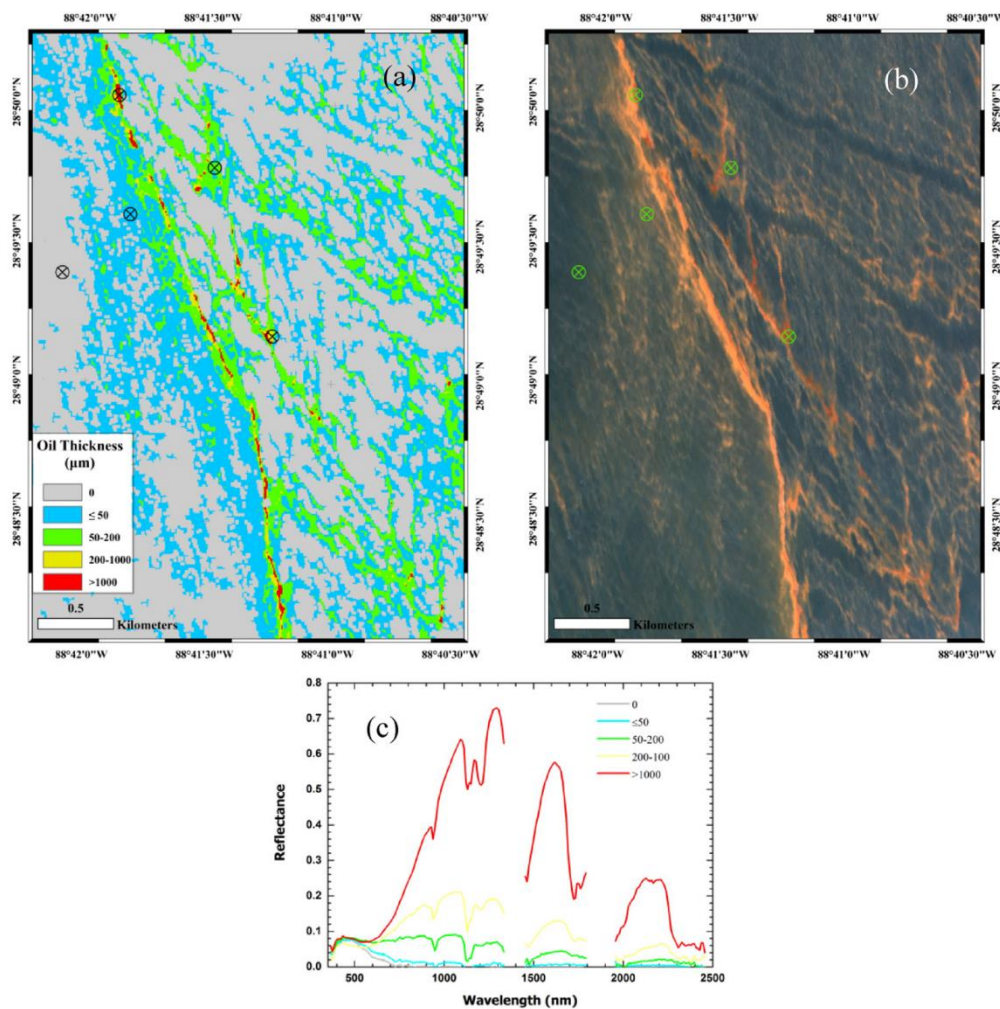


Fig. 3. Examples showing a) sub-region oil thickness products generated by USGS (Clark et al., 2010) based on AVIRIS measurements on 17 May 2010 (the oil thickness classes for this study were ≤ 50 , 50–200, 200–1000 and $> 1000 \mu\text{m}$); and b) the corresponding AVIRIS RGB true color image (R: 638.2 nm; G: 550.3 nm; B: 462.8 nm). The location of this image is indicated with the green arrow in Fig. 1. (c) Typical spectra of AVIRIS pixels of various oil thickness classes and oil-free seawater, using the same color scheme for thickness classes as in (a).

including a thinning method that shrank a slick to just one pixel wide, in the hope that the slick length could be estimated as the number of pixels in the thinning result and the width could be derived as the area of the slick (number of pixels) divided by the length. However, after thinning, many of the slick metrics were subsequently incorrect, leading to significantly overestimated length. Ultimately, in this study we digitized the oil slicks to polygons, and approximated the dimensions of each slick polygon by assuming that the slick area was a rectangle, with a length corresponding to the diameter of a circle bounding the slick (Fig. 4a), and a width represented by the ratio of slick area to slick length (Fig. 4b).

The procedure was applied to each of the four oil thickness classes separately, and then applied to oil slicks when all classes were combined. Statistics of length, width, and length/width ratio were generated and tabulated.

As noted previously, AVIRIS data used in this study had a spatial resolution of 7.6 m. Most remote sensing sensors have coarser spatial resolution (e.g., 30 m for Landsat, 250 m for MODIS and 300 m for MERIS). To understand the effect of variable resolution on a sensor's capacity to capture oil slicks within a pixel, the AVIRIS data products were binned into 4×4 pixel (~30 m) resolution, 8×8 pixel (~60 m), and 40×40 pixel (~300 m) resolution, with each resolution representing the current Landsat sensors, future HypSIRI sensor (Lee et al., 2015), and current MERIS or MODIS sensor. For each spatial bin, the percentage of oil coverage of the various oil thickness classes within a bin was calculated. For example, if one AVIRIS pixel of the 4×4 pixel bin contains oil in the 50–200 μm class, the percentage of oil coverage (for that class) is 1/16 or 6.25%. Statistics of all bins were generated and tabulated, with their frequency distributions plotted.

3. Results

3.1. Oil slick morphology

Table 2 lists the statistics of oil slick morphology (length, width, length/width ratio) for each oil thickness class as well as for all classes combined. The histogram distributions of these parameters are shown in Figs. 5, 6, and 7. Typically, one large slick comprises numerous smaller slicks of different thickness classes. Thus, the number of slicks for all classes combined is much lower than the sum of the number of slicks in each individual thickness class (Table 2).

The median length for each oil thickness class ranged between 22 and 38 m, while the median width ranged between 6.8 and 10.5 m. When all oil classes were combined to outline larger slicks, the median length and width were 92 and 21 m, respectively. The most frequent length and width for each individual thickness is the smallest bin, but almost none of the combined slicks are that small, reflecting the heterogeneous distribution of thicknesses within any one slick. In addition, for each thickness class and all classes combined, there is large variability in

Table 2

Statistics of oil slick morphology derived from five AVIRIS flight lines over the DWH oil spill. The oil slicks are partitioned to individual thickness classes and considered all together without partitioning to different classes (last row). Because each individual slick typically comprises many smaller slicks of different thickness classes, the total number of combined slicks is lower than that of the individual classes, and the length and width parameters are much higher.

Thickness class (μm)	# of slicks	Morphology	Mean	Standard deviation	Min	Median	Max
≤50	29,274	Length (m)	58.1	85.1	10.8	38.0	5885.5
		Width (m)	13.3	11.5	5.4	10.5	796.4
		Length/width ratio	3.8	2.0	1.9	3.3	55.5
50–200	16,828	Length (m)	64.4	123.7	10.8	34.0	5815.0
		Width (m)	12.9	11.5	5.4	9.3	458.0
		Length/width ratio	4.0	2.7	1.7	3.3	55.1
200–1000	4867	Length (m)	36.4	46.2	10.8	21.5	730.4
		Width (m)	9.0	5.6	5.4	6.8	64.8
		Length/width ratio	3.4	2.1	2.0	2.5	27.3
>1000	1131	Length (m)	43.8	73.4	10.8	21.5	976.4
		Width (m)	10.4	10.0	5.4	6.8	116.4
		Length/width ratio	3.5	2.1	2.0	2.6	24.9
All	7361	Length (m)	160.8	298.7	38.0	91.5	7363.0
		Width (m)	26.4	33.4	8.1	20.6	1894.4
		Length/width ratio	5.6	4.0	1.9	4.6	114.5
		ratio					

their length and width parameters, as indicated by the high standard deviations relative to the means. Such variability is clearly shown in the histogram distributions in Figs. 5 and 6 for length and width, respectively. This suggests that oil slick morphologies do not follow normal distributions but instead are asymmetric, with more slicks at smaller scales. Slick lengths generally ranged between 1 AVIRIS pixel (~7.6 m) to ~24 pixels (~180 m), while slick widths ranged between 1 AVIRIS pixel to ~4 pixels (~30 m). The number of slicks appears to decrease exponentially with increasing length and width.

Although the procedure to estimate length and width is not perfect, there is a clear disparity in length and width statistics. The median length/width ratio ranged between 2.5 and 3.3, indicating that most slicks had elongated shape. More than 90% of the slicks have length/width ratios between 1.6 and 10, while only a small percentage have the ratios of >15 (Fig. 7). The histogram distributions of length/width ratios were asymmetric for all oil classes, revealing that few slicks in this data set were significantly elongated. This suggests that oil slicks tend to break after being elongated to a certain extent. The median length/width ratio of the combined oil class is about 5, much higher than the median ratio of 3 for the individual thickness classes. This suggests that the smaller slicks within each thickness class are less elongated than the overall outline of the slick that combines all

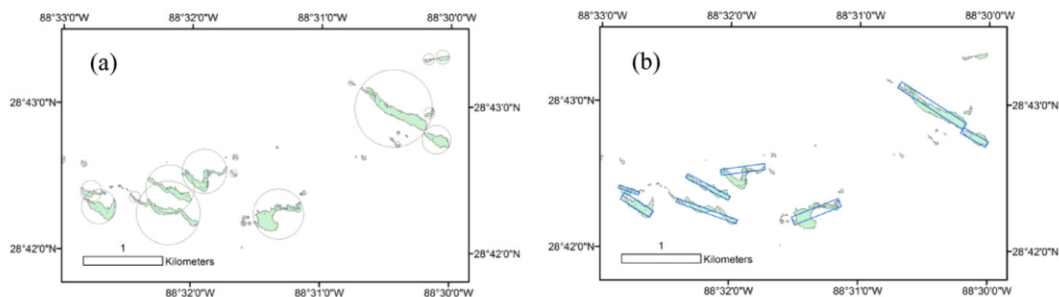


Fig. 4. Illustration of the procedure to determine length and width of each oil slick. a) Each slick is encompassed by a circle; b) The diameter of the circle is used to represent the length, while the ratio of slick area to length is used to approximate the width.

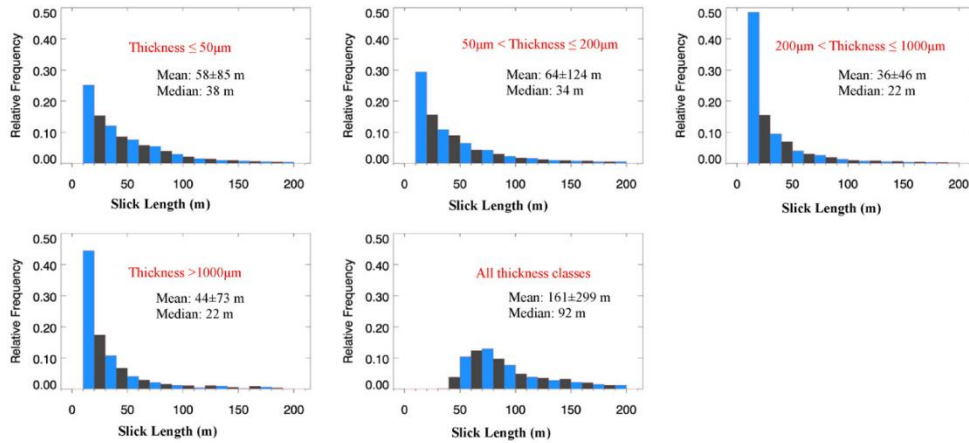


Fig. 5. Statistics of oil slick length for different thickness classes. Alternating bin colors are for better visualization. Note: mean value \pm standard deviation and median value are annotated in plot for each thickness class. Same applies for the following figures.

thickness classes. Likewise, thin oil ($\leq 200 \mu\text{m}$) tends to be more elongated than thicker oil ($> 200 \mu\text{m}$), with their median length/width ratios being about 3.3 and 2.5, respectively.

3.2. Requirement on spatial resolution

The length and width statistics suggest that remote sensors with 30- or 300-m spatial resolution can rarely capture oil slicks with 100% pixel coverage. In other words, most of the 30- and 300-m pixels will have only partial coverage of oil. Indeed, Fig. 6 shows that even for the combined oil class, $> 75\%$ of the oil slicks have widths < 30 m. To simulate the effect of coarser spatial resolution, AVIRIS pixels were binned into 4×4 (30 m), 8×8 (60 m) and 40×40 (300 m) pixels maps, with percentage oil coverage estimated from each spatial bin. Table 3 shows the coverage statistics while the distribution histograms are shown in Figs. 8 and 9 for 30- and 300-m, respectively.

For the 30-m bin, the median percent oil coverage was 31% or less for each individual thickness class (Table 3; Fig. 8). In fact, for the 200–1000 μm class, more than half of the pixel-bins have oil coverage $< 19\%$ within the pixel-bins. Even when all classes are combined, more than half of the pixel-bins have oil coverage $< 50\%$ within the pixel-bins. In each of the thickness classes, less than 10% of the pixel-bins were fully covered (i.e., 100%) with oil (Fig. 8). Complete oil coverage increased to 20% of pixel-bins when all oil thickness classes were combined. Thus, only a small portion of 30-m resolution pixel-bins may contain full (100%) oil coverage.

The partial oil coverage (areal fraction) decreases significantly for the 300-m pixel-bins. The median percent oil coverage for pixel-bins in the thin oil classes ($\leq 200 \mu\text{m}$) was $< 3.5\%$, while for the thicker classes ($> 200 \mu\text{m}$) the median percent oil coverage decreased to 0.6% (Table 3; Fig. 9). Even when all classes are combined, the likelihood of finding 100% oil coverage within a 300-m pixel-bin was negligible ($< 0.1\%$). This patchiness of oil slicks is clearly visible in Figs. 3 and 4, where

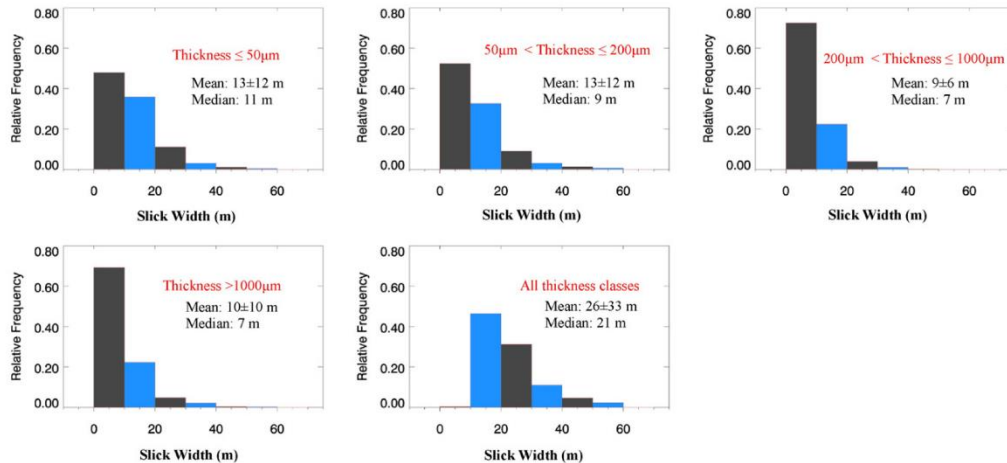


Fig. 6. Statistics of oil slick width for different thickness classes. Alternating bin colors are for better visualization. Note that although the step in the x-axis appears wider, it is the same (10 m) as in Fig. 5.

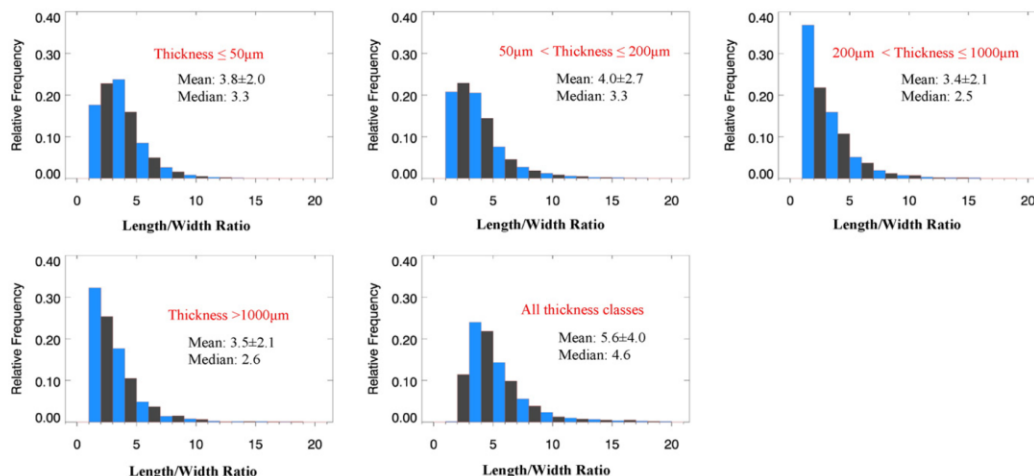


Fig. 7. Statistics for oil slick length/width ratio for different thickness classes. Alternating bin colors are for better visualization.

there are no 300 m by 300 m areas with uniform oil coverage. For the intermediate bin (60-m), the statistical results are between the 30-m and 300-m bins (Table 3). It is interesting to note that the median coverage for the combined class is roughly inversely proportional to the bin size, for example by decreasing from 50.0%, 28.1%, to 6.6% for the 30-m, 60-m, and 300-m bins.

4. Discussion and conclusions

As with any other analyses of remote detection of oil slicks, the validity of these results relies on the accuracy of AVIRIS measurements and accuracy of the methodology for morphology assessment. As explained in Clark et al. (2010), the Tetracorder command file did not spectrally distinguish thin sheens but instead focused on the volumetrically significant thick oil slicks (>25 µm) from fractional AVIRIS pixel

coverage. For example, if 10% of an AVIRIS pixel was covered by oil (this fractional number was determined by examining the spectral magnitude contrast in the SWIR band between the pixel of interest and the nearby oil-free pixels) and oil thickness of this fractional pixel was 25 µm, the equivalent thickness for this AVIRIS pixel was then $10\% \times 25 = 2.5 \mu\text{m}$. Thus, all analyses here are based on oil slicks >25 µm in thickness. If oil sheens were included, the results for the ≤50 µm class and the combined oil class would both need to be changed, and it would be more likely that 30-m and 300-m pixel-bins would have full oil coverage for the ≤50 µm class and the combined oil class. Furthermore, there may be also some uncertainties in the estimates of the top thickness class and its associated calculations in the 30-m and 300-m bins. This is because that light in the NIR can only penetrate the upper few millimeters of oil; thus the current estimate represents a conservative lower bound for thick oil. Indeed, the difficulty in measuring oil thickness in the field or estimate oil thickness remotely has been well recognized by the community (Fingas, 2012), as “we currently do not have tools, not even simple rules by which to gauge thickness regimes of slicks for calibration of new instruments.” As such, none of previous works on remote estimation of oil thickness had concurrent quantitative validation in the field, and all those laboratory-based remote sensing methods can only provide relative thicknesses when applied in the field (Clark et al., 2010; Svejkský et al., 2012; Lu et al., 2013). Nevertheless, the AVIRIS-based estimates represent our best knowledge to date on the DWH oil thickness distributions.

AVIRIS spatial resolution could pose a limitation on the statistics. For the data used in this study, no length or width parameter could be smaller than 7.6 m (the minimum width of 5.9 m in the table was due to an extreme case when the pixels, treated as small squares, were aligned in their diagonal direction so the overall width of the slick could be smaller than the width of the individual pixels). In reality, if a finer spatial-resolution sensor (e.g., with $1 \times 1 \text{ m}$ pixels) were used, the statistics of slick length and slick width might change. However, given the fact that most slicks of any thickness are at least several pixels long, finer resolution data would be more likely to decrease the slick widths with little change in slick lengths, thus increasing the length/width ratios. The conclusion that most slicks have elongated shapes will therefore be reinforced.

Another limiting factor is the methodology used to determine the length and width of each slick. The assumption that a slick can be

Table 3

Statistics of percentage oil coverage within 30-, 60-, and 300-m bins for each thickness class. For a thickness class, if a pixel-bin (30, 60, or 300 m) contains ≥ 1 AVIRIS pixel, it is counted for the number of pixel-bins listed in column three below. The frequencies of the partial coverage for the 30-m and 300-m pixel-bins are shown in Figs. 8 and 9, respectively. Note that Max (%) represents the maximum coverage for all pixel-bins corresponding to the thickness class, and it does not indicate how many pixel-bins contain the maximum coverage.

Pixel-bin size (m)	Thickness (µm)	# of pixel-bins	Mean oil coverage (%) of pixel-bins	Standard deviation (%)	Min (%)	Median (%)	Max (%)
30 (4 × 4)	≤50	142,155	36.4	26.6	6.3	31.3	100.0
	50–200	92,662	38.9	29.1	6.3	31.3	100.0
	200–1000	11,561	24.4	20.5	6.3	18.8	100.0
	>1000	3669	35.6	31.3	6.3	25.0	100.0
	All	172,077	53.4	33.2	6.3	50.0	100.0
60 (8 × 8)	≤50	59,064	22.0	19.8	1.6	15.6	100.0
	50–200	41,508	21.8	21.4	1.6	14.1	100.0
	200–1000	6395	11.1	12.2	1.6	6.3	100.0
	>1000	1999	16.4	22.0	1.6	7.8	100.0
	All	64,921	35.6	29.1	1.6	28.1	100.0
300 (40 × 40)	≤50	59,064	22.0	19.8	1.6	15.6	100.0
	50–200	6796	7.9	10.9	0.1	3.5	100.0
	200–1000	5937	6.4	9.1	0.1	2.8	100.0
	>1000	1675	1.7	2.7	0.1	0.6	20.9
	All	605	2.2	4.7	0.1	0.6	38.1
All	7050	13.6	17.3	0.1	6.6	100.0	

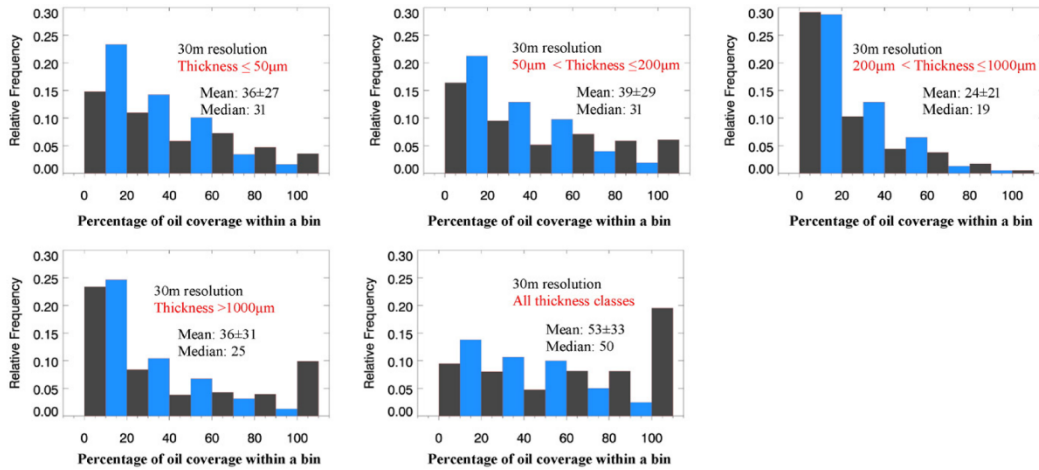


Fig. 8. Statistics of percentage of oil coverage within a 30-m resolution pixel-bin (4×4 AVIRIS pixels) for each thickness class (≤ 50 , 50–200, 200–1000 and $> 1000 \mu\text{m}$) and all-combined thickness.

approximated using a rectangle is certainly a crude assumption, as oil slicks generally have irregular shapes. However, visual inspection of the slicks indicate that although there are many slicks with irregular shapes, most of them tend to be elongated in one direction, possibly due to oil convergence along wind-induced Langmuir cells (Lehr and Simecek-Beatty, 2000). On the other hand, if a slick were curved, the method used here would lead to an underestimate of length and overestimate of width. Thus, the length/width ratios derived here represent the lower bound, and in reality they may be higher, further supporting the conclusion that slicks are elongated.

Given the availability of various sensors to detect and monitor oil spills, a critical question is what spatial resolution may be optimal. Although the finer the resolution the smaller an oil slick that can be detected, fine-spatial-resolution sensors typically have less spatial coverage (i.e., narrower swaths). For example, the swath width of Landsat

(30 m resolution) is about 180 km, compared with 2330 km for MODIS (250 m resolution). Ideally, images with 1-m (or finer) resolution and swaths > 500 km wide (to cover the entire DWH oil footprint) would be required to fully understand the impact of spatial resolution on the statistics of oil slick morphology of large oil spills, especially when mixed oil–seawater pixels frequently occur. Such a requirement on spatial resolution and spatial coverage is not currently available. Even if it were available, a single $500 \text{ km} \times 500 \text{ km}$ image at 1 m resolution would have 250 billion pixels with values for multiple channels per pixel, inhibiting the practicality of collecting, transmitting, storing, and analyzing the data. Thus, AVIRIS data at ~ 7.6 m resolution were used in this study as a compromise to address this question.

The study is focused on spatial resolutions while spectral and radiometric (i.e., signal-to-noise ratio or SNR) resolutions are not considered. In reality, they both affect the detection of oil slicks of different classes.

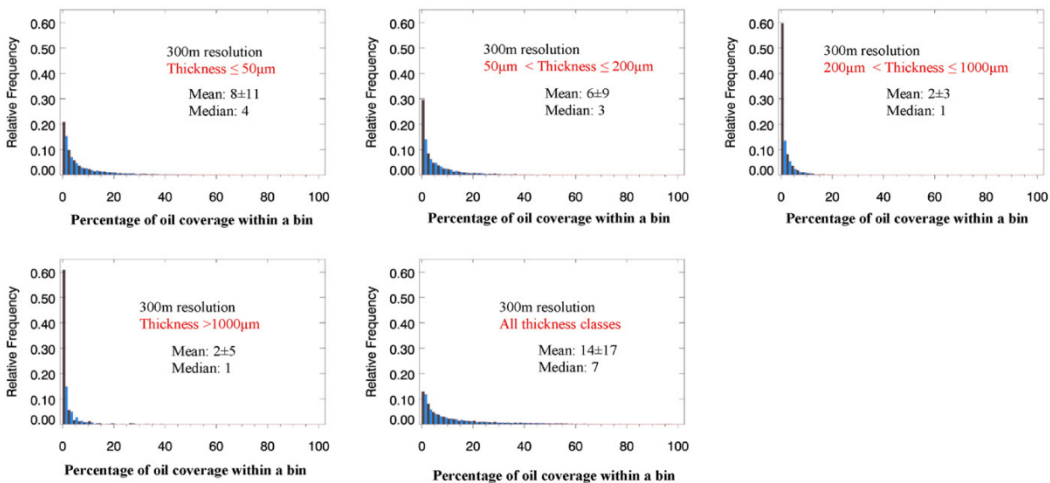


Fig. 9. Statistics of percentage of oil coverage within a 300-m resolution pixel-bin (40×40 AVIRIS pixels) for each thickness class (≤ 50 , 50–200, 200–1000 and $> 1000 \mu\text{m}$) and all-combined thickness. For the last panel, even if it is difficult to visualize, there are a total of $> 5\%$ cases with coverage $> 50\%$.

Sensors with fine spatial resolutions tend to have coarse spectral resolutions (e.g., 60–80 nm for Landsat). Such spectral resolutions would make it impossible to apply the hyperspectral Tetracorder method to estimate thickness, yet some band ratio combinations may still be applicable for the same purpose (Svejkovsky et al., 2012). SNRs of AVIRIS between 0.6 μm and 1.7 μm are typically in a range of 60:1–100:1 (Gao, 1993), and most coarse resolution sensors (e.g., Landsat 7 and Landsat 8) have their SNRs comparable to or higher than AVIRIS (Hu et al., 2012; Pahlevan et al., 2014), leading to at least comparable performance to AVIRIS in terms of SNRs. For a given sensor with finite spectral resolution and SNR, the minimal fraction of oil within a pixel that can be detected may be assessed in a future study using AVIRIS reflectance spectra (rather than the morphological parameters here) and the simulation methods detailed in Hu et al. (2015).

The results from the sensitivity analysis to determine the partial oil coverage statistics using two commonly available spatial resolutions (30 m for Landsat and 300 m for MERIS) are interesting. For the DWH spill on 17 May 2010, only 17% of surface oil can be captured by 30-m pixel-bins with full oil coverage within a pixel-bin. When the oil slicks are partitioned to different thickness classes, the percentage of full oil coverage within a bin decreases sharply to only a few percent. Most of the 30-m pixel-bins have areal oil coverage of <50%. For 300-m bins, the percentage of full oil coverage within a pixel-bin is negligible for each thickness class and for the combined oil classes, and the mean percentage of full oil coverage is only a few percent. However, these results should not be interpreted as Landsat or MODIS (MERIS) are not capable of detecting oil with their relatively coarse-resolution pixels, but rather they are capable of finding oil with fractional pixel coverage. This is particularly true when considering that AVIRIS oil maps excluded thin oil due to technical difficulty. If thin oil were derived from AVIRIS and then used in this analysis, the results for the $\leq 50 \mu\text{m}$ class and the combined oil class would be changed. Indeed, under sun glint conditions, optical sensors such as MODIS can capture even thin oil sheens (Adamo et al., 2009; Hu et al., 2009; Sun and Hu, submitted for publication).

The analysis was based on AVIRIS data collected in the NE Gulf of Mexico on 17 May 2010, where both surface currents and winds were small. Surface currents derived from satellite altimetry data and a GOM HYCOM model showed minimal water movements on this day ($\sim < 10 \text{ cm s}^{-1}$, Liu et al., 2013), while wind speed was generally $< 3 \text{ m s}^{-1}$ according to NOAA NCEP reanalysis. Other conditions such as sun glint strength (a function of wind and solar/viewing geometry) may affect the interpretation of oil thickness. Although AVIRIS flight time and flight direction were optimized to minimize sun glint (Clark et al., 2010), sun glint “contamination” is still inevitable; but these “contaminated” pixels were masked and not included in the analysis (Clark et al., 2010). The results are also restricted to the local oceanographic and weather conditions on 17 May 2010. Under different conditions these statistics might change, which needs further investigation once oil maps from AVIRIS observations on other days are available.

Nevertheless, several important conclusions can be drawn from this analysis. First, most oil slicks are elongated, with a medium length/width ratio ranging from 2.5 to 4.6 depending on the thickness class. This information may be used to help differentiate oil from other look-alike features. Second, spectral and spatial analyses or modeling using coarse-spatial-resolution sensors such as MODIS or MERIS need to consider mixed pixels for thick oil, as most pixels will have thick oil coverage of only a few percent of a given pixel footprint even though full-pixel coverage may be possible when thinner oil is considered. Third, among all existing satellite sensors, Landsat may be an optimal compromise between spatial resolution and swath width in order to capture actual thick-oil coverage within a pixel and full oil spill footprint. Although the 180-km swath of Landsat is not able to capture the full extent of the DWH spill ($\sim 300\text{--}400 \text{ km}$), most spills should be much smaller than DWH in their spatial coverage. However, Landsat sensors (including the most recent OLI on Landsat 8) have limited

spectral channels compared to the hyperspectral AVIRIS sensor, thus reducing their capacity to differentiate various oil thicknesses spectrally.

Although the AVIRIS flight lines only captured about 30% of the core oil spill area (Fig. 1a), these flight lines did capture both the edge and the center of oil spill, with both thick and thin oil regions included. Thick oil occupied a small areal fraction but contained a considerably larger amount of oil volume (e.g., oil with thickness $> 200 \mu\text{m}$ occupied only 5% of the total oiled area but contained $> 45\%$ of the total oil volume; Fig. 1b & c), which agrees generally with those determined from experiments (Hollinger and Mennella, 1973) although the details are slightly different (e.g., Hollinger and Mennella (1973) found 90% of the oil was in 10% of the slick area with oil thickness $> 1000 \mu\text{m}$). In this study, oil thickness $> 200 \mu\text{m}$ was deemed as thick oil since as it falls in the range that can be effectively recovered or removed, although the thickness threshold may change with environmental conditions (e.g., age of the slick, wind, oil type, sea state) (Fingas, 2012). Thus, these AVIRIS-based findings on slick morphology and size distributions may be regarded as valid for typical oceanographic and weather conditions for the northern Gulf of Mexico in the spring. For the same reason, whether these observations hold true for other major spills still needs to be tested in order to further refine these generalized conclusions.

Acknowledgments

This work was supported by the NASA Ocean Biology and Biogeochemistry Program (Grant NNX13AD08G), the BP/Gulf of Mexico Research Initiative through C-IMAGE [SA 15-16], and support from the Bureau of Ocean Energy Management (BOEM, contract M12PC00003). We thank the European Space Agency and NASA for providing MERIS and MODIS data, and thank the NASA JPL and U.S. Geological Survey for providing AVIRIS and Landsat data. We also thank the two anonymous reviewers for their useful comments. Any use of trade, firm, or product names is for descriptive purposes only and does not imply endorsement by the U.S. Government.

References

- Adamo, M., De Carolis, G., De Pasquale, V., Pasquariello, G., 2009. Detection and tracking of oil slicks on sun-glittered visible and near infrared satellite imagery. *Int. J. Remote Sens.* 30, 6403–6427.
- Analytical Imaging and Geophysics LLC (AIG), 2001. ACORN User's Guide, Stand Alone Version. Analytical Imaging and Geophysics LLC (64 pp.).
- Bonn Agreement, 2012. Bonn Agreement Aerial Operations Handbook, Version 19, May 2009. Publication of the Bonn Agreement, p. 93.
- Brekke, C., Solberg, A.H.S., 2005. Oil spill detection by satellite remote sensing. *Remote Sens. Environ.* 95, 1–13.
- Brown, C.E., Fingas, M.F., 2001. New space-borne sensors for oil spill response. *Int. Oil Spill Conf. Proc.* 2001 (2), 911–916.
- Bulgarelli, B., Djavidnia, S., 2012. On MODIS retrieval of oil spill spectral properties in the marine environment. *IEEE Geosci. Remote Sens. Lett.* 9 (3), 398–402.
- Clark, R.N., Swayze, G.A., Livo, K.E., Kokaly, R.F., Sutley, S.J., Dalton, J.B., McDougal, R.R., Gent, C.A., 2003. Imaging spectroscopy: earth and planetary remote sensing with the USGS Tetracorder and Expert Systems. *J. Geophys. Res.* 108 (E12), 5131. <http://dx.doi.org/10.1029/2002JE001847>.
- Clark, R.N., Swayze, G.A., Leifer, I., Livo, K.E., Kokaly, R., Hoefen, T., Lundeen, S., Eastwood, M., Green, R.O., Pearson, N., 2010. A method for quantitative mapping of thick oil spills using imaging spectroscopy. US Geological Survey Open-File Report, 1167, pp. 1–51.
- Crone, T.J., Tolstoy, M., 2010. Magnitude of the 2010 gulf of Mexico oil leak. *Science* 330, 634.
- De Carolis, G., Adamo, M., Pasquariello, G., 2014. On the estimation of thickness of marine oil slicks from sun-glittered, near-infrared MERIS and MODIS imagery: the Lebanon oil spill case study. *IEEE Trans. Geosci. Remote Sens.* 52, 559–573.
- De Gouw, J.A., Middlebrook, A.M., Warneke, C., Ahmadov, R., Atlas, E.L., Bahreini, R., Blake, D.R., Brock, C.A., Brioude, J., Fahey, D.W., Fehsenfeld, F.C., Holloway, J.S., Le Henaff, M., Lueb, R.A., McKeen, S.A., Meagher, J.F., Murphy, D.M., Paris, C., Parrish, D.D., Perring, A.E., Pollack, I.B., Ravishankara, A.R., Robinson, A.L., Ryerson, T.B., Schwarz, J.P., Spackman, J.R., Srinivasan, A., Watts, L.A., 2011. Organic aerosol formation downwind from the Deepwater Horizon oil spill. *Science* 331, 1295–1299.
- Fingas, M., 2011. An overview of in-situ burning. *Oil Spill Science and Technology Gulf Professional Publishing, Boston*, pp. 737–903.
- Fingas, M., 2012. How to measure slick thickness (or not). *Proceedings of the 35th Arctic and Marine Oil Spill Program Technical Seminar* 35, No. 1, pp. 617–652.
- Fingas, M., Brown, C., 1997. Review of oil spill remote sensing. *Spill Sci. Technol. Bull.* 4, 199–208.

- Fingas, M., Brown, C., 2015. Response to Svejtkovsky et al. *Mar. Pollut. Bull.* 93, 298–300.
- Gao, B.-C., 1993. An operational method for estimating signal to noise ratios from data acquired with imaging spectrometers. *Remote Sens. Environ.* 43, 23–33.
- García-Pineda, O., MacDonald, I., Hu, C., Svejtkovsky, J., Hess, M., Dukhovskoy, D., Moorey, S., 2013. Detection of floating oil anomalies from the Deepwater Horizon oil spill with synthetic aperture radar. *Oceanography* 26 (2), 124–137. <http://dx.doi.org/10.5670/oceanog.2013.38>.
- Goodman, R.H., 2009. Why Does it Work or Not Work? In: Proceedings of the Thirty-Second Arctic and Marine Oil Spill Program Technical Seminar. Environment Canada, Ottawa, Ontario, pp. 515–520.
- Hollinger, J.P., Mennella, R.A., 1973. Oil spills: measurements of their distributions and volumes by multifrequency microwave radiometry. *Science* 181, 54–56.
- Hu, C., Muller-Karger, F.E., Taylor, C., Myhre, D., Murch, B., Odriozola, A.L., Godoy, G., 2003. MODIS detects oil spills in Lake Maracaibo, Venezuela. *EOS Trans. Am. Geophys. Union* 84, 313–319.
- Hu, C., Li, X., Pichel, W.G., Muller-Karger, F.E., 2009. Detection of natural oil slicks in the NW gulf of Mexico using MODIS imagery. *Geophys. Res. Lett.* 36, L01604.
- Hu, C., Weisberg, R.H., Liu, Y., Zheng, L., Daly, K., English, D., Zhao, J., Vargo, G., 2011. Did the northeastern gulf of Mexico become greener after the Deepwater Horizon oil spill? *Geophys. Res. Lett.* 38, L09601. <http://dx.doi.org/10.1029/2011GL047184>.
- Hu, C., Feng, L., Lee, Z., Davis, C.O., Mannino, A., McClain, C.R., Franz, B.A., 2012. Dynamic range and sensitivity requirements of satellite ocean color sensors: learning from the past. *Appl. Opt.* 51, 6045–6062.
- Hu, C., Feng, L., Hardy, R.F., Hochberg, E.J., 2015. Spectral and spatial requirements of remote measurements of pelagic *Sargassum* macroalgae. *Remote Sens. Environ.* 167, 229–246. <http://dx.doi.org/10.1016/j.rse.2015.05.022>.
- Lee, C.M., Cable, M.L., Hook, S.J., Green, R.O., Ustin, S.L., Mandl, D.J., Middleton, E.M., 2015. An introduction to the NASA Hyperspectral InfraRed Imager (HyspIRI) mission and preparatory activities. *Remote Sens. Environ.* 167, 6–19.
- Lehr, W., 2009. Visual observations and the Bonn agreement. Proceedings of the 33 AMOP Technical Seminar on Environmental Contamination and Response 2. Environment Canada, Canada, p. 1332.
- Lehr, W.J., Simecek-Beatty, D., 2000. The relation of Langmuir circulation processes to the standard oil spill spreading, dispersion, and transport algorithms. *Spill Sci. Technol. Bull.* 6, 247–253.
- Leifer, I., Lehr, W.J., Simecek-Beatty, D., Bradley, E., Clark, R., Dennison, P., Hu, Y., Matheson, S., Jones, C.E., Holt, B., Reif, M., Roberts, D.A., Svejtkovsky, J., Swayze, G., Wozencraft, J., 2012. State of the art satellite and airborne marine oil spill remote sensing: application to the BP Deepwater Horizon oil spill. *Remote Sens. Environ.* 124, 185–209.
- Liu, Y., Weisberg, R.H., Hu, C., Zheng, L., 2013. Trajectory forecast as a rapid response to the Deepwater Horizon oil spill. Monitoring and Modeling the Deepwater Horizon Oil Spill: A Record-Breaking Enterprise. American Geophysical Union, pp. 153–165. <http://dx.doi.org/10.1029/2011GM001121>.
- Lu, Y., Tian, Q., Wang, X., Zheng, G., Li, X., 2013. Determining oil slick thickness using hyperspectral remote sensing in the Bohai Sea of China. *Int. J. Digital Earth* 6, 76–93.
- Macdonald, I.R., Guinasso Jr., N.L., Ackleson, S.G., Amos, J.F., Duckworth, R., Sassen, R., Brooks, J.M., 1993. Natural oil slicks in the Gulf of Mexico visible from space. *J. Geophys. Res.* 98 (C9), 16351–16364. <http://dx.doi.org/10.1029/93JC01289>.
- MacDonald, I.R., García-Pineda, O., Beet, A., Daneshgar Asl, S., Feng, L., Graettinger, G., French-McCay, D., Holmes, J., Hu, C., Huffer, F., Leifer, I., Muller-Karger, F., Solow, A., Silva, M., Swayze, G., 2015. Natural and unnatural oil slicks in the Gulf of Mexico. *J. Geophys. Res. Oceans* <http://dx.doi.org/10.1002/2015JC011062>.
- McNutt, M., Camilli, R., Guthrie, G., Hsieh, P., Labson, V., Lehr, B., Maclay, D., Ratzel, A., Sogge, M., 2011. Assessment of flow rate estimates for the Deepwater horizon/Macondo well oil spill. Flow Rate Technical Group report to the National Incident Command, Interagency Solutions Group, March 10, 2011.
- National Research Council, 2003. Biological Effects of oil Releases. Oil in the Sea III: Inputs, Fates, and Effects, Chap. 5. National Academies Press, Washington, D. C., pp. 119–157.
- Otremba, Z., Zielinski, O., Hu, C., 2013. Optical contrast of oil dispersed in seawater under windy conditions. *J. Eur. Opt. Soc. Rapid Publ.* 8. <http://dx.doi.org/10.2971/jeos.2013.13051>.
- Pahlevan, N., Lee, Z., Wei, J., Schaaf, C.B., Schott, J.R., Berk, A., 2014. On-orbit radiometric characterization of OLI (Landsat-8) for applications in aquatic remote sensing. *Remote Sens. Environ.* 154, 272–284.
- Sun, S., Hu, C., 2015. Sun glint requirement for the remote detection of surface oil film. *Geophys. Res. Lett.* 42. <http://dx.doi.org/10.1002/2015GL066884>.
- Svejtkovsky, J., Lehr, W., Muskat, J., Graettinger, G., Mullin, J., 2012. Operational utilization of aerial multispectral remote sensing during oil spill response. *Photogramm. Eng. Remote Sens.* 78, 1089–1102.
- Svejtkovsky, J., Lewis, A., Muskat, J., Andersen, J.H.S., Benz, S., García-Pineda, O., 2015. Rebuttal to published article “Review of oil spill remote sensing” by M. Fingas and C. Brown. *Mar. Pollut. Bull.* 93, 294–297.
- Swayze, G.A., Clark, R.N., Goetz, A.F.H., Chrien, T.G., Gorelick, N.S., 2003. Effects of spectrometer band pass, sampling, and signal-to-noise ratio on spectral identification using the Tetracorder algorithm. *J. Geophys. Res. Planets* 108, 5105. <http://dx.doi.org/10.1029/2002JE001975>.
- United States of America v. BP Exploration & Production, Inc., et al., 2015. Findings of fact and conclusions of law: phase two trial. In re: oil spill by the oil rig “Deepwater Horizon”. The Gulf of Mexico, on April 20, 2010, No. MDL 2179, 2015 WL 225421 (LA. E.D. Jan. 15, 2015). (Doc. 14021). U.S. District Court for the Eastern District of Louisiana (Retrieved from <http://www.laed.uscourts.gov/OilSpill/Orders/1152015FindingsPhaseTwo.pdf>).
- Zhao, J., Temimi, M., Ghedira, H., Hu, C., 2014. Exploring the potential of optical remote sensing for oil spill detection in shallow coastal waters—a case study in the Arabian Gulf. *Opt. Express* 22, 13755–13772.

APPENDIX D:

**SURFACE OIL FOOTPRINT AND TRAJECTORY OF THE IXTOC-I OIL SPILL DETERMINED FROM
LANDSAT/MSS AND CZCS OBSERVATIONS**

Sun, S., Hu, C., and Tunnell, J.W. (2015). Surface oil footprint and trajectory of the Ixtoc-I oil spill determined from Landsat/MSS and CZCS observations. *Marine Pollution Bulletin*, 101, 632-641, doi:10.1016/j.marpolbul.2015.10.036



Contents lists available at ScienceDirect

Marine Pollution Bulletin

journal homepage: www.elsevier.com/locate/marpolbul

Surface oil footprint and trajectory of the Ixtoc-I oil spill determined from Landsat/MSS and CZCS observations



Shaojie Sun^a, Chuanmin Hu^{a,*}, John W. Tunnell Jr.^b

^a College of Marine Science, University of South Florida, 140 Seventh Avenue South, St. Petersburg, FL 33701, United States

^b Harte Research Institute for Gulf of Mexico Studies, Texas A&M University-Corpus Christi, 6300 Ocean Drive, Unit 5869, Corpus Christi, TX 78412, United States

ARTICLE INFO

Article history:

Received 31 August 2015

Received in revised form 15 October 2015

Accepted 16 October 2015

Available online 24 October 2015

Keyword:

Ixtoc-I oil spill

Oil trajectory

Remote sensing

Landsat/MSS

CZCS

ABSTRACT

The Ixtoc-I oil spill occurred in 1979 in shallow waters (50 m) of the Bay of Campeche, Mexico. Although it is known that a large portion of the released oil from this second largest accidental marine oil spill in history reached the surface, to date there has been no attempt to document the surface footprint and trajectory of the released oil. Our study attempts to fill this knowledge gap using remote sensing data collected by Landsat/MSS and CZCS. Both showed the same general patterns of oil trajectory to the northwest and north, nearly parallel to the coastline of the western Gulf of Mexico (GoM) with possible oil landing on Mexican and Texas beaches. Field observations at selected beaches and islands along the coast of the western and southern GoM during and after the spill confirmed these satellite-based findings, which were also used to help in planning a recent field campaign to collect sediment samples in the southern GoM.

© 2015 Elsevier Ltd. All rights reserved.

1. Introduction

On 3 June 1979, the Mexican state-owned oil company Pemex (Petróleos Mexicanos) exploratory well, Ixtoc-I, blew out in the Bay of Campeche, southern Gulf of Mexico (GoM), about 80 km northwest of Ciudad del Carmen, Mexico. It was not until 23 March 1980, 290 days after the blowout that the well was finally capped (Jernelöv and Liden, 1981). According to Pemex estimates, a total of about 475,000 metric tons of oil spilled into the Gulf, making it the second largest accidental release of oil into the marine environment following the *Deepwater Horizon* (DWH) oil spill in 2010. Although there were no official estimates on the fate of the Ixtoc oil, Jernelöv and Liden (1981) suggested that 50% evaporated into the atmosphere, 25% sank to the bottom, 12% degraded biologically and (photo)chemically, and the remainder landed on Mexico and Texas beaches or was mechanically removed or burned at the well site. The Ixtoc oil spill's ecological impacts to the environment were not extensively studied during and immediately after the spill, but benthic habitats and the long-term fate of oil deposition could serve as a window into the future for the ongoing assessment of the DWH oil spill environmental effects. Unlike the DWH oil spill, which had a large oil plume at 1000–1200 m deep (Camilli et al., 2010), the Ixtoc oil spill occurred on the continental shelf at a water depth of 50 m, and the majority of the oil reached the sea surface under high pressure. Thus the surface oil footprint and trajectory may provide critical information on where oil may have

impacted the marine ecosystem and sedimentology. This information is particularly important for a recently funded project by the GoM Research Initiative (GoMRI), which will attempt to sample sediments on the ocean floor in search of Ixtoc oil residues. Accurate knowledge of the surface oil footprint and trajectory could help plan field excursions to determine where these residues are located and thus where to sample. Unfortunately, after more than three decades since the Ixtoc oil spill, such information is largely unavailable.

Hence, given the pressing need for knowledge of the surface oil footprint and oil trajectory from the Ixtoc oil spill in order to help plan field campaigns to sample the sediments, the objectives of this paper are two-fold: 1) to develop a practical approach to map surface oil slicks from the Ixtoc oil spill from Landsat/MSS and CZCS measurements and 2) to derive surface oil footprint and transport trajectory from the same measurements.

2. Data and methods

2.1. Satellite data sources and processing methods

Due to limited field data available during the Ixtoc spill, satellite remote sensing is the only feasible means to achieve the objectives. Indeed, satellite remote sensing has been used effectively detecting and monitoring oil spills, including the most recent DWH spill (Brekke and Solberg, 2005; Fingas and Brown, 1997; Klemas, 2010; Leifer et al., 2012). Of all remote sensing techniques, Synthetic Aperture Radar (SAR) offers medium- to high-resolution data under all weather conditions during day and night, representing the most frequently used oil

* Corresponding author.

E-mail addresses: suns@mail.usf.edu (S. Sun), huc@usf.edu (C. Hu).

spill detection technique (Brekke and Solberg, 2005; Garcia-Pineda et al., 2013). Optical remote sensing, although suffering from cloud cover, can complement SAR observations for more synoptic and repeated measurements (Macdonald et al., 1993). For example, Hu et al. (2003 & 2009) used the 250-m resolution imagery collected by the Moderate Resolution Imaging Spectroradiometers (MODIS) to detect and quantify oil slicks from oil spills and natural seeps under non-sunglint and glint conditions. More recent studies also showed the possibility to estimate slick thickness (or surface oil volume) based on the spectral shapes and magnitudes of the oil slicks (Clark et al., 2010; Svejksky et al., 2012).

Unfortunately, during the Ixtoc spill in 1979–1980, satellite SAR data were not available. Of the few satellite data collected during that period, there are datasets from the Coastal Zone Color Scanner (CZCS, 1978–1986 on Nimbus-7 satellite) and Landsat Multispectral Scanner (MSS) [1972–1999 on Landsat 1–5 satellites] providing relatively short revisit time, as well as relatively high spatial resolution. Therefore, these data were used in the study to detect and quantify surface oil slicks due to the Ixtoc spill.

CZCS has 4 ocean bands with 20 nm bandwidth centered at: 443, 520, 550, and 670 nm. Band 5 has a 100 nm bandwidth centered at 750 nm. CZCS full Local Area Coverage (LAC) has ~800 m nadir resolution with a swath width of 1556 km and a revisit time of 6 days. Level-1A data were obtained from NASA/GSFC, resampled to 500 m resolution, then processed using the NASA software package SeaDAS (version 6.4) to correct for Rayleigh scattering, resulting in Rayleigh corrected reflectance (R_{rc}) for every spectral band. Red–Green–Blue (RGB) true color images were generated from the R_{rc} data at 670 nm (R), 550 nm (G), and 443 nm (B).

Landsat/MSS had four spectral bands (500–600, 600–700, 700–800, 800–1100 nm) with 60-meter spatial resolution. Approximate scene size is 170 km north–south by 185 km east–west and a revisit time is 18 days. Landsat/MSS Level-1 data were obtained from USGS and calibrated to top of atmosphere radiance. Landsat data were also processed to generate the spectral R_{rc}, from which RGB false color images were produced (R: 950 nm, G: 750 nm, B: 650 nm).

The CZCS and Landsat/MSS data obtained covered locations of the western GoM (Fig. 1a) and time period from 3 June 1979 to December 1982. During this period, images from the start of the oil spill on 3 June 1979 to the capping of the oil well on 23 March 1980 (spill period) were used to generate the oil trajectory. Images from Jan. 1981 to Dec. 1982 (natural oil slick reference period) were used to track natural slicks in the western GoM.

2.2. Oil slick interpretation

The presence of an oil slick can dampen surface capillary waves, leading to changes in surface roughness. Such changes in images under sunglint conditions can make the slicks appear brighter or darker than the surrounding waters (Adamo et al., 2009; Hu et al., 2009; Jackson and Alpers, 2010). Such appearance can even result from the thinnest oil films from natural seeps (Hu et al., 2009). In the absence of sunglint effect, oil can also be discriminated from oil-free clear water and chlorophyll-dominated waters when considering their spectral differences (Bulgarelli and Djavidnia, 2012). On the other hand, a mixture of oil and water droplets, as well as air bubbles, marine organisms, and dispersants can form oil emulsions, which often show a brownish color in satellite RGB true color images. This is because of the enhanced absorption in the blue and UV wavelengths due to the asphaltic compounds and enhanced backscattering in the red-NIR (Near InfraRed)–SWIR (ShortWave Infrared) wavelengths (Clark et al., 2010). Such an effect can be observed even in images without sunglint. Overall, the spatial contrast was used first to identify oil-like slicks in CZCS and Landsat/MSS imagery.

However, oil is not the only material that can cause a spatial contrast. Other materials or ocean features can also cause similar spatial contrast in satellite imagery. These look-alike features in the GoM include *Sargassum* (brown algae) and *Trichodesmium* (cyanobacteria/blue-green algae) mats (Gower et al., 2006; Hu et al., 2010; Hardy, 2014) as well internal waves (Apel, 2004). To distinguish them from oil slicks, spectral and spatial shapes of the identified slicks were examined. Specifically, the high pigment absorption in CZCS band 4 (660–680 nm) and low pigment absorption in CZCS band 2 (540–560 nm) makes these algal mats appear greenish in the CZCS RGB imagery (R: 670 nm, G: 550 nm, B: 443 nm). For Landsat/MSS imagery, the high absorption of water in the SWIR band (950 nm) and the floating algae's reflectance peak in NIR band (750 nm), as well as the high pigment absorption around the red band (650 nm) (Gower et al., 2006; Hu et al., 2010), would also make a greenish color for floating algae in the Landsat/MSS RGB false color imagery (R: 950 nm, G: 750 nm, B: 650 nm). In contrast, oil emulsions' increasing reflectance toward NIR (Clark et al., 2010) would make a brownish color in both CZCS and Landsat/MSS RGB imagery. Some *Sargassum* mats may be brownish, and in such cases the feature's morphology was used to differentiate *Sargassum* from emulsified oil. The former tended to be thin and elongated slicks, while the latter tended to be more diffuse. These characteristics differentiate the

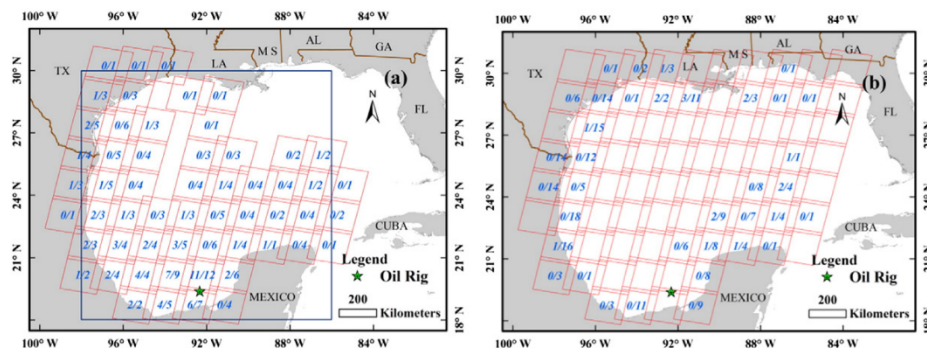


Fig. 1. Landsat/MSS and CZCS images were examined for (a) 3 June 1979–23 March 1980 and (b) January 1981–December 1982. (a) represents the Ixtoc oil spill period (the accident occurred on 3 June 1979 and the well was capped on 23 March 1980). The ratio in each cell denotes (# of images with oil detected)/(# of images examined). A total of 197 Landsat MSS images were examined, with 65 showing oil slicks. The dark blue box denotes the geographic boundary of CZCS images examined in this study, and a total of 267 CZCS images were examined, with 48 showing oil slicks. (b) represents a reference period without oil spills, where a total of 377 CZCS images and 228 Landsat/MSS images were examined. The empty cells indicate no Landsat coverage during that period.

algae mats from oil slicks. On the other hand, internal waves are characterized by long, quasilinear stripes in satellite imagery (Apel, 2004), and they tend to appear as alternative bright and dark stripes (Apel et al., 1975; Jackson, 2007). In contrast, although oil slicks often show elongated shapes (Sun et al., submitted for publication), they tend to have irregular shapes that would not form patterns of a striped packet, such as internal waves. These characteristics were used to rule out internal waves from the identified slicks.

2.3. Differentiation of natural slicks from Ixtoc oil spill

The GoM is known to have numerous natural seeps, with natural slicks often caught in satellite imagery (MacDonald et al., 1993; Hu et al., 2009). It is critical to separate these natural slicks from those due to the Ixtoc spill in order to understand the spill's footprint and trajectory. However, oil slicks from natural seeps and oil spills are similar in both their spatial shapes and spectral shapes, and alternative ways must

be used to differentiate them. In this study, they were separated using the statistical method below.

The method compared the maximum area of slick appearance in a particular location between two periods: the Ixtoc spill period (June 1979–March 1980) and non-spill period (January 1981–December 1982). During the latter period, 377 CZCS images and 228 Landsat/MSS images were examined to determine natural oil slicks. For each Landsat WRS-1 path row (squares in Fig. 1), the maximum area of all oil slicks in a particular square in a single day from all images was recorded. This maximum area was compared to the total oil area of every image in the same square during the former period. The ratio between the two was defined as a Maximum Area Ratio (MAR), which was used to determine whether the slicks detected in a particular path row during the Ixtoc spill period were from natural seeps or the spill. If MAR is comparable or > 1.0 , it is assumed that the oil slicks found during the spill period on that particular day were likely from natural seeps. If $MAR < 1.0$, the detected slicks were likely from the Ixtoc spill. For the two

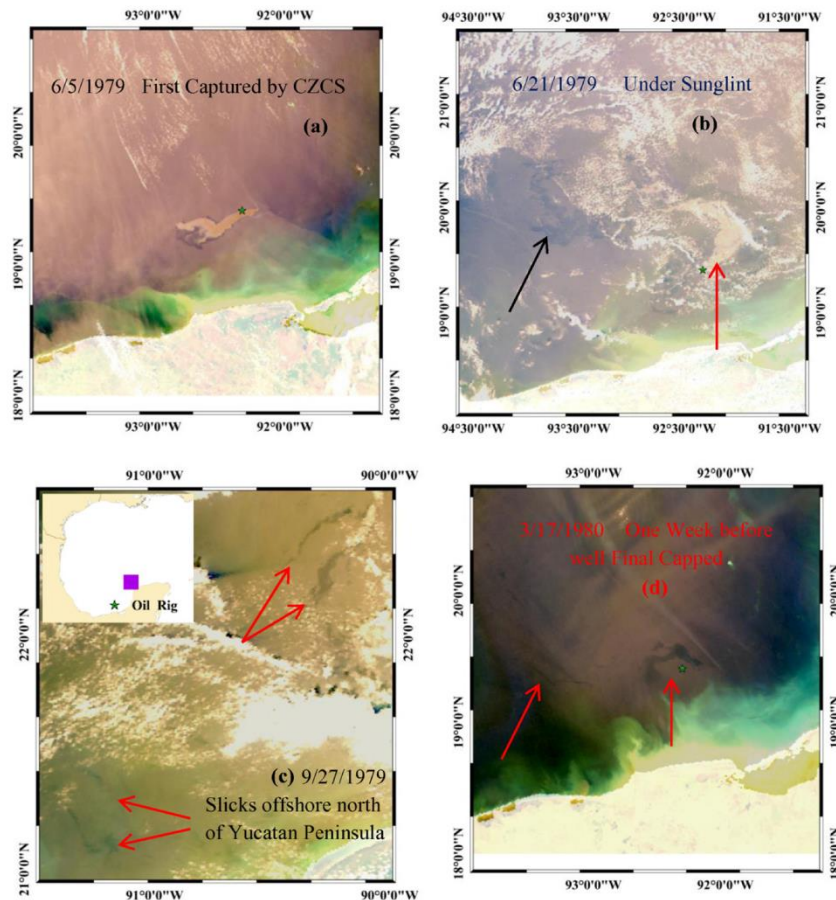


Fig. 2. Oil slicks captured in CZCS Red–Green–Blue true color composite images (R: 670 nm, G: 550 nm, B: 443 nm) during the Ixtoc spill. The green star shows the oil site location. a) Oil slick first captured by CZCS two days after the oil blowout. Oil emulsions show brownish colors. b) Oil slicks captured by another CZCS image under sunlight, where both positive (red arrow) and negative (black arrow) contrasts can be observed. c) Oil slicks found offshore north of Yucatan Peninsula in late September 1979. The inset figure shows the approximate location (purple area) of the slicks. d) Oil slicks near the oil site one week before the well was capped.

squares nearest the oil well site, the proximity of each slick to the oil spill site was examined to determine whether it was from the spill. This is because oil was still released from that site after the well was capped on March 23, 1980.

2.4. Estimating oil trajectory

After excluding oil look-alikes, all identified oil slicks together with their time/location information were imported to the ESRI/ARCMAP software (version 10.1). Oil footprint polygon vectors were documented in shapefile format, and all footprints during the spill period were mapped together in ARCMAP with the shoreline base layer of Global Self-consistent, Hierarchical, High-resolution Geography Database (GSHHG), obtained from NOAA/NCEI. Some major (large area) oil footprints away from the spill site were detected by either Landsat/MSS or

CZCS, and these were selected to show oil transport trajectories during the spill.

2.5. Validation using field observations

A number of shoreline locations along the western and southern GoM were visited in 1979 and 1980 to observe oil and tar by Wes Tunnell and his students. These trips included one major trip in October 1979 by two students (Quenton Dokken and Leo Trevino) to the Veracruz shoreline, including Enmedio Island and Reef, one longer trip in 1980, when Tunnell took an extended field investigation to many southern Mexican beaches and rocky shorelines during July and August 1980. In addition, some observation were continued in later years at Enmedio Island and Reef during annual Coral Reef Ecology Class field trips; others were made when Tunnell lived in the Yucatan for one

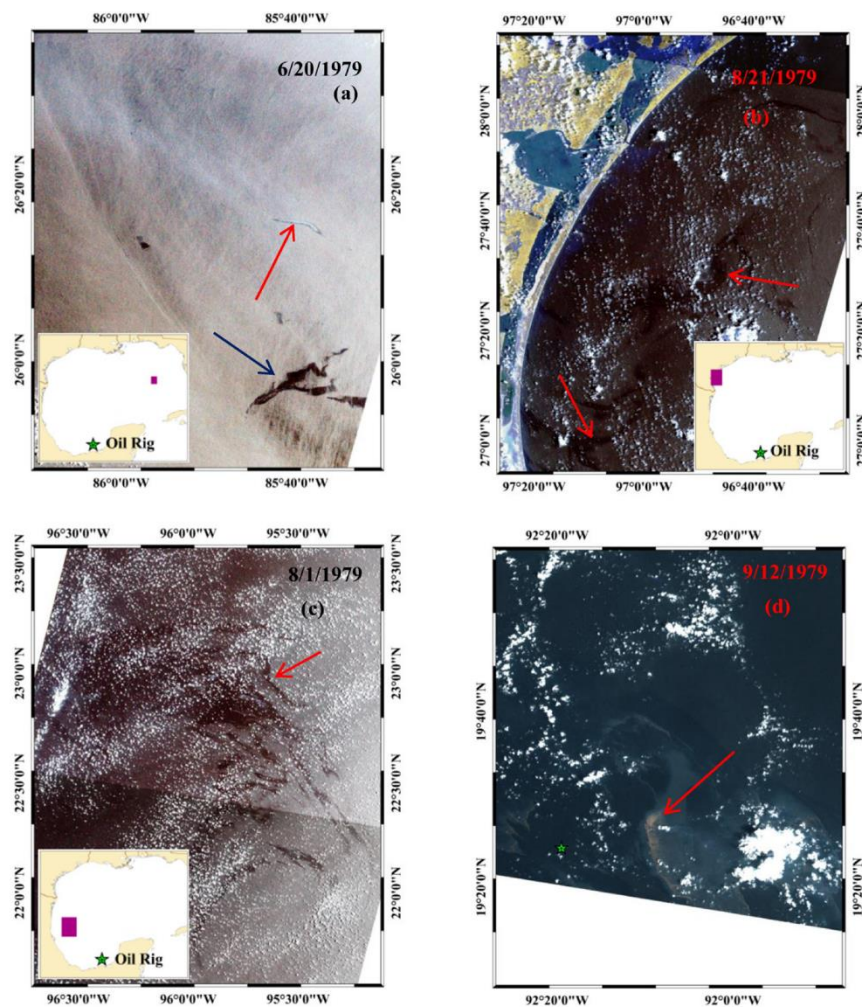


Fig. 3. Oil slicks captured by Landsat MSS RGB (R: 950 nm, G: 750 nm, B: 650 nm) stretched image. a) Natural oil slicks in the middle of the GoM; b) oil slicks along the South Texas coast; c) oil slicks along the coast of Mexico; d) oil emulsions around the spill site.

year (1985–86), and still others were made in 2010 after the BP Macondo Deepwater Horizon Spill when Tunnell took three separate expeditions back to selected southern Gulf sites. Photographs are available from all of these sites noted, except one (Montepio, Veracruz). Google Earth was used to determine the approximate locations for coordinates (latitude and longitude) of each site examined. These locations were overlaid on the surface oil trajectory maps to conduct a qualitative validation of the remote sensing interpretations. Given the lack of field observations in the same place and same day of the remotely detected slicks, this is perhaps the best method for an indirect validation of the surface oil trajectory.

The first Ixtoc trajectory estimate or map was prepared by J.A. Galt of NOAA (Figure 2.2 of Galt, 1981) just 10 h after notification of the spill. Based on numerous field trips and field observations over the past 35 years, as well as publications immediately after the spill and more recently, Tunnell (2010, 2011) prepared an Ixtoc oil trajectory map together with an oil footprint map from the DWH oil spill in the northern GoM. The Tunnell Ixtoc-DWH map was developed in summer

2010 at the Harte Research Institute for Gulf of Mexico Studies with the main purpose of providing a visual tool to help the public to understand the size and location of both spills and their respective locations in the GoM. The Tunnell Ixtoc oil trajectory maps were prepared with the knowledge that the oil slick primarily moved westward in June 1979 (Ross et al., 1980) and then northward in July (IMP, 1980). In addition, based on today's physical oceanography (Zavala-Hidalgo et al., 2003; DiMarco et al., 2005; Morey et al., 2005), the plume was speculated to follow dominant surface current velocity and direction. These maps (Galt and Tunnell) were used in this paper to cross check with the remote sensing maps.

3. Results

Fig. 2 shows several CZCS images, where oil slicks show different appearances. As the oil was saturated with gas, when blowing out from a depth of 50 m with a pressure of 350 kg/cm², the oil usually rose quickly to the surface as a three-phase emulsion, with gas bubbles

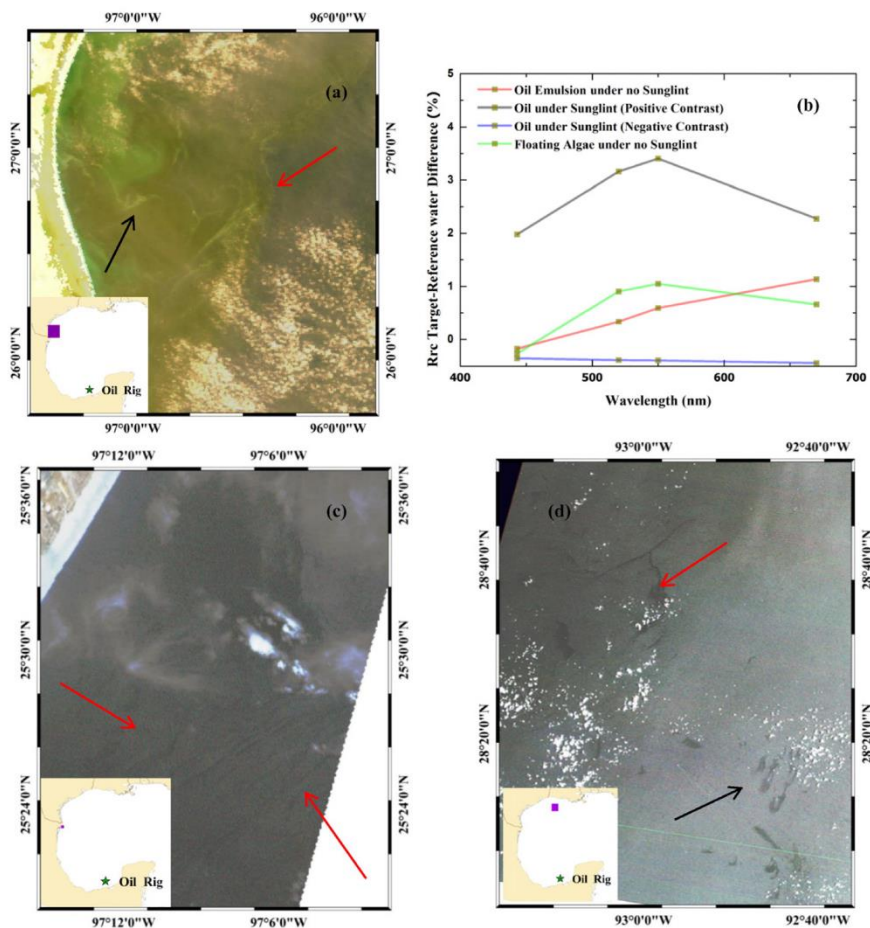


Fig. 4. Differentiation between oil slicks and other surface features. a) Floating algae show greenish colors on CZCS RGB images without sunglint. b) Spectral shapes in Rayleigh corrected reflectance show difference between floating algae and oil. c) Internal waves show parallel and alternative light and dark patterns; d) natural oil slicks in the northwestern GoM.

in oil and about 50% of water droplets (Jernelöv and Liden, 1981). Thus most of the oil slicks around the spill site were found to be emulsified oil. Fig. 2a shows the brownish color of oil emulsions around the spill site. Fig. 2b shows oil slicks in both positive (brighter) and negative (darker) contrasts as compared with the surrounding oil-free water; this is due to changes in sunglint intensity (Hu et al., 2009; Jackson and Alpers, 2010). Fig. 2c shows several slicks north of the Yucatan Peninsula far away from the spill site in late September 1979. Even after 9 months of the blowout, one week before the oil well capped, there were still extensive amounts of oil leaking out from the spill site (Fig. 2d).

Fig. 3 shows several examples of Landsat/MSS images where oil slicks were detected. Oil slicks were observed in the mid-GoM in 20 June 1979 (Fig. 3a), which were eventually classified as natural oil slicks. Oil slicks in South Texas and Mexico were observed in August 1979 (Fig. 3b, c). Oil emulsions from Landsat/MSS were also found near the spill site (Fig. 3d), which showed high reflectance in the NIR band compared to surrounding oil free water.

Fig. 4 shows examples of differentiation between oil slicks and other look-alikes. The floating algae spectrum in Fig. 4b shows a reflectance peak in the green band because of high absorption in the red and blue bands, making the feature appear greenish in the CZCS true color image (Fig. 4a). In contrast, oil emulsion tends to have increased reflectance toward red, making the slick feature appear red/brownish in the CZCS true color image when sunglint is absent. Under sunglint conditions, oil contrast (to the surrounding water) could be positive or negative for the entire spectrum (Fig. 4b).

Natural slicks in each Landsat WRS-1 path row were excluded using slick area statistics (MAR). Fig. 5a shows a summary of natural and unnatural oil slicks found in each square during the spill period, where the number in each square indicates the MAR between non-spill period and spill period. The brownish color without annotated numbers indicates where oil slicks were found during the spill period only, and the green color without annotated numbers indicates where oil slicks were found during the non-spill period only. The brownish color squares with and without annotated numbers show that oil from the Ixtoc spill reached that location at least once during the spill period. It is clear in Fig. 5a that natural oil slicks mainly appeared in offshore waters to the north and northeast of the spill site, where these areas are known to contain numerous natural oil seeps (Hu et al., 2009; MacDonald et al., 1993).

After excluding all oil look-alikes and natural oil slicks, a map with all observed oil footprints from the Ixtoc oil spill was generated. Fig. 5b shows the map where oil footprints were derived from Landsat/MSS and CZCS between June 1979 and March 1980. Most of the large oil slicks are confined and frequently occurred within 200 km north and west of the spill site. Significant numbers of oil slicks were found along the western coast of GoM, some even reached as far north as Corpus Christi, Texas. Northern offshore Yucatan Peninsula areas were also detected with slicks.

While Fig. 5b presents the overall oil footprint for the entire spill period, it is difficult to visualize the temporal sequence. Such a sequence is presented in Fig. 6a and b for Landsat/MSS and CZCS, respectively, where for clarity only the major slicks are plotted, each annotated with a date. These slicks tend to transport further north-west from the spill site after late July 1979. Large slicks were observed offshore of Tampico and Cabo Rojo Mexican coast, and then appeared along the northern Mexican coast and eventually were transported to the Texas coast. From mid-September, oil slicks were frequently observed to the northeast direction of the spill site. Some of slicks after mid-September also reached the south coast or southeast of the spill site, with fewer slicks found in the northwest direction than in late July. There were still continuous large slicks detected around the spill site from November 1979 to 23 Mar. 1980 when the oil well was finally capped. However, during the 5-month period most of the oil slicks were found within 200 km of the spill site.

A number of field observations were selected to validate these remote sensing observations. The field observations were located along the western and southern coast of GoM (Fig. 5b), from either the literature (location nos. 1–3) or Wes Tunnell and his students' field trips (location nos. 4–14) during and after the oil spill. Ixtoc oil was first observed to enter the US waters in south Texas on 6 August 1979 (Gundlach et al., 1981), and eventually extended about 250 km along the South Texas coast until a tropical storm in mid-September "cleaned" the beaches of about 90% of the oil (Gundlach et al., 1981). Fig. 7a shows heavy oil coverage on Mustang Island on 24 August. The oil pollution on beaches and islands along the South Texas coast was documented more explicitly than on Mexican beaches and islands, where only occasional records reported oil pollution. Several other selected photos of oil coverage in coastal areas are presented in Fig. 7. Indeed, each of the annotated 14 locations (triangles in Fig. 5b) was reported to be polluted by oil or

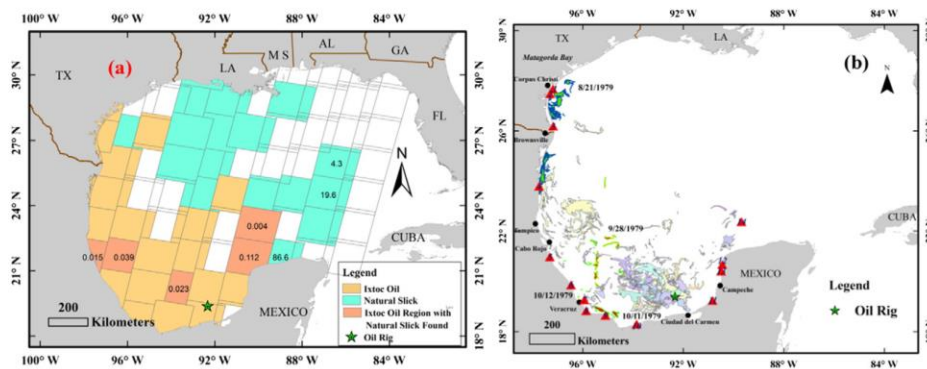


Fig. 5. a) Differentiation between natural oil slick and Ixtoc oil slick using a Maximum Area Ratio (MAR), defined as the ratio between maximal slick area in the reference period (no oil spill) and the maximal slick area in the spill period, if both existed in the same cell. If MAR is < 1 , then the cell is dominated by slicks from the spill; if MAR is > 1 , then the cell is dominated by natural slicks. The reddish color (with numbers) indicates cells dominated by slicks from the spill, while the green color (with numbers) shows cells dominated by natural slicks in the Ixtoc spill period. The brownish and green colors without numbers indicate that oil slicks were found only during one period. b) Oil slick trajectory of the Ixtoc spill generated from CZCS and Landsat/MSS imagery after eliminating natural slicks. Also annotated are the locations (the numbered red triangles) where oil slicks, tar mats, or oil-contaminated sediments were found from field observations. The polygons with different colors show surface oil footprints found in different days. Of these, the green polygons with thick blue outlines were oil footprints detected on 21 August 1979 around locations 1 and 2, while the red polygons with thick green outlines were oil footprints detected in October 1979 around location 7.

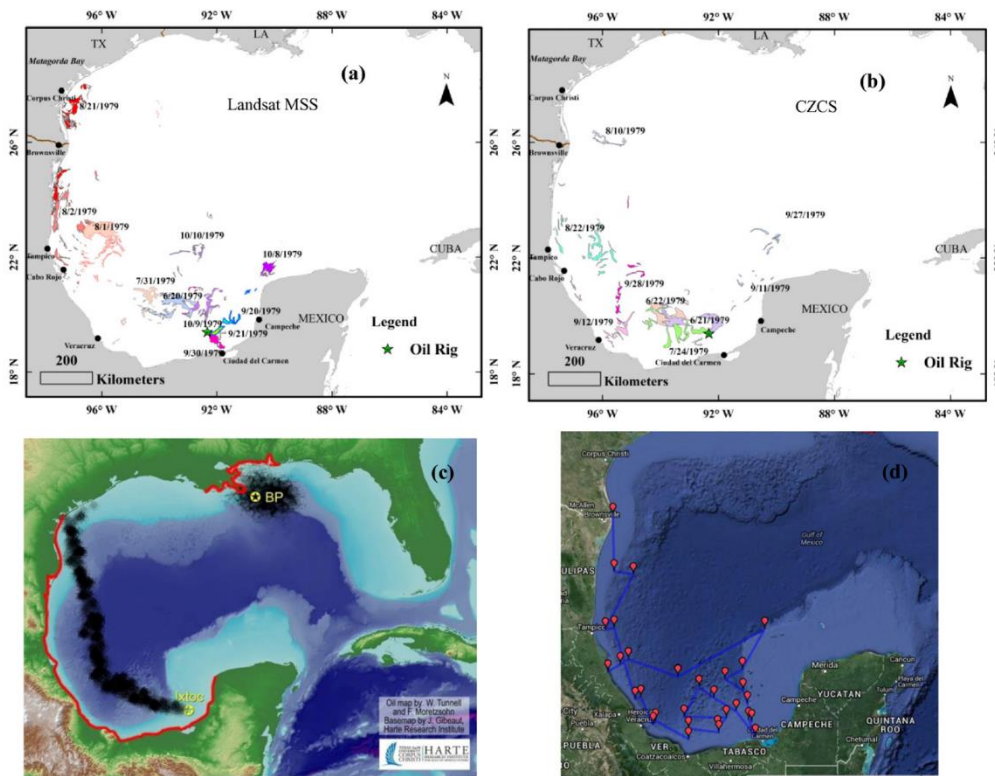


Fig. 6. Oil trajectories derived from a) Landsat/MSS and b) CZCS, where the green star annotates the site location. The green polygons with blue outlines (annotated as “9/20/1979” and “9/21/1979”) were confirmed in the same direction by observations from a helicopter (Farrington, 1983). c) Ixtoc oil pathway generated by Wes Tunnell. d) Sampling locations (red balloon) of the first field campaign to collect sediment samples between 7/29/2015 and 08/11/2015, conducted by the C-IMAGE II research consortium supported by the GoM Research Initiative. These station locations were determined from the findings from this paper (Figs. 5 and 6; <http://www.marine.usf.edu/c-image/about-us/ship-schedule>).

tar (in Table 1), confirming the oil trajectory pathway derived by both Landsat/MSS and CZCS.

4. Discussions

Most oil slicks were found to the north and northwest of the spill site (Fig. 5b), and the temporal sequence in Fig. 6 suggest a north and north-west trajectory along the Mexican and Texas coast especially in early August 1979. Such patterns were not only verified by the field observations along these beaches and islands but they also agreed with predictions by physical models (Galt, 1981). According to the surface current and wind conditions, the oil slicks were predicted to firstly drift west to west-northwest (Galt, 1981). Once they arrived offshore along the Mexican coast between Cabo Rojo and Tampico, they would transport north with the northward Mexican coastal current. In addition, a counterclockwise circulation off Tampico was seen to recirculate oil that was near shore extending 50 km offshore toward the Mexican coastal rather than allow it to continue farther north. Thus the main slick that entered the US water might come from 50 km off shore of Tampico (Galt, 1981). As shown in Fig. 6a, two large oil patches, with each being continuous in its spatial extent, were found offshore Tampico on 1 August 1979 and along Mexico coastal line between Tampico and Brownsville on 2 August 1979, respectively. These two patches appeared to follow the above pathway from the offshore of Tampico to reach the northeastern

coast of Mexico. According to these results, the surface oil could be transported further north to the South Texas water by the northward Mexican coastal current. Indeed, Ixtoc oil was firstly reported to impact Texas shoreline on 6 August 1979, with 27 km of shoreline contaminated by light tar balls. The satellite-based observations also showed general agreement with the Tunnell map (Fig. 6c), where they both followed the northwestern direction toward Texas waters by passing far outside of Tampico, Mexico. The two maps, although derived independently from each other, both showed that oil reached as far north as Matagorda Bay, north of Corpus Christi, Texas. While the Tunnell map was generated primarily based on physical oceanographic conditions, the new remote sensing maps (Fig. 6a & b herein) now provide remote-sensing based evidence for the general oil trajectory directions.

Although direct validation of the satellite-based maps is impossible due to lack of field observations at exactly the same time and same location of the satellite observations, field sampling and observations during and after the spill still provided indirect validation of the remote sensing based interpretations. Extensive oil slicks were detected along and offshore Texas water on 21 August 1979 in Landsat/MSS imagery while oil slicks were sighted on Texas coastal line between Brownsville and Corpus Christi and very thick oil emulsions were reported to be washed ashore on Mustang Island (location no. 1 in Fig. 5b) on 24 August 1979 (Gundlach et al., 1981). Oil tar balls were found in water between mainland and Enmedio Island and Reef

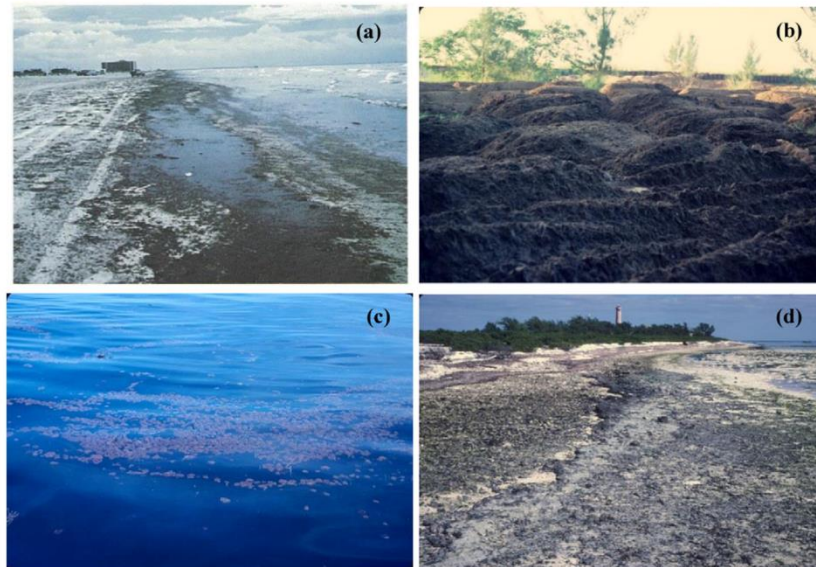


Fig. 7. Photos of oil/tar along the western and southern coasts of GoM. a) Heavy oil washed ashore Mustang Island on 24 August 1979 (location no. 1 in Fig. 5b) (Gundlach et al., 1981); b) piles of oily sand observed on the Tuxpan beach in October 1979 (location no. 5 in Fig. 5b) [photo by Q.R. Dokken]; c) floating tar balls observed in water between Veracruz mainland and Enmedio Island and Reef (about 5 miles offshore) in October 1979 (location no. 7 in Fig. 5b) [Photo by Q.R. Dokken]; d) A large tar mat observed in the southeastern corner of Isla Perez on Alacran Reef in January 1986 (location no. 14 in Fig. 5b) [Photo by J.W. Tunnell].

(about 5 miles offshore) on an October 1979 field trip (location no. 7 on Fig. 5b). The remote sensing imagery showed several surface oil distributions near this location around October (Fig. 5b highlighted red polygons with green outlines). In addition to field observations at locations 1, 2 and 7, observations at locations 4, 5, 8, 9, 12, 13, and 14 (all marked on Fig. 5b) all revealed oil presence throughout the Ixtoc oil spill period. Locations 3, 6, 10, and 11 seem a little further away from the oil coverage areas, but they cannot be reasonably ruled out of oil coverage since these locations all enveloped by surrounding oil presence (Fig. 5b).

Oil slick appearance frequency and area of coverage were found to increase in the east and northeast direction of the spill site after September 1979. ERCO (1982) reported that the northward-flowing western GoM current reversed direction during September 1979, and major surface concentrations of oil were then found to the northeast, east and southeast of the well (Farrington, 1983). As shown in Fig 6a and b, large slicks were found more in the north, northeast, south and southeast direction of the oil well site than in other directions since September 1979. Helicopter overflight found that oil plumes were in the northeast direction of the oil well from 15 September–20 September 1979 and shifted to southeast direction for 12 h on 21 September 1979 (Farrington, 1983). Landsat/MSS images (Fig. 6a annotated “9/20/1979” and “9/21/1979” slicks) showed the same direction of oil distributions as reported in the two days. North of the Yucatan Peninsula, large patches of oil were firstly detected in September 1979. However, no apparent slicks were found entering water north off Tampico after September 1979. Therefore, without a direct field validation at the same time and same location of the oil slicks, these published reports indirectly supported the remote sensing interpretations here.

However, due to the inherent limitations of the two satellite sensors, the information from this analysis cannot be considered as complete. CZCS revisit time is 6 days with nadir spatial resolution of 800 m,

while Landsat/MSS revisit time is about 18 days with spatial resolution of 60 m. Even after combining both observations, there are still spatial and temporal gaps due to both their infrequent coverage (Fig. 1) and weather conditions (clouds). For example, there was a tropical depression across the south Texas area on 13 September 1979 which removed more than 90% of the oil on the Texas shoreline by wave activities (Gundlach et al., 1981). Another tropical storm moved across the southwestern Gulf, which affected the plume area on 16&17 September 1979 (Atwood and Benjamin, 1980). During and immediately after the storms, most of the areas in the western GoM were covered by clouds, resulting in no remote sensing observations. Even under cloud free conditions, storm-induced sediment resuspension made it difficult to interpret oil signals in remote sensing imagery in nearshore waters. Thus, the results presented here can only be interpreted as incomplete although they perhaps represent the best information we can obtain in such a retrospective way. Likewise, satellite remote sensing of oil spills is limited to the very surface (top centimeters) unless oil droplets develop uniformly through the top meters. In the case of the Ixtoc spill, a subsurface oil plume of suspended oil droplets was observed within 40 km of the spill site, where its movement was influenced more by currents than by winds, and the plume was possibly moving in the same direction as with surface oil slicks (Boehm and Fiest, 1982). Although the subsurface oil plume was estimated to represent only ~3% of total spilled oil, it could not be observed from remote sensing. However, such an inherent limit in remote sensing would not impact the observations of the surface oil trajectory, even when infrequent satellite observations were used. In this regard, the trajectory presented in Figs. 5 and 6 may be used to help plan field surveys to sample the bottom sediment in order to determine the spill's impact on the benthic habitats after >30 years. Indeed, at the time of this writing, with the help of Figs. 5 and 6 to determine the sampling locations such a field campaign has already been planned and conducted (07/29/2015–08/11/2015, Fig. 6d) under the support of the Gulf

Table 1
Field observations along the western and southern Gulf of Mexico coast.

Number	Time	Location	Area	Latitude	Longitude	Oil type	Description
1	Aug. & Sep. 1979	Mustang Island	Texas, US	27°39' 20" N	97°11' 11" W	Oil slick, emulsions and tar mats	Similar conditions applied to North Padre Island (no. 2)
2	Aug. & Sep. 1979	North Padre Island	Texas, US	27°27' 53" N	97°17' 51.5" W	Oil slick, emulsions and tar mats	By 15 August, coverage of North Padre Island was mostly light, by 26 August, most of North Padre Island had moderate coverage, heaviest period of oil impact occurred from 29 August through 1 September 1979. From 2 September until 13 September, only scattered sheen was observed offshore, and no new impacts occurred. On 13 September, a tropical storm "cleaned" the beaches of much of the oil (Gundlach et al., 1981).
3	Aug. & Sep. 1979	South Padre Island	Texas, US	26°11' 05" N	97°10' 34" W	Oil slick, emulsions and tar mats	Similar conditions applied to North Padre Island (no. 2)
4	March 1980	La Pesca beaches	Tamaulipas, MX	23°47' 07.14" N	97°44' 08.53" W	Grated oil/tar	Observed oil/tar grated into wind-rows oriented north south on backshore of beach
5	October 1979	Tuxpan beach	Veracruz, MX	20°58' 23.87" N	97°18' 25.85" W	Oily sand	Observed piles of oily sand that had been raked or scooped from the beach and piled on the backshore near and in the dunes
6	October 1979	Punta Delgado rocky point	Veracruz, MX	19°51' 36.09" N	96°27' 35.86" W	Oil/tar	Observed oil/tar in among rocks on rocky shoreline and on rocky cobblestone beach.
7	October 1979	Enmedio Island and Reef off Anton Lizardo	Veracruz, MX	19°16' 05.07" N	95°56' 19.46" W	Oil in water	Observed lots of oil in water between mainland and Enmedio Island and between mainland and reef, lots of oil all around island and much oil in shallow lagoon around island in seagrass beds
8	27 July 1980	La Gaviota Beach	Veracruz, MX	18°49' 55.89" N	95°51' 42.71" W	Tar ball and oily sand	Observed small tar balls on the upper beach and piles of oily sand spaced out every 50–100 m along the beach
9	28 July 1980	Montepio, San Andres Tuxtlas Mountains	Veracruz, MX	18°38' 44.28" N	95°05' 45.31" W	Solid tar mats	Observed some very solid tar mats in intertidal zone.
10	30 July 1980	Sanchez Magallanes	Tabasco, MX	18°17' 56.30" N	93°51' 23.37" W	Oily sand	Observed layer of oily sand about 1 ft thick at a level about 6 ft or so above high tide.
11	2 August 1980	Remote highway area south of Champoton	Campeche, MX	19°14' 39.29" N	90°49' 56.26" W	Heavy tar mats	Large tar mats in supratidal zone above limestone rocky shore and among rocks along rocky shore.
12	2010	Mangrove coastline	Campeche, MX	20°40' 18.42" N	90°26' 41.16" W	Tar mats	Found thin tar mats among the roots of the mangroves in the mangrove forest/swamp that was about 3/4 in. thick in both places
13	2010	Mangrove coastline	Campeche, MX	20°24' 24.58" N	90°29' 30.81" W	Tar mats	Similar conditions applied to no. 12
14	January 1986	Isla Perez, Alacran Reef	Yucatan, MX	22°22' 44.78" N	89°41' 05.00" W	Tar mat	Observed a large tar mat on the southeastern corner of Isla Perez on Alacran Reef

of Mexico Research Initiative in order to have a comparative study with the DWH (BP) oil spill in the northern GoM (Fig. 6c).

5. Conclusions

For the first time, a comprehensive retrospective analysis of Landsat/MSS and CZCS imagery was used to develop partial surface oil footprint and trajectory maps from the Ixtoc oil spill in the southern GoM between 1979 and 1980. Practical methods have been developed and used to differentiate surface oil slicks from other look-alikes, and to differentiate oil spill from natural oil slicks. Such derived oil footprint and trajectory maps provide a synoptic view of locations, timing, and relative amount of surface oil in the GoM following the oil transport pathway. Such observed oil trajectory and occurrence of major oil slicks agree well with field observations and previous modeling results, yet they provide independent information to assess the spill's impact on the marine environment. Such derived maps have been used to guide field measurements, thus providing another practical use. The availability of CZCS and Landsat/MSS since the 1970s may make such approaches extendable to other spill cases.

Acknowledgments

This study was possible because of the financial support from the NASA Ocean Biology and Biogeochemistry (OBB) program [Grant NNX13AD08G], the BP/Gulf of Mexico Research Initiative through

C-IMAGE [SA 15–16], and the Bureau of Ocean Energy Management (BOEM, contract M12PC00003). We thank the USGS for providing Landsat/MSS imagery, NASA for providing CZCS imagery and NOAA for providing GSHHG shoreline data.

References

- Adamo, M., Carolis, G.D., Pasquale, V.D., Pasquariello, G., 2009. Detection and tracking of oil slicks on sun-glittered visible and near infrared satellite imagery. *Int. J. Remote Sens.* 30 (24), 6403–6427. <http://dx.doi.org/10.1080/01431160902865772>.
- Apel, J.R., 2004. Oceanic internal waves and solitons. In: Jackson, C.R., Apel, J.R. (Eds.), *Synthetic Aperture Radar Marine User's Manual*. NOAA NESDIS Office of Research and Applications, Washington DC, pp. 189–206 (464 pp.).
- Apel, J.R., Byrne, H.M., Proni, J.R., Charnell, R.L., 1975. Observations of oceanic internal and surface waves from the earth resources technology satellite. *J. Geophys. Res.* 80, 865–881.
- Atwood, D.K., Benjamin, J.A., 1980. The mission of the September 1979 Researcher/Pierce Ixtoc-1 cruise and the physical situation encountered. In: Atwood, D.K. (Ed.), *Proceedings of a Symposium on Preliminary Results From the September 1979 Researcher/Pierce Ixtoc-1 Cruise*, Key Biscayne, Florida, June 9–10, 1980, pp. 1–19 (591 pp.).
- Boehm, P.D., Fiest, D.L., 1982. Subsurface distributions of petroleum from an offshore well blowout. *The Ixtoc 1 blowout*, Bay of Campeche. *Environ. Sci. Technol.* 16, 67–74.
- Brekke, C., Solberg, A.H.S., 2005. Oil spill detection by satellite remote sensing. *Remote Sens. Environ.* 95, 1–13.
- Bulgarelli, B., Djavidnia, S., 2012. On MODIS retrieval of oil spill spectral properties in the marine environment. *IEEE Geosci. Remote Sens. Lett.* 9 (3), 398–402.
- Camilli, R., Reddy, C.M., Yoerger, D.R., Van Mooy, B.A., Jakuba, M.V., Kinsey, J.C., McIntyre, C.P., Sylva, S.P., Maloney, J.V., 2010. Tracking hydrocarbon plume transport and biodegradation at Deepwater Horizon. *Science* 330, 201–204.
- Clark, R.N., Swayze, G.A., Leifer, I., Livo, K.E., Kokaly, R., Hoefen, T., Lumden, S., Eastwood, M., Green, R.O., Pearson, N., 2010. A method for quantitative mapping of thick oil spills using imaging spectroscopy. *US Geol. Surv. Open-File Rep.* 1167, 1–51.

- DiMarco, S.F., Nowlin Jr., W.D., Reid, R.O., 2005. A statistical description of the velocity fields from upper ocean drifters in the Gulf of Mexico. In: Sturges, W., Lugo-Fernandez, A. (Eds.), *Circulation in the Gulf of Mexico: Observations and Models*. Geophysical Monograph 161. American Geophysical Union, Washington, D.C., pp. 101–110 (347 pp.).
- ERCO (Energy Resources Co., Inc.), 1982. Ixtoc oil spill assessment. Final report. Executive summary. Report prepared for the Bureau of Land Management, AA851-CTO-71, Cambridge, MA (37 pp.).
- Farrington, J.W., 1983. NOAA Ship Researcher/Contract Vessel Pierce cruise to Ixtoc-1 oil spill: overview and integrative data assessment and interpretation. Report prepared for the Office of Marine Pollution Assessment, NOAA, NA80RAC0017.
- Fingas, M.F., Brown, C.E., 1997. Review of oil spill remote sensing. *Spill Sci. Technol. Bull.* 4, 199–208.
- Galt, J.A., 1981. Transport, distribution, and physical characteristics of the oil: part 1 – offshore movement and distribution. In: Hooper, C.H. (Ed.), *The Ixtoc I Oil Spill: The Federal Scientific Response*. NOAA Hazardous Materials Response Project, Boulder, Colorado, pp. 13–39.
- García-Pineda, O., MacDonald, I., Hu, C., Svejkský, J., Hess, M., Dukhovskoy, D., Morey, S., 2013. Detection of floating oil anomalies from the Deepwater Horizon oil spill with synthetic aperture radar. *Oceanography* 26 (2), 124–137.
- Gower, J., Hu, C., Borstad, G., King, S., 2006. Ocean color satellites show extensive lines of floating Sargassum in the Gulf of Mexico. *IEEE Trans. Geosci. Remote Sens.* 44, 3619–3625.
- Gundlach, E.R., Finkelstein, K.J., Sadd, J.L., 1981. Impact and persistence of Ixtoc I oil on the south Texas coast. *Int. Oil Spill Conf. Proc.* 477–485.
- Hardy, R.F., 2014. Assessments of surface-pelagic drift communities and behavior of early juvenile sea turtles in the northern Gulf of Mexico. MA thesis, University of South Florida (Publication No. 1569947).
- Hu, C., Müller-Karger, F.E., Taylor, C., Myhre, D., Murch, B., Odriozola, A.L., Godoy, G., 2003. MODIS detects oil spills in Lake Maracaibo, Venezuela. *EOS Trans. Am. Geophys. Union* 84, 313–319. <http://dx.doi.org/10.1029/2003EO330002>.
- Hu, C., Li, X., Pichel, W.G., Müller-Karger, F.E., 2009. Detection of natural oil slicks in the NW Gulf of Mexico using MODIS imagery. *Geophys. Res. Lett.* 36, L01604. <http://dx.doi.org/10.1029/2008GL036119>.
- Hu, C., Cannizzaro, J., Carder, K.L., Müller-Karger, F.E., Hardy, R., 2010. Remote detection of *Trichodesmium* blooms in optically complex coastal waters: examples with MODIS full-spectral data. *Remote Sens. Environ.* 114, 2048–2058.
- IMP (Instituto Mexicano del Petróleo), 1980. Informe de los trabajos realizados para el control del pozo Ixtoc I, el combate del derrame de petróleo y determinación de sus efectos sobre el ambiente marino. Programa Coordinado de Estudios Ecológicos en la Sonda de Campeche. Instituto Mexicano del Petróleo (242 pp.).
- Jackson, C., 2007. Internal wave detection using the Moderate Resolution Imaging Spectroradiometer (MODIS). *J. Geophys. Res.* 112, C11 (1978–2012).
- Jackson, C.R., Alpers, W., 2010. The role of the critical angle in brightness reversals on sunglint images of the sea surface. *J. Geophys. Res.* 115, C09019. <http://dx.doi.org/10.1029/2009JC006037>.
- Jernelöv, A., Liden, O., 1981. Ixtoc I: a case study of the world's largest oil spill. *Ambio* 10, 299–306.
- Klemas, V., 2010. Tracking oil slicks and predicting their trajectories using remote sensors and models: case studies of the sea princess and deepwater horizon oil spills. *J. Coast. Res.* 265, 789–797.
- Leifer, I., Lehr, W.J., Simecek-Beatty, D., Bradley, E., Clark, R., Dennison, P., Hu, Y., Matheson, S., Jones, C.E., Holt, B., Reif, M., Roberts, D.A., Svejkský, J., Swayze, G., Wozenraft, J., 2012. State of the art satellite and airborne marine oil spill remote sensing: application to the BP deepwater horizon oil spill. *Remote Sens. Environ.* 124, 185–209.
- MacDonald, I.R., Guinasso, N.L., Ackleson, S.G., Amos, J.F., Duckworth, R., Sassen, R., Brooks, J.M., 1993. Natural oil slicks in the Gulf of Mexico visible from space. *J. Geophys. Res.* 98 (C9), 16351–16364. <http://dx.doi.org/10.1029/93JC01289>.
- Morey, S.L., Zavala-Hidalgo, J., O'Brien, J.J., 2005. The seasonal variability of continental shelf circulation in the northern and western Gulf of Mexico from a high-resolution numerical model. In: Sturges, W., Lugo-Fernandez, A. (Eds.), *Circulation in the Gulf of Mexico: Observations and Models*. Geophysical Monograph 161. American Geophysical Union, Washington, D.C., pp. 203–218 (347 pp.).
- Ross, S.L., Ross, C.W., Lepine, F., Langtry, R.K., 1980. Ixtoc-I oil blowout. Proceedings of a Symposium on Preliminary Results From the September 1979 Researcher/Pierce Ixtoc-I Cruise, Key Biscayne, Florida, June 9–10, 1980, pp. 25–38 (591 pp.).
- Sun, S., Hu, C., Feng, L., Swayze, G., Holmes, J., Graettinger, G., MacDonald, I., Garcia, O., Leifer, I., 2015. (submitted for publication). Oil slick morphology derived from AVIRIS measurements of the Deepwater Horizon oil spill: implications for spatial resolution requirements of remote sensors. Unpublished results.
- Svejkský, J., Lehr, W., Muskat, J., Graettinger, G., Mullin, J., 2012. Operational utilization of aerial multispectral remote sensing during oil spill response. *Photogramm. Eng. Remote Sens.* 78, 1089–1102.
- Tunnell, J.W., 2010. Environmental impacts of marine oil spills: spatial, temporal, and historical lessons learned, or not? SAFGOF Oil Spill Symposium. Kotka Maritime Research Center, Kotka, Finland (16 Nov. 2010).
- Tunnell, J.W., 2011. Ixtoc I oil spill impacts, short-term and long-term. Gulf of Mexico Oil Disaster Symposium. National Council for Science and the Environment, Washington, DC (19 January 2011).
- Zavala-Hidalgo, J., Morey, S.L., O'Brien, J.J., 2003. Seasonal circulation on the western shelf of the Gulf of Mexico using a high-resolution numerical model. *J. Geophys. Res.* 108 (C12), 3389. <http://dx.doi.org/10.1029/2003JC001879>.

APPENDIX E:

REMOTE SENSING ASSESSMENT OF OIL SPILLS NEAR A DAMAGED PLATFORM IN THE GULF OF MEXICO

Sun, S., Hu, C., Garcia-Pineda, O., Kourafalou, V., Le Hénaff, M., and Androulidakis, Y. (2018). Remote sensing assessment of oil spills near a damaged platform in the Gulf of Mexico. *Marine Pollution Bulletin*, 136, 141-151, doi:10.1016/j.marpolbul.2018.09.004



Contents lists available at ScienceDirect

Marine Pollution Bulletin

journal homepage: www.elsevier.com/locate/marpolbul

Remote sensing assessment of oil spills near a damaged platform in the Gulf of Mexico



Shaojie Sun^a, Chuanmin Hu^{a,*}, Oscar Garcia-Pineda^b, Vassiliki Kourafalou^c,
Matthieu Le Hénaff^{d,e}, Yannis Androulidakis^c

^a College of Marine Science, University of South Florida, 140 Seventh Avenue South, St. Petersburg, FL 33701, USA

^b Water Mapping LLC, 3010 Coral Strip Parkway, Gulf Breeze, FL 32563, USA

^c Rosenstiel School of Marine and Atmospheric Science, University of Miami, 4600 Rickenbacker Causeway, Miami, FL 33149, USA

^d Cooperative Institute for Marine and Atmospheric Studies, University of Miami, 4600 Rickenbacker Causeway, Miami, FL 33149, USA

^e NOAA Atlantic Oceanographic and Meteorological Laboratory, 4301 Rickenbacker Causeway, Miami, FL 33149, USA

ARTICLE INFO

Keywords:

Oil spill
Optical remote sensing
Taylor Energy
MC-20
Gulf of Mexico
Hurricane

ABSTRACT

An oil platform in the Mississippi Canyon 20 (MC-20) site was damaged by Hurricane Ivan in September 2004. In this study, we use medium- to high-resolution (10–30 m) optical remote sensing imagery to systematically assess oil spills near this site for the period between 2004 and 2016. Image analysis detects no surface oil in 2004, but ~40% of the cloud-free images in 2005 show oil slicks, and this number increases to ~70% in 2006–2011, and > 80% since 2012. For all cloud-free images from 2005 through 2016 (including those without oil slicks), delineated oil slicks show an average oil coverage of 14.9 km²/image, with an estimated oil discharge rate of 48 to ~1700 barrels/day, and a cumulative oil-contaminated area of 1900 km² around the MC-20 site. Additional analysis suggests that the detected oil slick distribution can be largely explained by surface currents, winds, and density fronts.

1. Introduction

During Hurricane Ivan in September 2004, the oil platform and 25 of the 28 connected wells at the Taylor Energy's Mississippi Canyon 20 (MC-20) site, located in the northern Gulf of Mexico (GoM), were damaged and impacted. Subsequently, oil was found leaking, which was reported as the Taylor Energy oil spill or MC-20 oil spill (Herbst et al., 2016; Warren et al., 2014). Although mitigation efforts have taken place (including removal of the platform deck and subsea debris, decommissioning of the oil pipeline, and plugging 9 of the 25 impacted wells), there has been a continuous oil discharge from the platform site. Beginning in September 2014, over 7 months of near-daily aircraft overflights reported oil sheen observations, with an oil slick generally about 1.6 km wide and 9 km long, and an average oil coverage area of 20 km² (BSEE, 2017). The United States Bureau of Safety and Environmental Enforcement (BSEE) estimated that the oil discharge could continue for 100 years or more if left uncontrolled (BSEE, 2017). This crude oil spill from the MC-20 site is also documented in the National Response Center (NRC) reports (NRC, 2018), containing information like spill locations, spill materials, spill size, etc., with involved material documented as crude oil (NRC, 2018; NOAA, 2013). The NRC reports,

however, depend largely on unverified reporting from responsible parties (polluters) and third parties, and therefore its reported slick size information was found to be significantly underestimated (Danesghar Asl et al., 2016). Moreover, those traditional airborne and shipborne surveys are often too limited spatially and temporally to construct statistics about the discharged oil, as they often result in data gaps. Satellite remote sensing, which serves as a vital tool in response to oil spills (Leifer et al., 2012), provides frequently synoptic observations of the MC-20 oil locations over the entire spill period (since 2004) and may fill these data gaps in objectively assessing the oil spill near the MC-20 site.

The proximity of the MC-20 site to the Mississippi River Delta suggests that the oil slick extensions and fate are under the direct effect of the river plume dynamics, which play a significant role in the circulation around the Delta and over the broader Northern Gulf circulation (Walker et al., 2005; Schiller et al., 2011; Androulidakis and Kourafalou, 2013; Androulidakis et al., 2015). The brackish plume may either extend over the MC-20 site, forming a near-surface vertical barrier layer, or determine the oil transport pathways along the river-induced fronts. Based on satellite (remote sensing imagery) and field (drifters, ship-borne measurements) observations, Androulidakis et al.

* Corresponding author.

E-mail address: huc@usf.edu (C. Hu).

<https://doi.org/10.1016/j.marpolbul.2018.09.004>

Received 16 March 2018; Received in revised form 10 August 2018; Accepted 5 September 2018
0025-326X/© 2018 Published by Elsevier Ltd.

(2018) showed that the locations of the river's multiple fronts (outer and inner density fronts) are vital for the evolution and fate of the material at the sea surface that originates from the MC-20 site. The buoyancy-driven Mississippi plume waters generally reveal three major pathways where the Coriolis effect is important (Garvine and Monk, 1974; Kourafalou et al., 1996): an anticyclonic bulge around the Delta, a “downstream” coastal current toward the northwestern Gulf shelves, and an “upstream” current toward the northeastern shelves (Schiller et al., 2011; Zhang et al., 2012; Androulidakis et al., 2015). Although several other atmospheric (e.g. winds) and oceanic (e.g. local eddies, Loop Current) conditions determined the oil spill fate during the DeepWater Horizon (DWH) accident in 2010 (Walker et al., 2011; Le Hénaff et al., 2012), the river plume contribution was vital to the spreading of the hydrocarbons over the Gulf and especially around the Mississippi River Delta region (Kourafalou and Androulidakis, 2013). The use of remote sensing imagery benefits both the observation of oil slick dynamics over short-term (a few hours to a few consecutive days) and the long-term oil distribution frequency near the Mississippi River Delta region, enabling the study of river plume impacts on oil slick spreading in a region under strong influence of the Mississippi River plume. Despite sporadic field and airborne surveys, no comprehensive long-term picture currently exists regarding the oil spill near the MC-20 site. Therefore, there are two main goals in this study: first to geo-statistically analyze oil slicks using medium- to high-resolution (10–30 m) satellite imagery around the MC-20 site from September 2004 to December 2016; and to study how atmospheric and ocean conditions affect the oil slick distributions observed in remote sensing imagery in this region under strong river plume influence.

2. Data and methods

The MC-20 site is located approximately 17 km offshore from the Mississippi Delta in the GoM (Fig. 1). The location is in the frontal region of the Mississippi river plume, with associated wells at a water depth of 145 m. This MC-20 site is ~60 km away from the DWH (Macondo) blowout location (Fig. 1). The catastrophic explosion and sinking of the DWH oil platform on 20 April 2010 caused the second largest marine oil spill in history (McNutt et al., 2012; Murphy et al., 2016). The Macondo well emitted 3.19 million barrels of crude oil into the northern GoM (McNutt et al., 2012; U.S. v. BP et al., 2015) until the wellhead was finally capped on 15 July 2010.

In optical remote sensing imagery, the contrast between surface oil and non-oil water comes from two sources. The first is the sun glint effect, which enhances the contrast of the otherwise non-observable oil due to the wave-damping effect (Adamo et al., 2009; Hu et al., 2009; Macdonald et al., 1993; Sun and Hu, 2016). The same mechanism affects the Synthetic Aperture Radar (SAR) detection of oil at the ocean surface (Brekke and Solberg, 2005). Depending on the viewing geometry and wind, the oil-water contrast can be either positive or negative in the optical imagery (Hu et al., 2009; Jackson and Alpers, 2010; Lu et al., 2016). The second is the difference between optical properties of oil and water. Crude oil is characterized by high absorption in blue wavelengths (Byfield, 1998) where the increased thickness of oil correlates to decreased reflectance in blue waves (Lu et al., 2013a; Wetzel et al., 2009) until oil is too thick for light penetration (Lu et al., 2013b). When oil is emulsified, the water-in-oil emulsion causes strong scattering in the red, near infrared (NIR), and shortwave infrared (SWIR) wavelengths (Bulgarelli and Djavidnia, 2012; Clark et al., 2010; Svejksky et al., 2012). A combination of sun glint and optical properties of the oil-water contrast has been used to efficiently characterize oil spills in a marine environment (Bulgarelli and Djavidnia, 2012; Clark et al., 2010; Hu et al., 2009; Leifer et al., 2012; Lu et al., 2013b; Sun et al., 2015).

In this study, for oil slick delineation we mainly used optical remote sensing imagery from Landsat-5 Thematic Mapper (TM), Landsat-7 Enhanced Thematic Mapper Plus (ETM+), Landsat-8 Operational Land Imager (OLI), and Sentinel-2 MultiSpectral Instrument (MSI). Landsat sensors have a nominal resolution of 30 m while MSI has a nominal resolution of 10 m. Oil slicks from the DWH oil spill between April and July 2010 have been shown to reach the MC-20 region (Hu et al., 2011; MacDonald et al., 2015). To avoid confusion from the DWH oil spill, images collected in 2010 around the MC-20 site were not included in this study. Landsat imagery has a revisit time of 16 days alone (Table 1), and 8 days combined (TM with ETM+ in 2004–2011, and ETM+ with OLI in 2013–2016). A total of 513 medium- to high-resolution images (10–30 m) were explored, with 294 cloud-free images found in this region. A summary of the medium- to high-resolution optical imagery used in this study is shown in Tables 1 and 2. The average cloud-free images per year are 26 (excluding year 2004 since the oil spill started in September of that year), 15 of which were taken during favorable sun glint season in the GoM (April–September, from Hu et al., 2009; Sun and Hu, 2016). Thin oil sheens may not be efficiently detected under

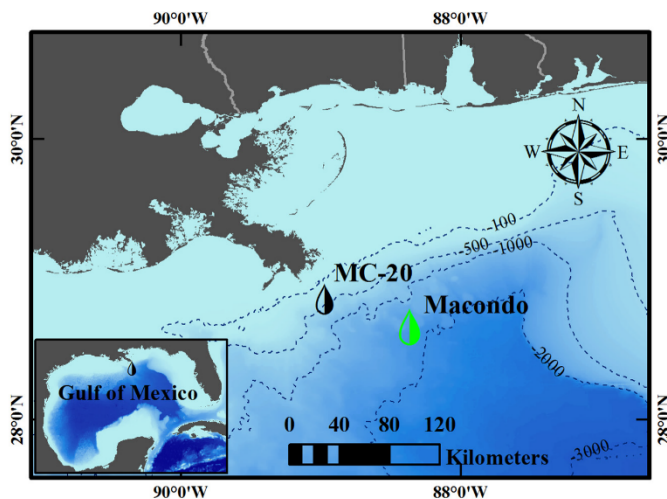


Fig. 1. The MC-20 site (black droplet top: latitude 28.94, longitude -88.97, which also applies to the following figures) is 17 km offshore of the Mississippi River Delta in the Gulf of Mexico (GoM) at a water depth of 145 m. The 2010 DeepWater Horizon (DWH) oil spill in the Macondo site (green droplet top: latitude 28.74, longitude -88.37) is ~60 km southeast of the MC-20 site with a water depth of ~1500 m. The background color in the GoM denotes the water depth, and major bathymetry contours (in units of meters) have been noted on the map.

Table 1
Characteristics of optical satellite sensors used for the oil spill assessment in the study.

Sensor	Data available (year)	Spatial resolution (m)	Spectral bands VIS-SWIR	Revisit time (days)
Landsat-5/TM	2004–2011	30	6	16
Landsat-7/ETM+	2004–2016	30 (Pan-15)	7	16
Landsat-8/OLI	2013–2016	30 (Pan-15)	9	16
Sentinel-2/MSI	2015–2016	10, 20, 60	13	10

weak glint conditions (Sun and Hu, 2016). Thick/emulsified oil may still be detected because of their different optical properties with respect to seawater (Wettle et al., 2009; Clark et al., 2010). These sampling frequencies (15 and 26 per year for sun glint images and cloud-free images) are comparable to and higher than the global average frequency of chlorophyll at a typical 1-km pixel from the Moderate Resolution Imaging Spectroradiometer (MODIS, every 20 days or 5%, see Feng and Hu, 2016). Therefore, we believe that the sampling frequency of oil slicks by those medium- to high-resolution imagery is statistical meaningful for assessing the oil spills near the MC-20 site.

MODIS imagery, although providing more frequent coverage (i.e., daily images), has a spatial resolution of 250 to 1000 m, which is too coarse to assess this moderate oil spill, for which the typical slick size ranges from 0 (100 m) to a few tens of kilometers. A statistical analysis during the DWH oil spill demonstrated that on average > 50% of 300-m pixels contain thick oil of < 6.6% of a 300-m pixel (Sun et al., 2016). For 1-km pixels, the sub-pixel percent cover is much lower than 1.0%. Thus, assessing the oil spill near the MC-20 region using MODIS imagery may fail to detect small slicks in oil presence/absence frequency analysis and add uncertainties in statistical analysis of oil slick area. However, occasionally large slicks (tens of kilometers in length and a few kilometers wide) under sun glint conditions can still be detected in MODIS imagery. Therefore, MODIS imagery was used in this study to detect the presence of oil slicks during the initial leaking stage of the spill when Landsat imagery failed to detect slicks in September–December 2004. Moreover, MODIS imagery was used in the analysis of short-term oil slick dynamics to enable more observations of the oil slicks in a few consecutive days. In addition, MODIS and Visible Infrared Imaging Radiometer Suite (VIIRS, 375 to 750 m in spatial resolution) chlorophyll concentration maps were also used to identify the river plume spreading in tandem with the detected oil slicks.

Finally, same day SAR imagery was used to cross-check with results from optical imagery analysis. SAR/optical imagery groups within two days were used with a numerical model and ocean color data to understand short-term dynamics of oil slicks near the MC-20 site.

TM, ETM+, OLI, and MSI Level-1 data were obtained from USGS/EarthExplorer, and then processed to Rayleigh-corrected Reflectance ($R_{rc}(\lambda)$, dimensionless) using the ACOLITE software (version V20161207.0). Red-Green-Blue composites were generated for visual inspection for all four sensors: OLI (R: 655, G: 561, B: 483 nm), ETM+ (R: 661, G: 561, B: 479 nm), TM (R: 660, G: 571, B: 486 nm) and MSI (R: 664, G: 560, B: 497 nm). Sun glint strength of the Landsat imagery was evaluated using sun glint coefficient (L_{GN} , in units of sr^{-1}), estimated with the Cox and Munk (1954) model, wind speed, and solar and satellite geometry. Wind speed was retrieved from the Reanalysis-2 wind speed product of the National Centers for Environmental Prediction

(NCEP). Solar and satellite geometry of Landsat was calculated using the “Landsat Angles Creation Tools” from USGS (<https://landsat.usgs.gov/solar-illumination-and-sensor-viewing-angle-coefficient-file>).

MODIS (on both Terra and Aqua) Level-0 data from September to December 2004 and 7–9 May 2015 were obtained from NASA Goddard Space Flight Center (GSFC) and processed to $R_{rc}(\lambda)$ using the SeaWiFS Data Analysis System (SeaDAS, version 7.3), and then resampled to 250 m spatial resolution using a sharpening scheme and mapped to an equidistant cylindrical projection. RGB composites were generated using the R_{rc} bands (R: 645, G: 555, B: 459 nm). Chlorophyll-a concentration Level-2 data from MODIS Aqua and VIIRS in 5–10 May 2015 were obtained from NASA/GSFC, and mapped to an equidistant cylindrical projection at 1 km spatial resolution.

SAR images used in this study were processed and analyzed as follows: First, a preliminary inspection of the SAR imagery was used to determine the overall ocean features. The texture of the image was evaluated to determine the wind conditions (Garcia-Pineda et al., 2008). When regions of very low wind speeds are present, ripple-free water and biogenic films create irregular, radar-dark regions that are difficult to distinguish from actual oil slicks. The SAR images used for this study were acquired under optimal wind conditions and the oil slick detected from the MC-20 site was clearly distinguishable. After initial inspection, a Textural Classifier Neural Network Algorithm (TCNNA) was applied to identify floating oil layers in a semi-supervised operation (Garcia-Pineda et al., 2008). The TCNNA is conditioned on a training set of SAR features of interest (i.e., floating oil) that previously have been identified by an operator over the natural hydrocarbon seep locations in the GoM (Garcia-Pineda et al., 2008, 2009). The final output of the TCNNA algorithm is a polygon that delineates the area of the slick. More details of the SAR processing can be found in Garcia-Pineda et al. (2008, 2009, 2010).

As mentioned above, oil slicks show spatial contrast from nearby water in optical remote sensing imagery because 1) oil has different optical properties from water and 2) oil can change the surface roughness, thus leading to redistribution of reflected light under sun glint conditions. In this study, oil slicks were identified as follows: 1) color stretched RGB images were visually inspected to detect spatial anomalies; 2) R_{rc} spectra from the anomalies were then diagnosed to rule out oil look-alikes (Hu et al., 2015). More details on the oil identification can be found in Sun et al. (2015). Then, for statistical analysis, the identified oil slicks were all counted for presence/absence in order to estimate oil appearance frequency. In this analysis, only slicks that follow the following rules were delineated and used in the areal statistical analysis: 1) slicks that originated from the MC-20 site and not blocked by clouds, which were treated as major slicks here; 2) smaller slicks near the major slicks. For example, in most cases, the major oil slicks originated from the MC-20 site and extended to one direction of the site (Fig. 2). In Fig. 2d, although the slicks indicated by the arrows can be inferred to be parts of major slicks originated from the MC-20 site, those slicks were only counted for the analysis of presence/absence frequency statistics; they were not delineated because an incomplete slick would not fit the purpose of areal statistical analysis. As a result, major slicks under cloud-free conditions (Fig. 2a and b), partially blocked by small clouds (Fig. 2c), and small slicks detached from major slick (Fig. 2b), were delineated manually using ArcMAP (version 10.3) software. ETM+ imagery suffers from scan line correction failure since 2003 (<https://landsat.usgs.gov/landsat-7>), causing line gaps (evenly

Table 2
Number of cloud-free (CF) images each year and the number of CF images in sun glint favorable period (April–September) in each year.

Year	2004	2005	2006	2007	2008	2009	2011	2012	2013	2014	2015	2016
# CF images	8	27	26	25	24	28	26	14	22	24	25	45
# CF images APR-SEPT	2	12	15	17	12	16	14	10	14	16	14	26

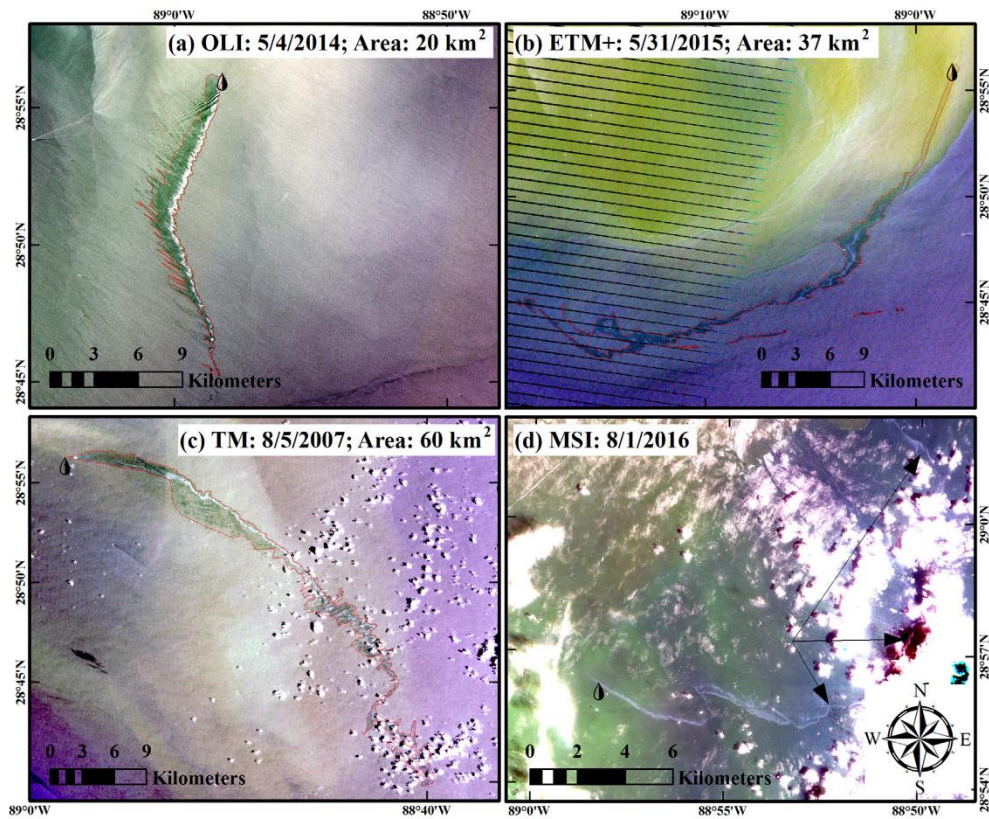


Fig. 2. Oil slicks captured by different sensors: a) OLI; b) ETM +; c) TM; d) MSI. They all appear to have originated from the MC-20 site, with different orientations. Delineated oil slick areas are annotated in (a)–(c). Oil slicks partially blocked by clouds, as shown in the example in (d), were not used for area estimates in this study.

distributed black lines in the left part of Fig. 2b) in all ETM + scenes since then. Fortunately, the MC-20 location is in the center of the image (Fig. 2b), where the image is least affected by this scan line correction off issue. When oil slicks extend long enough to reach these line gap regions, delineated oil slick polygons on both sides of the missing data line were manually re-connected if oil slicks were present on both sides, as shown in Fig. 2b. The swaths of Landsat imagery and Sentinel-2 MSI imagery are large enough to cover the slicks near the MC-20 site. Because only oil slicks originated from the MC-20 site were considered, the impact of natural oil seeps was minimized in this study.

Simulated fields of surface currents were used to describe the ocean circulation over the study region and compare it with the oil spreading detected by the satellites. The simulation was based on the Hybrid Coordinate Ocean Model (HYCOM; (<https://hycom.org/>), implemented at a $1/50^\circ$ (~ 1.8 km) resolution and 32 vertical levels over the GoM (GoM-HYCOM 1/50; Le Hénaff and Kourafalou, 2016). Based on a combination of various vertical coordinates (hybrid model), the HYCOM model is particularly suitable for regional domains with complex topography of wide shelves, steep slopes, and deep oceanic areas such as the GoM (Bleck, 2002; Chassignet et al., 2006; Kourafalou et al., 2009; Halliwell et al., 2009). The GoM-HYCOM 1/50 simulation employed here was forced at the surface by the NAVY Global Environmental Model (NAVEM, $1/2^\circ$ resolution at 3 hourly frequency), and benefited from realistic river representation. The simulated fields used in this study are part of a long-term simulation that assimilates

observations (based on an Ensemble Optimal Interpolation scheme) and provides publicly available daily forecast ocean fields of the GoM in a weekly basis operated by the Coastal and Shelf Modeling Group (University of Miami/RSMAS; <http://coastalmodeling.rsmas.miami.edu/>). GoM-HYCOM 1/50 uses daily river forcing for the 15 larger rivers in the U.S. part of the domain, including around the Mississippi Delta, while other rivers are represented with their monthly climatology. The river discharge data were obtained through the U.S. Geological Survey (<https://www.usgs.gov/>) and the Army Corps of Engineers. The high-resolution (~ 1.8 km) of the model in combination with the use of the updated river parameterization by Schiller and Kourafalou (2010), is adequate to efficiently resolve mesoscale and coastal processes around the Mississippi Delta (Le Hénaff and Kourafalou, 2016), where the oil source is located. The river plume dynamics and the formation of the accompanying strong density fronts, dominant over the region around the Mississippi, have been found relevant to the evolution of the shape and orientation of the oil patches during both short-term (a few hours after their formation) and long-term (pathways over a few days and fate) periods (Kourafalou and Androulidakis, 2013; Androulidakis et al., 2018).

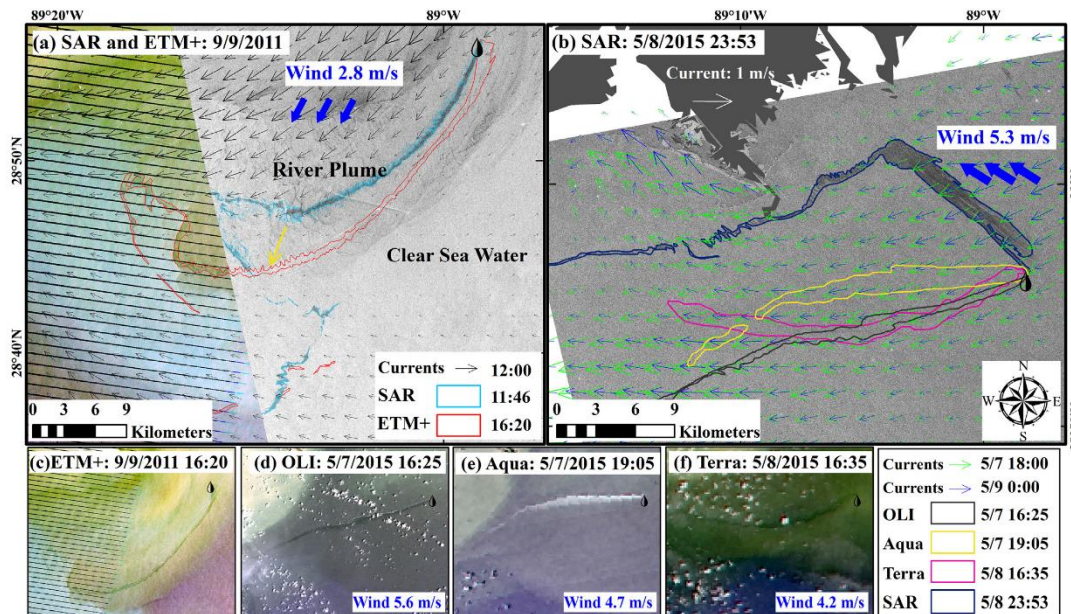


Fig. 3. a) Same day SAR (COSMO-SkyMed-4 collected on 9/9/2011, UTC 11:46, with spatial resolution of 30 m; Dark grey area indicates the River Plume and light grey area the clear sea water; Part of the slick tale was missing in the SAR image because of the image footprint limit) and ETM+ (9/9/2011, UTC 16:20, left part of the image and the entire slick captured by ETM+ was displayed in(c) with delineated oil slick). Four images of oil slicks captured by optical and SAR imagery in two consecutive days; b) SAR acquired by RADARSAT-2 (spatial resolution: 6 m) on 5/8/2015 UTC 23:53, with colored slicks representing those delineated from images in (d)–(f) (legend shown in the bottom right corner); d) OLI on 5/7/2015 UTC 16:25; e) MODIS/Aqua on 5/7/2015 UTC 19:05; and f) MODIS/Terra on 5/8/2015 UTC 16:35. The arrows in (a) and (b) indicate simulated surface current fields, where the current velocity scale in (b) applies to both (a) and (b). The thick blue arrows represent the mean wind direction, estimated between both images on panel a and between the last two images (16:35–23:53, 5/8/2015) in panel b. Wind direction does not change much between 5/7/2015 and 5/8/2015, with a standard deviation of 12.6° over the two days.

3. Results

3.1. Short-term dynamics

Taking advantage of occasions when distinct remote sensing observations of the oil slicks are available a few hours apart or over a few consecutive days, here we analyze the short-term dynamics of oil slicks, together with the wind conditions and the simulated current fields over the MC-20 region. Fig. 3a shows two images of the same slick, captured ~4.5 h apart by SAR and ETM+ on September 9, 2011. The slick on both images generally followed the modeled current directions. On Fig. 3a, the darker area represents the river plume area, while the lightest grey area is characterized by clear ocean waters; the simulated currents inside the plume follow the direction of the downstream river current (southwestward), while the currents over the open ocean were northwestward. The oil pathway in both satellite images is aligned with the river front, in agreement with observational findings by Androulidakis et al. (2018). The southern part of the slick (indicated by the yellow arrow in Fig. 3a) was observed to move ~5 km to the southwest during this time period. The modeled average current field (~0.1–0.3 m/s in a southwestward direction, Fig. 3a) alone cannot fully explain the movement. The wind, which had almost the same direction as the current, must have also contributed to the southwestward movement of the slick. With wind and current in different directions, the group of images during 7–8 May 2015 in Fig. 3b displayed the dominance of current and wind on slick movement at different periods. The oil slick was first captured by OLI to the southwest (7 May 2017 16:25; Fig. 3d). Over time it wandered north and south, as observed by

MODIS Aqua (7 May 2017 19:05; Fig. 3e), and Terra (8 May 2017 16:35; Fig. 3f), before heading northwest (8 May 2017 23:53; Fig. 3b blue highlighted). The modeled currents were mostly westward in May 7, with current direction agreeing well with the westward slicks. Current directions near the MC-20 site shows little change between May 7 and May 9, while the simulated currents field does indicate drastic decrease of magnitude in the site region (0.89 m/s at 18:00 May 7 to 0.39 m/s at 0:00 May 9). Both wind speed and direction showed little changes over the two days. However, the wind direction agreed well with the northward slick observed at 23:53 on May 8 (Fig. 3b), indicating apparent wind shift affecting the slick. Obviously, there is a shift, from surface currents to winds, of the driver of the displacement of the oil slicks between May 7 and May 9.

This shift of dominant forces is further revealed in sequential chlorophyll-a concentration from VIIRS and MODIS between 7–10 May 2015 (Fig. 4), which indicates an onshore shift of the river plume. On May 7 and 8, the river plume encompassed the MC-20 site (Fig. 4a and b). On May 9, the MC-20 site was on the outer edge south of the major plume region (Fig. 4c). This plume shift was further confirmed by the chlorophyll-a image on May 10 (Fig. 4d). The northward shift of the river front allowed the onshore propagation of the oil toward the Delta, visible on May 9 (Fig. 4c), in contrast to the previous days, when the front was over the oil source, leading the oil directly westward. However, even when shifted northward, the oil eventually reached a strong river-induced front and was directed westward along the downstream current in agreement with the observational study at the MC-20 site by Androulidakis et al. (2018). The evolution of the river plume determined the hydrocarbon pathways and can keep the oil away from the

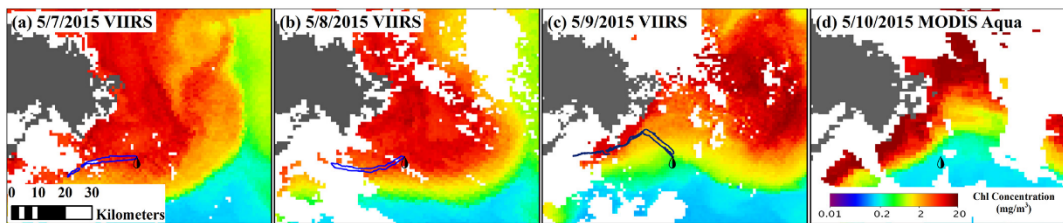


Fig. 4. Chlorophyll-a concentration in the Mississippi River Delta indicates river plume between 5/7/2015 and 5/10/2015. Oil slicks detected on 19:05 5/7/2015, 16:35 5/8/2015 and 23:53 5/8/2015 are added to (a), (b) and (c), respectively.

Delta, especially in cases where the outer river front is located north of the MC-20 site (Androulidakis et al., 2018); similar interactions were discussed for hydrocarbons released at the Macondo well during the DWH incident (Kourafalou and Androulidakis, 2013). Downwelling-favorable (i.e., southeasterly) winds may determine the location of the river front and then push the surface oil toward the front, where it can be trapped and then follow the prevailing upstream (northeastward) or downstream (westward) river current, as demonstrated in Fig. 4c.

3.2. Statistical analysis from 2004 to 2016

Observations from ETM+ in September–December 2004 (Fig. 5a) did not reveal any oil slicks, while < 50% of the cloud-free images in 2015 showed slicks. This percentage increased through 2007 (79%) and fluctuated from 2008 to 2011 (ranging from 57% to 93%). Since 2012, however, the percentage was relatively stable between 71 and 100%. Similar results were found from TM, OLI and MSI observations in the

same period: 0% in 2004, < 50% in 2005, 89% in 2006 and relatively stable since 2012 (> 90%) (Fig. 5b). Differences between ETM+ and other sensors also exist: 53% of the cloud-free ETM+ images in 2006 showed oil slicks while this percentage was as 89% for TM images in the same year; in 2008, 2009, 2011, the ratio of oil-presence to cloud-free images was 75%, 93% and 57% for ETM+, respectively, and was 67%, 64% and 83% for TM, respectively. Combining all sensors together, the ratio of oil-presence images to cloud-free images was 0% in 2004, ~40% in 2005, ~70% in 2006–2011 and > 80% since 2012 (most of the years showed > 90%, Table 3). Fig. 5c shows delineated slick areas from individual images from all sensors. For oil-presence images, the slick area ranged from 0.06 to 394 km², with an average oil coverage area of 19.0 km² and a median area of 7.6 km² after excluding those extremely large oil slicks (> mean + 2 * standard-deviation). For all cloud-free images combined, the average oil coverage area was estimated to be 14.9 km²/image between 2005 and 2016 (with 2010 excluded). From the size of delineated oil slicks, no clear trend has been

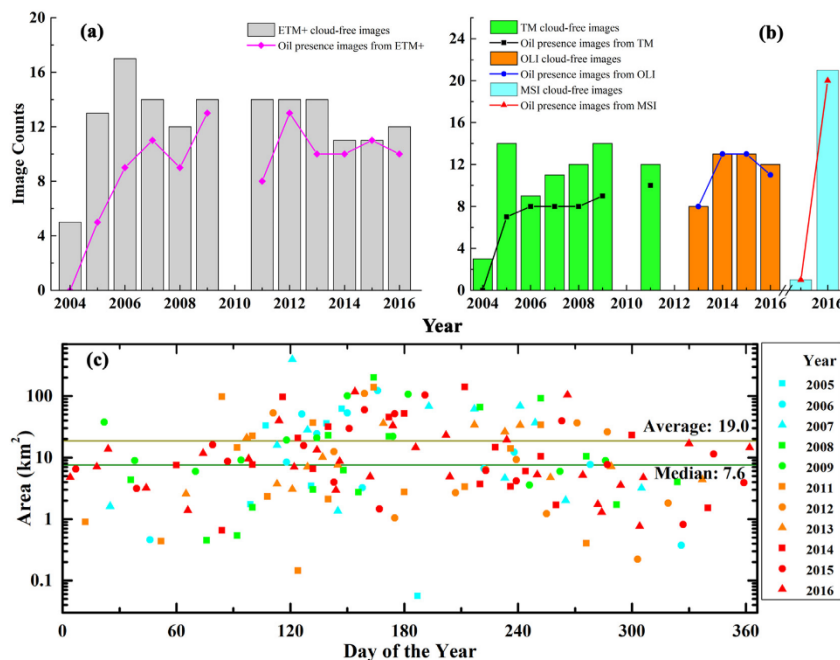


Fig. 5. Number of cloud-free images (vertical bars) and number of oil-presence images (lines) around the MC-20 site between 2004 and 2016 captured by a) ETM+ and b) TM, OLI, and MSI. c) Oil slick area from individual images of all sensors; The average and median area of slicks presented in the graph are for oil-presence images only, after excluding those extremely large oil slicks (> mean + 2 * standard-deviation).

Table 3
Percentage ratio of oil presence images to all cloud-free images (including those without sun glint) combining observations from all four sensors.

Year	2004	2005	2006	2007	2008	2009	2010	2011	2012	2013	2014	2015	2016
%	0	44	65	76	71	79	–	69	93	82	96	100	91

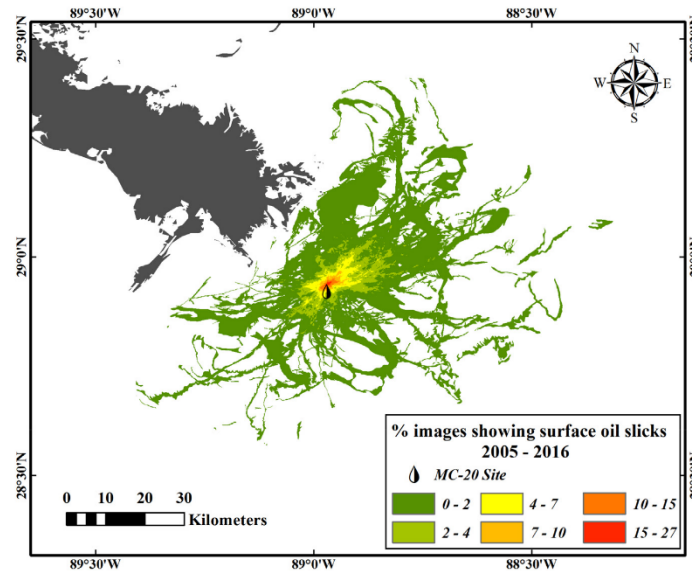


Fig. 6. Oil appearance frequency from all cloud-free images (including those without sun glint) in 2005–2016, which shows a cumulative area of 1888 km² near the MC-20 site. The appearance frequency ranges from 0.5% to 27% in this cumulative footprint map.

observed from 2005 to 2016. However, there is an obvious seasonal cycle: most of the large slicks (> 19 km²) were detected between April and September each year (Fig. 5c).

From all delineated oil slicks from 2005 through 2016, the cumulative oil footprint shown in Fig. 6 indicates that an area of ~1900 km² over the regions surrounding the Mississippi Delta has been contaminated by oil originated near the MC-20 site. Statistical results shows that 98% of the above polluted areas had oil pollution only occasionally (< 5% of cloud-free observations) while the more frequently oil polluted regions (> 20% of the cloud free observations) had an area of 0.17 km² surrounding the MC-20 site. Although the average oil slick size is 14.9 km²/image, because slicks are mostly narrow, elongated lines around the MC-20 site, only 0.17 km² around the site was covered by oil > 20% of the time. Indeed, this oil appearance frequency map (Fig. 6) is composed largely (> 50%) by oil slick size < 10 km² per image (Fig. 7a), while occasionally (8.6%) by oil slick size > 90 km² per image (Fig. 7a). This slick size frequency explains the more frequent coverage near the MC-20 site but lower frequent coverage away from the site.

The region with high-frequency oil presence (yellow to red in Fig. 6) displays a northeast-southwest pattern around the MC-20 site, which agrees well with the circulation patterns of the Mississippi River plume: an anticyclonic bulge around the Delta (where most oil has concentrated), with influence from the downstream westward current, and/or the northeastward upstream current (Schiller et al., 2011; Zhang et al., 2012; Androulidakis et al., 2015, 2018). The prevailing wind corresponding to all oil-presence images in Fig. 6, however, is to the west and northwest (Fig. 7b). This dominantly northeast-southwest oil coverage pattern suggests that the most frequent slick spreading

orientation is more likely dominated by the river plume induced currents (e.g. Fig. 3a, c–f) rather than directed by the winds. However, slicks derived from sequential images between May 7 and 8 in Fig. 3b indicate that wind can play a major role in the slick spreading near the MC-20 site when river front is located north of the MC-20 and the current is weak. Overall, the distribution of observed northeastward and westward oil slicks agrees well with the downstream westward current and northeastward upstream current of the Mississippi River plume, and the southeast extensions of the oil slicks are likely to be dominated by wind forces (Le Hénaff et al., 2012) or the offshore river plume extensions into the GoM which often occur due to regional ocean dynamics effects, such as the Loop Current and its frontal eddies (Liu et al., 2013; Androulidakis et al., 2018).

3.3. Imagery cross check

Landsat sensors' (TM with ETM+, ETM+ with OLI) image sensing time is offset in 8 days, thus there are no concurrent (i.e., same-day) measurements of the same location from these Landsat sensors. MSI, however, may sometimes sense the same location with OLI/ETM+ in the same day. For example, Fig. 8a and b show oil slicks captured on the same day by OLI and MSI, with a time difference of 15 min. The derived shape, location, distribution and area of oil slicks (38.7 km² vs 39.1 km²) agree well between each other. Fig. 8c and d show the same day ETM+ and SAR imagery over the same location with a time difference of 7.4 h. The detected oil slicks by both sensors, although both extending to the west, display large differences in location, slick shape and distribution. The derived slick areas are 5.6 km² from SAR while 8.1 km² from ETM+. Table 4 summarizes all the same-day image pairs

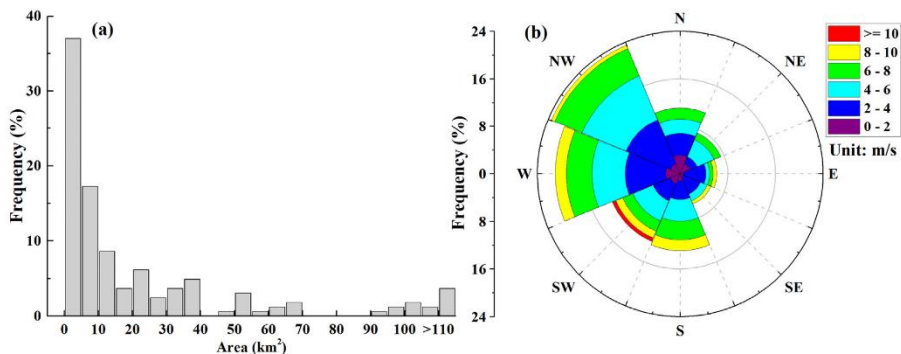


Fig. 7. (a) Area frequency of all delineated oil slicks per image, which include all slicks here contributing to the cumulative oil footprint map in 2005–2016 shown in Fig. 6. (b) Statistics of wind speeds and directions near the MC-20 site at the time of the same delineated slicks. Here the angular axis refers to the direction to which the wind is blowing, and the radial axis refers to the wind speed frequency of particular wind speed range. From the wind rose plot, dominant wind directions are to the west and northwest, and wind speeds are mostly 2–8 m/s for the delineated slicks.

that captured oil slicks over the MC-20 locations with time difference of 8 h or less. The SAR/ETM+ image pair on 9 Sept. 2011 have slick shape and orientation close to each other, though wider slick close to the MC-20 site has been observed in the ETM+ image after 4.5 h (Fig. 3a), which is reflected in the slick area change (8.6 km² in SAR vs 16.5 km² in ETM+) from the MC-20 site to the yellow arrow location in Fig. 3a.

There are also slicks for which the area drastically changed after 4.6 h, like the SAR/OLI image pair on 18 Jan. 2016. As described in Section 3.1, the short term dynamics of oil slicks can be affected by both wind and current conditions, and are strongly influenced by the Mississippi River plume dynamics. Here we use an Unbiased Mean Relative Error (UMRE) to estimate the relative error the delineated slick area in

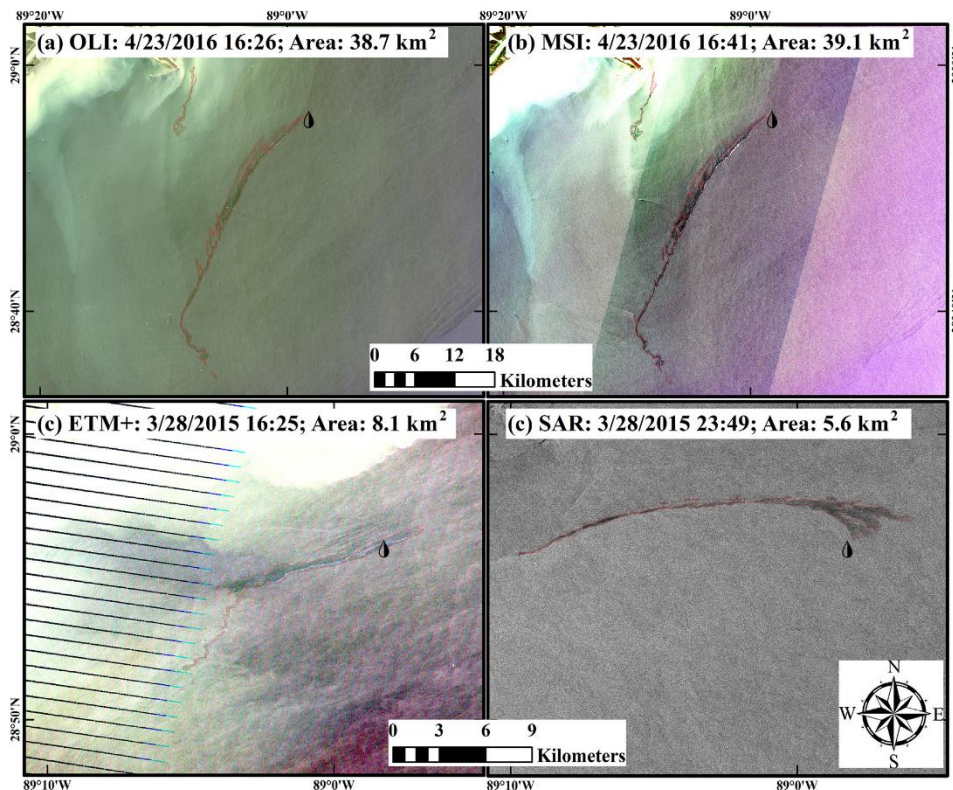


Fig. 8. Examples of oil slick size estimation using same-day image pairs captured by (a) OLI with (b) MSI, and (c) ETM+ with (d) SAR from Radarsat-2.

Table 4

Same-day image pairs between optical sensors and optical/SAR sensors over the MC-20 area. SAR1 is from COSMO-SkyMed-4 with spatial resolution of 30 m, SAR2 from Radarsat-2 with spatial resolution of 6 m, and SAR3 from Sentinel-1A with spatial resolution of 10 m. Note that in the 9/9/2011 image pair, area of the slick part from the MC-20 site to the yellow arrow location in Fig. 3a that captured by both the SAR and ETM+ images was compared in the table.

Sensor 1	Date	Time	Area (km ²)	Sensor 2	Date	Time	Area (km ²)
SAR1	9/9/2011	11:46	8.6	ETM+	9/9/2011	16:20	16.5
SAR2	3/28/2015	23:49	5.6	ETM+	3/28/2015	16:25	8.1
MSI	12/25/2015	16:41	3.7	ETM+	12/25/2015	16:27	2.2
SAR3	1/18/2016	11:49	1.2	OLI	1/18/2016	16:26	6.9
MSI	4/23/2016	16:41	39.1	OLI	4/23/2016	16:26	38.7
MSI	9/30/2016	16:46	4.9	OLI	9/30/2016	16:26	6.0

Table 4, as either of the areas from the two datasets may contain uncertainties:

$$UMRE = \frac{1}{n} \sum_{i=1}^n \left| \frac{x_i - y_i}{0.5x_i + 0.5y_i} \right| \quad (1)$$

where x_i , y_i are the areas of the delineated oil slicks from the two images of the image pair, respectively. The calculated area UMRE is 52.3%, which represents the relative difference of oil slick area caused by oil interpretation uncertainties (i.e., interpretation difference between different sensors) and slick short-term dynamics by the current/wind (as shown in Section 3.1). Because the imaging time as well as observation geometry vary largely among different sensors, these results from the same-day image pairs represent the best estimates of the relative error in oil slick area.

4. Discussions

4.1. Uncertainties

The accuracy of slick size detection through optical imagery relies on sun glint strength. The MSI/OLI pairs on 23 Apr. 2016 and 30 Sept. 2016 agree well in slick distribution and slick areas because all images contain strong sun glint. On the other hand, the slick area detected by ETM+ on 25 Dec. 2015 is significantly lower than the slick area detected by MSI on the same day, partly because of the very low sun glint strength of the two images ($< 10^{-5} \text{sr}^{-1}$) and partly because of the lower signal-to-noise ratio of ETM+ compared to MSI. Those oil features not captured by the ETM+ image are thin oil, which displays little contrast under very weak sun glint conditions. Therefore, only when sun glint is strong enough can the detection be regarded as accurate. The sun glint strength (L_{GN}) of all cloud-free optical images was estimated and partitioned into two groups for images with and without oil detected. The median value of L_{GN} for the first group ($1.6 \times 10^{-3} \text{sr}^{-1}$) was found to be about two orders of magnitude higher than for the second group ($2.2 \times 10^{-5} \text{sr}^{-1}$). The images of the first group were mainly from April to September where sun glint strength is higher than in October through March, when most images of the second group were collected. Similarly, images collected between April and September contributed to only 15% of the oil-absence images, but they contributed to 70% of the oil-presence images. Such a seasonality can also be visualized clearly in the slick area plot in Fig. 5c, with average delineated slick area per image to be 23.8 km² from April to September (from 107 oil presence images), but 8.4 km² from October to March (from 49 oil presence images). Since there is no reason, to our knowledge, why the

oil discharge should change seasonally, we can only assume this is most likely due to the seasonality of sun glint strength. For this reason, the oil presence and footprint estimates are likely biased low.

It is interesting to see that none of the 2004 images between September and December showed oil slicks, possibly due to the same reason as above: most images collected during this period did not show significant sun glint. Indeed, a cloud-free MODIS/Terra image on 28 September 2004 did show oil slicks around the MC-20 site because MODIS could provide much more frequent observations than those medium- to high-resolution sensors. Nevertheless, the many available medium- to high-resolution images from multiple sensors since 2005 should lead to statistically meaningful results even though there may exist systematic biases due to seasonality in oil slick detection, which suggests that the inter-annual changes and long-term trend should be realistic.

4.2. Oil discharge volume

Airborne measurements and cruise surveys reported crude oil featured slicks near the MC-20 site, ranging from oil sheens to oil emulsions as thick as 1–2 mm (BSEE, 2017; Garcia-Pineda, 2016; Herbst et al., 2016; Jones and Holt, 2018). In optical remote sensing imagery, oil emulsions show elevated reflectance in the NIR-SWIR wavelengths (Clark et al., 2010; Sun et al., 2018). The reflectance contrast (relative to water) of the delineated oil slick at ~1600 nm (1609 nm for OLI and 1614 nm for MSI) was inspected, yet no oil emulsions were found in any cloud-free images used in this study (Table 1). This does not suggest that oil emulsions did not occur; an oil emulsion patch could be too small to be captured by the relatively large pixels ($30 \times 30 \text{m}^2$ for OLI and $20 \times 20 \text{m}^2$ for MSI SWIR bands). On the other hand, even if the size of the thick emulsion is much smaller than a pixel size, (i.e., $30 \times 30 \text{m}^2$ for OLI), the oil slick (including both thin oil and thick emulsion) can still be larger than a pixel. A rule of thumb has been used in the past, in which thick oil occupies only 10% of the oil slick area, while 90% of the area is composed of thin oil sheens (NOAA, 2016). A recent study from the DWH oil spill (Sun et al., 2016) showed that thick oil ($> 200 \mu\text{m}$) occupied only 5% of the total area covered by thicker than sheen oil slicks. Statistical analysis of the delineated slicks from the present study shows that 92% of the slicks have an area $> 1 \text{km}^2$ (Fig. 5c), which corresponds to > 1100 Landsat pixels ($30 \times 30 \text{m}^2$). Moreover, same-day image pair of OLI (30 m resolution) and MSI (10 m resolution) images (time difference of 15 min, Fig. 8a and b) do not show large differences in the delineated oil slick area. Based on the analysis above, we are confident that the 30-m spatial resolution used here is sufficient for oil slick detection in the MC-20 region.

The question then becomes whether the oil discharge volume can be estimated from these observations. Here we attempted this challenge using field measurements and empirical values published in the literature. Specifically: 1) Various oil thicknesses have been reported from cruise surveys, ranging from rainbow sheens, to dark fresh oil, and thick emulsions (Herbst et al., 2016; Garcia-Pineda, 2016). Several oil thickness-color codes have been developed to visually estimate oil thicknesses based on oil's color appearance, including the Bonn Agreement Oil Appearance Code (2017) and American Society of Test Materials (ASTM F2534-17, 2017) code. The ASTM code is widely used as a guide in oil spill responses, providing information criteria for estimating oil thicknesses using visual clues, but the ASTM guide is only applicable to thin sheens up to about $3 \mu\text{m}$ (see ASTM F2534-17, 2017). In this study, we used the oil thickness table from the Bonn Agreement (2017) and NOAA (2016), which distinguishes thick and thin oil in appearance and gives thickness ranges for both thick and thin oil. The Bonn Agreement code has been widely used in recent studies (Leifer et al., 2012; Jones and Holt, 2018; Svejkovsky et al., 2016) and in industrial oil spill responses (IPIECA-IOPG, 2015). NOAA (2016) has adapted the Bonn Agreement (2017) code with slight differences in oil "Sheens" category, now corresponding to oil thicknesses up to $5 \mu\text{m}$. In

Table 5
Input parameters to Eq. (2) and the calculated daily oil discharge rate.

	Area (km ² / day)	Sheens- thickness (μm)	Metallic- thickness (μm)	Residence- time (hours)	V _d (m ³ / day)	V _d (US barrels/ day)
Lower Bound	7.1	0.04	5	6.4	7.7	48
Upper Bound	22.7	5	50	14.4	274.1	1724

this study, we adopt the thickness ranges from NOAA (2016) category of “Sheens” for thin oil and “Metallic” for thick oil. “Sheens” is in the range of 0.04–5 μm with grey/silver to rainbow-appearance while thicker than sheens “Metallic” oil (reflect the color of the sky but with some element of oil color) is in the range of 5–50 μm (NOAA, 2016). 2) A ratio of thick to thin oil of 5:95 from a previous study on the DWH oil spill (Sun et al., 2016) was adopted for thickness estimation in this study; 3) From a hindcast model based on various wind and current conditions over the natural hydrocarbon seeps around the Green Canyon 600 lease block in the northern GoM, average slick surface residence-time was estimated to be 6.4 h while slicks of > 10 km in length had an average surface residence-time of 14.4 h (Daneshgar Asl et al., 2017). The two residence times here were assumed to be applicable to oil slicks around the MC-20 site on the lower and upper bounds of the average oil footprint size per day: 14.9 * (1 ± 0.523) km², where the relative uncertainty term in the parenthesis came from the same-day cross-check between image pairs. Then, assuming dynamic balance and continuous oil release, the daily oil discharge rate (V_d) was estimated as:

$$V_d = \text{Area} \times (5\% \times \text{Metallic} - \text{Thickness} + 95\% \times \text{Sheen} - \text{Thickness}) \times 24 \text{ h} / (\text{Residence} - \text{Time} - \text{in-hours}) \quad (2)$$

The inputs to Eq. (2) are listed in Table 5. After converting to US barrels, the calculated average V_d is in the range of 48–1724 barrels/day. Given the factors impacting the oil detection accuracy (due to lack of strong sun glint half of the year), this range is likely to be biased low. The same can be said for the cumulative oil footprint and average oil slick size. Therefore, the average daily oil discharge ranging from 48 to ~1700 US barrels per day represents a conservative estimate if all assumptions used in the calculation are reasonable.

5. Conclusions

Using optical remote sensing imagery from Landsat TM, ETM+, OLI and Sentinel-2A MSI, oil slicks around the MC-20 well site in the northern Gulf of Mexico were objectively assessed for the first time after the hurricane-induced damage of the oil platform and wells in September 2004. The results show that the percentage of cloud-free images containing oil slicks around the MC-20 site has increased from ~40% in 2005, ~70% in 2006–2011, to > 80% since 2012, suggesting an increase in oil discharge in recent years. From 2005 to 2016, about 14.9 km² of the area surrounding the MC-20 site is covered by oil on an average day, with a cumulative oil footprint of ~1900 km² and an estimated daily discharge volume ranging from 48 to ~1700 barrels.

Having observations in the same day (or a few consecutive days from different sensors) improves the understanding of oil slick movement over short temporal periods, especially in this region influenced by a large river plume. For the most part, oil slick distribution agrees well with circulation patterns that are largely controlled by the Mississippi River plume, but can also be affected by direct wind forcing. The locations of the river induced fronts with respect to the oil source also contribute to both onshore propagation and longer-term pathways of the hydrocarbons. Moreover, wind forces may dominate the oil spreading process when the Mississippi River plume does not encompass the MC-20 site.

Acknowledgments

This study was made possible in part by the BP/Gulf of Mexico Research Initiative (awards GOMA 23160700 and C-IMAGE II) and in part by a NASA Earth and Space Science Fellowship (NESSF, grant NNX16AN95H). Data are publicly available through the Gulf of Mexico Research Initiative Information & Data Cooperative (GRIIDC) at <https://data.gulfresearchinitiative.org> (doi: <https://doi.org/10.7266/N7M9072W>). We thank the USGS for providing Landsat data, which are openly accessible from <https://earthexplorer.usgs.gov/>, NOAA for providing NCEP wind data, which are openly accessible from <https://www.esrl.noaa.gov/psd/data/gridded/data.ncep.reanalysis2.html>, ESA for providing Sentinel-2 MSI data, which are openly accessible from <https://scihub.copernicus.eu>, and NASA for providing MODIS and chlorophyll-a concentration data, which are openly accessible from <https://oceancolor.gsfc.nasa.gov/>. M. Le Hénaff acknowledges partial support from the Physical Oceanography Division at NOAA's Atlantic Oceanographic and Meteorological Laboratory, AOML. We thank Dr. HeeSook Kang for preparing the current model fields, and we acknowledge the help from Brock Murch (University of South Florida) to improve the presentation of the manuscript. Three anonymous reviewers also provided comments to help improve the manuscript.

References

- Adamo, M., De Carolis, G., De Pasquale, V., Pasquariello, G., 2009. Detection and tracking of oil slicks on sun-glittered visible and near infrared satellite imagery. *Int. J. Remote Sens.* 30 (24), 6403–6427. <https://doi.org/10.1080/01431160902865772>.
- Androulidakis, Y.S., Kourafalou, V.H., 2013. On the processes that influence the transport and fate of Mississippi waters under flooding outflow conditions. *Ocean Dyn.* 63 (2–3), 143–164.
- Androulidakis, Y.S., Kourafalou, V.H., Schiller, R.V., 2015. Process studies on the evolution of the Mississippi River plume: impact of topography, wind and discharge conditions. *Cont. Shelf Res.* 107, 33–49.
- Androulidakis, Y., Kourafalou, V.H., Özgökmen, T., Garcia-Pineda, O., Lund, B., Le Hénaff, M., Hu, C., Haus, B.K., Novelli, G., Guigand, C., Kang, H., Hole, L., Horstmann, J., 2018. Influence of river induced fronts on hydrocarbon transport: a multi-platform observational study. *J. Geophys. Res. Oceans* 123, 3259–3285.
- ASTM F2534-17, 2017. Standard Guide for Visually Estimating Oil Spill Thickness on Water. ASTM International, West Conshohocken, PA. www.astm.org.
- Bleck, R., 2002. An oceanic general circulation model framed in hybrid isopycnic-Cartesian coordinates. *Ocean Model* 4, 55–88.
- Bonn Agreement, 2017. Bonn agreement aerial operations handbook. Publication of the Bonn Agreement, April 2016. Retrieved on July 24, 2018 from https://www.bonnagreement.org/site/assets/files/17600/aoh_part_iii_guidelines_detection_investigation_evaluation.pdf.
- Brekke, C., Solberg, A.H.S., 2005. Oil spill detection by satellite remote sensing. *Remote Sens. Environ.* 95 (1), 1–13. <https://doi.org/10.1016/j.rse.2004.11.015>.
- Bulgarelli, B., Djavidnia, S., 2012. On MODIS retrieval of oil spill spectral properties in the marine environment. *IEEE Geosci. Remote Sens. Lett.* 9 (3), 398–402. <https://doi.org/10.1109/LGRS.2011.2169647>.
- Bureau of Safety and Environmental Enforcement, 2017. Taylor Energy oil discharge at MC-20 site and ongoing response efforts. Retrieved June 30, 2017 from <https://www.bsee.gov/newsroom/library/incident-archive/taylor-energy-mississippi-canyon/ongoing-response-efforts>.
- Byfield, V., 1998. Optical Remote Sensing of Oil in the Marine Environment (Doctoral dissertation). University of Southampton.
- Chassignet, E.P., Hurlburt, H.E., Smedstad, O.M., Halliwell, G.R., Wallcraft, A.J., Metzger, E.J., Blanton, B.O., Lozano, C., Rao, D.B., Hogan, P.J., Srinivasan, A., 2006. Generalized vertical coordinates for eddy-resolving global and coastal ocean forecasts. *Oceanography* 19 (1), 118–129. <https://doi.org/10.5670/oceanog.2006.95>.
- Clark, R.N., Swayze, G.A., Leifer, L., Livo, K.E., Kokaly, R., Hoefen, T., Lundeen, S., Eastwood, M., Green, R.O., Pearson, N., 2010. A method for quantitative mapping of thick oil spills using imaging spectroscopy. In: US Geological Survey Open-File Report. vol. 1167, pp. 1–51.
- Cox, C., Munk, W., 1954. Measurement of the roughness of the sea surface from photographs of the sun's glitter. *J. Opt. Soc. Am.* 44 (11), 838–850. <https://doi.org/10.1364/JOSA.44.000838>.
- Daneshgar Asl, S., Amos, J., Woods, P., Garcia-Pineda, O., MacDonald, I.R., 2016. Chronic, anthropogenic hydrocarbon discharges in the Gulf of Mexico. *Deep-Sea Res. II Top. Stud. Oceanogr.* 129, 187–195.
- Daneshgar Asl, S., Dukhovskoy, D.S., Bourassa, M., MacDonald, I.R., 2017. Hindcast modeling of oil slick persistence from natural seeps. *Remote Sens. Environ.* 189, 96–107. <https://doi.org/10.1016/j.rse.2016.11.003>.
- Feng, L., Hu, C., 2016. Comparison of valid ocean observations between MODIS Terra and Aqua over the global oceans. *IEEE Trans. Geosci. Remote Sens.* 54, 1575–1585.
- Garcia-Pineda, O., 2016. Taylor. Retrieved March 6, 2018 from <https://www.youtube.com/watch?v=RlaAX0G3IU>.

- Garcia-Pineda, O., MacDonald, I., Zimmer, B., 2008. Synthetic aperture radar image processing using the supervised textural-neural network classification algorithm. In: Paper presented at IGARSS 2008, IEEE International Geoscience and Remote Sensing Symposium, 7–11 July 2008.
- Garcia-Pineda, O., Zimmer, B., Howard, M., Pichel, W., Li, X., MacDonald, I.R., 2009. Using SAR images to delineate ocean oil slicks with a texture-classifying neural network algorithm (TCNNA). *Can. J. Remote. Sens.* 35 (5), 411–421. <https://doi.org/10.5589/m09-035>.
- Garcia-Pineda, O., MacDonald, I., Zimmer, B., Shedd, B., Roberts, H., 2010. Remote-sensing evaluation of geophysical anomaly sites in the outer continental slope, northern Gulf of Mexico. *Deep-Sea Res. II Top. Stud. Oceanogr.* 57 (21–23), 1859–1869. <https://doi.org/10.1016/j.dsr2.2010.05.005>.
- Garvine, R.W., Monk, J.D., 1974. Frontal structure of a river plume. *J. Geophys. Res.* 79 (15), 2251–2259.
- Halliwel, G.R., Barth, A., Weisberg, R.H., Hogan, P.J., Smedstad, O.M., Cummings, J., 2009. Impact of GODAE products on nested HYCOM simulations of the West Florida Shelf. *Ocean Dyn.* 59, 139–155. <https://doi.org/10.1007/s10236-008-0173-2>.
- Herbst, L., DeCola, E., Kennedy, K., 2016. New pathways for developing and testing oil spill response equipment in real world conditions. In: Paper Presented at OCEANS 2016 MTS/IEEE, Monterey, CA, 19–23 Sept. 2016.
- Hu, C., Li, X., Pichel, W.G., Muller-Karger, F.E., 2009. Detection of natural oil slicks in the NW Gulf of Mexico using MODIS imagery. *Geophys. Res. Lett.* 36 (1). <https://doi.org/10.1029/2008gl036119>.
- Hu, C., Weisberg, R.H., Liu, Y., Zheng, L., Daly, K., English, D., Zhao, J., Vargo, G., 2011. Did the northeastern Gulf of Mexico become greener after the Deepwater Horizon oil spill? *Geophys. Res. Lett.* 38, L09601. <https://doi.org/10.1029/2011GL047184>.
- Hu, C., Feng, L., Hardy, R.F., Hochberg, E.J., 2015. Spectral and spatial requirements of remote measurements of pelagic *Sargassum* macroalgae. *Remote Sens. Environ.* 167, 229–246. <https://doi.org/10.1016/j.rse.2015.05.022>.
- IPIECA-IOGP, 2015. Aerial observation of oil spills at sea. London, February 2015: IPIECA-IOGP. Retrieved from <http://www.ipecta.org/resources/good-practice/aerial-observation-of-oil-spills-at-sea/>.
- Jackson, C.R., Alpers, W., 2010. The role of the critical angle in brightness reversals on sunglint images of the sea surface. *J. Geophys. Res.* 115 (C9). <https://doi.org/10.1029/2009jc006037>.
- Jones, C.E., Holt, B., 2018. Experimental L-band airborne SAR for oil spill response at sea and in coastal waters. *Sensors* 18 (2), 641. <https://doi.org/10.3390/s18020641>.
- Kourafalou, V.H., Androulidakis, Y.S., 2013. Influence of Mississippi River induced circulation on the Deepwater Horizon oil spill transport. *J. Geophys. Res. Oceans* 118 (8), 3823–3842.
- Kourafalou, V.H., Oey, L.-Y., Wang, J.D., Lee, T.N., 1996. The fate of river discharge on the continental shelf. Part I: modeling the river plume and the inner-shelf coastal current. *J. Geophys. Res. Oceans* 101 (C2), 3415–3434. <https://doi.org/10.1029/95JC03024>.
- Kourafalou, V.H., Peng, G., Kang, H., Hogan, P.J., Smedstad, O.M., Weisberg, R.H., 2009. Evaluation of global ocean data assimilation experiment products on South Florida nested simulations with the hybrid coordinate ocean model. *Ocean Dyn.* 59 (1), 47–66. <https://doi.org/10.1007/s10236-008-0160-7>.
- Le Hénaff, M., Kourafalou, V.H., 2016. Mississippi waters reaching South Florida reefs under no flood conditions: synthesis of observing and modeling system findings. *Ocean Dyn.* 66 (3), 435–459.
- Le Hénaff, M., Kourafalou, V.H., Paris, C.B., Helgers, J., Hogan, P.J., Srinivasan, A., 2012. Surface evolution of the Deepwater Horizon oil spill: combined effects of circulation and wind induced drift. *Environ. Sci. Technol.* 46, 7267–7273. <https://doi.org/10.1021/es301570w>.
- Leifer, I., Lehr, W.J., Simecek-Beatty, D., Bradley, E., Clark, R., Dennison, P., Hu, Y., Matheson, S., Jones, C.E., Holt, B., Reif, M., Roberts, D.A., Svejksky, J., Swayze, G., Wozencraft, J., 2012. State of the art satellite and airborne marine oil spill remote sensing: application to the BP Deepwater Horizon oil spill. *Remote Sens. Environ.* 124 (0), 185–209. <https://doi.org/10.1016/j.rse.2012.03.024>.
- Liu, Y., Weisberg, R.H., Hu, C., Kovach, C.C., Riethmüller, R.R., 2013. Evolution of the Loop Current system during the Deepwater Horizon oil spill event as observed with drifters and satellites. In: Liu, Y., MacFadyen, A., Ji, Z., Weisberg, R.H. (Eds.), *Monitoring and modeling the Deepwater Horizon oil spill: a record-breaking enterprise*, pp. 91–101.
- Lu, Y., Li, X., Tian, Q., Zheng, G., Sun, S., Liu, Y., Yang, Q., 2013a. Progress in marine oil spill optical remote sensing: detected targets, spectral response characteristics, and theories. *Mar. Geod.* 36 (3), 334–346. <https://doi.org/10.1080/01490419.2013.793633>.
- Lu, Y., Tian, Q., Wang, X., Zheng, G., Li, X., 2013b. Determining oil slick thickness using hyperspectral remote sensing in the Bohai Sea of China. *Int. J. Digital Earth* 6, 76–93.
- Lu, Y., Sun, S., Zhang, M., Murch, B., Hu, C., 2016. Refinement of the critical angle calculation for the contrast reversal of oil slicks under sunglint. *J. Geophys. Res. Oceans* 121 (1), 148–161. <https://doi.org/10.1002/2015jc011001>.
- Macdonald, I.R., Guinasso, N.L., Ackleson, S.G., Amos, J.F., Duckworth, R., Sassen, R., Brooks, J.M., 1993. Natural oil slicks in the Gulf of Mexico visible from space. *J. Geophys. Res.* 98 (C9), 16351. <https://doi.org/10.1029/93jc01289>.
- MacDonald, I.R., et al., 2015. Natural and unnatural oil slicks in the Gulf of Mexico. *J. Geophys. Res. Oceans* 120 (12), 8364–8380. <https://doi.org/10.1002/2015JC011062>.
- McNutt, M.K., Camilli, R., Crone, T.J., Guthrie, G.D., Hsieh, P.A., Ryerson, T.B., Savas, O., Shaffer, F., 2012. Review of flow rate estimates of the Deepwater Horizon oil spill. *Proc. Natl. Acad. Sci.* 109 (50), 20260–20267. <https://doi.org/10.1073/pnas.1112139108>.
- Murphy, D., Gemmill, B., Vaccari, L., Li, C., Bacosa, H., Evans, M., Gemmill, C., Harvey, T., Jalali, M., Niepa, T.H., 2016. An in-depth survey of the oil spill literature since 1968: long term trends and changes since Deepwater Horizon. *Mar. Pollut. Bull.* 113, 371–379.
- National Response Center, 2018. Oil spill, chemical release or maritime security incident report. Retrieved July 17, 2018 from <http://www.nrc.uscg.mil>.
- NOAA, 2013. Taylor Energy platform “Saratoga”. In: National Oceanic and Atmospheric Administration Incident News. Retrieved on 9 August 2018 from <https://incidentnews.noaa.gov/incident/8634>.
- NOAA, 2016. Open Water Oil Identification Job Aid for Aerial Observation. With Standardized Oil Slick Appearance and Structure Nomenclature and Codes. NOAA Office of Response and Restoration, Emergency Response Division, Seattle, Washington, pp. 1–51. Retrieved from https://response.restoration.noaa.gov/sites/default/files/OWJA_2016.pdf.
- Schiller, R.V., Kourafalou, V.H., 2010. Modeling river plume dynamics with the HYbrid Coordinate Ocean Model. *Ocean Model* 33 (1–2), 101–117.
- Schiller, R.V., Kourafalou, V.H., Hogan, P., Walker, N.D., 2011. The dynamics of the Mississippi River plume: impact of topography, wind and offshore forcing on the fate of plume waters. *J. Geophys. Res. Oceans* 116 (C6). <https://doi.org/10.1029/2010JC006883>.
- Sun, S., Hu, C., 2016. Sun glint requirement for the remote detection of surface oil films. *Geophys. Res. Lett.* 43, 309–316.
- Sun, S., Hu, C., Tunnell, J.W., 2015. Surface oil footprint and trajectory of the Ixtoc-1 oil spill determined from Landsat/MSS and CZCS observations. *Mar. Pollut. Bull.* 101 (2), 632–641. <https://doi.org/10.1016/j.marpolbul.2015.10.036>.
- Sun, S., Hu, C., Feng, L., Swayze, A.S., Holmes, J., Graettinger, G., MacDonald, I., Garcia, O., Leifer, I., 2016. Oil slick morphology derived from AVIRIS measurements of the Deepwater horizon oil spill: implications for spatial resolution requirements of remote sensors. *Mar. Pollut. Bull.* 103 (1–2), 276–285. <https://doi.org/10.1016/j.marpolbul.2015.12.003>.
- Sun, S., Lu, Y., Liu, Y., Wang, M., Hu, C., 2018. Tracking an oil tanker collision and spilled oils in the East China Sea using multisensor day and night satellite imagery. *Geophys. Res. Lett.* 45, 3212–3220.
- Svejksky, J., Lehr, W., Muskat, J., Graettinger, G., Mullin, J., 2012. Operational utilization of aerial multispectral remote sensing during oil spill response. *Photogramm. Eng. Remote. Sens.* 78 (10), 1089–1102.
- Svejksky, J., Hess, M., Muskat, J., Nedwed, T.J., McCall, J., Garcia, O., 2016. Characterization of surface oil thickness distribution patterns observed during the Deepwater Horizon (MC-252) oil spill with aerial and satellite remote sensing. *Mar. Pollut. Bull.* 110 (1), 162–176. <https://doi.org/10.1016/j.marpolbul.2016.06.066>.
- United States of America v. BP Exploration and Production, Inc. et al., 2015. Findings of fact and conclusions of law: phase two trial. In: re: oil spill by the oil rig “Deepwater Horizon”. In: The Gulf of Mexico, on April 20, 2010, No. MDL 2179, 2015 WL 225421 (L.A.E.D. Jan. 15, 2015). (Doc. 14021). U.S. District Court for the Eastern District of Louisiana Retrieved from <http://www.laed.uscourts.gov/OilSpill/Orders/1152015FindingsPhaseTwo.pdf>.
- Walker, N.D., Wiseman Jr., W.J., Rouse Jr., L.J., Babin, A., 2005. Effects of river discharge, wind stress, and slope eddies on circulation and the satellite-observed structure of the Mississippi River plume. *J. Coast. Res.* 21 (6), 1228–1244.
- Walker, N.D., Pilley, C.T., Raghunathan, V.V., D’Sa, E.J., Leben, R.R., Hoffmann, N.G., Brickley, P.J., Coholan, P.D., Sharma, N.N., Graber, H.C., Turner, R.E., 2011. Impacts of Loop Current frontal cyclonic eddies and wind forcing on the 2010 Gulf of Mexico oil spill. In: *Monitoring and Modeling the Deepwater Horizon Oil Spill: A Record-breaking Enterprise*. American Geophysical Union, Washington, D. C. <https://doi.org/10.1029/2011GM001120>.
- Warren, C.J., MacFadyen, A., Henry, C., 2014. Mapping oil for the destroyed Taylor Energy site in the Gulf of Mexico. In: *International Oil Spill Conference Proceedings*. vol. 2014, No. 1, pp. 299931.
- Wettle, M., Daniel, P.J., Logan, G.A., Thankappan, M., 2009. Assessing the effect of hydrocarbon oil type and thickness on a remote sensing signal: a sensitivity study based on the optical properties of two different oil types and the HYMAP and Quickbird sensors. *Remote Sens. Environ.* 113 (9), 2000–2010. <https://doi.org/10.1016/j.rse.2009.05.010>.
- Zhang, X., Hetland, R.D., Marta-Almeida, M., DiMarco, S.F., 2012. A numerical investigation of the Mississippi and Atchafalaya freshwater transport, filling and flushing times on the Texas-Louisiana Shelf. *J. Geophys. Res. Oceans* 117, C11009. <https://doi.org/10.1029/2012JC008108>.

APPENDIX F:

TRACKING AN OIL TANKER COLLISION AND SPILLED OILS IN THE EAST CHINA SEA USING MULTISENSOR

DAY AND NIGHT SATELLITE IMAGERY

Sun, S., Lu, Y., Liu, Y., Wang, M., and Hu, C. (2018). Tracking an oil tanker collision and spilled oils in the East China Sea using multisensor day and night satellite imagery. *Geophysical Research Letters*, 45, 3212-3220, doi:10.1002/2018GL077433



Geophysical Research Letters

RESEARCH LETTER

10.1002/2018GL077433

Key Points:

- VIIRS nighttime data and wind-adjusted model show unprecedented value in tracking an oil tanker over >350 km after a major collision
- Other satellite imagery capture smokes and spilled oils in the East China Sea
- A combination of all remote sensing and modeling efforts proves to be effective in monitoring the tragic accident

Correspondence to:

C. Hu,
huc@usf.edu

Citation:

Sun, S., Lu, Y., Liu, Y., Wang, M., & Hu, C. (2018). Tracking an oil tanker collision and spilled oils in the East China Sea using multisensor day and night satellite imagery. *Geophysical Research Letters*, 45, 3212–3220. <https://doi.org/10.1002/2018GL077433>

Received 1 FEB 2018

Accepted 15 MAR 2018

Accepted article online 23 MAR 2018

Published online 6 APR 2018

Tracking an Oil Tanker Collision and Spilled Oils in the East China Sea Using Multisensor Day and Night Satellite Imagery

Shaojie Sun¹ , Yingcheng Lu^{1,2} , Yongxue Liu³ , Mengqiu Wang¹ , and Chuanmin Hu¹ 

¹College of Marine Science, University of South Florida, St. Petersburg, FL, USA, ²International Institute for Earth System Science, Nanjing University, Nanjing, China, ³Department of Geographic Information Science, Nanjing University, Nanjing, China

Abstract Satellite remote sensing is well known to play a critical role in monitoring marine accidents such as oil spills, yet the recent SANCHI oil tanker collision event in January 2018 in the East China Sea indicates that traditional techniques using synthetic aperture radar or daytime optical imagery could not provide timely and adequate coverage. In this study, we show the unprecedented value of Visible Infrared Imaging Radiometer Suite (VIIRS) Nightfire product and Day/Night Band data in tracking the oil tanker's drifting pathway and locations when all other means are not as effective for the same purpose. Such pathway and locations can also be reproduced with a numerical model, with root-mean-square error of <15 km. While high-resolution optical imagery after 4 days of the tanker's sinking reveals much larger oil spill area (>350 km²) than previous reports, the impact of the spilled condensate oil on the marine environment requires further research.

Plain Language Summary The Iranian oil tanker SANCHI collided with a grain freighter on 6 January 2018 in the East China Sea, causing major fires and oil spills. For event response, nighttime data collected by the Visible Infrared Imaging Radiometer Suite (VIIRS) satellite instrument show unprecedented value in monitoring the fires and tracking the >350 km drifting pathway of the SANCHI tanker. A numerical model to combine surface currents and wind can also simulate the tanker's locations until it sank on 14 January. Satellite remote sensing during daytime shows smokes and spilled oil on the ocean surface, some of which appears to be oil emulsion. A combination of all available remote sensing and modeling techniques can provide effective means to monitor marine accidents and oil spills to assist event response.

1. Introduction

The Iranian oil tanker SANCHI (IMO: 9356608), carrying ~1 million U.S. barrels (136,000 metric tons) of condensate oil heading to South Korea from Iran with 32 crews on board, collided with the Chinese grain freighter CF Crystal (IMO: 9497050) in the East China Sea (ECS) at ~8 p.m. on 6 January 2018 [Beijing time = GMT + 8 hr; hereafter time used in this paper is all Beijing time; Ministry of Transport of the People's Republic of China (MOT), 2018a]. The accident caused SANCHI on fire and tilted, drifting ablaze for a week, until it exploded and sunk at ~3 p.m. on 14 January 2018. Three bodies of the 32 crew members were found, with the other 29 missing members presumed dead. During the drift, SANCHI leaked oil since 7 January, according to online reports (MOT, 2018a; State Oceanic Administration (SOA), People's Republic of China 2018a, 2018b). Oil slicks have been observed and reported around the tanker's sinking location since 14 January 2018 through airborne and shipborne surveys (SOA, 2018b).

Monitoring the tanker's drifting pathway and potential spills from a moving target represents a critical need for event response and mitigation. Unfortunately, for this specific event it has proven extremely difficult for two reasons: (1) persistent cloud cover during and after the collision prevented any effective use of optical remote sensing from satellites; (2) the use of synthetic aperture radar (SAR, immune to cloud cover) required a response time, which can vary between hours and days because it includes time for event reporting, image acquisition planning, and execution of image acquisition over the targeted area (IPIECA-IOGP, 2014). Airborne surveys, on the other hand, were limited in space and time. As a result, traditional means through satellite remote sensing and airborne surveys appeared inadequate for event response of this disaster.

Here we demonstrate the unprecedented value of nighttime data collected by the Visible Infrared Imaging Radiometer Suite (VIIRS) in monitoring such an event. Additionally, a numerical model is calibrated using

Table 1
Number of Days With Imagery or Data Product Coverage From Individual or Multiple Sensors Along the Tanker's Drifting Trajectory (7–14 January 2018) and Around the Tanker Sinking Site (15–18 January 2018)

	Satellite sensor/products	7–14 January	15–18 January
Optical cloud-free coverage	MODIS	1	3
	OLCI	1	1
	VIIRS	1	1
	GOCI	2	3
	ETM+	0	0
	OLI	0	0
SAR coverage	MSI	1	1
	Sentinel-1	0	0
	Radarsat-2	2	1
	COSMO-SkyMed	0	4
Fire/Night-light anomalies	TerraSAR-X	0	0
	FIRMS	2	0
	VIIRS Nightfire	7	1
	VIIRS DNB	8	4

Note. As multiple images/products per day are possible from some sensor(s) (e.g., MODIS Terra and MODIS Aqua, and GOCI), the statistics is based on daily frequency (in Beijing time).

these data to track the tanker location, and high-resolution optical satellite imagery collected after 4 days of the tanker sinking shows the area of oil slicks much larger than those reported, which also shows signs of oil emulsions. The objective of this paper is to show the worth of combining all remote sensing imagery (day and night) and numerical modeling in event response, therefore possibly serving as a template when responding to other similar events.

2. Data and Methods

2.1. Satellite Data

Data from all civilian satellites, whenever available for public access, were downloaded from the corresponding agencies. These include Terra/Aqua Moderate Resolution Imaging Spectroradiometer (MODIS), Suomi-NPP VIIRS, Sentinel-3 Ocean and Land Color Instrument (OLCI), COMS Geostationary Ocean Color Imager (GOCI), Landsat ETM+/OLI, Sentinel-2 MultiSpectral Instrument (MSI), and Sentinel-1 SAR. Commercial Radarsat-2, COSMO-SkyMed and TerraSAR-X SAR data archives have also been checked. Detailed information of imagery coverage is provided in Table 1.

After the collision accident, all optical imagery collected during the daytime showed persistent cloud cover until 13 January when the images showed scattered clouds to allow for inspection of some of the pixels. During this period, oil spill detection was impossible but smoke from the burning tanker could be detected on 13 January (see below). Between 7 and 14 January, the above SAR data showed only 2 days of coverage over the tanker's drifting trajectory, while more frequent coverage after the tanker's sinking (on 14 January) was available from COSMO-SkyMed. The Chinese Gaofen-3 (GF-3) satellite launched in 2016 carries a C-band SAR sensor, which works in 12 imaging modes with spatial resolution ranging from 1 m to 500 m and swath ranging from 10 to 650 km (<https://chinaspacereport.com/spacecraft/gaofen/>). GF-3 was reported to have collected data over the SANCHI location since 8 January (CRESDA, 2018), yet the data were not open to research communities or the public.

Because of the limitations above, the only possibly useful data during the initial phase of the accident were VIIRS nighttime data. There are two types of nighttime data used in this study. The first is the VIIRS Nightfire (v3.0) data product (https://ngdc.noaa.gov/eog/viirs/download_viirs_fire.html), obtained from the National Oceanic and Atmospheric Administration Earth Observation Group every day. A multispectral algorithm was used to detect subpixel hot sources (Elvidge et al., 2013). Candidate hot pixels were first identified by the nighttime M10 (1,601 nm) band. Six other spectral bands including the Day/Night Band (DNB), M7 (862 nm), M8 (1,238.5 nm), M11 (2,250 nm), M12 (3,694.5 nm), and M13 (4,066 nm) were used to confirm the initial detection. A black-body emission curve fitting was then applied to the confirmed hot source

using these bands, from which the hot source temperature and area were determined (Elvidge et al., 2015). Similar fire products from both MODIS and VIIRS for both day and night were also explored from the Fire Information for Resource Management System (FIRMS, <https://firms.modaps.eosdis.nasa.gov/map/>). FIRMS uses reflectance and/or brightness temperature thresholds to first classify cloud pixels on both day and night imagery (Giglio et al., 2016; Schroeder et al., 2014) and then mask these pixels from fire detection (Schroeder et al., 2014). Because of the cloud masking before fire detection, FIRMS products showed no valid coverage before 12 January due to persistent cloud cover (Table 1). In contrast, the VIIRS Nightfire algorithm is applied to all pixels, with cloud cover conditions recorded in the final product (Elvidge et al., 2013).

The second type of nighttime data was collected by the low-light imaging DNB (500–900 nm), designed primarily to detect light sources such as city lights (Miller et al., 2013). In this study, VIIRS DNB SDR (Sensor Data Records) calibrated radiance data were obtained from National Oceanic and Atmospheric Administration/Comprehensive Large Array-data Stewardship System (NOAA/CLASS).

Lastly, after persistent cloud cover for many days, MSI images with some cloud-free spots were available on 13 January (1 day before the tanker's sinking) and 18 January (4 days after the tanker's sinking). The Level-1C data were processed using the ACOLITE software (<https://odnature.naturalsciences.be/remsem/software-and-data/acolite>) to produce spectral Rayleigh-corrected reflectance (R_{TC} , dimensionless), with all the spectral bands resampled to 10 m resolution. Red-Green-Blue (RGB) true color (R = 664 nm, G = 560 nm, B = 497 nm) images were generated for smoke detection while false-color RGB images (R = 1614 nm, G = 835 nm, B = 664 nm) were generated to detect spilled oils. Normalized sun glint reflectance (L_{GN} , sr^{-1}) was estimated using the Cox and Munk model and National Centers for Environmental Prediction (NCEP) wind data (Cox & Munk, 1954; Lu et al., 2016; Wang & Bailey, 2001). Oil slicks were manually delineated in the ArcMap software (version 10.3) using methods described in Sun et al. (2015).

2.2. Numerical Model to Track Tanker Locations

The tanker's drifting pathway was simulated using Global HYCOM daily surface currents and the NCEP Reanalysis daily wind data (10 m above sea level). HYCOM surface currents data were obtained from the Global Reanalysis (experiment 91.2). A Runge-Kutta fourth-order method was used to model the tanker trajectories with a time step of 15 min. In modeling oil spill trajectory, a factor of 3% was often applied to wind velocity (IPIECA-IOGP, 2015; Lehr & Simecek-Beatty, 2000). The large size of the tanker (overall length of 274 m, beam width of 50 m, and full-load draught of 17 m) enables a larger cross section (than surface oil) to the wind direction. Therefore, wind was expected to play a more important role than the usual assumption of 3%. A sensitivity test by varying the factor from 1% to 7% was conducted to determine the optimal wind factor that led to the least difference between modeled SANCHI locations and observed locations.

3. Results

3.1. SANCHI Locations From VIIRS Night Time Data and Numerical Modeling

Before 13 January 2018, optical remote sensing data collected by all sensors during daytime were useless due to persistent and complete cloud cover. In contrast, VIIRS nighttime data, specifically the Nightfire data product and DNB data, showed locations of the tanker as well as the size of the hot spot footprint every night starting 8 January (Figure 1). After the tanker's sinking on 14 January, VIIRS showed three separate fire sources in the following night (last panel of Figure 1), indicating surface drifting of floating oil.

The tanker's drifting trajectory could be reproduced by the numerical model (Figure 2). With a wind factor of 4.1%, the modeled tanker locations agreed well with those observed from the VIIRS nighttime data, with a root-mean-square difference of 14.3 km. When other wind factors between 1% and 7% were applied, root-mean-square difference was significantly higher (e.g., ~ 40 km at 3%).

3.2. The Value of Optical Remote Sensing Data During Daytime

On 13 January, after persistent and complete cloud cover since the collision, some optical remote sensing imagery covering the area of interest showed smoke around the tanker location. The example in Figure 3 from the MSI image clearly reveals the smoke, which appears brownish in the RGB image. Wind is about

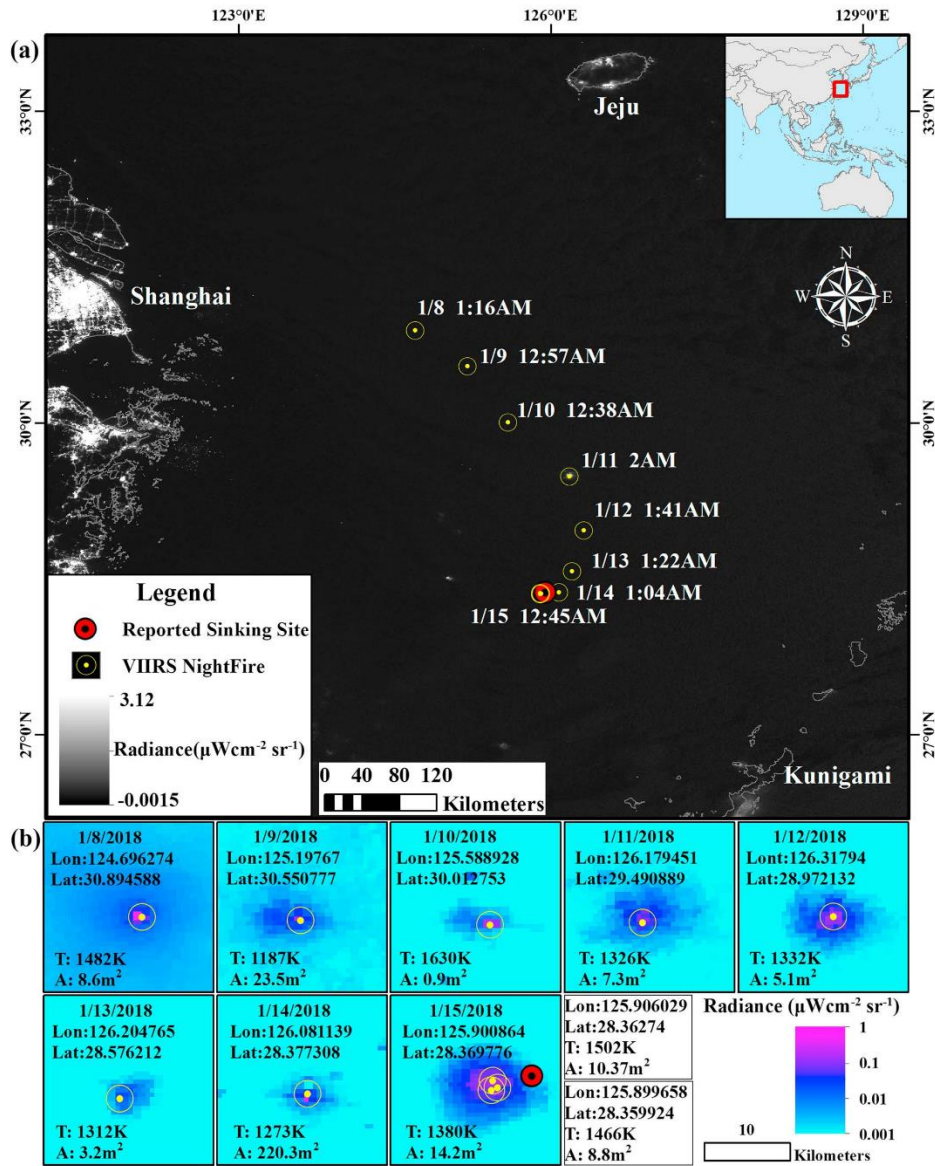


Figure 1. (a) SANCHI oil tanker locations derived from VIIRS Nightfire product in the East China Sea, overlaid on the VIIRS Day/Night Band image captured at 2 a.m. on 11 January 2018. The initial collision was at 8 p.m. on 6 January 2018 (Beijing time = GMT + 8), while the first VIIRS capture was at 1:16 a.m. on 8 January. The last detection was at 12:45 a.m. on 15 January. SANCHI was reported to sink at 3 p.m. on 14 January (red circle), but fires on ocean surface did not stop until ~10 a.m. on 15 January (SOA, 2018b). The sinking location was reported to be ~280 km southeast of the initial collision location (MOT, 2018b). The VIIRS-based results agree well with both reports. (b) VIIRS Day/Night Band radiance shows local hot spots from 8 to 15 January, with temperature (T , in Kelvins) and location of the hotspot as well as the footprint area (A , in m^2) annotated. Three active fires (yellow dots in the last panel) were detected in the vicinity of the sinking location (red circle in the last panel).

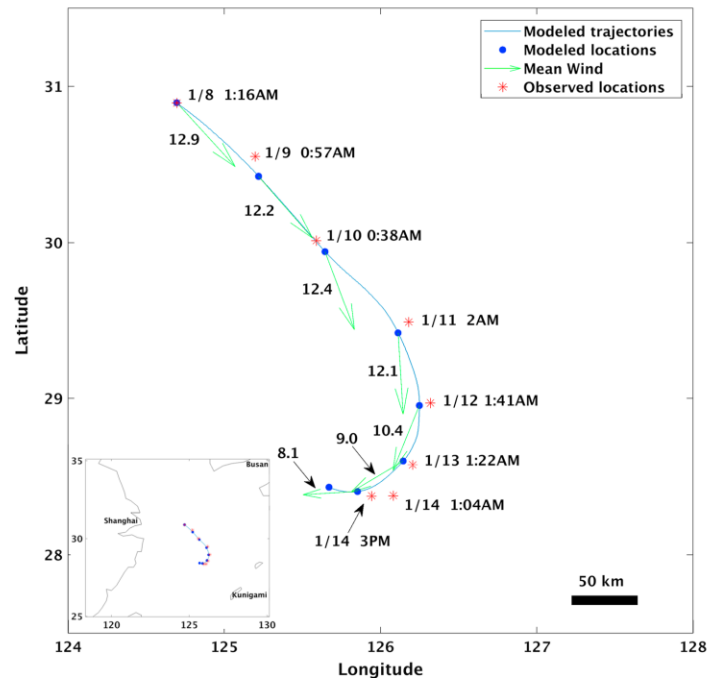


Figure 2. Trajectory and locations of the SANCHI tanker movement determined from VIIRS Nightfire data product (except for the last point at 3 p.m. on 14 January, which is the reported sinking location) and a numerical model. In the model, a 4.1% factor was applied to wind, which resulted in a minimal root-mean-square difference between modeled and observed locations (~14.3 km). A 3% wind factor would lead to RMS difference of ~40 km. Average wind speed and direction for each day are plotted as green arrows, with wind speed (m/s) annotated to the left of the wind vector.

8.1 m/s blowing from the NNE to SSW. Correspondingly, the smoke is about 15 km SSW of the tanker's location 9 hr ago, and 14 hr later the tanker's location is to the SSW of the smoke. Other than the smoke, the images could not be used to detect spilled oils due to cloud cover surrounding the smoke area.

Four days after the tanker's sinking, on 18 January, the first high-resolution optical image that could be used to detect spilled oils was captured by MSI (Figure 4). One slick was detected 3 km north of the sinking location, with a slick size of ~86 km² elongated in the west to east direction (Figure 4b, Slick 2). The slick shows mostly negative contrast from water (i.e., darker than water) due to weak sun glint ($L_{GN} = 1.5E-4 \text{ sr}^{-1}$) (Sun & Hu, 2016). Another larger slick was captured 30–40 km northeast of the sinking location, with a slick size of ~270 km² (Figure 4a, Slick 1). In the center of this slick, some oil stripes in the NNE-SSW direction show signs of oil emulsions as they appear reddish (elevated 1,614 nm reflectance) in the false-color RGB image (Figure 4a). The NNE-SSW stripes within both slicks in Figures 4a and 4b are apparently due to wind-driven Langmuir circulation, with the direction of the stripes aligned with the NNE-SSW wind direction. These slick size estimations, although biased low due to lack of MSI data coverage to the east of the slicks, are significantly higher than those reported online (SOA, 2018c).

4. Discussion

Massive oil spills and possible application of dispersant could cause severe and long-term impacts on the marine ecosystem and local economies (Joye, 2015; Michel et al., 2013; Peterson et al., 2003), thus calling

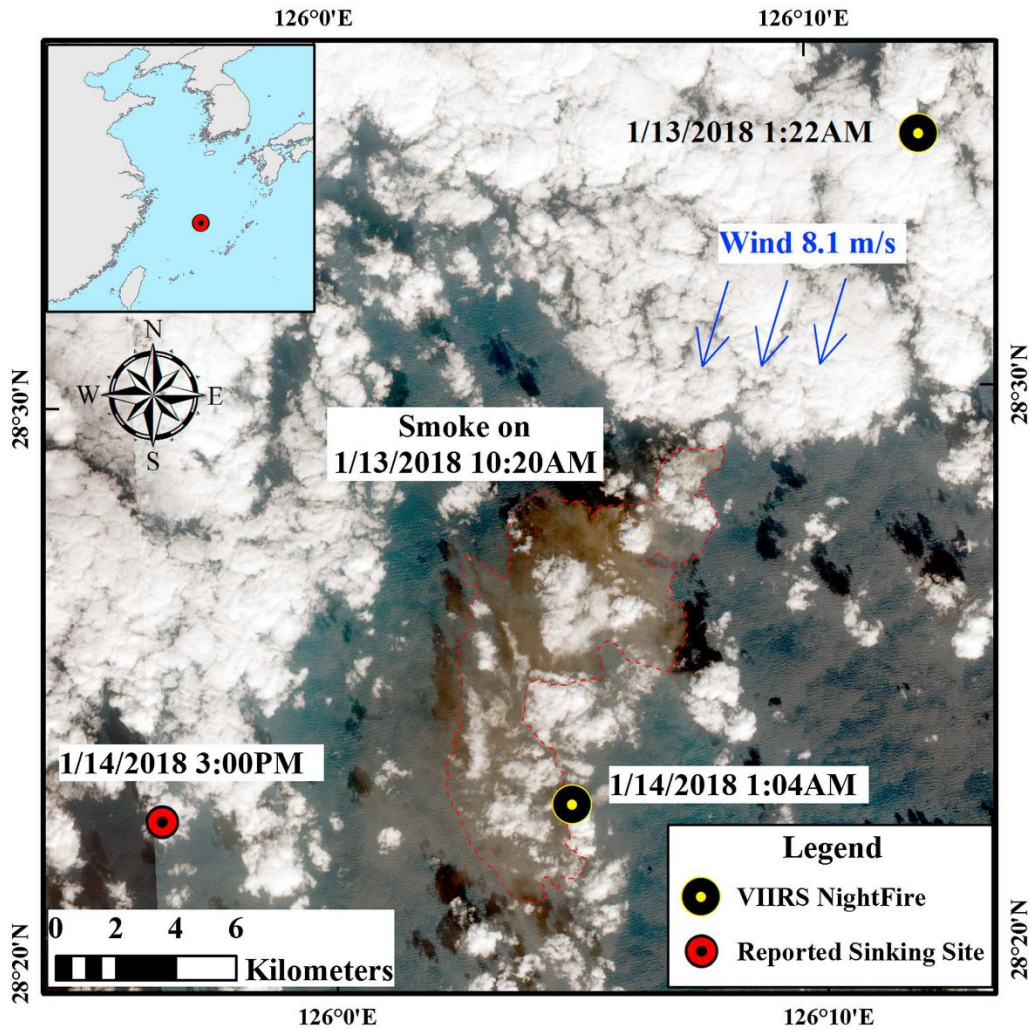


Figure 3. MSI RGB image ($R = 664 \text{ nm}$, $G = 560 \text{ nm}$, $B = 497 \text{ nm}$) on 13 January 2018 (10:20 a.m.) shows smoke (outlined in red), where VIIRS-detected SANCHI locations on 13 January (1:22 a.m.) and 14 January (1:04 a.m.) are annotated. At the time of imaging, wind blew from northeast to southwest at a speed of 8.1 m/s.

for accurate and timely assessment during and after the spill. Unfortunately, due to persistent cloud cover and lack of coverage, none of the traditional remote sensing techniques (SAR, daytime optical imagery) proved to be fully effective for this particular event. Here nighttime imagery from VIIRS showed unprecedented value in tracking the tanker's location and fire footprint, thus providing first-hand timely knowledge every night to assist in event response. On the other hand, identifying the tanker's location through locating fires is not trivial, as active fires from gas flares of offshore platforms could confuse the findings. In this study, hot sources from gas flares in the East China Sea were ruled out using a global oil

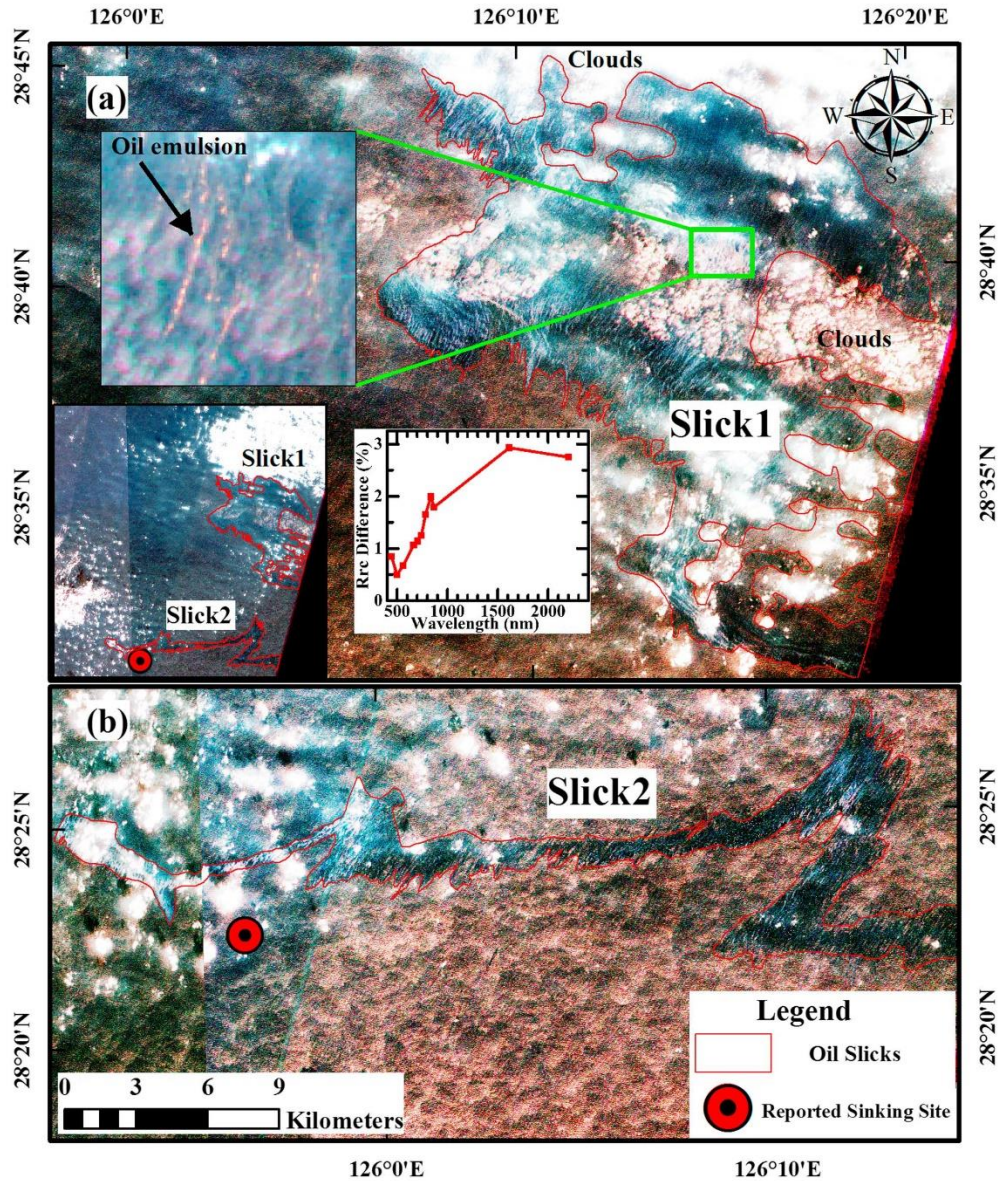


Figure 4. MSI false-color RGB image (R = 1614 nm, G = 835 nm, B = 664 nm) at 10:20 a.m. on 18 January 2018 shows two major slicks (locations annotated in inset figure): (a) Slick 1 is 30–40 km northeast of the reported sinking site, with a slick size of $\sim 270 \text{ km}^2$. This number is an underestimate, as the area east of the oil slick was not covered by the MSI image. The center of the slick shows signs of oil emulsion (enlarged area from the green rectangle) as they appear reddish in the false-color RGB image. Spectral analysis (inset reflectance spectrum) of a randomly selected point (black arrow) shows elevated reflectance at 1,614 nm, a clear indication of oil emulsion. (b) Slick 2 is 3 km north of the sinking site, with a slick size of $\sim 86 \text{ km}^2$ (also underestimated due to lack of MSI coverage to the east). The total area ($270 + 86 \text{ km}^2$) is significantly higher than any reported numbers (SOA, 2018c) that ranged between $\sim 160 \text{ km}^2$ from field observations and 20.7 km^2 from satellite interpretation. The slicks appear darker than water due to the presence of weak sun glint ($L_{GN} = 1.5E-4 \text{ sr}^{-1}$).

platform database (Liu et al., 2016), making the detection of tanker location reliable. The ability of emissive radiation to penetrate thin clouds makes it possible to detect hot sources even under thin cloud cover, although the temperature of the hot source may contain large degree of uncertainties due to cloud absorption of the radiant emissions (Elvidge et al., 2013).

Oil released to the ocean from this accident was from two sources: the remaining condensate oil after combustion and evaporation, and the remaining bunker fuel or heavy fuel oil. The latter strongly absorbs blue light (Byfield, 1998), while the former is nearly transparent in the visible and near-infrared (NIR) wavelengths (470–1,000 nm) at a thickness of $<200 \mu\text{m}$ (Wettle et al., 2009). Both will dampen the surface wave, thus detectable in SAR imagery (Alpers et al., 2017; Brekke & Solberg, 2005; Garcia-Pineda et al., 2013), and optical imagery (Adamo et al., 2009; Hu et al., 2009; Pisano et al., 2015; Sun & Hu, 2016) under optimal wind conditions. Because condensate oil is believed to evaporate fast, it was expected that oil emulsions could not be observed. However, a surprising result from this analysis is that oil emulsion patches appear to have formed on the sea surface after the tanker's sinking (Figure 4). Spectral analysis of selected pixels in the reddish patches of the oil slicks showed significantly elevated reflectance at 1,614 nm (Figure 4a inset), an indication of oil emulsion (Clark et al., 2010; Svejkovsky et al., 2016). Because condensate oil evaporates fast, it is speculated that the oil emulsion originated from the bunker oil released by the tanker after its sinking. Indeed, HYCOM surface currents showed NNE direction after the tanker's sinking, suggesting that the spilled oil could originate from the tanker after its sinking.

By no means does this work de-emphasize the value of SAR and other remote sensing techniques in oil spill response. Instead, the study here is to demonstrate how VIIRS nighttime data can provide critical location information on marine accidents through its unprecedented capacity in identifying fire sources and observing low light at night. Indeed, although due to data restriction policy the commercial SAR data could not be accessed, some quick-look images posted online did show oil slicks in the study region. Additionally, post-sinking MSI imagery showed more spilled oils than those determined from airborne and shipborne surveys, once again proving the value of optical remote sensing. On the other hand, the combination of surface currents and wind data provided a relatively accurate estimate on the tanker's drifting pathway, indicating that numerical modeling can also provide guidance on search and rescue, similar to the search of the Air France 447 in the Equatorial Atlantic (Chen et al., 2012).

Altogether, the multisensor observations from day and night provide way more complete information than any individual sensors alone. This is particularly important for event response during the initial phase as opposed to postevent assessment. For example, without satellite remote sensing providing approximate locations at the very beginning, it would be difficult to narrow down targeted regions to point high-resolution satellite sensors. The case study here demonstrates the value of VIIRS nighttime data in providing such critical information within 30 hr of the accident, therefore complementing other means for event response.

At the time of this writing, postspill assessments are still ongoing, for example, to evaluate the potential impact of the tragic event to the marine environment. Such assessments have proven to be difficult from the Deepwater Horizon oil spill event in the northern Gulf of Mexico in 2010, mainly due to the lack of "baseline" data before the event. Modern satellite remote sensing has provided continuous ocean measurements since 1997 when Sea-viewing Wide Field-of-view Sensor began collecting data, where surface ocean transparency and chlorophyll-a concentration data records may serve as baseline (mean conditions and natural variability) to evaluate the potential impact of the event on nearby ocean environment. Such an impact assessment may be an immediate follow-on study for this tragic event.

5. Conclusion

Although VIIRS nighttime data have been widely used to map city lights and fires, this study demonstrates its value in tracking a major collision and oil spill event. More importantly, during the initial days after the collision, VIIRS nighttime data were the only publically available satellite data proven to be effective in tracking the tanker's drifting pathway and daily locations, as all other satellite sensors suffer from lack of coverage or cloud cover. This capacity, along with the numerical tool to track the oil tanker and other sensors to map spilled oil, may serve as a template for similar events in the future.

Acknowledgments

This work was made possible because of a NASA Earth and Space Science Fellowship (NESSF, grant NNX16AN95H), a grant from the Gulf of Mexico Research Initiative/C-IMAGE II, and support from the National Natural Science Foundation of China (grant 41771376). Data are publicly available through the Gulf of Mexico Research Initiative Information and Data Cooperative (GRIDC) at <https://data.gulfresearchinitiative.org> (<https://doi.org/10.7266/N7639N85>). We thank the European Space Agency for providing Sentinel-1 SAR, MSI and OLCI data (<https://scihub.copernicus.eu/>), the USGS for providing Landsat data (<https://earthexplorer.usgs.gov/>), the Korea Ocean Satellite Center for providing GOCI data (http://kosc.kiost.ac.kr/eng/p10/kosc_p11.html), NASA for providing FIRMS active fire data and MODIS data (<https://oceancolor.gsfc.nasa.gov/>), and NOAA for providing VIIRS Nightfire and VIIRS DNB data (<https://www.class.ngdc.noaa.gov/saa/products/welcome>). We also thank the two anonymous reviewers for their suggestions to improve this manuscript.

References

Adamo, M., De Carolis, G., De Pasquale, V., & Pasquariello, G. (2009). Detection and tracking of oil slicks on sun-glittered visible and near infrared satellite imagery. *International Journal of Remote Sensing*, 30(24), 6403–6427. <https://doi.org/10.1080/01431160902865772>

Alpers, W., Holt, B., & Zeng, K. (2017). Oil spill detection by imaging radars: Challenges and pitfalls. *Remote Sensing of Environment*, 201, 133–147. <https://doi.org/10.1016/j.rse.2017.09.002>

Brekke, C., & Solberg, A. H. S. (2005). Oil spill detection by satellite remote sensing. *Remote Sensing of Environment*, 95(1), 1–13. <https://doi.org/10.1016/j.rse.2004.11.015>

Byfield, V. (1998). Optical remote sensing of oil in the marine environment (Doctoral dissertation). University of Southampton.

Chen, C., Limeburner, R., Gao, G., Xu, Q., Qi, J., Xue, P., et al. (2012). FVCOM model estimate of the location of Air France 447. *Ocean Dynamics*, 62(6), 943–952. <https://doi.org/10.1007/s10236-012-0537-5>

China Center for Resources Satellite Data and Application (2018). Emergency surveillance of tanker collision accident in the East China Sea by earth observing satellites. Retrieved March 9, 2018 from <http://www.cresda.com/CN/xwzx/xwdt/11355.shtml>

Clark, R. N., Swayze, G. A., Leifer, I., Livo, K. E., Kokaly, R., Hoefen, T., et al. (2010). A method for quantitative mapping of thick oil spills using imaging spectroscopy. *US Geological Survey Open-File Report*, 1167, 1–51.

Cox, C., & Munk, W. (1954). Measurement of the roughness of the sea surface from photographs of the Sun's glitter. *Journal of the Optical Society of America*, 44(11), 838–850. <https://doi.org/10.1364/JOSA.44.000838>

Elvidge, C., Zhizhin, M., Baugh, K., Hsu, F.-C., & Ghosh, T. (2015). Methods for global survey of natural gas flaring from visible infrared imaging radiometer suite data. *Energies*, 9(12), 14. <https://doi.org/10.3390/en9010014>

Elvidge, C., Zhizhin, M., Hsu, F.-C., & Baugh, K. (2013). VIIRS Nightfire: Satellite pyrometry at night. *Remote Sensing*, 5(9), 4423–4449. <https://doi.org/10.3390/rs5094423>

Garcia-Pineda, O., MacDonald, I., Hu, C., Svejksky, J., Hess, M., Dukhovskoy, D., & Morey, S. (2013). Detection of floating oil anomalies from the Deepwater Horizon oil spill with synthetic aperture radar. *Oceanography*, 26(2). <https://doi.org/10.5670/oceanog.2013.38>

Giglio, L., Schroeder, W., & Justice, C. O. (2016). The collection 6 MODIS active fire detection algorithm and fire products. *Remote Sensing of Environment*, 178, 31–41. <https://doi.org/10.1016/j.rse.2016.02.054>

Hu, C., Li, X., Pichel, W. G., & Muller-Karger, F. E. (2009). Detection of natural oil slicks in the NW Gulf of Mexico using MODIS imagery. *Geophysical Research Letters*, 36, L01604. <https://doi.org/10.1029/2008GL036119>

IPIECA-IOGP (2014). *An assessment of Surface surveillance capabilities for oil spill response using satellite remote sensing* (p. 23). Hampshire, UK, April 2014: IPIECA-IOGP. Retrieved from <http://www.ipieca.org/resources/awareness-briefing/an-assessment-of-surface-surveillance-capabilities-for-oil-spill-response-using-satellite-remote-sensing/>

IPIECA-IOGP (2015). *Aerial observation of oil spills at sea* (p. 19). London, February 2015: IPIECA-IOGP. Retrieved from <http://www.ipieca.org/resources/good-practice/aerial-observation-of-oil-spills-at-sea/>

Joye, S. B. (2015). Deepwater Horizon, 5 years on. *Science*, 349(6248), 592–593. <https://doi.org/10.1126/science.aab4133>

Lehr, W. J., & Simecek-Beatty, D. (2000). The relation of Langmuir circulation processes to the standard oil spill spreading, dispersion, and transport algorithms. *Spill Science & Technology Bulletin*, 6(3–4), 247–253. [https://doi.org/10.1016/S1353-2561\(01\)00043-3](https://doi.org/10.1016/S1353-2561(01)00043-3)

Liu, Y., Sun, C., Yang, Y., Zhou, M., Zhan, W., & Cheng, W. (2016). Automatic extraction of offshore platforms using time-series Landsat-8 Operational Land Imager data. *Remote Sensing of Environment*, 175, 73–91. <https://doi.org/10.1016/j.rse.2015.12.047>

Lu, Y., Sun, S., Zhang, M., Murch, B., & Hu, C. (2016). Refinement of the critical angle calculation for the contrast reversal of oil slicks under sunglint. *Journal of Geophysical Research: Oceans*, 121, 148–161. <https://doi.org/10.1002/2015JC011001>

Michel, J., Owens, E. H., Zengel, S., Graham, A., Nixon, Z., Allard, T., et al. (2013). Extent and degree of shoreline oiling: Deepwater Horizon oil spill, Gulf of Mexico, USA. *PLoS One*, 8(6), e65087. <https://doi.org/10.1371/journal.pone.0065087>

Miller, S., Straka, W., Mills, S., Elvidge, C., Lee, T., Solbrig, J., et al. (2013). Illuminating the capabilities of the Suomi National Polar-orbiting Partnership (NPP) Visible Infrared Imaging Radiometer Suite (VIIRS) Day/Night Band. *Remote Sensing*, 5(12), 6717–6766. <https://doi.org/10.3390/rs5126717>

Ministry of Transport of the People's Republic of China (2018a). Update on oil tanker SANCHI collision and on fire in the East China Sea. Retrieved January 24, 2018 from http://www.mot.gov.cn/jiaotongyaowen/201801/t20180107_2969411.html

Ministry of Transport of the People's Republic of China (2018b). Update on oil tanker SANCHI exploded and sunk yesterday. Retrieved January 24, 2018 from http://www.mot.gov.cn/jiaotongyaowen/201801/t20180115_2972106.html

Peterson, C. H., Rice, S. D., Short, J. W., Esler, D., Bodkin, J. L., Ballachey, B. E., & Irons, D. B. (2003). Long-term ecosystem response to the Exxon Valdez oil spill. *Science*, 302(5653), 2082–2086. <https://doi.org/10.1126/science.1084282>

Pisano, A., Bignami, F., & Santoleri, R. (2015). Oil spill detection in glint-contaminated near-infrared MODIS imagery. *Remote Sensing*, 7(1), 1112–1134. <https://doi.org/10.3390/rs7010112>

Schroeder, W., Oliva, P., Giglio, L., & Csiszar, I. A. (2014). The new VIIRS 375m active fire detection data product: Algorithm description and initial assessment. *Remote Sensing of Environment*, 143, 85–96. <https://doi.org/10.1016/j.rse.2013.12.008>

State Oceanic Administration (SOA), People's Republic of China (2018a). SOA response to SANCHI accident (I). Retrieved January 24, 2018 from http://www.soa.gov.cn/xw/hyyw_90/201801/t20180112_59951.html

State Oceanic Administration (SOA), People's Republic of China (2018b). SOA response to SANCHI accident—A joint monitoring effort in East China Sea. Retrieved January 24, 2018 from http://www.soa.gov.cn/xw/hyyw_90/201801/t20180116_59990.html

State Oceanic Administration (SOA), People's Republic of China (2018c). SOA response to SANCHI accident (VII). Retrieved January 24, 2018 from http://www.soa.gov.cn/xw/hyyw_90/201801/t20180118_60031.html

Sun, S., & Hu, C. (2016). Sun glint requirement for the remote detection of surface oil films. *Geophysical Research Letters*, 43, 309–316. <https://doi.org/10.1002/2015gl066884>

Sun, S., Hu, C., & Tunnell, J. W. (2015). Surface oil footprint and trajectory of the Ixtoc-1 oil spill determined from Landsat/MSS and CZCS observations. *Marine Pollution Bulletin*, 101(2), 632–641. <https://doi.org/10.1016/j.marpolbul.2015.10.036>

Svejksky, J., Hess, M., Muskat, J., Nedwed, T. J., McCall, J., & Garcia, O. (2016). Characterization of surface oil thickness distribution patterns observed during the Deepwater Horizon (MC-252) oil spill with aerial and satellite remote sensing. *Marine Pollution Bulletin*, 110(1), 162–176. <https://doi.org/10.1016/j.marpolbul.2016.06.066>

Wang, M., & Bailey, S. W. (2001). Correction of sun glint contamination on the SeaWiFS ocean and atmosphere products. *Applied Optics*, 40, 4790–4798. <https://doi.org/10.1364/AO.40.004790>

Wettle, M., Daniel, P. J., Logan, G. A., & Thankappan, M. (2009). Assessing the effect of hydrocarbon oil type and thickness on a remote sensing signal: A sensitivity study based on the optical properties of two different oil types and the HYMAP and Quickbird sensors. *Remote Sensing of Environment*, 113(9), 2000–2010. <https://doi.org/10.1016/j.rse.2009.05.010>

APPENDIX G:

PUBLICATION LIST AND COPYRIGHT CLEARANCES

1. Publication list

- Sun, S.**, and Hu, C. (2018). The challenges of interpreting oil–water spatial and spectral contrasts for the estimation of oil thickness: Examples from satellite and airborne measurements of the Deepwater Horizon oil spill. *IEEE Transactions on Geoscience and Remote Sensing*, doi:10.1109/TGRS.2018.2876091
- Sun, S.**, Hu, C., Garcia-Pineda, O., Kourafalou, V., Le Hénaff, M., and Androulidakis, Y. (2018). Remote sensing assessment of oil spills near a damaged platform in the Gulf of Mexico. *Marine Pollution Bulletin*, 136, 141-151, doi:10.1016/j.marpolbul.2018.09.004
- Sun, S.**, Lu, Y., Liu, Y., Wang, M., and Hu, C. (2018). Tracking an oil tanker collision and spilled oils in the East China Sea using multisensor day and night satellite imagery. *Geophysical Research Letters*, 45, 3212-3220, doi:10.1002/2018GL077433
- Sun, S.**, and Hu, C. (2016). Sun glint requirement for the remote detection of surface oil films. *Geophysical Research Letters*, 43, 309–316, doi:10.1002/2015GL066884
- Sun, S.**, Hu, C., Feng, L., Swayze, G.A., Holmes, J., Graettinger, G., MacDonald, I., Garcia-Pineda, O., and Leifer, I. (2016). Oil slick morphology derived from AVIRIS measurements of the Deepwater Horizon oil spill: Implications for spatial resolution requirements of remote sensors. *Marine Pollution Bulletin*, 103, 276-285, doi:10.1016/j.marpolbul.2015.12.003
- Sun, S.**, Hu, C., and Tunnell, J.W. (2015). Surface oil footprint and trajectory of the Ixtoc-I oil spill determined from Landsat/MSS and CZCS observations. *Marine Pollution Bulletin*, 101, 632-641, doi:10.1016/j.marpolbul.2015.10.036
- Wen, Y., Wang, M., Lu, Y., **Sun, S.**, Zhang, M., Mao, Z., Shi, J., and Liu, Y. (2018). An alternative approach to determine critical angle of contrast reversal and surface roughness of oil slicks under sunglint. *International Journal of Digital Earth*, 11, 972-979, doi:10.1080/17538947.2018.1470687
- Zhang, H., Wang, S., Qiu, Z., Sun, D., Ishizaka, J., **Sun, S.**, and He, Y. (2018). Phytoplankton size class in the East China Sea derived from MODIS satellite data. *Biogeosciences*, 15, 4271–4289, doi:10.5194/bg-2017-508
- Liu, Y., Hu, C., Sun, C., Zhan, W., **Sun, S.**, Xu, B., and Dong, Y. (2018). Assessment of offshore oil/gas platform status in the northern Gulf of Mexico using multi-source satellite time-series images. *Remote Sensing of Environment*, 208, 63-81, doi:10.1016/j.rse.2018.02.003.

- Lu, Y., Zhou, Y., Liu, Y., Mao, Z., Qian, W., Wang, M., Zhang, M., Xu, J., **Sun, S.**, and Du, P. (2017). Using remote sensing to detect the polarized sunglint reflected from oil slicks beyond the critical angle. *Journal of Geophysical Research: Oceans*, 122, 6342-6354, doi:10.1002/2017JC012793
- Lu, Y., Li, L., Hu, C., Li, L., Zhang, M., **Sun, S.**, and Lv, C. (2016). Sunlight induced chlorophyll fluorescence in the near-infrared spectral region in natural waters: Interpretation of the narrow reflectance peak around 761 nm. *Journal of Geophysical Research: Oceans*, 121(7), 5017-5029, doi:10.1002/2016jc011797
- Lu, Y., Hu, C., **Sun, S.**, Zhang, M., Zhou, Y., Shi, J. and Wen, Y. (2016). Overview of optical remote sensing of marine oil spills and hydrocarbon seepage. *Journal of Remote Sensing*, 20, 1259-1269 doi:10.11834/jrs.20166122
- Lu, Y., **Sun, S.**, Zhang, M., Murch, B. and Hu, C. (2016). Refinement of the critical angle calculation for the contrast reversal of oil slicks under sunglint. *Journal of Geophysical Research: Oceans*, 121, 148-161, doi:10.1002/2015JC011001.

2. Copyright clearances

Fig. 1.1a:

ELSEVIER LICENSE TERMS AND CONDITIONS

Nov 10, 2018

This Agreement between University of South Florida -- Shaojie Sun ("You") and Elsevier ("Elsevier") consists of your license details and the terms and conditions provided by Elsevier and Copyright Clearance Center.

License Number	4465510878022
License date	Nov 10, 2018
Licensed Content Publisher	Elsevier
Licensed Content Publication	Remote Sensing of Environment
Licensed Content Title	Assessing the effect of hydrocarbon oil type and thickness on a remote sensing signal: A sensitivity study based on the optical properties of two different oil types and the HYMAP and Quickbird sensors
Licensed Content Author	Magnus Wettle,Paul J. Daniel,Graham A. Logan,Medhavy Thankappan
Licensed Content Date	Sep 1, 2009
Licensed Content Volume	113
Licensed Content Issue	9
Licensed Content Pages	11
Start Page	2000
End Page	2010
Type of Use	reuse in a thesis/dissertation
Portion	figures/tables/illustrations
Number of figures/tables /illustrations	1
Format	both print and electronic
Are you the author of this Elsevier article?	No
Will you be translating?	No
Original figure numbers	Figure 3
Title of your thesis/dissertation	Optical remote sensing of oil spills in the Gulf of Mexico
Expected completion date	Nov 2018
Estimated size (number of pages)	150
Requestor Location	University of South Florida 140 7th Avenue South SAINT PETERSBU, FL 33701 United States Attn: University of South Florida
Publisher Tax ID	98-0397604
Total	0.00 USD
Terms and Conditions	

INTRODUCTION

1. The publisher for this copyrighted material is Elsevier. By clicking "accept" in connection with completing this licensing transaction, you agree that the following terms



Title: The Challenges of Interpreting Oil-Water Spatial and Spectral Contrasts for the Estimation of Oil Thickness: Examples From Satellite and Airborne Measurements of the Deepwater Horizon Oil Spill

Author: Shaojie Sun

Publication: Geoscience and Remote Sensing, IEEE Transactions on

Publisher: IEEE

Date: Dec 31, 1969

Copyright © 1969, IEEE

Logged in as:
Shaojie Sun
University of South Florida
Account #:
3001250180

LOGOUT

Thesis / Dissertation Reuse

The IEEE does not require individuals working on a thesis to obtain a formal reuse license, however, you may print out this statement to be used as a permission grant:

Requirements to be followed when using any portion (e.g., figure, graph, table, or textual material) of an IEEE copyrighted paper in a thesis:

- 1) In the case of textual material (e.g., using short quotes or referring to the work within these papers) users must give full credit to the original source (author, paper, publication) followed by the IEEE copyright line © 2011 IEEE.
- 2) In the case of illustrations or tabular material, we require that the copyright line © [Year of original publication] IEEE appear prominently with each reprinted figure and/or table.
- 3) If a substantial portion of the original paper is to be used, and if you are not the senior author, also obtain the senior author's approval.

Requirements to be followed when using an entire IEEE copyrighted paper in a thesis:

- 1) The following IEEE copyright/ credit notice should be placed prominently in the references: © [year of original publication] IEEE. Reprinted, with permission, from [author names, paper title, IEEE publication title, and month/year of publication]
- 2) Only the accepted version of an IEEE copyrighted paper can be used when posting the paper or your thesis on-line.
- 3) In placing the thesis on the author's university website, please display the following message in a prominent place on the website: In reference to IEEE copyrighted material which is used with permission in this thesis, the IEEE does not endorse any of [university/educational entity's name goes here]'s products or services. Internal or personal use of this material is permitted. If interested in reprinting/republishing IEEE copyrighted material for advertising or promotional purposes or for creating new collective works for resale or redistribution, please go to http://www.ieee.org/publications_standards/publications/rights/rights_link.html to learn how to obtain a License from RightsLink.

If applicable, University Microfilms and/or ProQuest Library, or the Archives of Canada may supply single copies of the dissertation.

BACK

CLOSE WINDOW

Appendix B:

JOHN WILEY AND SONS LICENSE TERMS AND CONDITIONS

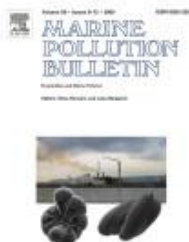
Nov 10, 2018

This Agreement between University of South Florida -- Shaojie Sun ("You") and John Wiley and Sons ("John Wiley and Sons") consists of your license details and the terms and conditions provided by John Wiley and Sons and Copyright Clearance Center.

License Number	4465511436882
License date	Nov 10, 2018
Licensed Content Publisher	John Wiley and Sons
Licensed Content Publication	Geophysical Research Letters
Licensed Content Title	Sun glint requirement for the remote detection of surface oil films
Licensed Content Author	Chuanmin Hu, Shaojie Sun
Licensed Content Date	Jan 14, 2016
Licensed Content Volume	43
Licensed Content Issue	1
Licensed Content Pages	8
Type of use	Dissertation/Thesis
Requestor type	Author of this Wiley article
Format	Print and electronic
Portion	Full article
Will you be translating?	No
Title of your thesis / dissertation	Optical remote sensing of oil spills in the Gulf of Mexico
Expected completion date	Nov 2018
Expected size (number of pages)	150
Requestor Location	University of South Florida 140 7th Avenue South SAINT PETERSBU, FL 33701 United States Attn: University of South Florida
Publisher Tax ID	EU826007151
Total	0.00 USD
Terms and Conditions	

TERMS AND CONDITIONS

This copyrighted material is owned by or exclusively licensed to John Wiley & Sons, Inc. or one of its group companies (each a "Wiley Company") or handled on behalf of a society with which a Wiley Company has exclusive publishing rights in relation to a particular work (collectively "WILEY"). By clicking "accept" in connection with completing this licensing transaction, you agree that the following terms and conditions apply to this transaction (along with the billing and payment terms and conditions established by the Copyright



Title: Oil slick morphology derived from AVIRIS measurements of the Deepwater Horizon oil spill: Implications for spatial resolution requirements of remote sensors

Author: Shaojie Sun, Chuanmin Hu, Lian Feng, Gregg A. Swayze, Jamie Holmes, George Graettinger, Ian MacDonald, Oscar Garcia, Ira Leifer

Publication: Marine Pollution Bulletin

Publisher: Elsevier

Date: 15 February 2016

Copyright © 2015 Elsevier Ltd. Published by Elsevier Ltd. All rights reserved.

Logged in as:
Shaojie Sun
University of South Florida
Account #:
3001250180

[LOGOUT](#)

Please note that, as the author of this Elsevier article, you retain the right to include it in a thesis or dissertation, provided it is not published commercially. Permission is not required, but please ensure that you reference the journal as the original source. For more information on this and on your other retained rights, please visit: <https://www.elsevier.com/about/our-business/policies/copyright#Author-rights>

[BACK](#)

[CLOSE WINDOW](#)

Copyright © 2018 [Copyright Clearance Center, Inc.](#) All Rights Reserved. [Privacy statement](#). [Terms and Conditions](#).

Comments? We would like to hear from you. E-mail us at customer@copyright.com

Appendix D:

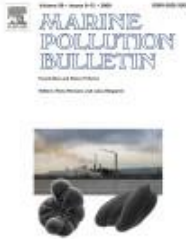


RightsLink®

Home

Account Info

Help



Title: Surface oil footprint and trajectory of the Ixtoc-I oil spill determined from Landsat/MSS and CZCS observations
Author: Shaojie Sun, Chuanmin Hu, John W. Tunnell
Publication: Marine Pollution Bulletin
Publisher: Elsevier
Date: 30 December 2015
Copyright © 2015 Elsevier Ltd. All rights reserved.

Logged in as:
Shaojie Sun
University of South Florida
Account #:
3001250180
[LOGOUT](#)

Please note that, as the author of this Elsevier article, you retain the right to include it in a thesis or dissertation, provided it is not published commercially. Permission is not required, but please ensure that you reference the journal as the original source. For more information on this and on your other retained rights, please visit: <https://www.elsevier.com/about/our-business/policies/copyright#Author-rights>

[BACK](#)

[CLOSE WINDOW](#)

Copyright © 2018 [Copyright Clearance Center, Inc.](#) All Rights Reserved. [Privacy statement.](#) [Terms and Conditions.](#)
Comments? We would like to hear from you. E-mail us at customer@copyright.com

Appendix E:



RightsLink®

Home

Account Info

Help



Title: Remote sensing assessment of oil spills near a damaged platform in the Gulf of Mexico

Author: Shaojie Sun, Chuanmin Hu, Oscar Garcia-Pineda, Vassiliki Kourafalou, Matthieu Le Hénaff, Yannis Androulidakis

Publication: Marine Pollution Bulletin

Publisher: Elsevier

Date: November 2018

© 2018 Published by Elsevier Ltd.

Logged in as:

Shaojie Sun
University of South Florida

Account #:
3001250180

LOGOUT

Please note that, as the author of this Elsevier article, you retain the right to include it in a thesis or dissertation, provided it is not published commercially. Permission is not required, but please ensure that you reference the journal as the original source. For more information on this and on your other retained rights, please visit: <https://www.elsevier.com/about/our-business/policies/copyright#Author-rights>

BACK

CLOSE WINDOW

Copyright © 2018 [Copyright Clearance Center, Inc.](#) All Rights Reserved. [Privacy statement.](#) [Terms and Conditions.](#)

Comments? We would like to hear from you. E-mail us at customercare@copyright.com

Appendix F:

**JOHN WILEY AND SONS LICENSE
TERMS AND CONDITIONS**

Nov 10, 2018

This Agreement between University of South Florida -- Shaojie Sun ("You") and John Wiley and Sons ("John Wiley and Sons") consists of your license details and the terms and conditions provided by John Wiley and Sons and Copyright Clearance Center.

License Number	4465520205164
License date	Nov 10, 2018
Licensed Content Publisher	John Wiley and Sons
Licensed Content Publication	Geophysical Research Letters
Licensed Content Title	Tracking an Oil Tanker Collision and Spilled Oils in the East China Sea Using Multisensor Day and Night Satellite Imagery
Licensed Content Author	Chuanmin Hu, Mengqiu Wang, Yongxue Liu, et al
Licensed Content Date	Apr 6, 2018
Licensed Content Volume	45
Licensed Content Issue	7
Licensed Content Pages	9
Type of use	Dissertation/Thesis
Requestor type	Author of this Wiley article
Format	Print and electronic
Portion	Full article
Will you be translating?	No
Title of your thesis / dissertation	Optical remote sensing of oil spills in the Gulf of Mexico
Expected completion date	Nov 2018
Expected size (number of pages)	150
Requestor Location	University of South Florida 140 7th Avenue South SAINT PETERSBU, FL 33701 United States Attn: University of South Florida
Publisher Tax ID	EU826007151
Total	0.00 USD
Terms and Conditions	

TERMS AND CONDITIONS

This copyrighted material is owned by or exclusively licensed to John Wiley & Sons, Inc. or one of its group companies (each a "Wiley Company") or handled on behalf of a society with which a Wiley Company has exclusive publishing rights in relation to a particular work (collectively "WILEY"). By clicking "accept" in connection with completing this licensing transaction, you agree that the following terms and conditions apply to this transaction